

# Synthesis and Analysis of Parallel Kinematic XY Flexure Mechanisms

By

Shorya Awtar

B.Tech., Mechanical Engineering, 1998  
Indian Institute of Technology, Kanpur, India

M.S., Mechanical Engineering, 2000  
Rensselaer Polytechnic Institute, Troy, NY

Submitted to the Department of Mechanical Engineering in partial fulfillment  
Of the requirements for the degree of  
Doctor of Science in Mechanical Engineering

at the

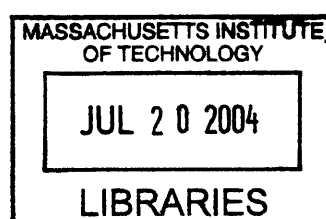
Massachusetts Institute of Technology  
February, 2004

© 2003 Massachusetts Institute of Technology  
All rights reserved

Signature of author                  ✓  
Department of Mechanical Engineering  
19 December 2003

Certified by                                   Alexander H. Slocum  
Professor of Mechanical Engineering, Mac Vicar Faculty Fellow

Accepted by                                                     
Chairman, Department Committee on Graduate Students



ARCHIVES



# Synthesis and Analysis of Parallel Kinematic XY Flexure Mechanisms

by Shorya Awtar

submitted to the Department of Mechanical Engineering  
on December 19, 2003 in partial fulfillment of the requirements for the  
degree of Doctor of Science in Mechanical Engineering

This thesis presents a family of XY flexure mechanisms with large ranges of motion, first-order decoupled degrees of freedom, and small parasitic error motions. Synthesis is based on an systematic and symmetric layout of constraints that are realized by means of common flexure building blocks. An analytical formulation incorporating geometric nonlinearities is used in deriving the characteristics of these flexure building blocks. Of concern are issues related to qualification and quantification of undesirable motions, mobility, stiffness variation within the range of motion, determination of center of stiffness, and sensitivity to manufacturing and assembly tolerances. Based on the properties of the building blocks, the performances characteristics of the resulting XY flexure mechanisms are discussed and the influence of symmetry in reducing error motions is analytically illustrated.

To verify the design theory, a 300mm x 300mm prototype stage was fabricated, assembled and tested at the National Institute of Standards and Technology (NIST). Measurements using laser interferometry, autocollimation and capacitance gauges indicate levels of performance much better than the capabilities of the current state of the art of precision flexure stages. The prototype flexure stage has a 5mm x 5mm range of motion, with cross-axis errors of the order of one part in one thousand, and motion stage yaw errors of the order of a few arc seconds.

Thesis Supervisor: Alexander H. Slocum

Title: Professor of Mechanical Engineering, Mac Vicar Faculty Fellow



## Acknowledgement

Prof. Alex Slocum has mentored, guided and inspired me in my academic as well as personal life, and therefore is my *guru*. I express my gratitude for the education that I have received from him.

I would like to acknowledge the help of my committee members Professors Samir Nayfeh and Martin Culpepper of MIT, and Dr. William Plummer of WTP Optics, during the course of this thesis. I would also like to acknowledge the role of my professors at Rensselaer Polytechnic Institute and the Indian Institute of Technology at Kanpur, in helping me learn the fundamentals of the mechanical engineering discipline.

The experimental part of this thesis would have been impossible without the unconditional help offered by Nicholas Dagalakis, Jason Gorman and Kevin Lyons of the Intelligent Systems Division at the National Institute of Standards and Technology, Gaithersburg, MD.

Finally, I want to acknowledge several machinists and instrument makers for their contribution to the hardware made for this thesis and to my learning of machine design. These include Gerry Wentworth of the MIT LMP machine shop, Ken Stone of MIT hobby shop, Mike Luparelli of the MIT Central Machine Shop, and Dwight Barry of the NIST Fabrication Division.



# List of Contents

Chapter 1. Introduction	11
1.1 Flexures	11
1.2 Background	13
1.3 Flexure Mechanisms for Motion Control	16
1.4 Contributions	18
Chapter 2. Synthesis of Parallel Kinematic XY Flexure Mechanisms	23
2.1 Design Requirements and Challenges	23
2.2 Proposed Design Principle for a Two Axis Flexure Mechanism	31
2.3 XY Flexure Mechanism based on the simple Beam Flexure	35
2.4 XY Flexure Mechanism based on the Parallelogram Flexure	37
2.5 XY Flexure Mechanism based on the Double Parallelogram Flexure	42
Chapter 3. Non-linear Beam Bending Static Analysis	51
3.1 Beam Bending Analysis	52
3.2 Engineering Approximations and Simplified Results	63
3.3 Observations and Comments on the Simplified Results	68
3.4 Mobility of Flexure Mechanisms	72
3.5 Error motions in Flexure Mechanisms	78
3.6 Energy Methods	80
Chapter 4. Analysis of Basic Flexure Building Blocks	83
4.1 Parallelogram Flexure	83
4.2 Double Parallelogram Flexure	94
Chapter 5. Static Non-Linear Analysis of Parallel Kinematic XY Flexure Mechanisms	101
5.1 Preliminary Discussion	102
5.2 XY Flexure Mechanism Design 3	105
5.3 XY Flexure Mechanism Design 4	118
5.4 XY Flexure Mechanism Design 5	130

5.5 XY Flexure Mechanism Design 6	142
5.6 Concluding Remarks	156
Chapter 6. Fabrication, Assembly and Experimental Test Set-up	157
6.1 Metrology Objectives	157
6.2 Choice of Material	158
6.3 Choice of Manufacturing Process	159
6.4 Actuation Methods	161
6.5 Sensor Schemes	167
6.6 In-plane Capacitance Probe/Actuator Clamping Mechanism	173
6.7 Metrology Alignments	176
Chapter 7. Experimental Measurements	181
7.1 Primary Motion and Stiffness	181
7.2 Cross-axes Coupling Error	183
7.3 Parasitic Yaw Error	187
Appendix A: Multiple DOF Flexure Mechanisms	189
References	193

**This page is intentionally left blank**

**This page is intentionally left blank**

# Chapter 1. Introduction

## 1.1 Flexures

Flexure mechanisms are a designer's delight. Except for the limits of elasticity, flexures present few other boundaries as far as applications are concerned. Flexures have been used as bearings to provide smooth and guided motion, for example in precision motion stages; as springs to provide preload, for example in the brushes of a DC motor or a camera lens cap; to avoid over-constraint, as in the case of bellows or helical coupling; as clamping devices, for example, the collet of a lathe; for elastic averaging as in a windshield wiper; and for energy storage, such as, in a bow or a catapult. This list encompasses applications related to the transmission of force, displacement as well as energy, thereby making the versatility of flexures quite evident.

Flexures are compliant structures that rely on material elasticity for their functionality. Motion is generated due to deformation at the molecular level, which results in two primary characteristics of flexures – smooth motion and small range of motion. From the perspective of precision machine design, one may think of flexures as being means for providing constraints. It is this capability of providing constraints that make flexures a specific subset of springs. In fact, all the applications listed above may be resolved in terms of constraint design.

The importance of properly constrained design is well known to the engineering community [1-5]. The objective of an ideal constraining element, mechanism, or device is to provide infinite stiffness and zero displacements along certain directions, and allow infinite motion and zero stiffness along all other directions. The directions that are constrained are known as *Degrees of Constraint* (DOC), whereas the directions that are unconstrained are referred to as *Degrees of Freedom* (DOF)<sup>1</sup>. While designing a machine or a mechanism so that it has appropriate constraints, the designer faces a choice between various kinds of constraining elements, two of which are considered in Fig. 1.1 for comparison: ball bearings and flexures.

Clearly, ball bearings meet the definition of a constraint quite well, since they are very stiff in one direction, and provide very low resistance to motion in other directions. Nevertheless, motion in the direction of DOF is associated with undesirable effects such as friction, stiction and backlash, that typically arise at the interface of two surfaces. These effects are non-deterministic in nature, and limit the motion quality.

---

<sup>1</sup> A more careful definition for DOF and DOC shall be discussed in the subsequent chapters.

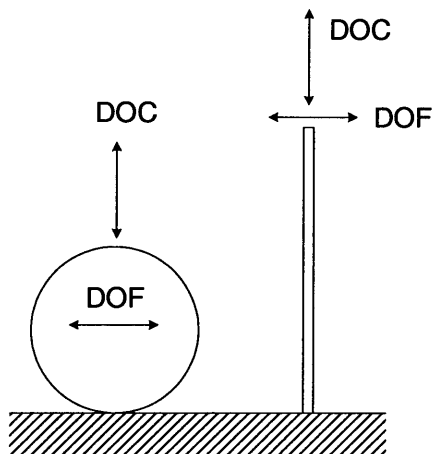


*Fig. 1.1 Examples of typical constraint elements*

Flexures, on the other hand, allow for very clean and precise motion. Since the displacement in flexures is an averaged consequence of molecular level deformations, the phenomena of friction, stiction and backlash are entirely eliminated. The questionable issue here, though, is the effectiveness of flexures in terms of providing constrained motion. Consider, for example, a thin strip of spring steel, which is a common flexure element, as illustrated in Fig. 1.1. It is obvious that the steel strip is very stiff in tension, producing a DOC, and compliant in flexion, resulting in some DOF. Yet, neither is the stiffness along the DOC infinite, nor is the range of motion along the DOF infinite. Furthermore, the stiffness values along the Degrees of Freedom and Constraint may vary with load and deformation, which is yet another critical deviation from ideal constraint behavior.

Thus, there exists a tradeoff between two important attributes in constraint elements – quality of motion along the DOF and quality of constraint along the DOC. In ball bearings, the quality of the DOC is close to ideal but the quality of motion along the DOF is compromised. Typically, a motion accuracy better than 0.1 micron is difficult to achieve [2]. In the case of flexures, while the quality of motion is several orders of magnitude better, the quality of constraint may be non-ideal. Despite this, there are at least two reasons that make flexures very desirable as constraint elements in mechanisms where small motion is acceptable. One, they are elegantly simple in construction and assembly and thus score over options like air bearings and magnetic bearings. Second, although the constraining effect of a flexure may not be ideal, it is repeatable and thoroughly predictable. Principles of mechanics provide all the tools that are necessary to determine the force-displacement characteristics of flexure mechanisms.

In fact, the non-ideal constraint behavior of flexures is not entirely a drawback. Finite stiffness along the DOF and DOC may be cleverly used to advantage in preloading and elastic averaging, respectively. For

example, while a multiple parallelogram rigid link mechanism (Fig.1.2a) is prone to over-constraint, a multi-parallelogram flexure mechanism (Fig. 1.2b) is not only feasible but also results in some performance improvements.

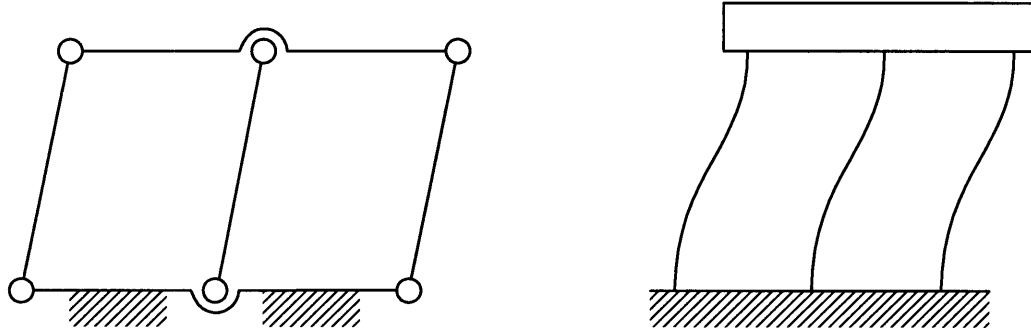


*Fig. 1.2 a) Multiple parallelogram linkage mechanism b) Multiple parallelogram flexure mechanism*

In applications such as nanometric positioning, the high quality motion attribute of flexures so strongly outweighs any limitations that most existing nanopositioners are essentially based on flexures. A further advantage of using flexures is that the trouble of assembly can be minimized by making the mechanism monolithic. This makes flexures indispensable for micro-fabrication, where assembly is generally difficult, or even impossible. Thus, despite small range of motion and a fundamental performance tradeoff between the DOF and DOC, flexures remain important machine elements.

## 1.2 Background

Given the wide applicability and advantages of flexures, there exists a considerable amount of design knowledge on these devices [1-19]. A historical background of flexures is presented in several texts [6-8]. While flexure design has been traditionally based on creative thinking and engineering intuition, analytical tools can aid the design conception, evaluation and optimization process. Consequently, a systematic study and modeling of these devices has been an active area of research.

Some of the existing literature deals with precision mechanisms that use flexures as replacements for conventional hinges, thus eliminating friction and backlash [7-10]. Analysis and synthesis of these mechanisms is simply an extension of the theory that has already been developed for rigid link mechanisms, except that in this case the range of motion is typically small. The key aspect of these mechanisms is flexure hinge design [10-12]. Unlike these cases where compliance in the system is limited to the hinges, other flexure mechanisms exist in which compliance is distributed over a larger part of the

entire topology[1-10, 16-19]. Both these kinds of mechanisms offer a rich mine of innovative and elegant design solutions for a wide range of applications.

Any systematic flexure design exercise has to be based on performance measures. While detailed performance measures can be laid out depending on specific applications, a general set of measures are highlighted here. These measures are based on the deviation of flexures from ideal constraints.

One set of important performance measures are the Degrees of Constraint and Freedom of a flexure mechanism. While Gruebler's criteria may be used for the constraint analysis of rigid-link mechanisms connected by flexible hinges [7-9], distributed compliance mechanisms pose significant challenges. Modifications to Gruebler's criteria based on a compliance number concept have been made to encompass compliant mechanisms as well [20-22]. Nevertheless, a generalized definition for DOF and DOC of a flexure element or mechanism, that addresses issues related to variable stiffness and overconstraint, is not readily available in the current literature.

Another important performance measure in flexure mechanisms is accuracy of motion. Any deviation from the intended motion trajectory may be termed as undesired motion or parasitic error motion [1-2,8]. Even though repeatability in flexure mechanisms is guaranteed because of continuum elastic medium, parasitic error motions affect the motion accuracy. Despite the importance of error motions in determining the performance of flexure mechanisms, the current literature discusses these terms in the context of specific mechanisms, and does not provide a broader definition based on qualitative and quantitative analyses. Typically, designers strive to eliminate or minimize these errors by making insightful use of geometry and symmetry.

The stiffness values along the DOF and DOC of a flexure mechanism are key dynamic performance measures while designing a motion system. Apart from damping, which is often added externally, the stiffness and mass properties of the mechanism determine its dynamic characteristics. While masses remain constant, stiffness may vary with displacements. In motion control applications, it is important to exactly characterize this variation in stiffness so that the controller in a feedback scheme may be designed to be robust against such variations. Such variations in the stiffness are commonly not addressed in flexure design. While, it may not be obvious immediately, parasitic errors, cross-axis coupling, variation in stiffness with deformations, DOF and DOC are all very related concepts and cannot be dealt with in isolation.

As observed earlier, small range of motion is inherent to the nature of flexures. The maximum allowable range of motion therefore also becomes a key performance metric for a flexure mechanism. Range of motion depends on static and fatigue failure criteria, all of which are well researched and documented

[23]. Measures such as sensitivity to thermal disturbances and manufacturing tolerances are also very important in characterizing the performance of a flexure mechanism, but are generally application specific.

The above-mentioned static and dynamic performance measures are only some of the most important considerations in flexure mechanism design. Based on such performance measures, many researchers have attempted the analysis and synthesis of flexure mechanisms. The biggest tradeoff in any analysis method is that between the generality of the theory, computational complexity involved, and scope of results. On one extreme are Finite Elements based methods that can be used for mechanisms of any shape and size, are computationally intensive, and provide little parametric information. On the other hand are simplified models, for example, pseudo-rigid-body models [9,16] that involve less computational complexity, provide parametric performance information, but are limited in their scope of application. Computationally efficient matrix based methods with macroscopic building blocks also exist for the small range motion analysis of 3D mechanisms [19]. But in general, analysis is not as big a challenge in flexure design as is synthesis.

Synthesis boils down to the simple question – how does one create a new flexure mechanism to meet certain requirements? Because of the vast and open-ended nature of mechanism design space, the answer remains somewhat elusive. Most designers rely on their intuition and experience for this step. Yet, for the sake of systematization, mechanism design is generally broken down into three hierarchies, topology synthesis, shape synthesis and size synthesis [17, 18]. Shape and size, in this context, refer to the shape and size of individual elements or building blocks that constitute a topology. Given a topology, there are several deterministic means of achieving shape and size synthesis. For mechanisms with compliance limited to the hinges, or those which can be approximated using pseudo-rigid-body models, there are methods of kinematic synthesis [24] and kinetostatic synthesis [14]. For mechanisms with distributed compliance, advanced methods based on structural optimization exist [25-27].

Topological synthesis of mechanisms has also been attempted based on multi-objective structural optimization using numerical and analytical techniques [25, 28-30]. While analytically very powerful, it is seen that these synthesis methods result in a somewhat narrow family of designs, which may be attributed to the fact that these optimization routines work within a specified design space. Numerical or analytical optimization is best suited for shape and size synthesis, when a topology already exists. In the true sense of synthesis, there really does not exist any topological or conceptual design methodology that can produce the best mechanism that will meet a given set of motion, force or stiffness requirements. A combination of creative thinking, aided with analytical tools and optimization techniques is probably the best available recipe for flexure mechanism design.

### **1.3 Flexure Mechanisms for Motion Control**

One of the primary applications of flexures is in the design of motion stages. A motion system is typically comprised of some fundamental components – payload stage, payload bearing system, actuator, sensors and a control strategy. When highly precise motion is desired, each of these components has to be chosen or designed carefully. Although flexures provide excellent payload bearings in terms of precise motion, the design of the motion system is not simply limited to the design of the flexure bearing, but has to encompass all the other components.

Numerous single DOF and multi DOF flexure systems have been presented in the technical literature, some of which are referenced in [31]. It is generally less difficult to design a single DOF motion system [32-35] because one does not have to worry about the interaction between the components of the various axes. Motion, actuation and sensing all take place in one direction only. To achieve large range of motion and yet high resolution, the use of coarse – fine positioning scheme is common. One can employ a coarse-fine bearing stage, a coarse-fine actuation system [33], mechanical amplifiers [35-36], and even a coarse-fine sensor arrangement.

The design of multi DOF motion systems becomes quite challenging, because the interaction between the components of the various axes in the system results in conflicting requirements being imposed on the flexure bearing design, as well as on the choice of actuators and sensors. These conflicts in requirements and their consequences on performance shall be discussed in Chapter 2.

There are two well-known configurations employed in the design of multi DOF flexure bearing stages – serial kinematics and parallel kinematics. Each configuration has its own set of pros and cons. In serial design, multiple DOF are achieved by stacking single DOF systems, one on other. The technical literature presents several such designs, where this stacking is done either out-of-plane [37-39] or in-plane [40-42]. Serial kinematic mechanisms are relatively simple to design, and have substantially decoupled degrees of freedom, but at the same time incorporate moving actuators and cables that limit the dynamic performance. Moving cables are sources of disturbance, which is detrimental for nanometric positioning. Moving actuators, specially when large range of motion is desired, are bulky and reduce the bandwidth of the axes that carry them. Furthermore, moving actuators and connections are also undesirable for flexure mechanisms used in MEMS applications due to fabricability reasons. Parallel kinematic designs [43-58] are free of these problems due to ground mounted actuators, and are also usually more compact, but on the other hand, provide smaller ranges of motion and exhibit significant cross-axis coupling. Furthermore, the stiffness of one axis varies with motion or force along the other axes. This affects the static as well as dynamic performance of the mechanism.

Most serial and parallel mechanisms do not follow a formal design procedure in their topological conception. As mentioned already, serial designs are usually constructed by stacking single DOF stages. Parallel designs, on the other hand, are constructed by adding the necessary number of constraints to achieve the desired DOF. Such a construction of parallel kinematic mechanisms limits the range of motion, for reasons explained in Chapter 2. Figures 1.3 and 1.4 illustrate typical examples of each kind.

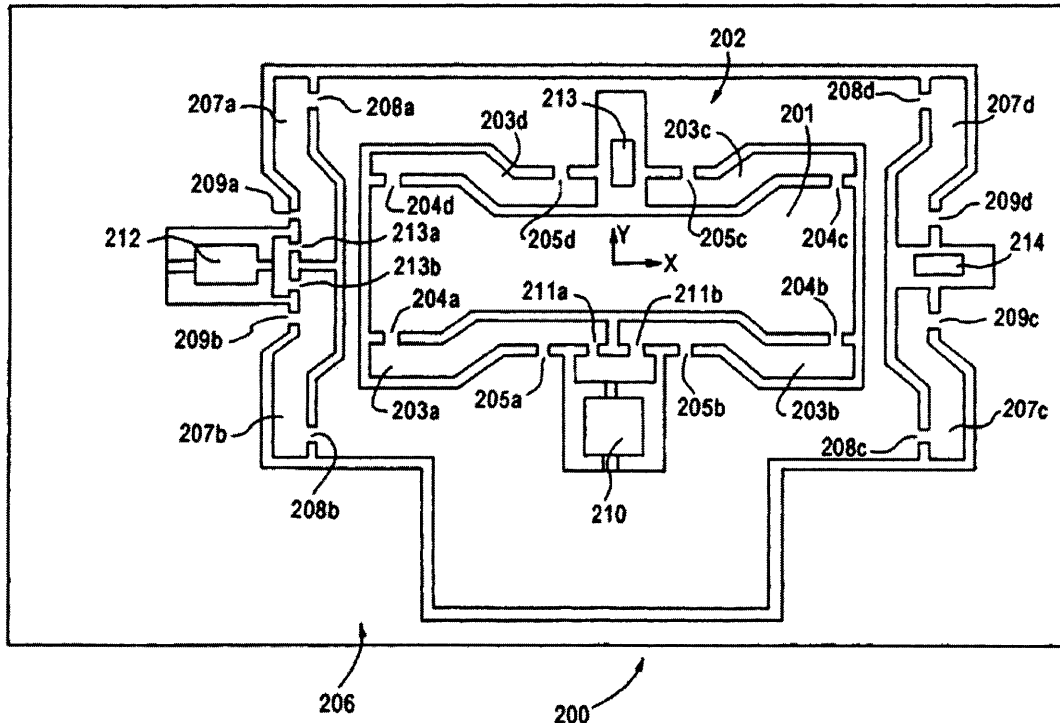


*Fig. 1.3 A Two DOF (X-Y) Serial Mechanism [45]*

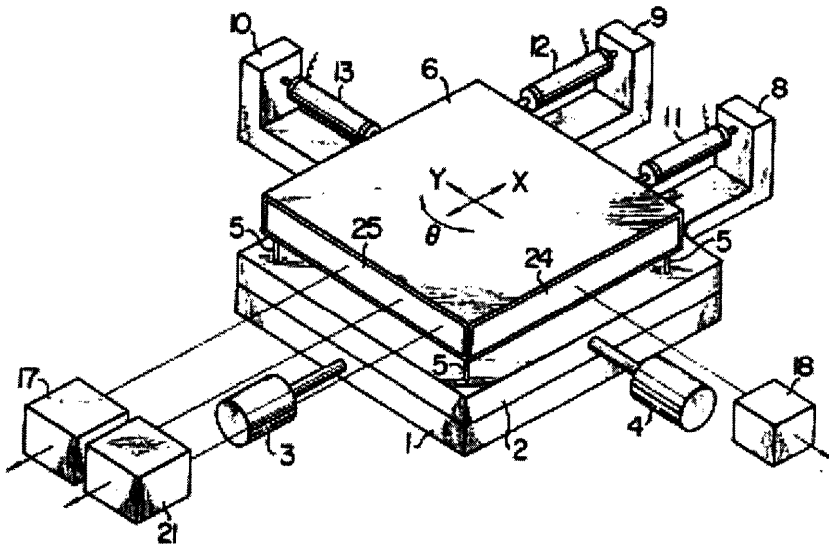


*Fig. 1.4 A Three DOF (XYθ) Parallel Mechanism [51]*

## 1.4 Contributions

Summarizing the above discussions, the metrics that influence the static and dynamic performance of flexure mechanisms, and are important considerations in mechanism design, include

- a) Range of motion and failure limits
- b) Degrees of Freedom, Degrees of Constraint and over-constraint
- c) Undesirable motions including parasitic errors and cross-axis coupling errors
- d) Variation in stiffness along DOF and DOC due to forces and/or displacements
- e) Thermal sensitivity
- f) Manufacturing sensitivity

If designed for motion control, some other factors that are of concern are

- g) Hysteresis and creep
- h) Choice of sensors and actuators
- i) Damping of critical vibration modes
- j) Choice of control strategy

These performance measures and design considerations shall be explained in more detail in the subsequent chapters, and it will also become apparent that several tradeoffs exist between these factors.

As indicated earlier, existing flexure mechanism design approaches fall under two distinct categories. There is a traditional approach that is based on creative thinking and intuition. While this approach has resulted in several new topologies, it has earned the reputation of being a black art. Due to the lack of an analytical basis and a systematic approach, only a percentage of the designs that are thus conceived have acceptable performance. On the other hand, there are approaches that have a mathematical foundation, but allow for little creative inputs from the designer, resulting in few new designs. If one thinks about the problem in terms of genetics, the first approach is an analog of mutation, whereas the latter approach loosely represents cross-over. While each method has its strengths, by themselves they have proved to be inadequate in terms of being able to address the concerns listed above.

This thesis strives to bridge the gap between intuition and mathematical analysis in flexure mechanism design. Based on an understanding of the challenges involved in multi DOF flexure mechanism design, it proposes several new XY mechanisms with large ranges of motion, and provides a performance evaluation of each variant. This thesis also presents simple analytical tools that aid the intuition of a design engineer – tools that can be used to quickly and accurately estimate the stiffness of a mechanism in various directions, that can help identify over-constraining arrangements, that can be used to estimate error motions in a mechanism, validate the role of symmetry in design, and at the same time provide parametric understanding of the design space.

Arguments based on intuition and symmetry can indeed be used in many cases to answer performance related questions without resorting to analysis. This is illustrated in Fig 1.5 by posing the following simple question – Where should a transverse load be applied to a uniform beam so as to produce zero rotation between the two ends? Rigid extension arms are attached to the two ends of the beam so that both transverse forces and moments may be applied without having to show the moments explicitly. The forces applied on each arm need to balance out and therefore are equal and opposite.

Intuition tells us that the transverse force should be applied at the mid-span of the beam to ensure zero slope between the two ends. This intuition is not baseless and is easily validated by symmetry arguments. Referring to Fig. 1.5B, where the load has been applied along the mid-line, consider a hypothetical deformed configuration of the beam such that the relative angle between the ends is not zero. Now flip this picture about Axis 1, to obtain the picture of Fig. 1.5C, and then once again about Axis 2 to obtain the picture shown in Fig 1.5D. Comparing figures 1.5B and 1.5D, one can see that the geometry and the loading are identical. Therefore, by symmetry the deformations in two cases also have to be identical. Clearly, this will not be the case if there is a relative rotation between the two ends, and the only deformation that satisfies the requirements of symmetry is one in which the two ends remain parallel. Thus, we see that only a load applied along the mid-line will produce a zero slope.

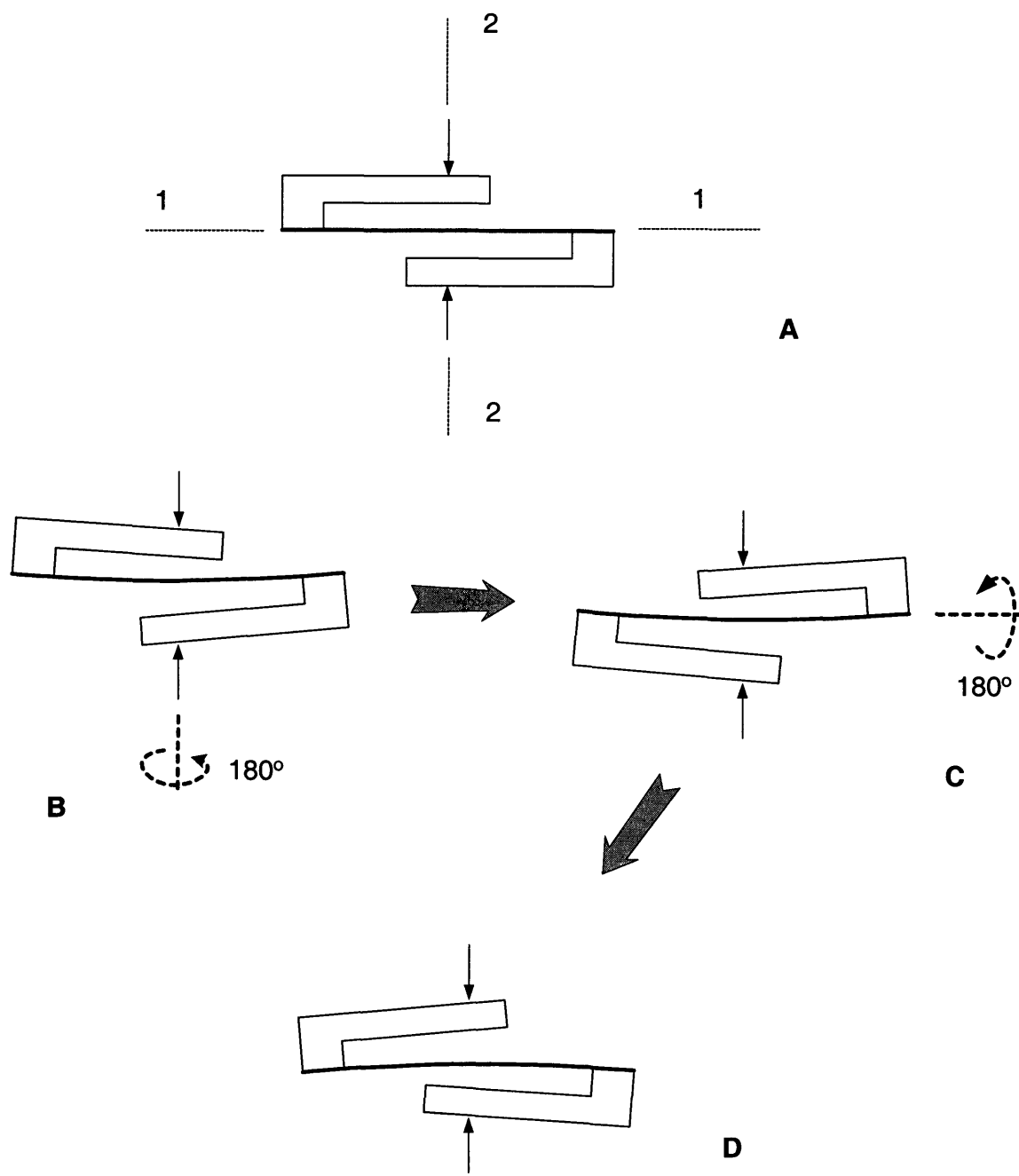


*Fig. 1.5 Arguments of symmetry applied to a uniform beam*

In fact, a symmetric S-shaped deformation with zero relative angle between the ends, passes the above test of symmetry. We are thus able to obtain an answer to our original question without involving the principles of solid mechanics, except force equilibrium, and irrespective of the constitutive properties of the material. Several variations of such symmetry based arguments may be used in many cases to obtain useful performance information. But as one adds further complexity to the problem, for example, apply an

axial load in the current case, the scenario changes. In the deformed configuration, one now has to add an additional moment due to the axial load, to satisfy force equilibrium. This additional moment results in a loss of loading symmetry, and the above arguments are no longer valid. It therefore becomes impossible to qualitatively determine the line of transverse force application that will produce a zero end slope.

Thus, we see that intuition is powerful and helps in design decisions, but only up to a certain extent, beyond which complexity in the system takes over. In such situations, mathematical analysis becomes a handy tool. The above example illustrates that both intuition as well as analysis are indispensable for design, and reflects the general flavor of this thesis.

Accordingly, the following list highlights the specific contributions of this thesis.

- 1) Several new parallel kinematic XY flexure mechanism designs are proposed based on a systematic and symmetric arrangement of flexure units, as opposed to the current methods of synthesis. This approach allows us to create flexure mechanisms in a deterministic fashion, and at the same time achieve impressive performance measures in terms of range of motion, cross-axis coupling and parasitic errors. Chapter 2 presents the XY mechanism designs, while Appendix A illustrates several other multiple DOF mechanisms.
- 2) A non-linear static analysis is presented to evaluate the proposed XY mechanism designs. The force-displacement characteristics of various flexure units are quantified, with specific consideration to the coupling effects between the displacements and forces along various directions. Chapters 3 presents the non-linear analysis of a uniform beam flexure, and based on several insightful engineering approximations, concludes with simplified symbolic results. These results allow us to analytically consider the concepts of mobility, error motions, variation in stiffness, center of stiffness, sensitivity to geometry and assembly, and generalization to other shapes. The application and limitations of energy principles in this context are also briefly discussed.

Chapter 4 provides a similar analysis for two other common flexure units, namely, the parallelogram and double parallelogram flexures. In Chapter 5, some of the mechanism designs from Chapter 2 are comparatively evaluated for their performance.

- 3) The fabrication, assembly and experimental test step-up of an XY flexure stage, chosen on the basis of the above synthesis and analysis exercise, is presented in Chapter 6. Issues related to choice of material, manufacturing process, sensors and actuators are discussed. The experimental set-up is designed to be modular so that it can accommodate multiple sensors and actuators. A preliminary comparison is made between the two potential fabrication techniques: water-jet cutting and electric discharge machining. To achieve an assembly that is free of friction and backlash, a new clamping

mechanism that effectively holds the cylindrical actuator and cap-probes has been invented. In the design of the metrology set-up, a classic alignment problem has been revisited and is discussed in detail.

A comprehensive measurement and characterization of the XY stage that has been performed, and is presented in Chapter 7. Impressive performance results have been obtained, that match the analytical predictions. The prototype XY mechanism has an overall size of 300mm x 300mm x 25mm, and provides a 5mm x 5mm range of motion. Over this range of motion, cross axes errors of less than 1 part in 1000, and parasitic motion stage yaw of less than 3 arc seconds are recorded. A simple motion control design, which incorporates a closed-loop coarse actuator and open-loop fine actuator has been implemented to achieve 5nm positioning accuracy, which is currently limited by the resolution of the laser interferometer transducer.

There are several areas directly related to this work presented in this thesis that offer much scope for future work. These topics are briefly listed here.

- 1) Given the XY Flexure mechanism designs, a thorough dynamic system analysis and controls design is necessary to achieve motion control over a large bandwidth. The passive dynamics of the system in terms of its natural frequencies, mode shapes, and internal resonance conditions need to be analytically and experimentally determined. The problem of colocated and non-colocated controls in the presence of a variable drive stiffness needs to be addressed. Passive damping strategies that can provide dissipation over large frequency ranges are desirable. Hysteresis and creep associated with piezo-actuators commonly used in micro/nanopositioners need to be addressed.
- 2) Performance sensitivity to geometry and manufacturing/assembly tolerances is an important aspect of flexure mechanism design that needs further work.
- 3) This thesis deals with the generation of new topologies and resulting performance based on a standard blade flexure based building blocks. Size and shape optimization that allow for variations in the beam geometry, are the next steps in fine-tuning a given XY mechanism to tailor it for specific applications.
- 4) While the thermocentricity of some of the XY mechanisms has been empirically suggested, a thorough thermal analysis and subsequent validating experiments are desirable to check the sensitivity of the mechanisms to thermal disturbances.

In Appendix A, several other flexure mechanism designs are also presented that were conceived during this research. Although not thoroughly analyzed, these designs embody the concepts and philosophy followed in the rest of this thesis.

# **Chapter 2. Synthesis of Parallel Kinematic XY Flexure Mechanisms**

## **2.1 Design Requirements and Challenges**

Compact XY flexure stages that allow for large ranges of motion are desirable in several applications such as semiconductor mask and wafer alignment [54-55], scanning interferometry and atomic force microscopy [39,48,59], micromanipulation and microassembly [60], single molecule experiments in physics and biology [61], high-density memory storage [62] and MEMS sensors [63] and actuators [41]. Since most of these applications require nanometer or even sub-nanometer positioning, flexure-based motion stages are the only bearing choice available [64]. But the limitation of existing XY flexure stages is their relatively small range of motion. Although magnetic and air bearings may be used to achieve large range high precision motion [2], these are not ideally suited for nanometric positioning because of their size. In some cases large range single DOF flexure stages have been designed [35-36], but large range XY flexure stages are rare in the current technical literature.

There are three relevant length dimensions: size of stage, maximum range of motion, and motion resolution. In this discussion, the ratio between range of motion and stage size is referred to as the specific range, and the ratio between the range of motion and the motion resolution is referred to as the dynamic range. In the applications above, high specific as well as dynamic ranges are desirable. The dynamic range of a precision milling machine axis [range ~ 0.5m, resolution ~ 5 $\mu$ m], and a motorized precision micrometer driven stage [range ~ 10mm, resolution ~ 0.1  $\mu$ m] is of the order of  $1e-5$ . While similar dynamic ranges are easily achievable in flexure stages, typical specific range of most designs is only about  $1e-3$  [54].

Large specific and dynamic range flexure stages are difficult to find because this range of motion requirement imposes several challenges on the design of the overall system, including the sensors, actuators and the flexure mechanism itself. Not only is it difficult to achieve a large specific range using flexure bearings, it is also very difficult to obtain sensors and actuators that have large dynamic ranges. In XY stages, the interaction between three physical components along with the control system, influences the design and choice of each, thereby further restricting the overall system design. Stage size, motion range and resolution depend on all of the motion system components.

This chapter addresses the issues related to designing an XY flexure stage that has a large specific range, given the constraints imposed by the overall motion system. Choice of sensors and actuators is addressed in Chapter 6, and control system design is briefly touched upon in Chapter 7.

As mentioned earlier, there are two kinds of design configurations – serial and parallel designs. Both these configurations present difficulties in meeting the large range motion objective. Since a serial configuration can be built by assembling single DOF systems, it may appear that this arrangement is better suited for large range multi-DOF mechanisms. In fact almost all macro-scale machines and metrology tools are built this way, for example, the milling machine and the coordinate measuring machine. But neither of these machines are designed either for high dynamic performance such as scanning, nor for nanometer resolution. Since actuators that can generate large motions are usually bulky, moving actuators become very undesirable for dynamic performance, and moving cables are sources of disturbance that are detrimental for high resolutions. Ground mounted actuators are therefore much preferred, but the existing parallel mechanisms provide a small specific range, unsuitable for the applications stated above. To understand the challenges in designing a flexure mechanism in a parallel configuration, a typical example is considered.

The conventional approach in a parallel mechanism design is to add the necessary number of constraints so as to achieve the desired degrees of freedom. This approach highlights the limitations imposed by parallel geometry and the other components of the motion system in the design of the flexure stage. If one desires an XY $\theta$  mechanism, for example, a common solution is to support a payload stage on three slender beams, as shown in Fig 2.1. This way, the three out of plane degrees of freedom are suppressed, and the payload stage is constrained to move within the XY plane. Several XY and XY $\theta$  flexure designs that exist in the literature are conceptually identical to this [48,51-56]. It should be mentioned that a fourth beam can also be added without resulting in an over-constraint, which is an advantage of flexures over rigid link mechanisms. If designed for motion control, this configuration of Fig. 2.1 results in the following tradeoffs.

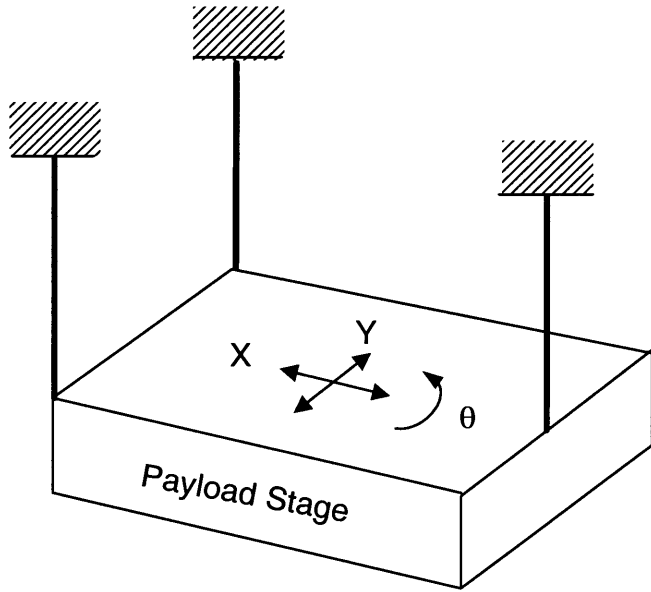


*Fig. 2.1 Typical parallel kinematic XY $\theta$ flexure mechanism*

1. Large range of motion requires that the beams be made as thin as possible, which in turn reduces the stiffness in the out-of-plane DOC directions. This is the classic tradeoff between the DOF and DOC – to increase the range of motion in DOF one ends up compromising the stiffness along DOC. This lowers the payload carrying capacity and stiffness associated with the out-of-plane motion. This limitation is a direct consequence of the fact the flexures are non-ideal constraining devices because their stiffness in various directions cannot be independently assigned. Due to the finite stiffness along DOC, flexure mechanisms are more tolerant to misalignments arising from fabrication and assembly, which is why a fourth beam may be added in this case to bolster the DOC stiffness without causing an overconstraint. But this strategy still doesn't provide an independent control over DOF and DOC.
2. Ideally, no motion is desirable in the DOC direction. In this particular arrangement, there is an undesired error motion in the out of plane directions associated with in-plane motion. Once again, this is due to the imperfect nature of beam flexures. Furthermore, the undesired error motion often has a higher order non-linear dependence on the primary motion, and therefore increases very fast with increasing ranges of motion. This problem, of course, is resolved if the constraints are designed to be in-plane [54-56].

3. One of the most critical challenges is that of integrating the actuators with the motion stage. In this particular case, three independent forces are to be applied on the motion stage to actuate X, Y and  $\theta$ . Force source actuators that do not require a physical interface, for example direct acting magnetic coil actuators, do not pose a problem in terms of integration. But these are unsuitable for large range of motion applications because of the low forces that they generate, the non-linear dependence of magnetic force with displacement, and loss in axial force due to transverse displacements [65]. Displacement source actuators, like motor driven micrometers or piezo-actuators, generate a much larger force but require a physical attachment between the actuator tip and the stage. Piezo-actuators do not allow for a large range of motion, and are either used for fine positioning in a coarse-fine scheme or in conjunction with a motion amplifiers [35-36]. Displacement source actuators have a preferred direction of motion, referred to as the axial direction, and are typically not designed to support transverse loads [66]. Referring to Fig. 2.2, a maximum displacement  $x_0$  of the motion stage in X direction results in the same amount of transverse displacement at the Y actuator tip. This shows that the actuators can't be rigidly connected to the motion stage and that a decoupler, for example a wobble pin or a double hour glasses flexure, is necessary.

The purpose of the decoupler is to transmit the axial force and absorb the transverse motion, without generating any transverse loads. This idealization, once again, is an unachievable if one uses a flexure-based decoupler to retain the high motion resolution. By making the flexure decoupler compliant in the transverse direction, one ends up compromising the axial direction stiffness as well. This in turn results in lost motion [8] and reduced dynamic performance as described in point 5 below. Thus, the range of the motion system is not limited by the failure limits of the flexure bearing stage itself, but is restricted to a much smaller level by the maximum transverse displacements that the decoupler allows without generating large enough transverse forces that will damage the actuator.

4. It is desirable to use non-contact sensors for the stage motion measurements, so as to avoid any sources of disturbance at the stage. A motion range of 5mm and resolution of 0.5nm results in a desired dynamic range of at least  $1e-7$ . The choice of sensors becomes a difficult task because until recently such large dynamic range non-contact sensors that are practical, have not existed. LVDTs that do have a satisfactory dynamic range require the motion stage to move along a straight line, which is not possible in an XY stage. Laser interferometry which also has a high dynamic ranges is suitable only for testing and characterization but is an impractical option for regular operation due to the bulky size, high costs and the set-up required. Capacitance probes do

provide high sensitivity and resolution but have a relatively poor dynamic range of the order of  $1e-5$ , for a given size. Linear scales also have the necessary range and resolution, and provide non-contact sensing, but are typically single axis sensors, and tolerate little off axis motions. Only recently, two-axis optical scales have become commercially available [67], and constitute one of the few options that are suitable for large range of motion flexure mechanisms.

5. The compliance of the components that lie between the actuator and the stage, for example, the decoupler, is important from a feedback control perspective. As illustrated in Fig. 2.2, a motion in X direction produces a transverse displacement at the Y decoupler. The axial stiffness of the decoupler flexure typically drops non-linearly with an a transverse displacement. Thus the dynamic characteristics of the Y axis become critically dependent on the X axis motion. Since the actuation and the point of interest are non-colocated, the inline stiffness between these two points plays very important role in determining the dynamic performance of the system, and any damping as well as controls strategy has to be robust against this variation in stiffness and corresponding natural frequencies. Clearly, this problem gets more severe with increasing ranges of motion.

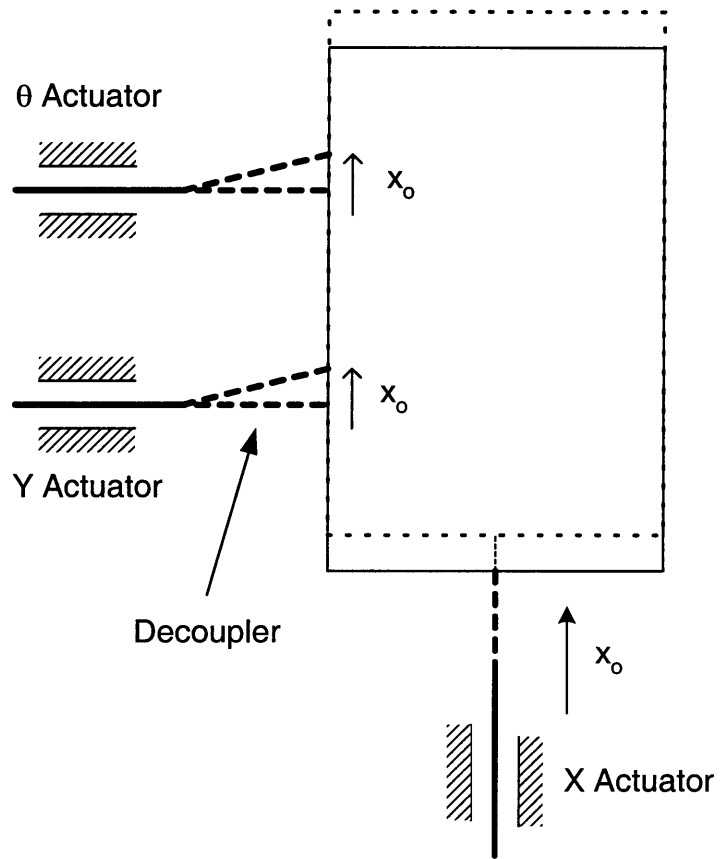


*Fig. 2.2 Actuator – Stage Integration*

It should be noted that for applications other than motion control, where integration with sensors and actuators is not required, for example in decouplers, probes, and certain sensors, it suffices for the motion stage to simply have the necessary degrees of freedom, and the existing designs are perfectly suitable. But for the purpose of motion control, constraints in the flexure bearing design should be chosen a bit more carefully, so that some of the challenges listed above can be mitigated.

So we see that neither the traditional approach of Fig. 2.1, nor the computational topology synthesis methods mention in Chapter 1, have so far produced parallel mechanism topologies that meet our stated requirements. Based on an understanding of the limitations and tradeoffs that we have identified in the current designs, we start approaching the problem from alternate paths. Rather than an ad hoc arrangement of constraints, we seek those arrangements that will help up mitigate the challenges that are laid out above. Such an arrangement should meet the following specific requirements.

1. In most applications that we are trying to address, the primary positioning objective is in X and Y, and that motion stage yaw is undesirable. Given this requirement, motion stage yaw,  $\theta$ , may be rejected passively or actively. Either the mechanism should be designed using appropriate flexure units such that the motion stage rotation is constrained to levels below the maximum acceptable yaw errors, or a third motion axis should be incorporated to actively measure and cancel the yaw errors. There are advantages as well as challenges associated with each technique. As explained earlier, adding a yaw control axis in the traditional parallel format can limit an otherwise large X and Y range of motion. Adding yaw control in the serial format will once again result in moving actuators and cables, although the requirements on this actuator will be less stringent because only small motion is needed to correct for  $\theta$ . From a dynamics point of view, adding a yaw control axis will also help actively reject any yaw vibrations resulting from ambient excitations or disturbances. But this issue may also be addressed passively by means of appropriate vibration isolation and damping design. In general, at both the MEMS scale and the macro scale it is very desirable to keep the number of actuators and sensors, and therefore the number of axes as low as possible. For these reasons, we choose the former approach where yaw motion of the stage is constrained and any observed  $\theta$  will be treated as *parasitic error motion*.
2. It is desirable to minimize the *cross-axis coupling* between the two degrees of freedom. Specifically, the motion along Y direction in response to a force or displacement along the X direction should be ideally zero, and vice versa. In the absence of an end-point feedback, if one relies on sensors that measure the actuator displacements, a calibration step, either analytical or experimental, is needed to determine the coordinate transformation matrix between the actuator coordinates and the motion stage coordinates. This typically limits the positioning accuracy of the motion stage if there are uncertainties involved in the actuator. In some micro scale applications, an experimental calibration may not even be possible, thereby making it very desirable to eliminate cross-axis coupling. Cross-axis coupling also plays a very important role in determining the dynamic characteristics of the flexure system, because an excitation in one direction can generate vibrations in the other direction, resulting in conditions of parametric excitation and internal resonance. In applications other than motion control when the two axes are not actively controlled, for example in some MEMS sensors [63], this effect is one of the primary performance metrics. In the presence of end-point feedback, and independent actuators, the effect of cross-axis coupling on static and dynamic is far less detrimental. A more mathematical definition of the cross-axes coupling error discussed here shall be provided in Chapter 3.

3. It is also desirable to minimize the *lost motion* between the actuator and the motion stage, for similar reasons as stated above. Otherwise, a calibration step is needed to map the displacements of the actuator to that of the motion stage. Furthermore, eliminating lost motion alleviates the need for end-point sensing, which can be difficult to achieve due space and packaging restrictions. For example, in MEMS scale applications, where all components of the system need be in the same plane for ease of fabrication, end-point sensing may be difficult or even impossible. The importance of the stiffness between the actuator and motion in determining dynamic performance has already been highlighted earlier.
4. Furthermore, the application point of the X actuation force should not be affected by any displacement of the motion stage in the Y direction, and vice versa, an attribute which we term as *actuator isolation*. This is different from the cross-axis coupling error discussed above. The lack of any transverse displacements at the Y actuation point, in response to an X actuation force, mitigates the dependence on the decoupler. While, the decoupler may still be needed to accommodate assembly and manufacturing misalignments, it can be designed to be much stiffer in the transverse direction, and therefore the axial direction, because it no longer limits the range of motion of the mechanism. As explained earlier, the stiffer the decoupler is axially, the better is the dynamic performance of the system. By the same token, in response to a Y force, the point of Y actuation itself should move in the Y direction only, and should not have any transverse motions. These requirements ensure the reliable functioning of the actuators by minimizing transverse loads.

A Y displacement of the Y actuation point in response to an X force is also generally not desirable because this generates an additional axial force at the Y actuator. But usually this is not as several problem because both the actuator and the mechanism are designed to handle axial loads. The implicit assumption in all this discussion is that the actuators are axial, which is reasonable.

5. For obvious reasons, low thermal and manufacturing sensitivity are desirable for the XY flexure mechanisms discussed here, and both these factors are strongly dependent on the mechanism geometry.
6. Since the primary objective of the XY mechanisms is to provide guided motion along the X and Y directions, and constrain all other motions, it is desirable to maintain the high stiffness and small parasitic errors in the three out of plane directions. In other words, the Degrees of Constraints should be as close to ideal as possible.

Based on an understanding of the challenges posed by flexures in general and the parallel configuration in particular, fundamental design principles [67], intuitive reasoning, and analytical insight, we propose a set of flexure mechanism topologies that meet the above requirements. These proposed designs deviate from the traditional approaches, mentioned earlier, in that they make unique use of known flexural units and geometric symmetry to minimize cross-axis coupling, parasitic yaw of the motion stage, and at the same time maximize actuator isolation. Towards the end of this chapter, a means for modifying these designs is also presented, which allows for out-of-plane motion, in addition to the in-plane translations.

## 2.2 Proposed Design Principle for a Two Axis Flexure Mechanism

In this entire document, X and Y are defined to be the in-plane axes and Z, the out of plane axis. Fig. 2.3 shows the arrangement of rigid and compliant units of which the proposed flexural mechanism must be composed. There are four rigid stages: ground, motion stage, and two intermediate stages. The motion stage should have two translational degrees of freedom with respect to ground. The intermediate stages are necessary to decouple the motion of the two axes and isolate the actuators that control these two axes. Since the ground mounted actuators cannot be directly connected to the motion stage, the intermediate stages provide the points for actuator force application.

In the rest of this thesis, we shall use the term *flexure unit* to represent building blocks that constitute a flexure mechanism. The rigid stages in Fig. 2.3 are connected to each other by means of flexure units, which act as frictionless bearings or guides and provide constraints to relative motion. Each of the flexure units A, B, C and D is a single degree of freedom mechanism that only allows translation in the direction shown by the double-sided arrow. The fixed stage is connected to Intermediate Stage 1 by means of Flexure A, which only allows for relative motion along the X direction and constrains all other the other degrees of freedom. This implies that no matter what the overall configuration of the entire mechanism is, Intermediate Stage 1 will always have a pure X displacement with respect to ground.

Intermediate Stage 1 and the Motion Stage are connected by means of Flexure B that allows for relative motion in the Y direction only and constrains relative motion along X direction and rotation. This implies that the X motion of Intermediate Stage 1 will be entirely transmitted to the Motion Stage, while any Y motion of the Motion Stage will not influence the Intermediate Stage 1 at all. Thus, Intermediate Stage 1 becomes an ideal location for the application of the X actuation force. Flexure A provides the linear guide/bearing for X actuator force. Furthermore, any X force applied at Intermediate Stage 1 is incapable of producing any Y motion of the Motion Stage due to the presence of Flexure B.

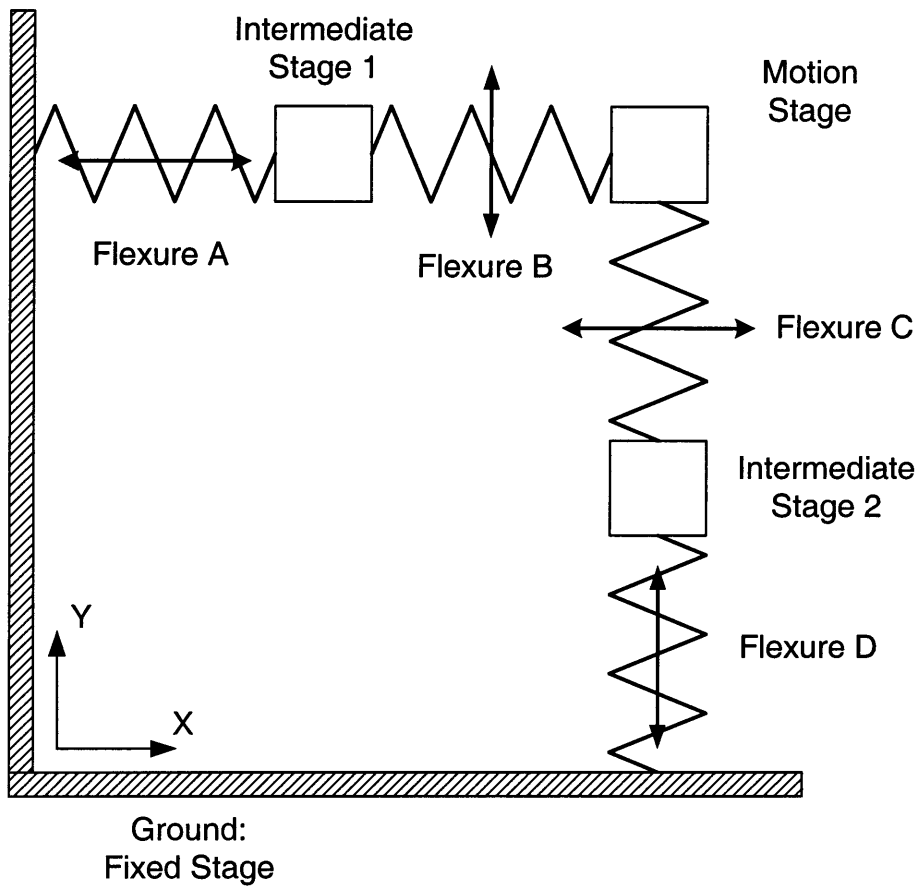


*Figure 2.3 XY Flexure Mechanism Topology*

On very similar lines, Intermediate Stage 2 is connected to ground by means of Flexure D, which constrains motion in X direction and rotation, but allows for perfect relative motion in the Y direction. Thus, Intermediate Stage 2 can only move along Y and shall have no motion in the X direction or rotation, no matter what the displacement of the Motion Stage is. Intermediate Stage 2 and the Motion Stage are connected via Flexure C, which allows only X motion between the two. Thus, any X motion at the Motion Stage will not affect the Intermediate Stage 2, which is therefore an ideal location for the application of Y actuation force. At the same time, all the Y motion that is generated at Intermediate Stage 2 due to the Y actuation force will be transmitted to Motion Stage, but is incapable of producing any X motion of the Motion Stage due to the presence of Flexure C.

Ideally, in any deformed configuration of the flexural mechanism, Intermediate Stage 1 always has a pure X displacement while Intermediate Stage 2 has a pure Y displacement. The Motion Stage inherits the X

displacement of Intermediate Stage 1 and the Y displacement of Intermediate Stage 2, thus acquiring two translational degrees of freedom. Since all the connecting flexure units constrain rotation, the rotation of the Motion Stage is also constrained with respect to ground.

This is an idealized scenario, where units A, B, C and D are perfect single degree of freedom flexure bearings or guides. The only degree of freedom that flexures A and C allow for is relative translation along X, while Flexures B and D are compliant only in relative translation along Y. We know that in reality, such flexure units do not exist. Any flexure unit will have only a finite compliance and range of motion along its DOF, and a finite stiffness along its DOC. As a consequence of this fact, the zero parasitic error, zero cross-axis coupling and perfect actuator isolation conclusions obtained above shall be compromised, the extent of which depends on the flexure building block that is chosen. Nevertheless, we can certainly say the conclusions shall hold good at a gross or first-order level, and the undesirable interactions and deviations from ideal behavior will be higher order in nature.

Flexures are chosen for the bearing units A, B, C and D, instead of ball bearing based guides, which would have allowed for much larger ranges of motion. One reason for this decision is to achieve high motion resolution and smoothness, as explained in Chapter 1. But this is not the only reason; there is another fundamental reason why only a flexure based mechanism can work effectively in this configuration. Let us consider a rigid body version of the arrangement shown in Fig. 2.3. As earlier, if we have an ideal frictionless linear bearing as shown in Fig. 2.4a, we can go ahead and assemble four such units in the fashion proposed above, to obtain the mechanism of Fig. 2.4b, and expect that that we have attained the zero error two axis mechanism. But that is not the case. Even if we ignore the concerns of motion quality, there is a mobility problem with the mechanism shown in Fig 2.4b. Applying Grubler's criteria to this mechanism, one obtains a DOF of one, as opposed to an expected value of two. Indeed, in a general configuration this mechanism has only one degree of freedom, but in the special case when Bearings A and C are aligned perfectly parallel, and bearings B and D are aligned perfectly parallel, one constraint becomes redundant and the mechanism exhibits two degrees of freedom. The result of Grubler's analysis simply indicates that any deviation from this perfect alignment will lead to a reduction in Degrees of Freedom which shall be manifested by jamming or locking of one axis. Since the constituent bearings are perfect constraints with infinite stiffness along their DOCs, any misalignment will produce infinitely high locking forces. Thus we see that even if we had perfect single DOF building blocks or constraints, we would need an absolutely perfect manufacturing and assembly to make the above idea work. But, as is well known, this is not possible in real life.

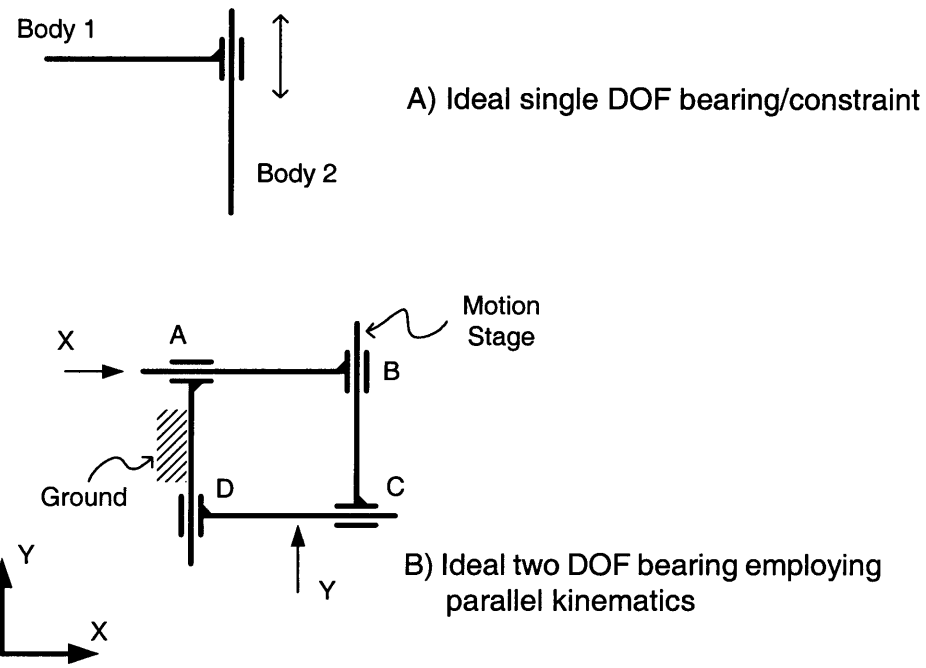


*Figure 2.4 XY Linkage Mechanism Topology*

The beauty of designing with flexures is that, while flexures can be blamed for being imperfect constraints and therefore producing an XY mechanism that is error prone, it is precisely this imperfection of flexures that makes the above arrangement realizable in the first place. Furthermore, any deviation from ideal behavior of the XY mechanism is exactly predictable using the principles of mechanics.

The level of manufacturing tolerances that are acceptable for the proposed XY mechanism topology to function as desired, depends on the constituent flexure units, and may be estimated using the analytical tools that shall be developed in the subsequent chapters.

This is a simple, maybe somewhat obvious, yet fundamental guideline that can be used in designing high performance planer two-axis flexural mechanisms. Any linear motion flexure unit, which in the designer's opinion comes close to the stated idealizations, can be used as a building block to produce a two DOF planer mechanism. The following sections present designs generated with three types of flexure units or building blocks: the simple beam flexure, the parallelogram flexure and the compound or double parallelogram flexure.

## 2.3 XY Flexure Mechanism based on the simple Beam Flexure

Although a simple beam is not a very good single degree of freedom flexure unit, nevertheless due to its simplicity it may be used as a building block in the arrangement discussed in the previous section. From beam bending analysis we know that the beam tip translates ( $\delta$ ) as well as rotates ( $\theta$ ) when it experiences a transverse force. Furthermore, it also exhibits a parasitic error motion in the X direction ( $\epsilon$ ).

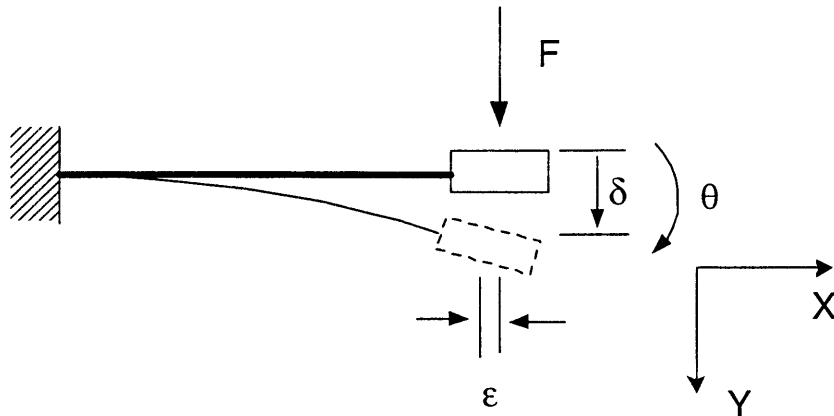


*Fig. 2.5 Simple Beam*

Using the beam flexure for flexure units A, B, C and D, the resulting two axis mechanism is illustrated in Fig. 2.6. This is a moderately reasonable design in terms of performance and may be used where accuracy can be compromised but space is at a premium. In-plane rotation of motion stage may be minimized by appropriate placement of actuation forces. Clearly, an  $X$  actuation force will produce a small displacement of the Motion Stage in  $Y$  direction as well, and vice versa, and therefore cross-axis coupling is present. The point of application of  $X$  actuation force on Intermediate Stage 1 also moves in the  $Y$  direction. Furthermore, an application of  $Y$  force moves the point of application of the  $X$  force. Hence, actuator isolation is not achieved either. Out of plane stiffness is low because of the overhanging motion stage.

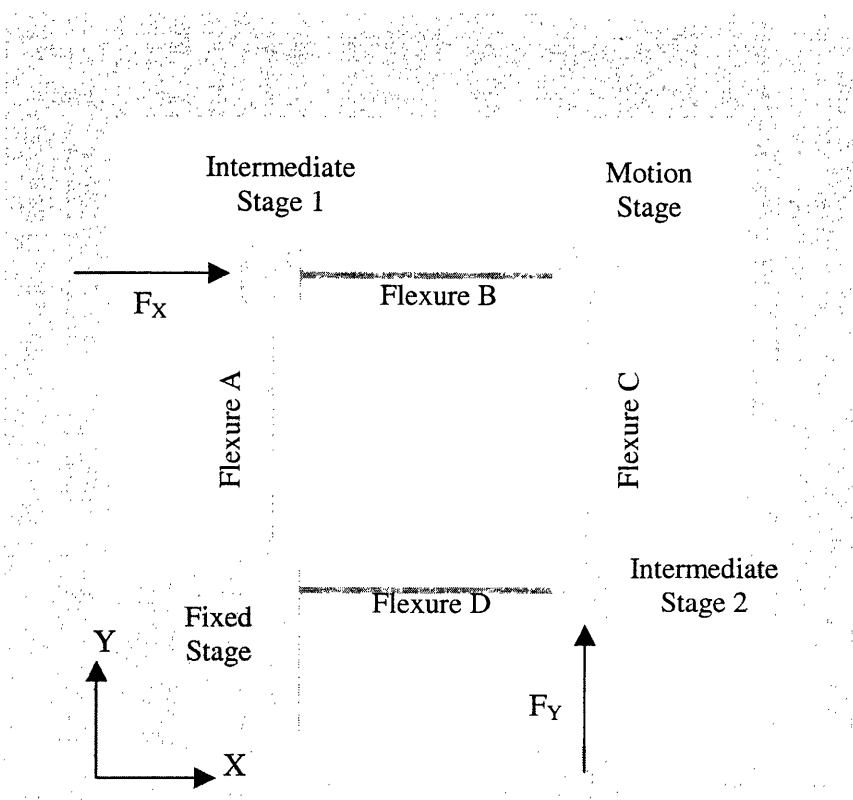


*Fig. 2.6 XY Design 1*

This relatively poor performance may be improved by making an insightful use of geometric symmetry where the design is mirrored about a diagonal axis, as shown in Fig. 2.7. The constraint pattern remains the same and the mechanism still has two in-plane translational degrees of freedom, once again due to the finite stiffness of flexures along their DOC. Primes denote the mirrored flexure units. On careful inspection, one can see that symmetry brings about some improvements in the performance of the XY mechanism. On the application of an X actuation force, the two sides of the mechanism tend to produce displacement of the motion stage in Y direction that oppose each other, and therefore cancel out. Out of plane stiffness is now better owing to an improved structural loop, since the motion stage in this design is supported from two sides. The design still suffers from lack of good actuator isolation. Also, there is no significant improvements in the parasitic yaw of the motion stage. Thus, we conclude that symmetry in this case may help in terms of some performance measures but doesn't bring about much improvements in others.

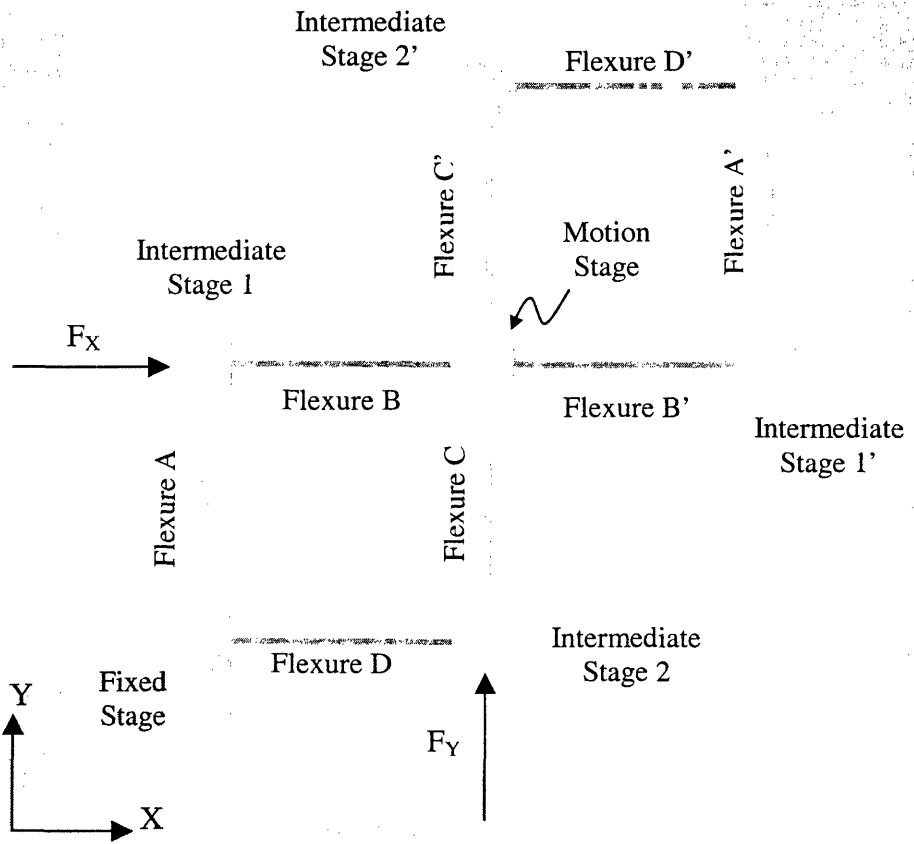
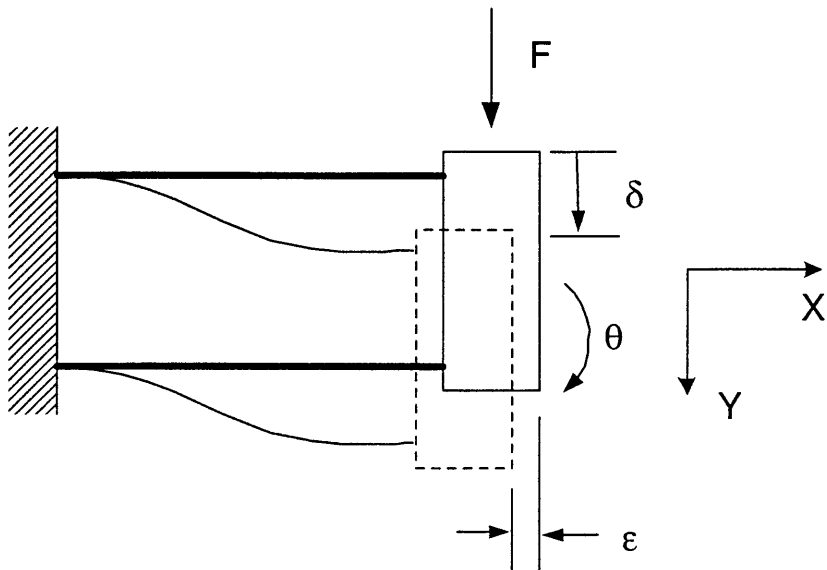


Fig. 2.7 XY Design 2

## 2.4 XY Flexure Mechanism based on the Parallelogram Flexure

The parallelogram flexure unit is a classic design that has been employed in many flexural mechanisms. Fig. 2.8 provides a schematic of the flexure in its deformed and undeformed configurations. Beam bending analysis can be used to predict the force-deformation characteristics of this flexure. It can be analytically shown that parallelogram flexure offers small resistance to relative motion in the Y direction but is stiff with respect to relative motion in X and rotation. Hence, it is a much better approximation for a single DOF flexure as compared to the simple beam flexure used in the previous case.



*Figure 2.8 Conventional Parallelogram Flexure*

However, the parallelogram flexure unit also suffers from undesirable parasitic errors. An application of force in the Y direction results in the desired motion  $\delta$ , in Y direction, and also in undesired motions:  $\epsilon$  in the negative X direction, and rotational twist  $\theta$ . While  $\theta$  may be eliminated by appropriate placement of the force  $F$ ,  $\epsilon$  is always present [1-2,8].

Following the design principle expounded earlier in this document, we come up with a two-axis planer flexure mechanism design, shown in Fig. 2.9, in which the parallelogram flexure is used for Flexure Units A, B, C and D. This is a better design in terms of performance as compared to the one illustrated in Fig. 2.6. The accuracy is better but nevertheless undesired motions still exist. In-plane rotation of the Motion Stage is constrained quite well because the parallelogram flexure unit is considerably stiff in rotation. An X actuation force still produces a small displacement of the Motion Stage in the Y direction, and vice versa. The point of application of X actuation force also moves slightly in the Y direction during force application. Furthermore, an application of X force moves the point of application of the Y force. Hence perfect actuator isolation is not achieved in this case either. Since the motion stage is supported only from one side, out of plane stiffness is also relatively low.

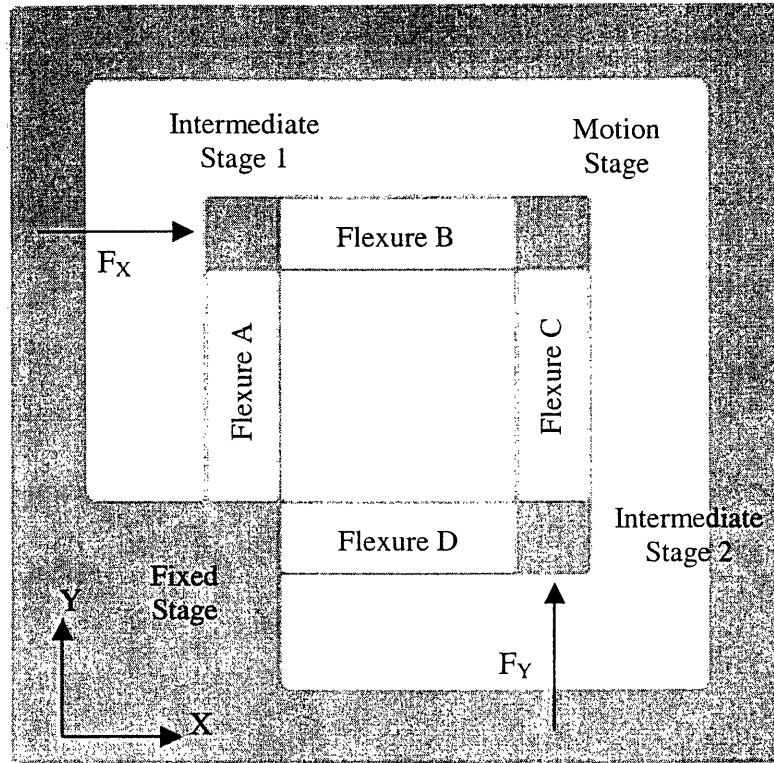


*Figure 2.9 XY Design 3*

Some of the above performance measures are improved, once again, by exploiting geometric symmetry as shown in Fig. 2.10. Due to their finite stiffness, the additional flexure units do not over-constrain the mechanism. This symmetric arrangement should result in several performance improvements. The motion stage yaw should be further reduced due to the additional rotational constraints arising from the parallelogram flexures. On the application of an X actuation force, the two sides of the mechanism tend to produce displacements in Y direction that counter each other, and therefore reduce the cross-axis coupling errors. Out of plane stiffness also improves due to better support of the motion stage. Perfect actuator isolation is still not achieved in this design.

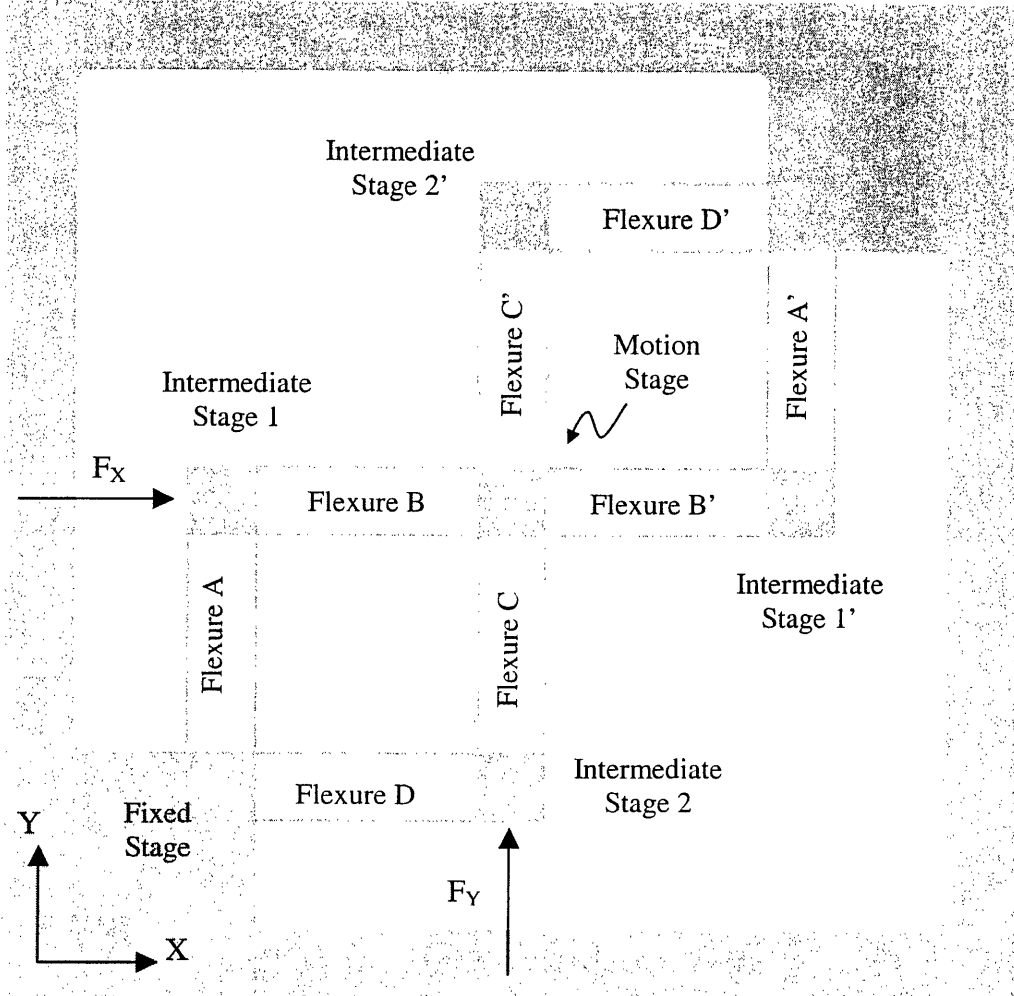
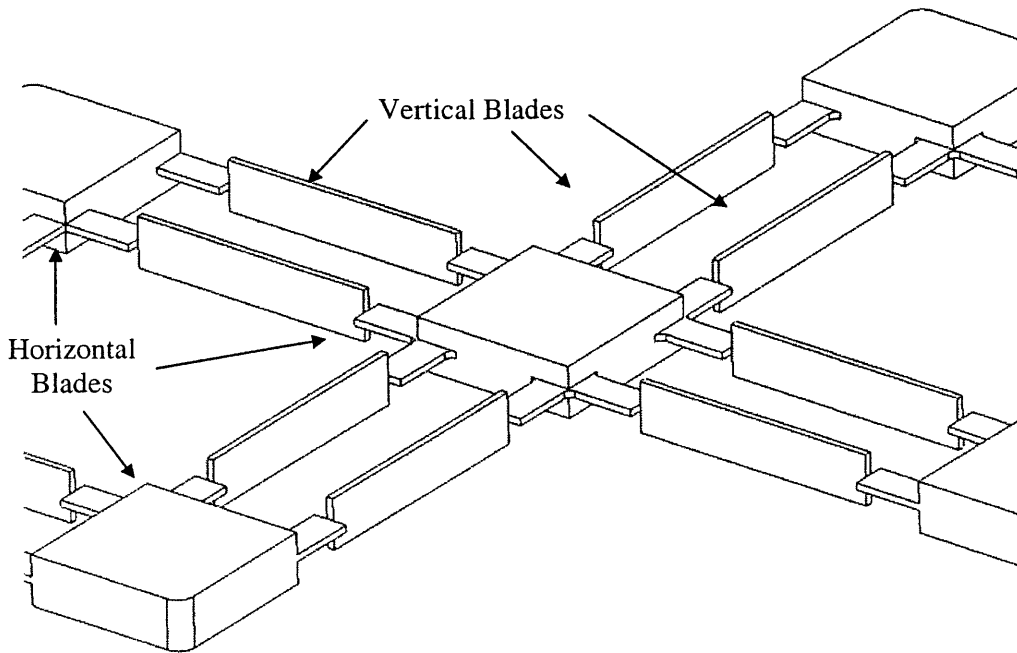


Figure 2.10 XY Design 4

Before proceeding to the next building block, we would like to point out that new features may be added to this design, which enhance its functionality. For example, small horizontal blades may be introduced in the mechanism in a manner as shown in Figure 2.11. The vertical blades belong to the original two-axis flexural mechanism design and the horizontal blades are new additions that now enable out of plane motion as well. By appropriately positioning these horizontal blades each of the intermediate stages, and the motion stage can be imparted with a Z degree of freedom.



*Figure 2.11 Combination of vertical and horizontal blades provides in-plane and out-of-plane motion*

By choosing actuator forces as shown in Figure 2.12, we can add another three out-of-plane degrees of freedom to the planer mechanism: translation of the Motion Stage along Z, and its rotations about the X and Y axes. If we choose to apply a Z direction force only on the Motion Stage, we obtain a three DOF mechanism with compliance in X, Y and Z directions.

Normal forces  $F_{xz1}$  and  $F_{xz2}$  acting on opposite intermediate stages result in rotation of the Motion Stage about the X-axis and similarly forces  $F_{yz1}$  and  $F_{yz2}$  produce a rotation about the Y axis. A combination of these four vertical forces can be used to generate any arbitrary motion along Z and angular twists about X and Y, adding three DOF. Once again, this could not have been possible in a rigid link mechanism, and is achievable only because we are using flexures.

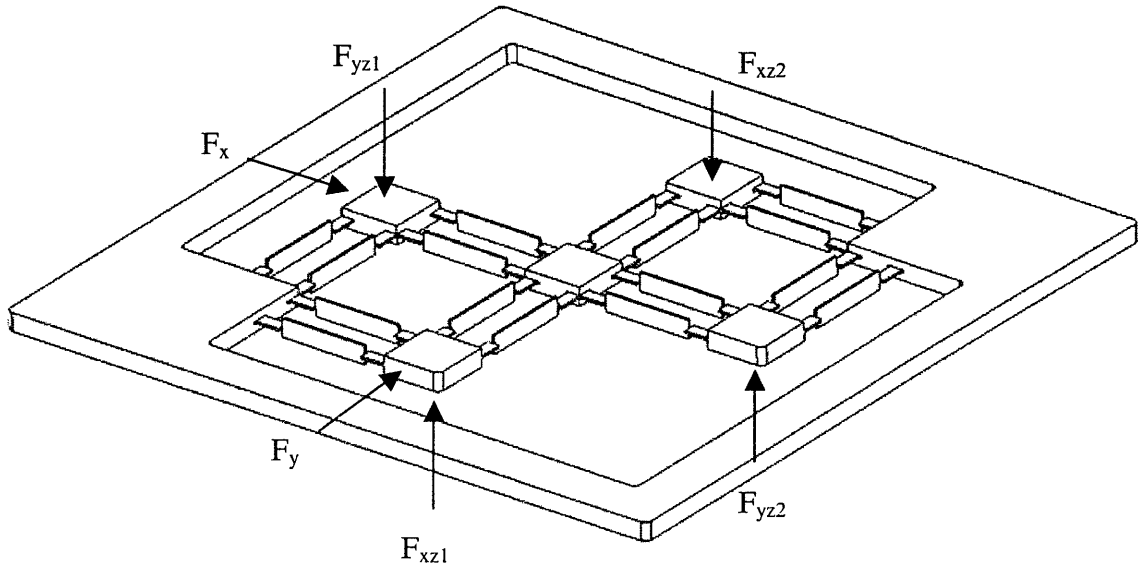


Figure 2.12 XYZ $\theta_x\theta_y$  Design 1

We can thus get five degrees of freedom from a planer flexure. The three newly added degrees of freedom fall in the traditional parallel kinematic topology category. Consequently, actuator isolation is poor for the out-of-plane actuators. Any out-of-plane motion of the intermediate stage causes the point of application of the in-plane forces to move. Similarly, any in-plane motion will cause the points of application of the normal forces to shift.

It is may be noticed that many of the anomalies of this design and the XY design of Fig. 2.10 are a consequence of using the parallelogram flexure unit, which has some inherent error motions. We therefore shift attention to other potential flexure units.

## 2.5 XY Flexure Mechanism based on the Double Parallelogram Flexure

Next, we use the double parallelogram flexure unit, shown in Fig. 2.13, as the building block for two-axis planer flexural mechanisms. In some of the technical literature this flexure unit is also referred to as a *compound parallelogram flexure*, *folded-beam flexure* or *crab-leg flexure*.

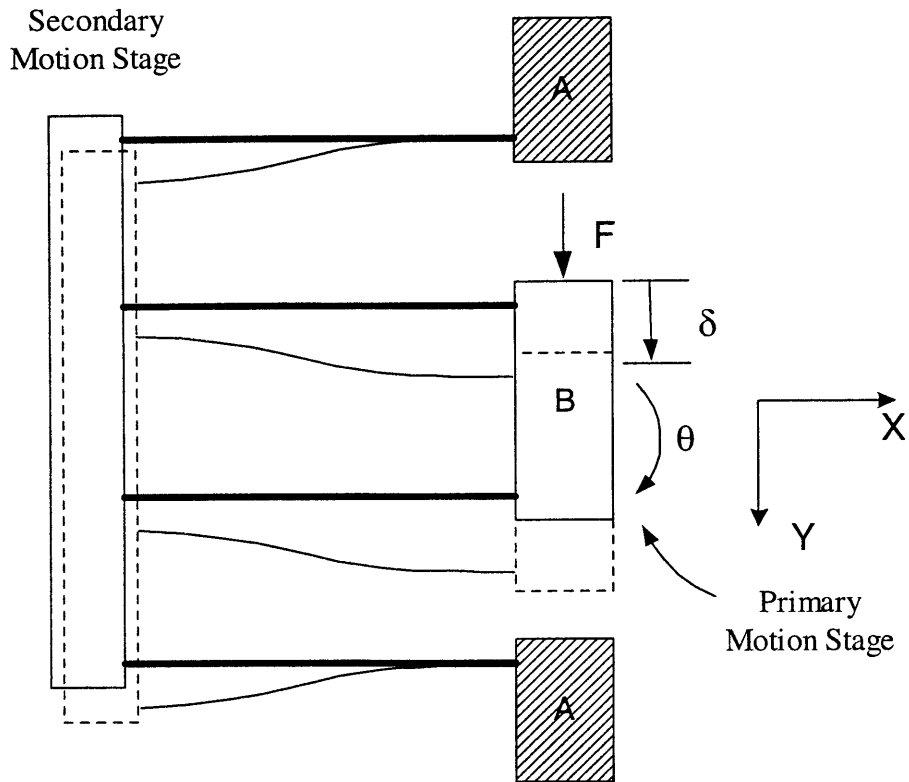


*Figure 2.13 Double Parallelogram Flexure*

Analysis shows that this flexure allows relative Y translation between bodies A and B, but is stiff in relative X displacement and rotation, although not as stiff as the parallelogram flexure. The parasitic error  $\epsilon$ , along X direction, is considerably smaller because any length contraction due to beam deformation is absorbed by a secondary motion stage. There does exist a rotational parasitic motion, which may be eliminated by appropriate location of the Y direction force. Hence, body A exhibits perfect Y-translation with respect to body B on the application of a Y direction force. These statements are true only in the absence of X direction forces.

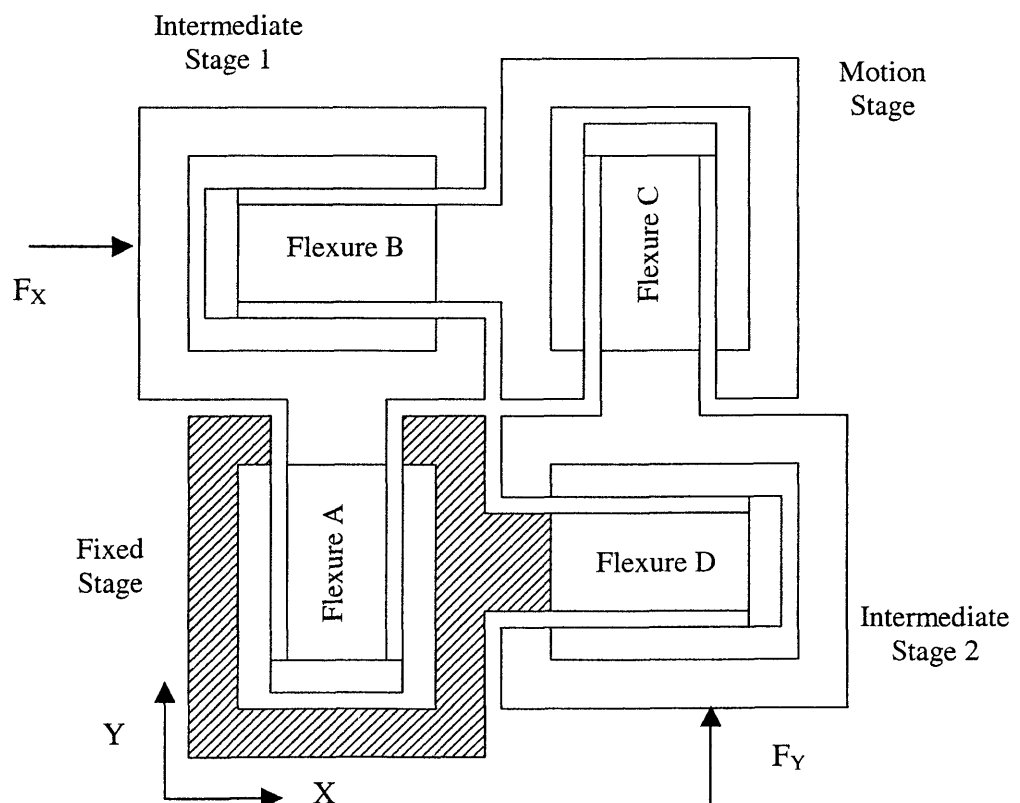
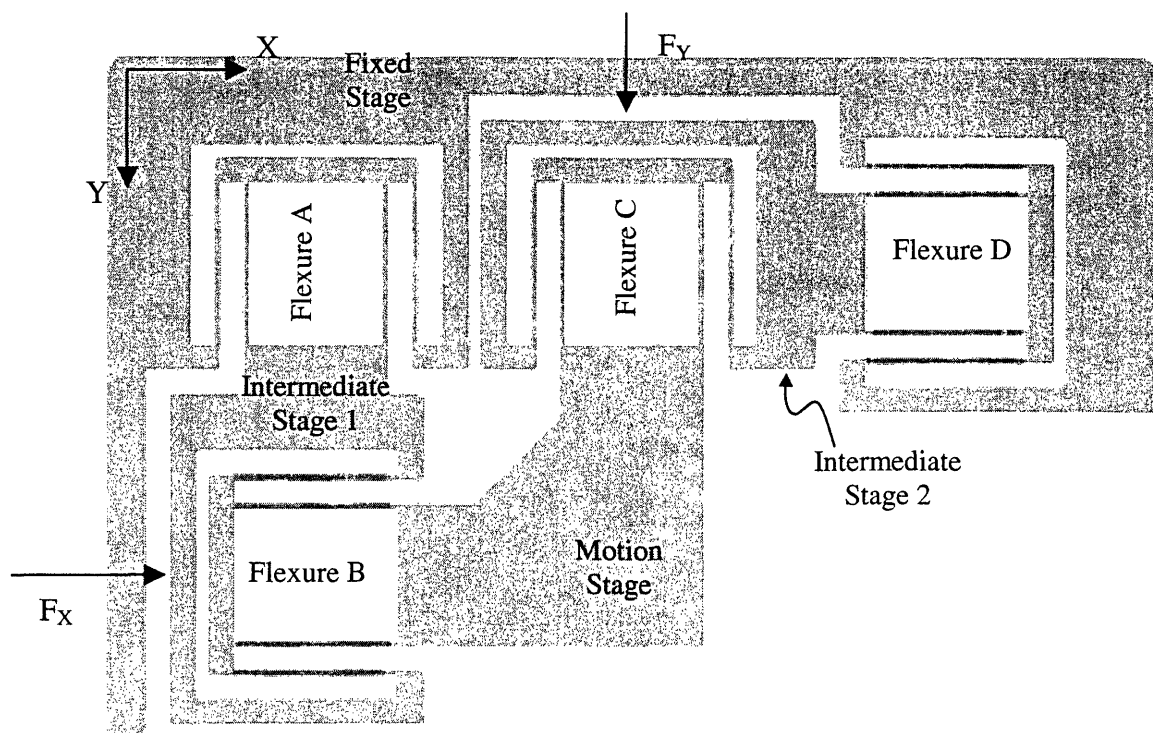


Figure 2.14 XY Design 5a and 5b

This time, the double parallelogram may be employed to construct XY mechanisms as shown in Fig 2.14. In these cases, cross axis coupling and motion stage yaw should be small and actuator isolation should also be better than previous designs. Further improvements may be obtained by mirroring the design as shown in Fig. 2.15.

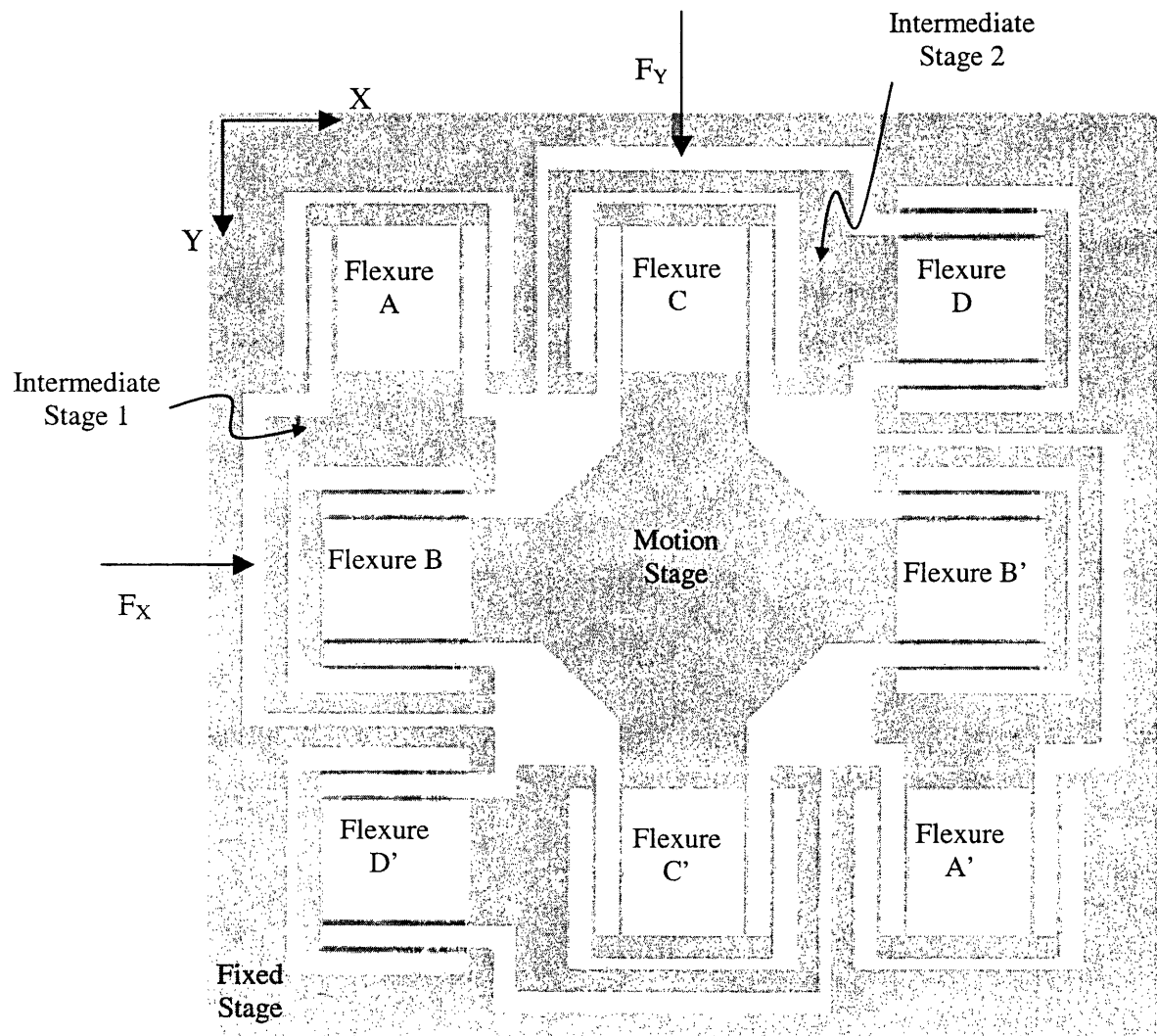
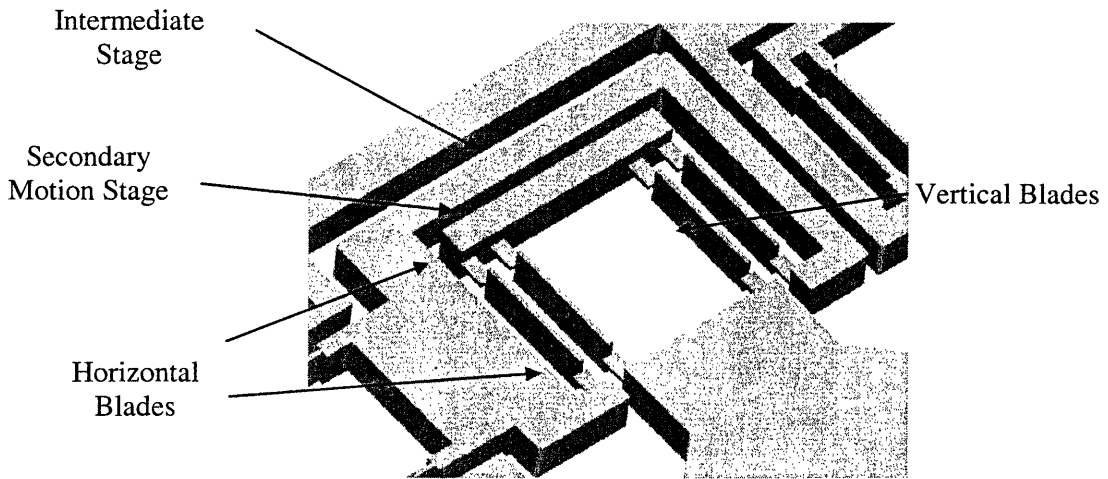


Figure 2. 15 XY Design 6: 'Biflex'

Apart from enhancement in the performance measures, the out-of-plane stiffness is also significantly improved because the motion stage is supported from all sides. More importantly, symmetry should make the design more robust against manufacturing variations and assembly errors. Furthermore, the double parallelogram flexure is fairly insensitive to uniform thermal disturbances, because the change in the beam lengths due to thermal disturbances is readily absorbed by the secondary motion stage. Based on this argument, one may conclude that the XY Mechanism Designs generated from the double parallelogram flexure are also better suited to reject any thermal variations. Furthermore, the XY Design of Figure 2.15, which we refer to as the ‘Biflex’, also allows for better space utilization and therefore has better specific range.

We can now impart out-of-plane motion to the planer mechanism by introducing horizontal blades in some of the double-parallelogram units, as shown in Figure 2.16. Horizontal blades are added such that the intermediate stages themselves do not have any significant Z motion. The secondary motion stages of the double-parallelogram flexures, the motion of which is inconsequential, are the ones that attain out of plane motion.



*Figure 2.16 Vertical and horizontal blades produce in-plane and out-of-plane motion*

Referring to Figure 2.17, by applying normal actuator forces, we can add another three out-of-plane degrees of freedom to the planer mechanism: translation of the Motion Stage along Z, and its rotations about X and Y axes. We may also choose to apply a single Z direction force on the Motion Stage, to obtain a three DOF mechanism with compliance in X, Y and Z directions.

Normal forces  $F_{xz1}$  and  $F_{xz2}$  result in a rotation of the motion stage about the X-axis and similarly forces  $F_{yz1}$  and  $F_{yz2}$  produce a rotation about the Y-axis. A combination of these four vertical forces can be used to generate any arbitrary motion along Z and angular twists about X and Y. It is important to observe that the normal forces are not applied on the intermediate stages; rather, they are applied on the secondary motion stages of the four double-parallelogram flexure units that support the Motion Stage. This isolates the normal forces from the in-plane forces to some extent. The affect of normal forces on the points of application of in-plane forces, is far less severe, thus improving actuator isolation. Furthermore, the out-of-plane rotations are much better decoupled as compared to the design of Fig. 2.12

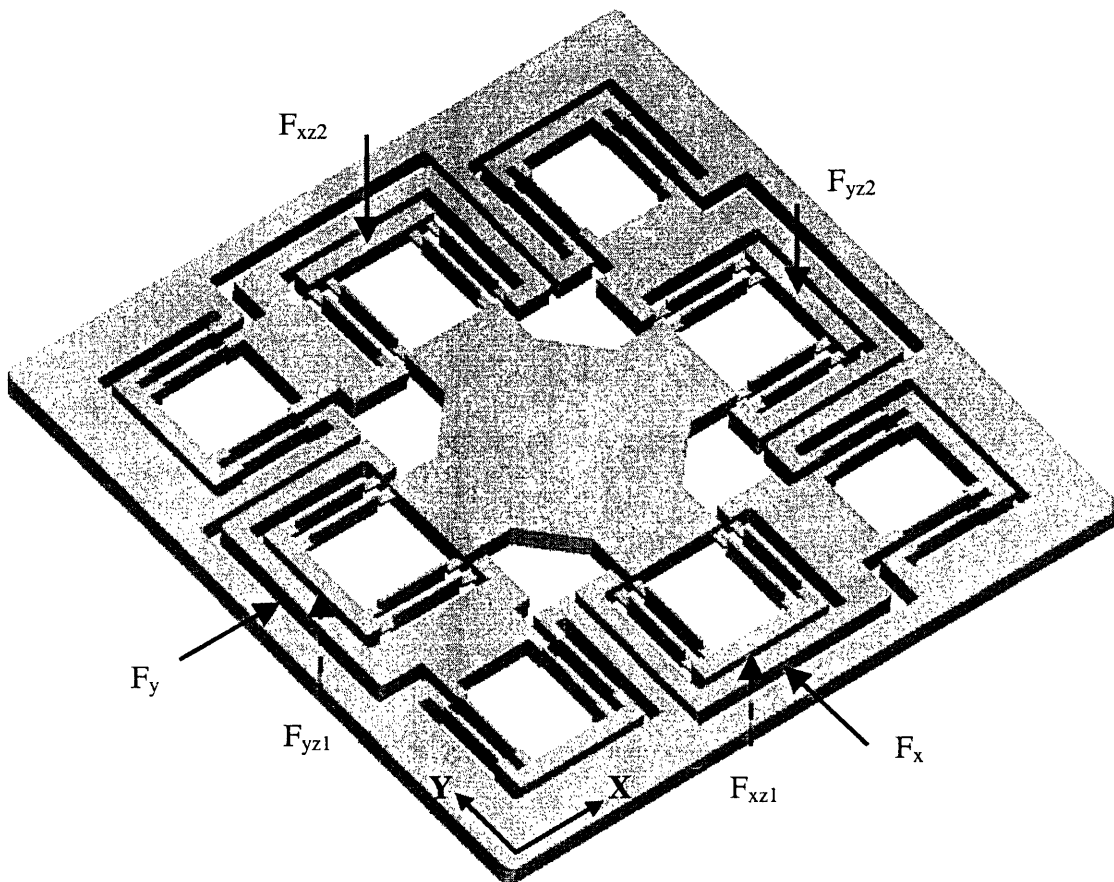


*Figure 2.17 XYZ $\theta_x\theta_z$  Design 2: 'Pentaflex'*

It may be noticed that while the XY design of Fig. 2.15 is rotationally symmetric, it lacks in symmetry about any axis in the XY plane. While it is yet to be seen if this has any significant effect on the performance, a yet another topology with even higher degree of symmetry is illustrated in Fig. 2.16. The evolution from XY Design 6 to XY Design 7 should be obvious.

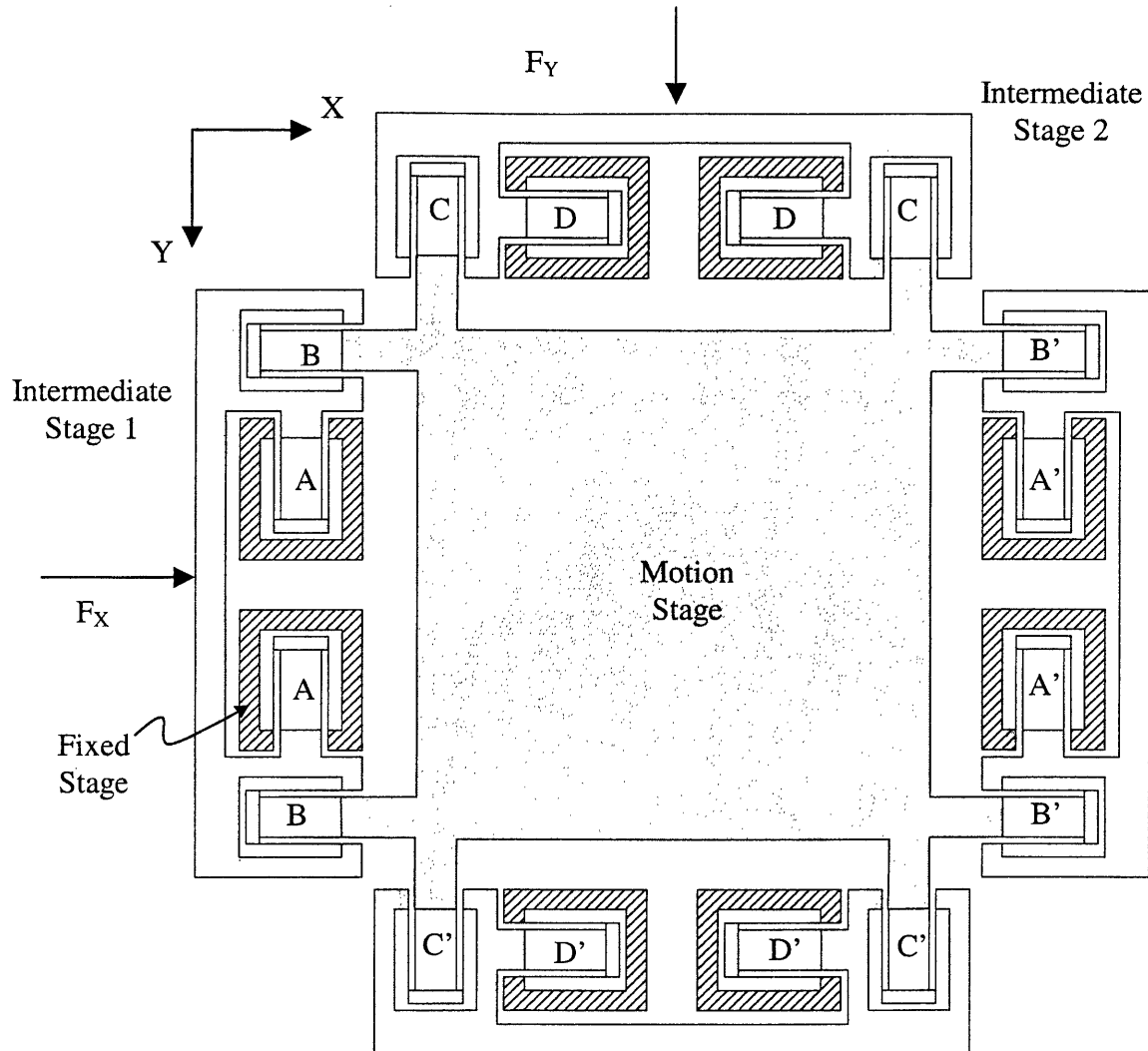


Fig. 2.16 XY Design 7

With smaller beams lengths in the constituent double parallelograms, this mechanism will have a smaller specific range. With respect to all other performance measures, like cross-axis coupling error, parasitic yaw error, out of plane stiffness, and actuator isolation, this appears to be better than the previous designs. Also, because of the increased number of flexures, elastic averaging will play an increasingly important role in making the design more tolerant to manufacturing variations. Such conjectures need to be verified by means of the analytical tools that shall be presented in the subsequent chapters.

Of course, several other XY designs can be generated based on the construction of Fig. 2.3. Any flexure unit that produces error-free single axis translation can be used as a building block for two-axis planer mechanisms. For example, the multiple beam parallelogram flexure, shown in Fig. 1.2b, is a promising candidate. Adding further beams to the conventional parallelogram flexure, increases the stiffness in the DOC and DOF in the same proportion. This is better than simply increasing the thickness of beams in a parallelogram flexure, which increases the DOF by a cubic factor. Multiple beams may be used in a parallelogram arrangement, without resulting in an overconstraint, because of the phenomenon of elastic averaging. Furthermore, a combination of different flexures units can also be used in constructing the XY mechanism. For example, one may use double-parallelogram units for Flexures A and D, and parallelogram units for Flexures B and C. Of course the suitability of one design over the other depends entirely on the requirements of an application.

Based on the challenges and trade-offs associated with parallel kinematic flexures, it appears that designing a large range of motion XY $\theta$  mechanism is no simple task. One may attempt this by extending the ideas presented here to a third in-plane axis. In fact, a three dimensional XYZ flexure mechanism, which allows for ground mounted actuators and large ranges of motion along its three substantially decoupled DOF, is proposed in Appendix A. But for the purpose of this thesis, we shall limit ourselves to XY planer mechanisms only.

In this chapter, we have proposed several XY flexure designs based on simple flexure units. In general, these mechanisms have a large range of motion because they avoid some of the limitations that arise in the conventional parallel mechanism designs. While we have made qualitative estimates about the advantages and disadvantages of each embodiment, the exact performance of these designs, including the range of motion prediction, remains to be evaluated analytically and experimentally. It has also become clear that not only the transverse, but also the axial stiffness properties of a flexure unit are very important. In parallel kinematic mechanisms such as the ones proposed here, each flexure unit or building block performs two distinct functions – that of providing DOF along one direction, and DOC along other directions. Therefore, the force displacement relationship of the flexure unit along each direction, and more importantly its dependence on the forces and displacements in other directions, plays a key role in determining the performance attributes such as variation in stiffness, cross-axes coupling, parasitic errors and actuator isolation, of the overall flexure mechanism.

With this understanding, we proceed to Chapters 3 and 4, which present these force-displacement relationships in a parametric form. These results then allow us to deterministically evaluate the performance of the designs proposed here, which is done in Chapter 5.

**This page is intentionally left blank.**

## Chapter 3. Static Non-Linear Beam Bending Analysis

In this chapter we revisit non-linear beam bending analysis, with the objective of understanding the basic attributes of flexure units. The reason for choosing a uniform beam is that it is one of the most common flexure elements, and at the same time is simple enough to allow for closed-form analysis. Based on the results of this analysis, we seek insights into the nature of concepts such as Degrees of Freedom, parasitic error, over-constraint and stiffness variation with displacements. Once this is done, we shall have the tools and terminology to investigate other more complex flexure elements and mechanisms. While thermal effects can play an important role in the performance of flexures, we limit our present analysis to only the structural aspects. Furthermore, although an explicit dynamic analysis is not performed at this stage, some key conclusions pertaining to the dynamic performance may be obtained from the results of the static analysis.

All the attributes and performance measures of interest, as outlined in Chapters 1 and 2, can be derived from the force displacement characteristics of a given flexure unit. Therefore, based on the principles of solid mechanics, we proceed to analyze these characteristics for the simple beam flexure. A typical formulation in mechanics consists of three components [69-70]

- a) Constitutive relationships
- b) Force equilibrium or force compatibility relationships
- c) Geometric equilibrium or geometric compatibility relationships

All three of the above relationships determine the overall nature of a problem, for example, whether the formulation will be linear or non-linear. Non-linearity in a formulation may be a consequence of either of the above.

At the macro scale, constitutive relationships relate loads to deformations. For an infinitesimally small differential element, these relationships relate the stresses to strain, and are dependent on the material properties.

Force equilibrium is commonly applied to a loaded elastic body in its undeformed configuration, but in reality, forces are truly in equilibrium only in the deformed configuration. Since the deformations are small, it is usually assumed that force equilibrium equations will not be affected significantly irrespective of whether they are applied in the deformed or undeformed configuration. While this is a reasonable assumption for many cases, there are other situations where force equilibrium in the system is critically dependent on the deformation that results from the forces on the system, for example, during a transverse

displacement of a string under tension. It is important to realize that, in such situations, even though force equilibrium conditions may include the non-linearities arising from displacement variables, these equations are necessarily linear in the load terms, as required by Newton's Laws.

Furthermore, systems obey certain geometric constraints which results in the conditions of geometric compatibility or geometric equilibrium. In almost all cases, geometric compatibility is a purely kinematic relationship, often non-linear in the displacement variables, but independent of loads. But this should not be mistaken for a rule. Although uncommon, there are cases, where geometric compatibility becomes dependent on the loading. Such a situation, and its consequence on the elastic analysis, is discussed later in this chapter.

A given mechanics problem may be approached by explicitly solving the equations resulting from all three of the above relationships simultaneously. This involves the internal forces and displacements, which may not be of interest as far as the final results are concerned. Energy methods arising from the Principles of Virtual Work and Complementary Virtual work offer a computationally efficient, and mathematically elegant alternative to the former approach. While all analysis in this chapter is done using the former approach, a discussion on the applicability and use of energy methods in this context is presented towards the end.

Finally, to be able to employ the principles of mechanics to achieve relationships that are useful for flexure design, and at the same time are accurate enough, several carefully justified engineering approximation need to made. One of the key steps in this analysis is recognizing what effects are important and what are not. This is achieved by making use of engineering judgment, mathematical insight and non-dimensional analysis.

### 3.1 Beam Bending Analysis

Classical beam bending analysis is commonly found in several undergraduate and advanced texts [69-71]. These derivations are based on a formulation that is attributed to Jacob Bernoulli and Leonard Euler [72]. Although the final results of Bernoulli's original analysis are known to be erroneous, the basic assumptions that he made are very powerful and hence constitute the starting point in classical beam bending theory.

Since we would like to study secondary effects resulting from axial forces in a beam, it is important to verify the validity of Bernoulli's assumptions. Fundamentally, these assumptions are based on arguments of symmetry. One can imagine an infinitely long slender beam with a uniform rectangular cross-section subjected to a pure bending moment. Consider a finite length segment of this beam centered about axis  $O-$

$O$ , in an undeformed and a deformed configuration, shown in Figures 3.1A and 3.1B, respectively. At this stage, no assumptions are made regarding either the height or depth of the beam.

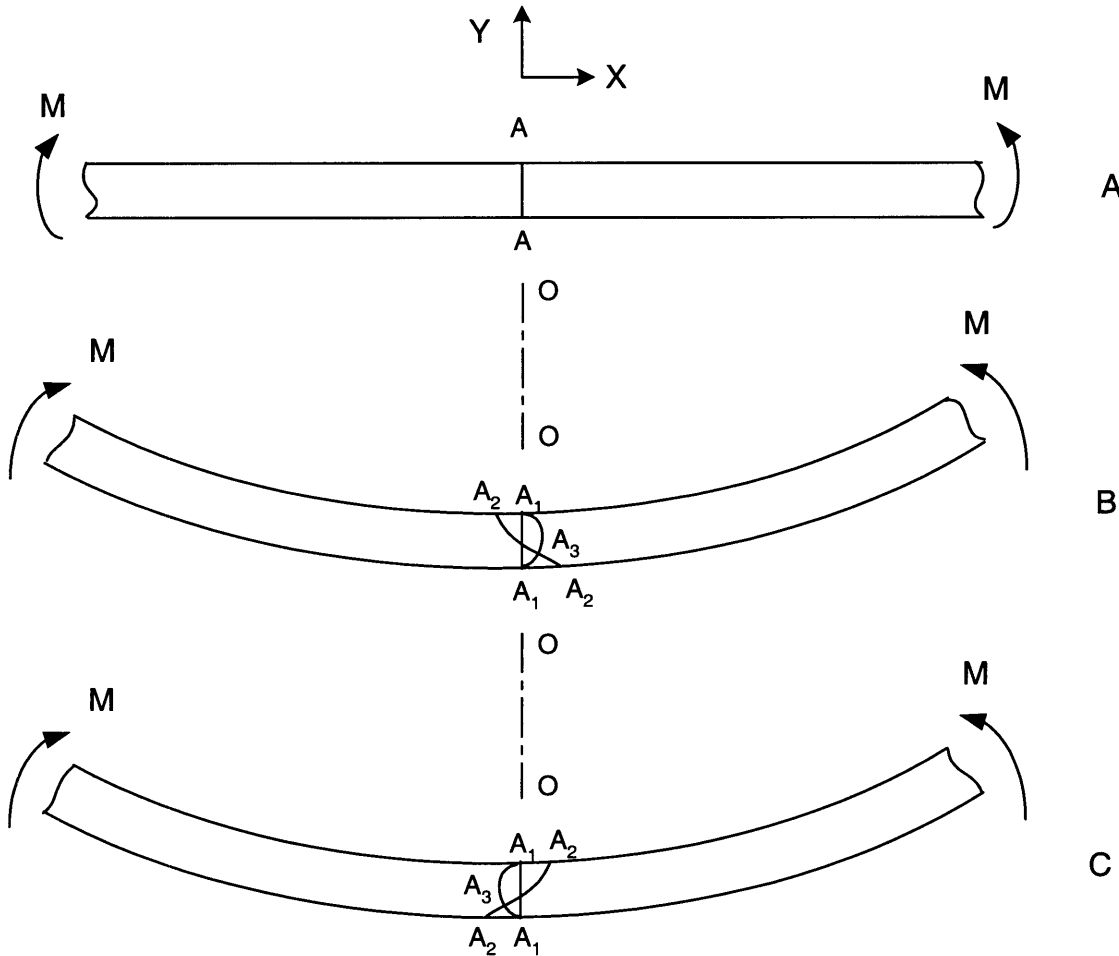


Fig.3.1 Infinite beam under pure moment load

Now let us reason what happens to a cross-section plane A-A that is initially aligned along the O-O axis in the undeformed beam. After deformation, the section A-A can assume one of several possible configurations for example,  $A_1$ ,  $A_2$  or  $A_3$ . It is easily seen from Fig. 3.1B that the loading and the geometry of the beam are perfectly symmetrical about the O-O axis. Therefore, if one flips the beam about the O-O axis, since the loading and external geometry of the beam remain unchanged, all the beam cross-sections in their deformed configuration should appear as though nothing changed. This argument rules out all possibilities like  $A_2$  and  $A_3$ . The only post deformation configuration of A-A that withstands the above requirements of symmetry is  $A_1$ . Based on this simple mental experiment, one can make two conclusions,

- a) Plane sections remain plane after deformation
- b) Plane sections remain normal to the top and bottom faces of the beam after deformation

The above set of arguments, and therefore the resulting conclusions, do not change if one chooses a different cross-section, as long as it is uniform and symmetric. More importantly, the presence of a uniform axial force along the beam doesn't affect these conclusions either.

For practical reasons, beams are not infinite. But a slender beam with a height much smaller in comparison to the length, is a close approximation. In this case, from the point of view of a cross-section in the beam, which is far away from either end, the beam appears *almost* infinite. The above arguments also assume that moment is constant along the length of the beam, which is clearly not the case when a shear force is present. Since shear forces break the loading symmetry, one would doubt the above conclusions. But once again, for small beam heights, variations in moment over the length of the beam do not appear very significant, and these conclusions may still be used as very good engineering approximations. In fact, finite element analysis and experimental evidence corroborates the validity of these approximations.

As the beam height is increased, one may no longer be able to treat the beam as being infinitely long, and therefore the approximations start to fail, and plane sections no longer remain plane. In this case, pursuing beam bending analysis based on Bernoulli's assumptions results in the contradictory situation where shear strains are zero, while the shear stresses are finite and large. This anomaly is elegantly resolved in Timoshenko's beam bending theory [71]. Although, physically less intuitive, Timoshenko's formulation provides a more accurate representation of non-slender beams, owing to its mathematical rigor.

Typically for flexure elements the height is kept significantly smaller than the length, and therefore Bernoulli's assumptions hold. Furthermore, even when the cross-sections warp, the final results of the classical beam bending theory stay valid as long as the axial and the shear forces remain constant [70], which is often the case.

Euler further made the assumption that apart from being thin in the Y direction, the beam is also thin in the Z direction. This then allows for a plane stress assumption in the XY and XZ planes. Commonly, in the case of flexures, a relatively large Z dimension is used to limit motion to the XY plane. In that case, it can be shown that the strains in the Z direction are negligibly small, resulting in plane strain in the XY plane, while the XZ plane still remains in plane stress. Thus, depending upon the Z dimension of the beam, the XY plane will either be in a state of plane stress or plane strain. For either case, the analysis that follows is straight forward. We simply state the final result, which applies at every cross-section of the beam, and is commonly known as *Euler's formula*.

$$\frac{E}{\rho} = \frac{M}{I} \quad (3.1)$$

where,

$M$  is the moment at a given cross-section in the beam,  $I$  is the second moment of area about the Z axis,  $\rho$  is the radius of curvature, and

$$\begin{aligned} E &= E^* && \text{if Plane Stress} \\ &= E^*/(1 - \nu^2) && \text{if Plane Strain, and} \end{aligned}$$

$E^*$  and  $\nu$  are the Young's modulus and Poisson's ratio of the material, respectively.

As we proceed through this analysis, there are several approximations that we will need to make, and these are appropriately justified wherever mentioned. To be able to make any decisions regarding dropping of terms, we should have an idea of the maximum amount of motion and forces that may be applied to the flexure beam. Since, parallelogram and double parallelogram flexures are the most frequently used flexure units in this thesis, and since the beams that constitute these units have an approximately S-shape deformation, we shall use the S-shape deformation to make some preliminary estimates.

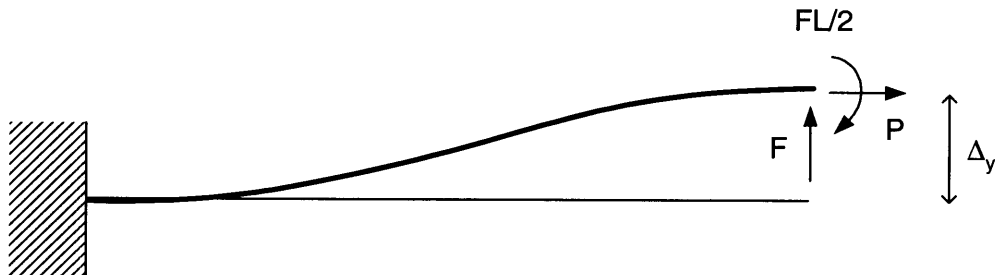


Fig 3.2 A beam deformed in S-shape

A beam experiences an S-shape deformation for the loading conditions shown in Fig 3.2. For this zero end slope condition, it can be shown that the buckling load of the beam is given by

$$P = -\frac{\pi^2 EI}{L^2} \Rightarrow \frac{PL^2}{EI} = -\pi^2 \approx -9.87$$

where all the quantities have standard meanings. As part of a parallel kinematic flexure the beam will transmit tensile as well as compressive loads. Hence we shall only be interested in axial loads that are within the buckling limit. Furthermore, the flexure units will transmit axial as well as transverse loads.

For a symmetric and balanced mechanism, the order of these loads will be approximately the same. Therefore, we shall use the limit determined above for the transverse loads  $F$  as well.

Using the maximum shear stress yield criteria, for example, one can show that the maximum allowable tip displacement is given by

$$\left(\frac{\Delta_y}{L}\right)_{\max} \leq \frac{1}{3\eta} \frac{S_y}{E} \frac{L}{T} \quad (3.2)$$

where  $T$  denotes the beam thickness,  $S_y$  is the material yield strength, and  $\eta$  is a chosen factor of safety. For flexures,  $L/T$  ratios of 50 are common, and  $S_y/E$  ratios range from  $4e-3$  for AL-6061 to  $1e-2$  for TI-13. The safety factor  $\eta$  may be chosen on the basis of stress concentration in the geometry. For typical values, the maximum deformation  $\Delta_y$  ranges from  $0.05L$  to  $0.1L$ . We will aim to obtain results for deformations as large as  $0.1L$ , but in practice the deformations are kept well within this number, especially if fatigue loading is considered.

Based on (3.2), it is useful to keep in mind that in designs where the maximum motion is dictated by the static yield criteria, the normalized maximum motion  $\Delta_y/L$  is inversely proportional to the normalized blade thickness  $T/L$ .

Now consider a Bernoulli beam in Fig. 3.3 with a set of generalized forces  $F$ ,  $M$  and  $P$  acting at its tip, representing transverse, moment and axial loads, respectively. The resulting displacements are  $\Delta_x$ ,  $\Delta_y$  and  $\theta$ . All forces and displacements are expressed in a reference frame that is aligned with the undeformed configuration of the beam. The constitutive relation for an X differential element of the beam is given by Euler's formula (3.1). The macroscopic geometric compatibility can be stated as an expression for the beam curvature at any given location  $X$  along the beam length.

$$\frac{1}{\rho} = \frac{Y''}{(1+Y'^2)^{3/2}} \quad (3.3)$$

The denominator in the above term makes the resulting differential equation non-linear, and requires the use of elliptical integrals for a closed-form solution [73-75]. The result of this non-linear formulation is too complex to be of use for the closed-form analysis of more complex flexure mechanisms. Instead of trying to work with the elliptical integrals, we consider the often made assumption of small slopes. For an S-shape deformation if the tip deflection is  $0.1L$ , then the maximum slope that exists in the beam is  $0.15$ , which occurs at the mid-length. Therefore, the maximum error in approximating the denominator by 1 is about 3.4 percent. To meet the objective of obtaining parametric results, we decide to accommodate this error.

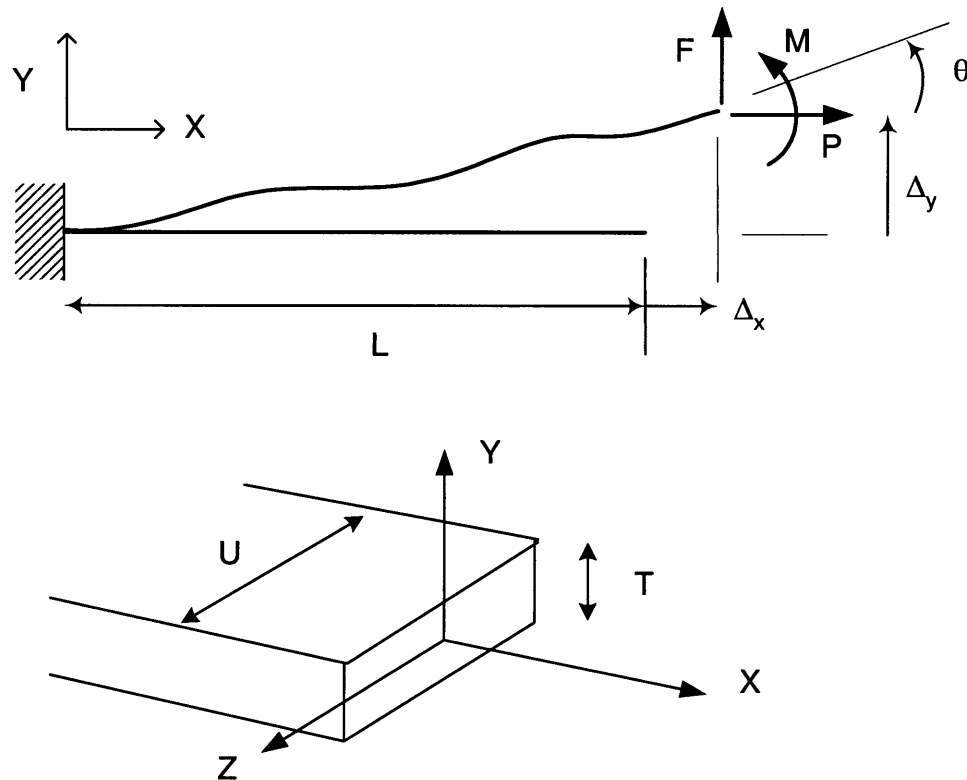


*Fig 3.3 Beam with a generalized end load*

In the next step, all displacements and length parameters are normalized by the beam length  $L$ , and all forces are normalized by  $EI/L^2$ .

$$\begin{aligned} y &= \frac{Y}{L} & x &= \frac{X}{L} & \delta_y &= \frac{\Delta_y}{L} & \delta_x &= \frac{\Delta_x}{L} & t &= \frac{T}{L} & u &= \frac{U}{L} \\ m &= \frac{ML}{EI} & f &= \frac{FL^2}{EI} & p &= \frac{PL^2}{EI} \end{aligned}$$

In the rest of this thesis, we follow the notation of representing all non-dimensionalized quantities by lower case alphabets, whereas their corresponding dimensional parameters are denoted in upper case.

The condition of force equilibrium when determined from the undeformed configuration results in,

$$M(X) = M + F(L - X) \Rightarrow m(x) = m + f(1 - x) \quad (3.4)$$

Equations (3.1)-(3.4) can be solved simultaneously to determine displacements in terms of loads or vice-versa. The results of this straightforward exercise are stated in a non-dimensionalized form.

$$\begin{bmatrix} \delta_y \\ \theta \end{bmatrix} = \begin{bmatrix} 1/3 & 1/2 \\ 1/2 & 1 \end{bmatrix} \begin{bmatrix} f \\ m \end{bmatrix} \quad (3.5)$$

$$\begin{bmatrix} f \\ m \end{bmatrix} = \begin{bmatrix} 12 & -6 \\ -6 & 4 \end{bmatrix} \begin{bmatrix} \delta_y \\ \theta \end{bmatrix}$$

$$\begin{aligned} \delta_x &= -[\delta_y \ \theta] \begin{bmatrix} 3/5 & -1/20 \\ -1/20 & 1/15 \end{bmatrix} \begin{bmatrix} \delta_y \\ \theta \end{bmatrix} + \frac{pt^2}{12} \\ &= -[f \ m] \begin{bmatrix} 1/15 & 5/48 \\ 5/48 & 1/6 \end{bmatrix} \begin{bmatrix} f \\ m \end{bmatrix} + \frac{pt^2}{12} \end{aligned} \quad (3.6)$$

Expression (3.6) is obtained by carrying out an integral of the beam arc length, and setting it equal to the undeformed length plus the elastic stretch. The resulting expression for  $\delta_x$  is comprised of two very independent components, a kinematic term and an elastic term. While the elastic term depends on the applied axial force, and vanishes when the axial force becomes zero, the kinematic term has a quadratic dependence on the transverse displacements. Although the kinematic term expression may be rewritten in terms of transverse loads instead of transverse displacements, resulting in a non-linear force displacement characteristic, it is emphasized that this is fundamentally a relationship between geometric parameters, arising from the condition of geometric constraint on the arc length.

Note that the non-dimensionalized axial force  $p$  does not appear in the force-displacement relationships in the transverse directions (3.5). Furthermore, the relations (3.6) does not provide any information about the change in the axial stiffness in the presence of a transverse force or displacements. Such interdependence is of key concern in designing parallel kinematic mechanisms, as has been explained earlier. This linear analysis is good for displacements of the order of 0.1, as long the axial force  $p$ , which was neglected in the force equilibrium relation, is small. The obvious questions that arise are: How small should  $p$  be for the expressions (3.5) and (3.6) to be effective? How are  $\delta_y$  and  $\theta$  affected by the presence of an axial load  $p$ ? To obtain answers to these questions, we next perform a non-linear beam bending analysis based on force equilibrium conditions applied in the deformed configuration.

$$M(X) = M + F(L + \Delta_x - X) - P(\Delta_y - Y) \quad (3.7)$$

Equations(3.1), (3.3) and (3.7) together yield

$$EIY'' = M + F(L + \Delta_x - X) - P(\Delta_y - Y) \Rightarrow y'' = m + f(1 + \delta_x - x) - p(\delta_y - y)$$

which upon double differentiation leads to

$$y^{iv} = py'' \Rightarrow y^{iv} - k^2 y'' = 0, \quad p \triangleq k^2 \quad (3.8)$$

$p$  may be positive or negative, resulting in a real or imaginary  $k$ , respectively. Both these situations are easily dealt with. The general solution to this equation is,

$$y = c_1 e^{kx} + c_2 e^{-kx} + c_3 x + c_4$$

Constants  $c_1$  through  $c_4$  can be determined using the boundary conditions. Depending on whether we want to obtain forces in terms of displacements or displacements in terms of forces, we can use either of two sets of boundary conditions

Set A    or    Set B

$y = 0$	$\text{@ } x = 0$	$y = 0$	$\text{@ } x = 0$
$y' = 0$	$\text{@ } x = 0$	$y' = 0$	$\text{@ } x = 0$
$y'' = m$	$\text{@ } x = l$	$y = \delta_y$	$\text{@ } x = l$
$y''' = -f + py'$	$\text{@ } x = l$	$y' = \tan \theta$	$\text{@ } x = l$

At this point, we introduce two other approximations.  $\tan \theta$  can be approximated by  $\theta$ , since for the maximum slope of 0.15 that the beam sees,  $\theta$  value is 0.149, which is less than 1 percent error. Furthermore, although the boundary conditions should be applied in the deformed configuration, that is, at  $x = l + \delta_x$ , this is of very small consequence for the pertinent calculation. In an S shape deflection, for a  $\delta_y$  of 0.1,  $\delta_x$  will be approximately 0.006, which can be dropped out in comparison to 1 in the above boundary conditions.

Using the first set of boundary conditions, we obtain

$$\begin{aligned} c_1 &= \frac{1}{e^k + e^{-k}} \left\{ \frac{m}{k^2} - \frac{f e^{-k}}{k^3} \right\} \\ c_2 &= \frac{1}{e^k + e^{-k}} \left\{ \frac{m}{k^2} + \frac{f e^k}{k^3} \right\} \\ c_3 &= f/k^2 \quad \text{and} \quad c_4 = -c_1 - c_2 \end{aligned}$$

With these values and some amount of mathematical manipulation, the end displacement of the beam can be shown to be,

$$\begin{aligned} \delta_y &= f \left( \frac{k - \tanh k}{k^3} \right) + m \left( \frac{\cosh k - 1}{k^2 \cosh k} \right) \\ \theta &= f \left( \frac{\cosh k - 1}{k^2 \cosh k} \right) + m \left( \frac{\tanh k}{k} \right) \end{aligned} \quad (3.9)$$

If one employed the second set of boundary conditions, the values for the constants  $c_1$  through  $c_4$  are,

$$c_1 = \frac{k(e^{-k} - 1)\Delta_y + (e^{-k} + k - 1)\theta}{k[k(e^k - e^{-k}) - 2(e^k + e^{-k}) + 4]}$$

$$c_2 = \frac{k(e^k - 1)\Delta_y - (e^k - k - 1)\theta}{k[k(e^k - e^{-k}) - 2(e^k + e^{-k}) + 4]}$$

$$c_3 = k(c_2 - c_1)$$

$$c_4 = -c_1 - c_2$$

Given the following relationships for end loads,

$$f = -y'''(I) + py'(I)$$

$$m = y''(I)$$

one can deduce,

$$\begin{aligned} f &= \frac{k^3 \sinh k}{k \sinh k - 2 \cosh k + 2} \delta_y + \frac{k^2(1 - \cosh k)}{k \sinh k - 2 \cosh k + 2} \theta \\ m &= \frac{k^2(1 - \cosh k)}{k \sinh k - 2 \cosh k + 2} \delta_y + \frac{k^2 \cosh k - k \sinh k}{k \sinh k - 2 \cosh k + 2} \theta \end{aligned} \quad (3.10)$$

Expressions analogous to (3.9) and (3.10) may be obtained similarly for compressive axial load, i.e., negative values of  $p$ . The results are obtained in terms of trigonometric functions rather than hyperbolic functions.

The next step in this derivation is to apply the constraint condition on the arc length of the beam in its deformed configuration, so as to determine  $\delta_x$ . As earlier, the displacement  $\delta_x$  can be resolved into two components – a kinematic component that results from the constant arc length requirement, and a purely elastic component that results due to elastic stretching.

$$\delta_x = \delta_x^k + \delta_x^e \quad (3.11)$$

The elastic component may be expressed as,

$$\delta_x^e = \frac{p}{d} \quad \text{where} \quad d = \frac{AL^2}{I} = 12 \left( \frac{L}{T} \right)^2 = \frac{12}{t^2} \quad (3.12)$$

The kinematic component is derived by performing an integration on differential arc elements.

$$ds = (1 + y'^2)^{1/2} dx \approx (1 + 1/2 y'^2) dx$$

Clearly, in the above expression, we cannot simply neglect the  $y'$  term as was done earlier, or else we shall not be able to obtain a difference between the integral of  $ds$  and  $dx$ . We do however make a different assumption this time, by retaining up to the second order term in the Binomial expansion of the  $ds$  expression. The subsequent term is fourth order and for a maximum  $y'$  of 0.15, this term is approximately  $5e-4$ , and is therefore neglected.

$$\int_0^{l+\delta_x^e} ds = \int_0^{l+\delta_x^e} (1 + \frac{1}{2}y'^2) dx$$

$$1 + \delta_x^e = (1 + \delta_x) + \frac{1}{2} \int_0^{l+\delta_x} y'^2 dx \Rightarrow \delta_x^k = -\frac{1}{2} \int_0^l y'^2 dx$$

We also note that the upper limit of integration has been changed in the last integral expression, on the basis that the small difference in the integral limit will not change the integral significantly. The length term appears in the integral appear in powers of three and higher, and since  $\delta_x$  is approximately 0.006 for a maximum tip displacement of 0.1 for a beam in an S-shape deflection, it reasonable to neglect the  $\delta_x$  with respect to the  $l$  that appears in the integral limit.

For the sake of mathematical convenience, this time we use an alternate expression for  $y$ , in terms of hyperbolic functions instead of exponentials. For this solution to be valid, we have to explicitly assume that the axial force is tensile. For compressive loads an analogous analysis can be conducted.

$$y = c_1 \cosh kx + c_2 \sinh kx + c_3 x + c_4$$

$$y' = c_1 k \sinh kx + c_2 k \cosh kx + c_3$$

Applying the boundary conditions,

$$@ x = 0$$

$$y = 0 \Rightarrow c_1 + c_4 = 0$$

$$y' = 0 \Rightarrow c_2 k + c_3 = 0$$

$$@ x = l$$

$$y = \Delta_y \Rightarrow c_1 \cosh k + c_2 \sinh k + c_3 + c_4 = 0$$

$$y' = \theta \Rightarrow c_1 k \sinh k + c_2 k \cosh k + c_3 = 0$$

one may solve for the unknown constants in the solution, and subsequently for  $y'$ .

$$\begin{bmatrix} c_1 \\ c_2 \end{bmatrix} = \frac{1}{k \sinh k - 2 \cosh k + 2} \begin{bmatrix} \cosh k - 1 & \frac{k - \sinh k}{k} \\ -\sinh k & \frac{\cosh k - 1}{k} \end{bmatrix} \begin{bmatrix} \Delta_y \\ \theta \end{bmatrix}$$

$$c_3 = -c_2 k$$

$$c_4 = -c_1$$

$$y' = c_1 k \sinh kx + c_2 k(\cosh kx - 1)$$

$$y'^2 = k^2 [c_1 \ c_2] \begin{bmatrix} \sinh^2 kx & \sinh kx (\cosh kx - 1) \\ \sinh kx (\cosh kx - 1) & (\cosh kx - 1)^2 \end{bmatrix} \begin{bmatrix} c_1 \\ c_2 \end{bmatrix}$$

$$\int_0^l y'^2 dx = k^2 [c_1 \ c_2] \begin{bmatrix} \int_0^l \sinh^2 kx dx & \int_0^l \sinh kx (\cosh kx - 1) dx \\ \int_0^l \sinh kx (\cosh kx - 1) dx & \int_0^l (\cosh kx - 1)^2 dx \end{bmatrix} \begin{bmatrix} c_1 \\ c_2 \end{bmatrix}$$

$$= \frac{k}{2} [c_1 \ c_2] \begin{bmatrix} (\cosh k \sinh k - k) & (\cosh^2 k - 2\cosh k + 1) \\ (\cosh^2 k - 2\cosh k + 1) & (\cosh k \sinh k - 4\sinh k + 3k) \end{bmatrix} \begin{bmatrix} c_1 \\ c_2 \end{bmatrix}$$

Ultimately, one can obtain

$$\delta_x^k = -[\delta_y \ \theta] \begin{bmatrix} r_{11} & r_{12} \\ r_{21} & r_{22} \end{bmatrix} \begin{bmatrix} \delta_y \\ \theta \end{bmatrix} \quad (3.13)$$

where,

$$r_{11} = \frac{k^2(\cosh^2 k + \cosh k - 2) - 3\sinh k(\cosh k - 1)}{2(k \sinh k - 2\cosh k + 2)^2}$$

$$r_{12} = r_{21} = -\frac{k^2(\cosh k - 1) + k \sinh k (\cosh k - 1) - 4(\cosh k - 1)^2}{4(k \sinh k - 2\cosh k + 2)^2}$$

$$r_{22} = \frac{-k^3 + k^2 \sinh k(\cosh k + 2) - 2k(2\cosh^2 k - \cosh k - 1) + 2\sinh k (\cosh k - 1)}{4k(k \sinh k - 2\cosh k + 2)^2}$$

As earlier,  $\delta_x^k$  may be stated in terms of the transverse loads instead of displacements, but it should be recognized that this is fundamentally an equation of geometric constraint – that the beam maintains a constant arc length. It may be noticed that this condition of geometric constraint is explicitly dependent on a load in the form of  $k$ . As indicated earlier, such situations are fairly uncommon. It will be shortly seen that this load dependence is very weak, nevertheless, its existence is of much importance.

The final results of this derivation are the five equations (3.9)-(3.13) relating five displacement variables -  $\theta, \delta_y, \delta_x, \delta_x^k, \delta_x^e$ , and three load terms  $f, m$ , and  $p$ . The last three equations may be combined to result in an overall three equations, and six variables. Given any three, the remaining three can be found. These results match with similar analysis that has been done in the past [76].

Based on the approximations made so far, these results should err by no more 3-4 % in predicting the true behavior of an ideal beam. It is noteworthy that in the above analysis, we have ignored the non-linearity in the geometric compatibility conditions but have incorporated the non-linearity from the force equilibrium equation. This judgment is based on the fact that, while the former approximation results in a few percent error in the displacement estimates, ignoring the non-linearities in the force equilibrium results in the loss of some fundamental physical effects that dictate the performance of flexures. Furthermore, it will be seen in the next section that the transcendental expressions (3.9) and (3.10), resulting from the force equilibrium non-linearity, can be readily simplified to obtain useful parametric information. Similar simplifications are difficult to obtain for elliptical integrals.

### 3.2 Engineering Approximations and Simplified Results

Several interesting observations can be made from the expressions stated above. For example, the end displacements  $y$  and  $\theta$  are not uniquely related to the end loads  $f$  and  $m$ . For any given loads,  $f$  and  $m$ , the displacements,  $y$  and  $\theta$ , can take a different set of values depending on the magnitude of  $k$ , or the axial load  $p$ . But given the transcendental nature of the above expressions, it is almost impossible for a design engineer to draw any parametric conclusions. We therefore proceed to make another set of engineering approximations, the most important so far, in an attempt to obtain expressions that offer better insight into the force displacement characteristics of the flexure beam.

We start with the simplification of the compliance terms in Equation (3.9). An obvious first guess to expand the hyperbolic expression in form of an infinite series and then use the first few terms.

$$C = \begin{bmatrix} \left( \frac{k - \tanh k}{k^3} \right) & \left( \frac{\cosh k - 1}{k^2 \cosh k} \right) \\ \left( \frac{\cosh k - 1}{k^2 \cosh k} \right) & \left( \frac{\tanh k}{k} \right) \end{bmatrix}$$

$$c_{11} = \left( \frac{k - \tanh k}{k^3} \right) \approx \frac{1}{3} \left( 1 - \frac{2}{5} k^2 + \frac{17}{105} k^4 - \frac{62}{945} k^6 \dots \right)$$

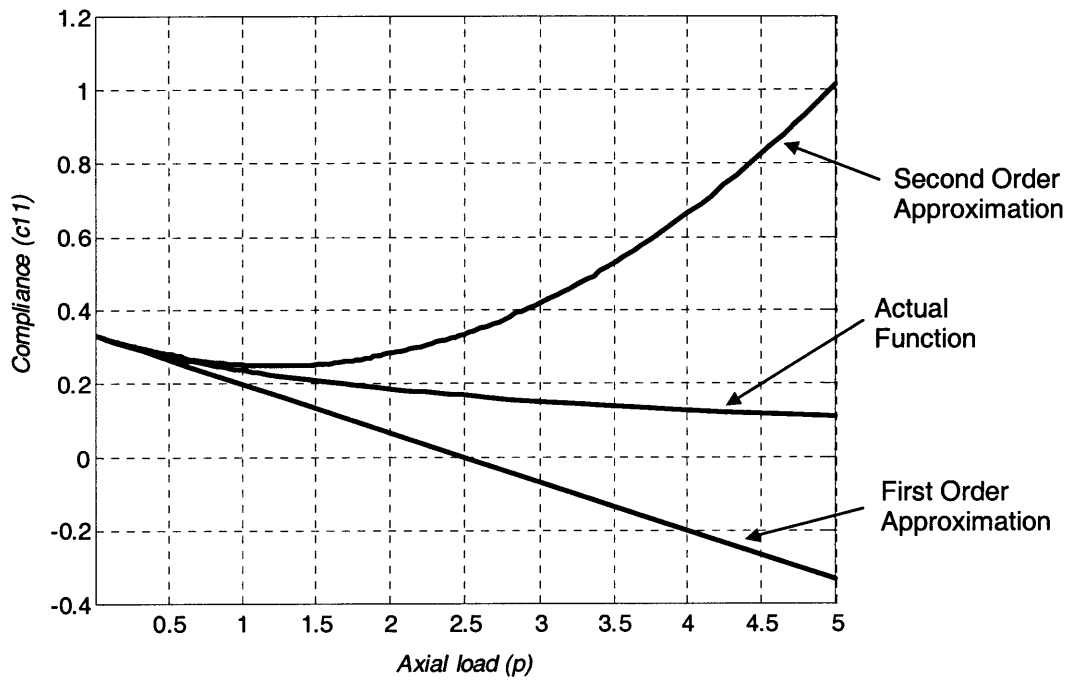


*Fig 3.4 Approximation of the Compliance term  $c_{11}$*

Simply taking the first few terms from the expansion series turns out to be a very poor approximation as is seen in the Fig. 3.4. Instead we look for other simple functions that may approximate the transcendental function. The following turns out to be a good fit.

$$\begin{aligned} \left( \frac{k - \tanh k}{k^3} \right) &\approx \frac{1}{3} \left( 1 - 0.4k^2 + 0.1619k^4 - 0.0656k^6 \dots \right) \\ \frac{1}{3\left(1 + \frac{2}{5}k^2\right)} &\approx \frac{1}{3} \left( 1 - 0.4k^2 + 0.1600k^4 - 0.0640k^6 \dots \right) \end{aligned}$$

Since the series expansion coefficients for the two functions are very close up to several higher order terms, the expression in the second line above seems to be a very good approximation. This becomes evident from Fig. 3.5 where the two functions are plotted for values of  $p$  ( $\triangleq k^2$ ) up to 10. At this value of  $p$ , the error in approximation is 2.6%. Mathematically speaking, this excellent match is purely a coincidence.

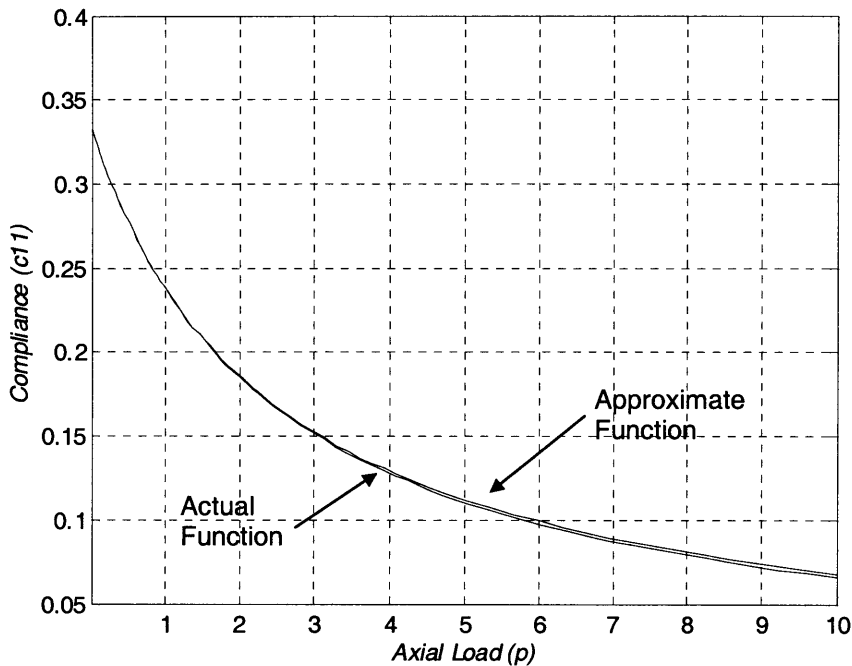


*Fig 3.5 Approximation of the Compliance term  $c_{11}$*

Similar approximations may be obtained for the other compliance terms.

$$c_{12} = c_{21} = \left( \frac{\cosh k - 1}{k^2 \cosh k} \right) \approx \frac{1}{2 \left( 1 + \frac{5}{12} k^2 \right)} = \frac{1}{2 \left( 1 + \frac{5}{12} p \right)}$$

$$c_{22} = \left( \frac{\tanh k}{k} \right) \approx \frac{1}{\left( 1 + \frac{1}{3} k^2 - \frac{1}{63} k^4 \right)} = \frac{1}{\left( 1 + \frac{1}{3} p - \frac{1}{63} p^2 \right)}$$

$$c_{22} = \left( \frac{\tanh k}{k} \right) \approx \frac{\left( 1 + \frac{1}{10} p \right)}{\left( 1 + \frac{17}{40} p + \frac{7}{600} p^2 \right)}$$

These approximate functions are plotted in Figures 3.6 and 3.7 respectively, along with the exact functions. Since these are not series based approximations,  $p$  does not have to be small for the approximations to hold. While the approximation for  $c_{11}$  and  $c_{12}$  is good for values of  $p$  up to 10, the approximation for  $c_{22}$  is not as accurate. In fact, simply an inverse linear term results in an inadequate match in this case, and therefore a quadratic term is also included, which improves the approximation for values of  $p$  up to 5. A combination of linear and inverse quadratic function, shown above, may also be used to get an even better approximation.

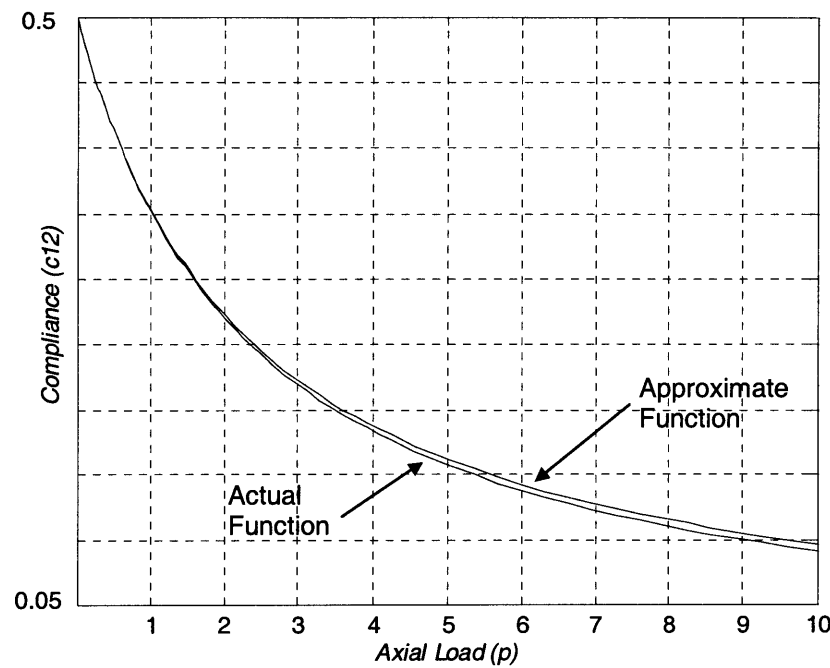


Fig 3.6 Approximation of the Compliance term  $c_{12}$

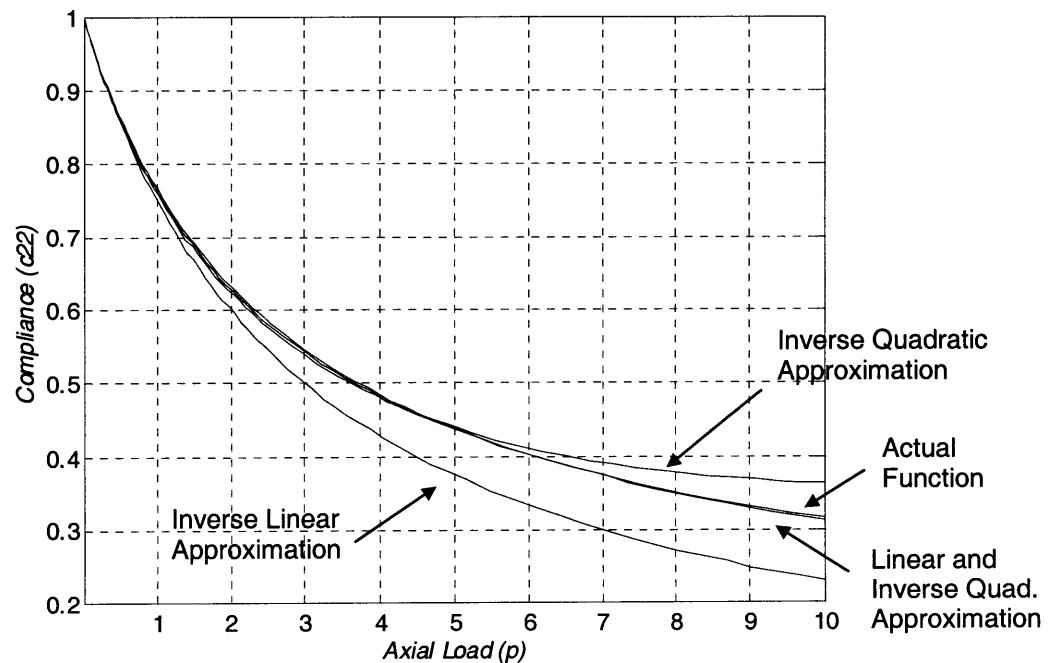


Fig 3.7 Approximation of the Compliance term  $c_{22}$

The fact that some compliance terms can be approximated by inverse linear functions of  $p$ , provides an indication that stiffness functions may be approximated by linear functions of  $p$ . That indeed is the case, and therefore approximations to the stiffness terms are obtained simply from the Taylor series expansion of the actual hyperbolic stiffness functions.

$$K = \begin{bmatrix} \frac{k^3 \sinh k}{k \sinh k - 2 \cosh k + 2} & \frac{k^2(1 - \cosh k)}{k \sinh k - 2 \cosh k + 2} \\ \frac{k^2(1 - \cosh k)}{k \sinh k - 2 \cosh k + 2} & \frac{k^2 \cosh k - k \sinh k}{k \sinh k - 2 \cosh k + 2} \end{bmatrix}$$

The following series expansions show that for the range of our interest, the coefficients of the higher order terms are small enough to be neglected.

$$k_{11} = \frac{k^3 \sinh k}{k \sinh k - 2 \cosh k + 2} \approx 12 \left( 1 + \frac{1}{10} k^2 - \frac{1}{8400} k^4 \dots \right) \approx 12 \left( 1 + \frac{1}{10} p \right)$$

$$k_{12} = \frac{k^2(1 - \cosh k)}{k \sinh k - 2 \cosh k + 2} \approx -6 \left( 1 + \frac{1}{60} k^2 - \frac{1}{8400} k^4 \dots \right) \approx -6 \left( 1 + \frac{1}{60} p \right)$$

$$k_{22} = \frac{k^2 \cosh k - k \sinh k}{k \sinh k - 2 \cosh k + 2} \approx 4 \left( 1 + \frac{1}{30} k^2 - \frac{11}{25200} k^4 \dots \right) \approx 4 \left( 1 + \frac{1}{30} p \right)$$

The first two simplifications above result in errors of less than 1 percent, and the third simplification deviates from the exact expression by less than 3 percent. But the advantage of these simplifications are far-fetched in terms of revealing the key attributes of the beam flexure, and producing valuable closed-form results. Although the above approximations are obtained for tensile axial loads, the approximations can be shown to be valid for compressive axial loads as well. It can also be shown that the product of the approximate stiffness matrix and the approximate compliance matrix, both restated below, is very close to the unity matrix.

$$\begin{bmatrix} \delta_y \\ \theta \end{bmatrix} = \begin{bmatrix} \frac{1}{3(1 + \frac{2}{5} p)} & \frac{1}{2(1 + \frac{5}{12} p)} \\ \frac{1}{2(1 + \frac{5}{12} p)} & \frac{(1 + \frac{1}{10} p)}{(1 + \frac{17}{40} p + \frac{7}{600} p^2)} \end{bmatrix} \begin{bmatrix} f \\ m \end{bmatrix} \quad (3.14)$$

$$\begin{bmatrix} f \\ m \end{bmatrix} = \begin{bmatrix} 12(1 + \frac{1}{10} p) & -6(1 + \frac{1}{60} p) \\ -6(1 + \frac{1}{60} p) & 4(1 + \frac{1}{30} p) \end{bmatrix} \begin{bmatrix} \delta_y \\ \theta \end{bmatrix} \quad (3.15)$$

Luckily, simple linear approximations are also available for the coefficients in the geometric constraint relation (3.13). It may be seen that the coefficients have an approximately linear dependence on  $p$ , and that this dependence is very weak.

$$\delta_x^k = -[\delta_y \quad \theta] \begin{bmatrix} \frac{3}{5}\left(1 - \frac{p}{420}\right) & -\frac{1}{20}\left(1 - \frac{p}{70}\right) \\ -\frac{1}{20}\left(1 - \frac{p}{70}\right) & \frac{1}{15}\left(1 - \frac{11p}{420}\right) \end{bmatrix} \begin{bmatrix} \delta_y \\ \theta \end{bmatrix} \quad (3.16)$$

It is therefore tempting to neglect the dependence of the coefficients on the axial loads. But it shall soon become clear that these terms play a critical role in determining the characteristics of the beam in particular, and flexures in general.

Based on the recent approximations, the force-displacement relations for a blade can be stated as follows.

$$\begin{bmatrix} f \\ m \end{bmatrix} = \begin{bmatrix} a & c \\ c & b \end{bmatrix} \begin{bmatrix} \delta_y \\ \theta \end{bmatrix} + p \begin{bmatrix} e & h \\ h & g \end{bmatrix} \begin{bmatrix} \delta_y \\ \theta \end{bmatrix} \quad (3.17)$$

$$\delta_x = \frac{1}{d}p + [\delta_y \quad \theta] \begin{bmatrix} i & k \\ k & j \end{bmatrix} \begin{bmatrix} \delta_y \\ \theta \end{bmatrix} + p [\delta_y \quad \theta] \begin{bmatrix} r & q \\ q & s \end{bmatrix} \begin{bmatrix} \delta_y \\ \theta \end{bmatrix} \quad (3.18)$$

These are three equations and six unknowns – three loads and three displacements. Given any three, the remaining can now be easily solved analytically for most cases. The coefficients  $a, b, c, d, e, g, h, i, j, k, q, r$  and  $s$  are all non-dimensional numbers and are characteristic of the uniform cross-section thin beam.

$a$	12	$e$	1.2	$i$	-0.6	$r$	1/700
$b$	4	$g$	2/15	$j$	-1/15	$s$	11/6300
$c$	-6	$h$	-0.1	$K$	1/20	$q$	-1/1400

These numbers obviously remain unchanged as the size of the beam varies, but do change when the geometry or the shape of the beam changes. The variation in above coefficients with changes in beam geometry forms the basis for a sensitivity analysis which shall be briefly discussed later in this chapter.

### 3.3 Observations and Comments on the Simplified Results

There are many interesting observations that may be drawn from the above derivations, also several comments that can be made on these derivations.

1. We see that the transverse stiffness terms are approximately a linear function of the axial force. Although it is intuitively known that the transverse stiffness of a beam increases with a tensile axial load and decreases with a compressive axial load, the actual dependence is stated here in a quantitative form. The non-linearity in force displacement relationships arises due to the fact that displacements are included in force equilibrium. It is common to refer to two kinds of stiffness, the

elastic stiffness matrix and the geometric stiffness matrix, clearly distinguished in expression (3.17). Apart from playing an important role in the analysis of more complex mechanisms, these expressions may be used to quickly and symbolically obtain results that would otherwise involve tedious analysis. For example, in the presence of an axial load  $p$ , one can easily derive the ratio between  $m$  and  $f$ , that is needed to maintain a zero end slope, to be

$$\frac{m}{f} = -\frac{1}{2} \frac{\left(1 + \frac{1}{60} p\right)}{\left(1 + \frac{1}{10} p\right)}$$

Similarly, the non-linear *Duffing effect* in a clamped-clamped beam, transversely loaded in the middle, can be obtained in a few steps to be,

$$f = (a - i d e \delta_y^2) \delta_y \quad (3.19)$$

2. Despite being based on several assumptions, these approximate results are accurate to within 5 percent of the real behavior of an ideal beam. This may be validated using known cases of beam buckling. One way of defining buckling is – the limit of compressive axial force when transverse stiffness becomes zero. For a fixed-free beam, applying the boundary condition of  $m=0$  in equation

(3.14), one obtains  $\delta_y = \frac{1}{3(1 + \frac{2}{5} p)} f \Rightarrow p_{crit} = -2.5$ . From the classical linear beam buckling

analysis, the critical buckling load for a fixed free beam is known to be  $P_{crit} = -\frac{\pi^2 EI}{4 L^2}$

$\Rightarrow p_{crit} = -\frac{\pi^2}{4} = -2.4674$ , which is about 1.3% off from the value predicted using the approximate

results. Similarly, one may consider the buckling of a beam that is fixed on one end, and is constrained to have a zero slope on the other end. This time we can make use of equation (3.15) to predict that the transverse stiffness of the beam will drop to zero for a compressive load of  $p=10$ , which is also 1.3% off from the value  $\pi^2$ , derived from linear beam buckling. For obvious reasons, these results may not be used for predicting the buckling of pinned-pinned or clamped-clamped beams.

3. While the analysis in Section 3.2 assumed that the loads in the deformed configuration stay aligned with the undeformed reference axes of the flexure beam, other situations are easily addressed using the results of the above derivation. Consider, for example, the loading situation of Fig. 3.8, where the loads translate and rotate with the beam tip.

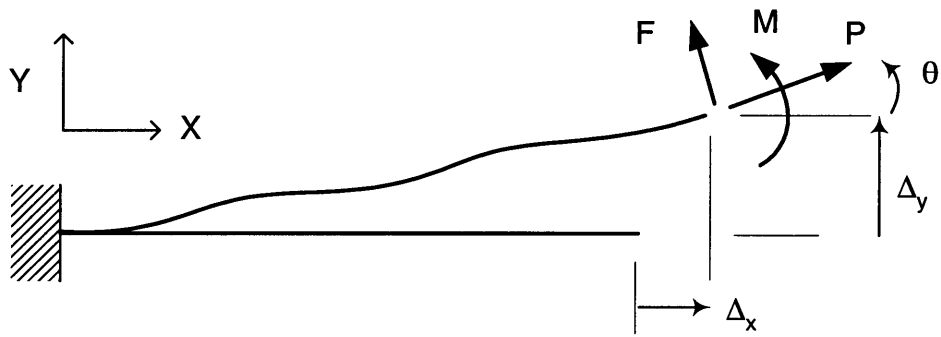


*Fig 3.8 End loading that maintains the orientation of beam tip*

Since  $\theta$  represents rotation of beam tip and is not a spatial variable, this loading condition offers no significant problems, other than some added mathematical complexity. The tip loads expressed along the XY axes may be stated as,

$$f^* = f \cos \theta + p \sin \theta \approx f(1 - \frac{1}{2}\theta^2) + p\theta$$

$$p^* = p \cos \theta - f \sin \theta \approx p(1 - \frac{1}{2}\theta^2) - f\theta$$

Substituting these in equations (3.14) and (3.15) yields interesting force displacement relationships.

For the particular case of  $p=0$  and  $m=0$ , it can be shown in a few steps that

$$\frac{\theta}{(1 + \frac{1}{3}\theta^2)} = \frac{f}{2} \quad \text{and} \quad \delta_y \approx \frac{f - \frac{1}{8}f^3}{3 - \frac{3}{5}f^2}$$

As expected, the transverse stiffness reduces as a consequence of this loading condition.

4. While the variation of transverse stiffness due to axial loads is very clear from equation (3.17), the change in axial stiffness due to the presence of a transverse displacement is quantified in equation (3.18). It may be seen that the kinematic component defined earlier may be further separated into a purely kinematic component, and an ‘elastokinematic’ component.

$$\delta_x^e = \frac{1}{d}p \quad \delta_x^k = [A_y \quad \theta] \begin{bmatrix} i & k \\ k & j \end{bmatrix} \begin{bmatrix} \delta_y \\ \theta \end{bmatrix} \quad \delta_x^{ek} = p [A_y \quad \theta] \begin{bmatrix} r & q \\ q & s \end{bmatrix} \begin{bmatrix} \delta_y \\ \theta \end{bmatrix}$$

The first term above represents a purely elastic component that results from stretching of the beam. The second term is a purely kinematic component, and is a consequence of the constant beam arc length requirement. The third term is the most interesting of three because it has both an elastic as well as a kinematic aspect. Although this term is also a consequence of the constant beam arc length requirement, it essentially captures the effect of the change in the beam’s deformed shape due to the

contribution of the axial force to the bending moments. The first and the third components contribute to the compliance in the X-direction, while the second component is independent of the axial force. The importance of the third term is due to its non-linear contribution to the axial compliance, which has a quadratic dependence on the transverse displacements. As has been mentioned earlier, the axial stiffness of a beam flexure determines the quality of its DOC, which in turn influences static as well as dynamic performance measures in a flexure mechanism.

5. Furthermore, a generalization of the above analysis for a uniform beam may be made by considering a different beam shape, for example, the common double notch flexure in Fig. 3.9.

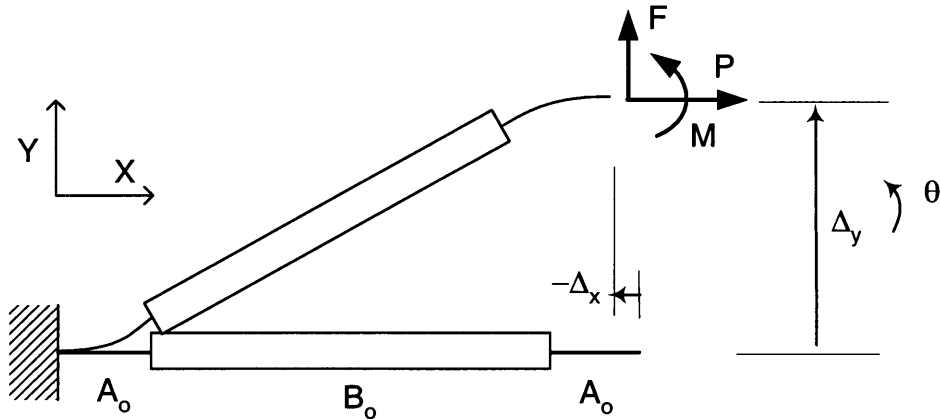


Fig. 3.9 Double Notch Flexure

The overall length of the beam is still  $L$  and is used as the characteristic length of the system. The two notches are  $A_o$  each, and the length of the rigid connector is  $B_o$ . Analysis analogous to that of Section 3.2 can be carried out, although this involves a bit more mathematical complexity. In general, the structure of resulting expressions remains the same, while the non-dimensional coefficients vary. The transverse force displacement relationships in the absence of the axial load  $p$  are given by

$$\begin{bmatrix} \delta_y \\ \theta \end{bmatrix} = \begin{bmatrix} \left(\frac{2}{3}a_o^3 - a_o^2 + a_o\right) & a_o \\ a_o & 2a_o \end{bmatrix} \begin{bmatrix} f \\ m \end{bmatrix}$$

$$\begin{bmatrix} f \\ m \end{bmatrix} = \begin{bmatrix} \frac{12}{1-b_o^3} & \frac{-6}{1-b_o^3} \\ \frac{-6}{1-b_o^3} & \frac{4+b_o+b_o^2}{1-b_o^3} \end{bmatrix} \begin{bmatrix} \delta_y \\ \theta \end{bmatrix}$$

These relations reduce to (3.14) and (3.15), if  $b_o$  is set to 0 or  $a_o$  is set to 0.5, and  $p=0$ . Obviously, if  $a_o$  is made very small, Bernoulli's assumptions will start to fail, and a more accurate analysis will be

needed. Nevertheless, these results provide us with an idea of how the non-dimensional coefficients vary with changing geometry. As is expected, increasing the ratio  $b_o$  will increase the transverse stiffness since this reduces the  $a_o$  segments that provide compliance. For small values of  $b_o$ , the stiffness matrix above can be approximated by

$$\begin{bmatrix} f \\ m \end{bmatrix} = \begin{bmatrix} 12(1+3b_o) & -6(1+3b_o) \\ -6(1+3b_o) & 4(1+3b_o) \end{bmatrix} \begin{bmatrix} \delta_y \\ \theta \end{bmatrix}$$

Interestingly, this is very similar to the effect that an axial load  $p$  has on transverse stiffness, as given by (3.15). In fact, even the deformations of the double notch flexure, and a beam flexure under a large axial load, are very similar. In the former case, the shape of the flexure is such that only the  $a_o$  segments bend and have a curvature, whereas the  $b_o$  segment, being rigid, obviously has no curvature. On the other hand, in the latter case, the effect of the axial force of the beam deformation is such that curvature is predominantly limited to beam ends, and the middle section of the beam remains relatively straight.

Furthermore, such a quantification of the effect of geometric shape variations of the beam on its force-displacement characteristics provides a perfect basis for shape synthesis or optimization, as discussed in Section 1.2. Other variations of the flexure unit in Fig. 3.9, for example, finite stiffness of the middle segment, may also be considered. Each such embodiment will produce a different set of non-dimensional coefficients, but the fundamental physical effects identified above will remain the same. For this reason, all the subsequent discussions on mobility and error motions is pertinent to flexure mechanisms based on a wide range of building blocks, and not simply the uniform beam.

### 3.4 Mobility of Flexure Mechanisms

Based on the understanding gained in the above analysis and subsequent simplifications, we are now in a position to discuss the concepts of Degrees of Freedom, Degrees of Constraint, and overconstraint in flexure mechanisms. A brief summary of the existing literature on mobility analysis of flexures mechanisms was presented in Chapter 1.

Before we proceed, it is worthwhile to first take a quick look at the DOF definition in the context of rigid-link mechanisms. In the case of rigid-link mechanisms, DOF is defined in several ways, the most fundamental of which is – the minimum number of independent displacement coordinates necessary to completely define the configuration of a mechanism. These displacement coordinates are a subset of the so called generalized coordinates, which exceed the DOF by the number of geometric constraints in the

system. This definition of DOF also translates to – the maximum number of independent displacement inputs that can be specified to a given mechanism without violating any geometric constraints. Externally applied loads do not play any role in the mobility of rigid-link mechanisms because the stiffness of constituent elements is either zero or infinite. As is obvious from these definitions, DOF is a purely kinematic property of rigid-link mechanisms, and remains the same for static as well as dynamic analysis.

Gruebler's criterion [24,77] is the most common method of determining the DOF of rigid-link mechanisms. This criterion is derived by considering the DOF of the various constituent rigid links, and the DOC of the elements that connect the rigid links. Since this derivation is based on a generalized geometry of constituent links and connections, Gruebler's criterion fails to correctly predict the mobility of mechanisms that have special geometric arrangements. Several two and three dimensional examples are available in the literature [77], and two cases are shown in Fig. 3.10.

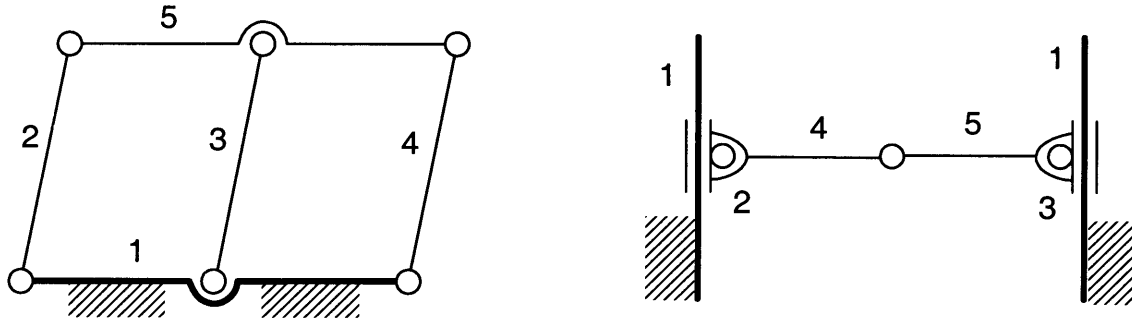


*Fig. 3.10 Mechanisms for which Guebler's Criteria fails*

Specifically, the method fails in situations where a particular geometric arrangement produces either redundant DOC or redundant DOF. For the first mechanism illustrated in Fig. 3.10, the DOF is predicted to be 0 for a general geometry, but for the particular case when links 2, 3 and 4 are perfectly parallel and equal in length, the constraint imposed by one of these three links and its associated pivots becomes redundant, making the actual DOF 1. In the second mechanism, a general geometry will result in two DOF, but for the specific case when the sum of lengths of beams 4 and 5 is exactly equal to the distance between the two perfectly parallel guide rails, one of the DOF becomes redundant and the overall DOF is reduced to 1.

This exposes a fundamental limitation of any mobility criterion that determines the DOF of a mechanism based on the DOF and DOC of its constituents. Because of its generality, which is a powerful as well as desirable attribute, any such criterion is unable to recognize any specific geometric configuration.

With this realization we now move on to flexure mechanisms. In somewhat loose terms, any stiff directions may be termed as Degrees of Constraint and compliant directions may be called Degrees of Freedom. But as soon as one defines DOF based on stiffness, it becomes necessary to specify the load and displacement that the stiffness is associated with.

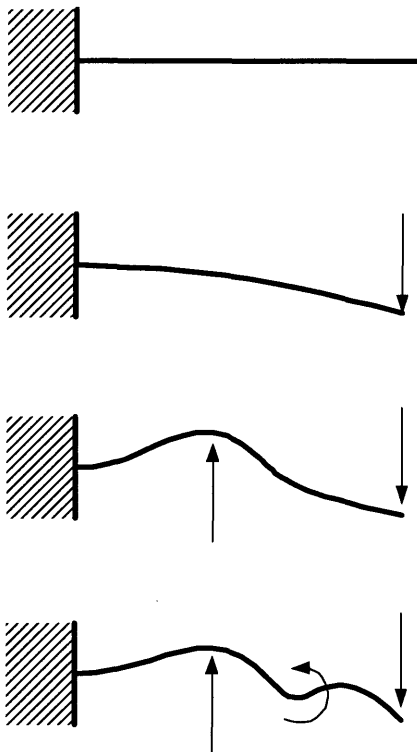


*Fig. 3.11 Loads applied to an elastic body*

It becomes obvious that, unlike rigid link mechanisms, applied loads have a role to play in determining the mobility in flexure mechanisms. In general, an infinite number of independent forces can be applied to an elastic body which result in infinite possible geometric configurations of the body, as shown in Fig. 3.11. With every new force that is added, the body takes a new shape, thereby requiring an ever-increasing number of independent coordinates to completely specify its geometry. To be able to talk about finite DOF in this context, one first needs to clearly identify all the possible locations on a given mechanism where generalized loads, three for a planer case and six for a general case, may be applied. The finite number of loads associated with these locations, or nodes, are referred to as the ‘allowable loads’ henceforth. The concept of introducing a real or imaginary node at locations where forces may be applied has been discussed in the literature [20-21]. This step is crucial as it allows one to associate a finite DOF with a compliant mechanism.

In this discussion we shall consider planer or two-dimensional cases only; an extension of these concepts to three dimensional mechanisms is analogous. Having identified the nodes where loads are allowed, we can associate three displacement coordinates with each. Although these displacement coordinates will be sufficient to determine the configuration of the entire mechanism, it remains to be determined which of these displacement coordinates contribute to Degrees of Freedom.

The extent of normalized displacements in response to nominal normalized loads, or simply the non-dimensional compliance, may be used as measure of mobility. For example, the maximum number of independently large displacement coordinates that can be obtained under any combination of the normalized allowable forces, each less than or equal to 1 unit in magnitude, can be defined as the DOF of the mechanism. If  $n$  is the number of nodes where forces may be applied, then the actual number of applied forces may be less than or equal to  $3n$ . The number of displacement coordinates will be equal to  $3n$ , and the DOF of the mechanism will be less than or equal to the number of applied loads. Note that the DOF doesn't have to be equal to either the number of applied loads or the total number of displacement coordinates. This is a robust definition for DOF and allows for the fact that a mechanism can have different DOF depending on the number of allowable loads.

Having obtained a clear definition of DOF in flexure mechanisms, the next step is to identify methods or criteria to determine it. Two possible approaches are considered here. The first approach is analogous to Gruebler's criterion, where the DOF of constituent flexure connections is predetermined using the above definition. The suggested exercise would in general be straightforward to perform on flexure units or building blocks. But as explained for the rigid-link mechanism case, any criterion that is based on the properties of the building blocks will be general and easy to apply, but will not account for special geometric configurations which can affect the mobility. Therefore, although simple, this may not always yield correct results. The alternate approach is to apply the above DOF definition to the entire mechanism without determining the DOF of the constituent flexure units. This becomes a case specific analysis, which gets more difficult with increasing complexity in the mechanism, but on the other hand is very reliable. Often, in the design flexure mechanisms, we consider cases with special geometric configurations to exploit the principles of reversal and symmetry. Due to the finite stiffness properties of flexures, they are more tolerant to underconstraint and overconstraint situations. In view of this, the second approach gains significance. The analytical tools presented earlier in this chapter help simplify the compliance estimates for the overall mechanism as required by this approach.

The entire discussion on DOF determination for flexure mechanisms has been based on large and small displacements in response to large and small forces. A non-dimensional analysis, as done in this chapter, is very helpful in this regard. To determine DOF of either a flexure unit or mechanism, a set of allowable

loads, each having a normalized magnitude of 1, should be applied. Next, the normalized compliance of each displacement coordinate, considered one at a time, with respect to every allowable load should be computed. Compliance that is computed in this fashion includes the effects of nominal loads and displacements on the force-displacement characteristics of the mechanism. If the value of a normalized compliance for a certain displacement coordinate is of the order of 0.01 – 1.0, the coordinate is a potential candidate for a DOF, and if it is of the order of 0.01 or smaller, it becomes a DOC. Of the potential DOF candidates, the maximum number that can be independently set to be in the 0.01 – 1.0 range, in response to any combination of applied loads less than 1 in magnitude, will be the DOF. The normalized compliance values also provide an estimate of the relative quality of a Degree of Freedom or Constraint.

Let us consider the beam of Fig. 3.3 as an example, where forces are allowable at the beam tip. Therefore, there are three displacement coordinates:  $\delta_x$ ,  $\delta_y$ , and  $\theta$ . From expressions (3.17) and (3.18), the normalized compliances associated with these displacement variables may be determined in the presence of unit normalized loads.

$$c_{11} = \frac{\partial \delta_y}{\partial f} = \frac{1}{3(1+0.4p)} = 0.283 \quad c_{12} = \frac{\partial \delta_y}{\partial m} = \frac{1}{2(1+\frac{5}{12}p)} = 0.353 \quad c_{13} = \frac{\partial \delta_y}{\partial p} = -0.376$$

$$c_{21} = \frac{\partial \theta}{\partial f} = \frac{1}{2(1+\frac{5}{12}p)} = 0.353 \quad c_{22} = \frac{\partial \theta}{\partial m} = \frac{(1+\frac{1}{10}p)}{\left(1+\frac{17}{40}p+\frac{7}{600}p^2\right)} = 0.7657 \quad c_{23} = \frac{\partial \theta}{\partial p} = -0.273$$

$$c_{33} = \frac{\partial \delta_x}{\partial p} = \frac{1}{d} + [\delta_y \quad \theta] \begin{bmatrix} r & q \\ q & s \end{bmatrix} [\delta_y \quad \theta]$$

Clearly, the first two displacement coordinates are large, and are potential candidates for DOF. Compliance of  $\delta_x$  with respect to all the three allowable forces is seen to be very low over nominal ranges of motion, and therefore this displacement coordinate qualifies as a DOC. If suppose only a transverse force were allowed at the beam tip, even though the compliance associated with both  $\delta_y$  and  $\theta$  would have been high, but the DOF would be 1 since the two displacements cannot be varied independently with the single allowable force  $f$ . The deterioration of the quality of DOF with increasing axial loads is evident in the first two sets of expressions above and the deterioration in the quality of DOC in the X direction with displacements in the transverse directions is evident from expression for  $c_{33}$ . Thus, the analysis of Section 3.1 allows one to gauge the change in quality of Degrees of Freedom and Constraints in a flexure mechanism as forces and displacements vary.

Several other flexure units or mechanisms may be similarly considered, and the effectiveness of the definition of mobility provided here can be verified. One particular example is considered in Fig. 3.12 to illustrate a case of overconstraint.

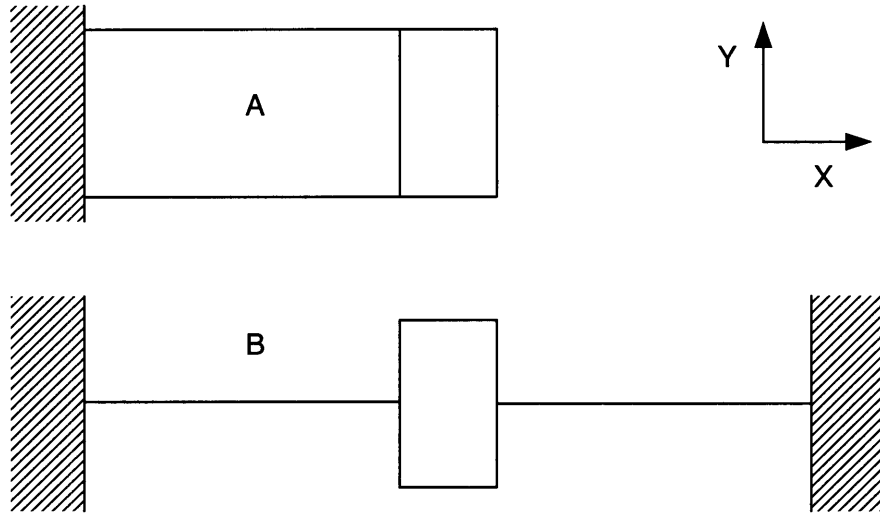


Fig. 3.12

The two cases considered in Fig. 3.12 are topologically identical. We have already shown that the DOF for the beam flexure unit given a general force at the tip is 2. Using the Gruebler's criterion, the DOF for the both the mechanisms should be 1. But we know from experience that this result is true for Mechanism A, but it is not entirely true for Mechanism B. We therefore resort to the latter approach explained earlier, where instead of relying on the DOF of the constituent units, the DOF of the mechanism is determined directly. In this case, the compliance in the Y direction can be determined from expression (3.19). It may be seen that the compliance is large ( $\sim 0.026$ ) for small displacements of the order of  $t$  and starts decreasing quadratically as the displacements are increased ( $\sim 4e-4$ , for  $\delta_y \sim 10t$ ). Based on this, it is can be recognized that the Y displacement coordinate in Fig. 3.12 B is a DOF for small ranges of motion, but becomes a DOC for larger ranges of motion.

An important question to ask is – what causes the over-constraints that are not recognized by Gruebler's criterion? Any geometric configuration that imposes a certain displacement on a displacement coordinate that corresponds to a DOF is harmless, because the internal forces generated as a result of this geometry are not large enough to affect the compliance of other displacement coordinates. However, if a specific geometric configuration imposes a displacement on a displacement coordinate that corresponds to a DOC, then depending on the magnitude of the imposed displacement, the geometric configuration could

potentially lead to an over-constraint. For example, the imposed displacement in the mechanism of Fig. 3.12B is large enough to generate internal axial forces that affect the transverse stiffness of the two beams. On the other hand, one may consider a geometric arrangement where the platform rotation of the parallelogram flexure in Fig. 13.2A is imposed to be zero. Platform rotation in this case is a direction of DOC, but the actual rotation without the geometric imposition is very small. Despite a large rotational stiffness, the internal forces that are generated in suppressing this rotation are too small to affect the transverse stiffness.

Thus, generally speaking, overconstraint is a consequence of both high stiffness along a DOC, and a relatively large displacement imposed along the DOC, because it is the product of these two factors that results in internal forces which in turn affect compliance and therefore the mobility in the other directions.

The above DOF discussion is based on a choice of finite number of applied forces and a related number of resulting displacements. This discussion is reasonable only in the static case. In the dynamic case, DOF determination becomes even more complicated, because the independent number of displacement variables required to specify the mechanism configuration no longer depends on the number of forces applied. Instead, this number depends on the mode shapes of the structure and the location of the applied forces with respect to these mode shapes. The modes that can be excited by either the actuation forces or disturbance forces determines the DOF in this case. Obviously the number of such modes is infinite, and one needs to select a finite number of these based on the methods of assumed modes, Rayleigh-Ritz or Galerkin. Once again, change in stiffness with applied forces and displacements will affect the mode shapes and therefore can affect the Degrees of Freedom and Constraint in the dynamic case as well.

### 3.5 Error motions in Flexure Mechanisms

While it is common to treat any undesired displacement of a mechanism as a parasitic motion, a clear generalized definition has not been found in the current literature. We deviate somewhat from this traditional practice and propose a more general description of error motions that has a mathematical basis. Let us assume that the ‘desired’ motion is one that occurs in the direction of the applied force. For any significant displacement to occur, this direction will have to be a DOC. Motions that occurs in any other direction in response to the applied force are deemed as ‘undesirable’. In a purely linear elastic formulation, this has a very simple implication. Keeping in mind that a finite set of forces are allowed, if the compliance matrix that relates these forces to corresponding displacements has any off diagonal terms, then the corresponding forces will lead to undesired motions.

We have already seen that displacements are not necessarily linear elastic in nature. The non-linear formulation presented earlier describes the presence and importance of purely kinematic and elastokinematic displacements. Therefore, from a flexure mechanisms point of view, undesired motion should be determined by first applying a generalized unit loading. This step is important because many effects that result in undesired motions arise in the deformed configuration of a mechanism. From this loaded and displaced configuration, we then vary only that force which is along the direction of primary motion while keeping all others constant, and measure the resulting change in displacements along all the displacement coordinates. All motions other than that in the direction of the applied force are undesired motions.

- a) The undesired motions along other Degrees of Freedom are defined here as cross-axis coupling or cross-axes error motions.
- b) The undesired motions along the Degrees of Constraint are defined here as parasitic error motions.

Each of these motions can be either purely elastic, or purely kinematic, or elastokinematic, or any combination of these. Let us consider some examples. For a simple beam, if one applies a force along the Y direction, then the displacement  $\delta_x$  and rotation  $\theta$  are undesired. Since  $\theta$  constitutes a DOF direction, the motion is a cross-axis error and is purely elastic in nature. Since  $\delta_x$  constitutes a DOC direction, it is a parasitic error motion, which has a kinematic as well as an elasto-kinematic component.

In a parallelogram flexure, a pure Y translation is the only desired motion in response to a transverse force; displacement  $\delta_x$  and rotation  $\theta$  are undesired. Based on the mobility test presented in the previous section, both  $\delta_x$  and  $\theta$  constitute DOC. Therefore the error associated with each of these is a parasitic error. For the case of  $\theta$ , the parasitic error has a purely elastic component as well as an elastokinematic component. The parasitic error  $\delta_x$  has a purely kinematic component and also an elastokinematic component.

We next consider a diaphragm flexure presented in Appendix A. It can be shown that this flexure has 3 DOF corresponding to the out of plane motions, and three stiff directions corresponding to the in plane motions. Once again if the center of the flexure is loaded by six generalized forces, and the Z direction force is increased while keeping others constant, there are cross-axis error motions associated with the  $\theta_x$  and  $\theta_y$  displacements, which are purely elastic in nature, and parasitic errors in the X, Y and  $\theta_z$  directions. The former two parasitic errors are elastic and elastokinematic in nature, and the  $\theta_z$  error is purely kinematic and elastokinematic in nature. The purely kinematic parasitic  $\theta_z$  is the most prominent of all these.

Similarly, several other examples can be considered. Such a quantification of error terms is important because it reveals what the various components of a given error motion are. Any purely elastic component, whether it appears in a cross-axis error or a parasitic error, may be removed by an appropriate combination of actuation forces. In many cases this simply translates to adjusting the point of force application to provide an additional moment. But kinematic terms that contribute to cross-axes or parasitic errors, are not dependent on forces and therefore may not be eliminated by any combination of forces. The magnitude of these terms may be altered by changing the shape of the constituent flexure building blocks, and a new geometric arrangement involving reversal and symmetry may be necessary to completely eliminate them. Elastokinematic terms are influenced by both of these two schemes – by adding actuation forces and by making geometric changes. This provides the designer important information regarding the kind of optimization and topological redesign that might be needed to improve the motion accuracy in a flexure mechanism.

### **3.6 Energy Methods**

Instead of solving the equations of force equilibrium, geometric equilibrium and constitutive relationships explicitly, as done in this chapter, one may instead make use of energy methods. There are two theorems that form the basis for all energy methods, the Principle of Virtual Work and the Principle of Complimentary Virtual Work [78-79].

The Principle of Virtual Work (PVW) is fundamentally a necessary and sufficient statement for the conditions of force equilibrium, without any restrictions on its applicability. In statics, the Principle of Minimum Potential Energy and Castigliano's Second Theorem may be derived from the PVW for the specific case of conservative systems. Furthermore, in conjunction with d'Alembert's Principle, the PVW becomes the basis for Hamilton's formulations in dynamics.

Similarly, the Principle of Complimentary Virtual Work is a necessary and sufficient statement for the conditions of geometric equilibrium, with some restrictions. The Principle of Minimum Complimentary Potential Energy and Castigliano's First Theorem are a direct consequence of the PCVW. Although not as commonly used, complimentary formulations in dynamics originating from the PCVW have also been developed [80] .

Although it is generally considered that the these two theorems offer a perfect symmetry and duality in formulation, the latter is actually a much weaker statement as compared to the first. There are two reasons that make the PVW more robust than the PCVW, and these are explained in the following paragraphs.

While solving a problem in mechanics, one is often interested in determining only the external force-displacement characteristics, and not the internal forces and displacements. Vector methods based on Newton's Laws involve all internal forces and displacements, thus making the process computationally tedious. Energy methods offer an alternate to the vector methods, by excluding the internal forces from the formulation.

Let us briefly look at the duality that exists between force equilibrium (or compatibility) and geometric constraints (or compatibility). For the sake of illustration, we consider a system with rigid geometric constraints. In such a system, it is the internal forces that enforce geometric compatibility, and it is because of geometric constraints that internal forces arise. In fact, internal forces are aligned along the direction of the corresponding geometric constraints. Given a system in a state of deformation under a set of external loads, this relationship between internal forces in equilibrium and geometric compatibility is well evident.

The principles of energy build upon virtual variations from this loaded and deformed configuration. In the presence of virtual displacements, which are defined as small variations in the real displacements that do not violate the conditions of geometric compatibility, the work done by the internal forces associated with the rigid constraints is zero. During these displacement variations, time is assumed frozen and forces remain unchanged – hence the name ‘virtual’. Since the virtual displacements cannot violate the geometric constraints, and since internal forces are aligned along the geometric constraints, the virtual displacements are orthogonal to the geometric constraints as well as the corresponding internal forces. It is because of this orthogonality between virtual displacements and internal forces, the internal forces do no virtual work, and therefore are eliminated from the principle of virtual work formulation.

The other possible variation is one that can be made to the applied forces such that these variations obey force equilibrium and do not affect the real displacements. The Principle of Complementary Virtual Work also attempts to exclude the internal forces by considering real displacements and virtual forces, but a problem arises in making a generalization. This is due to the fact that conditions of geometric constraints can be non-linear in the displacement variables. This implies that, while differential displacements are orthogonal to internal forces, real displacements need not be so. Thus, the computation of complementary virtual work by taking a scalar product of real displacements and virtual forces does not always result in an elimination of internal force dependent terms. Since force equilibrium conditions are necessarily linear in the force terms, the true internal forces and the differential virtual internal forces are always in the same direction. On the other hand, displacements and differential virtual displacements are proportional, or collinear, only when the conditions of geometric compatibility are linear in displacement terms. In many large displacement problems, this is not the case. The resulting loss of orthogonality between real

displacements and virtual forces restricts the applicability of PCVW to problems that are geometrically linear, or ones where the true displacements are small enough to justify a linear approximation of the geometric constraints. For the reasons explained above, no such issue arises in the case of the Principle of Virtual Work, thus making it far more robust and versatile as compared to its sibling.

The second problem associated with the PCVW is the lack of an absolute reference for displacements, which leads to ambiguity in the definition for Complementary Virtual Work. On the other hand, PVW is immune to this because neither forces nor differential virtual differential displacements require a reference frame.

For these reasons, one has to exercise caution in the use of PCVW. In fact all the successful applications of complementary principles are not really based on the PCVW but instead are indirectly derived from the PVW [80-81]. For the purpose of this research, PVW work was applied for the uniform beam discussed in Section 3.1, and results identical to expressions 3.9 and 3.10 were obtained. Clearly this is a situation where the conditions for geometric compatibility are non-linear, and therefore a direct application of PCVW resulted in incorrect expressions, as expected. A complementary formulation similar to [81], based on PVW, was not but can be attempted.

The preceding sections have highlighted the importance of overconstraint and error motions in flexure mechanisms. Overconstraint is a direct consequence of internal forces, whereas some components of error motions are a consequence of geometric constraints. While energy methods capture both these effects very well, and although the PVW is applicable in this case, there are two reasons why we decide to not utilize it for the subsequent analyses.

1. PVW yields the final results in the form of forces expressed in terms of displacements. Because of non-linearities involved, it is extremely tedious to invert these relations to obtain displacements in terms of forces which is what is ultimately desired in this analysis.
2. Contrary to what is commonly understood, an unusual geometric compatibility condition is encountered in the non-linear beam bending analysis. Normally, geometric compatibility is purely a relationship between the various displacement variables in the system. In this case, the condition of geometric constraint (3.13) actually has a force term explicitly embedded in it. While the PVW is still applicable but its usefulness in terms of eliminating the internal forces is somewhat diminished because one still needs to include the internal axial force  $p$  in the formulation of the beam to obtain virtual displacements.

# Chapter 4. Analysis of Basic Flexure Building Blocks

Based on the results obtained for simple beams in the previous chapter, we next proceed to analyze some other common flexure units that are based on the beam flexure. Since, the spatial variables  $x$  and  $y$  do not show up in the rest of this thesis, for the sake of convenience we shall use the symbols  $x$  and  $y$ , instead of  $\delta_x$  and  $\delta_y$ , to denote the non-dimensionalized end displacements in all subsequent discussions.

## 4.1 Parallelogram Flexure

The parallelogram flexure is a very common flexure unit that is frequently employed to provide approximate straight line motion. Some of the earliest work on the parasitic deflections of a parallelogram flexure was done by Jones [1], and has been referenced in subsequent texts [2,7]. Despite the fact that the parallelogram flexure has been thoroughly studied, we shall take another close look at it to understand the non-linearities in its force-displacement characteristics.

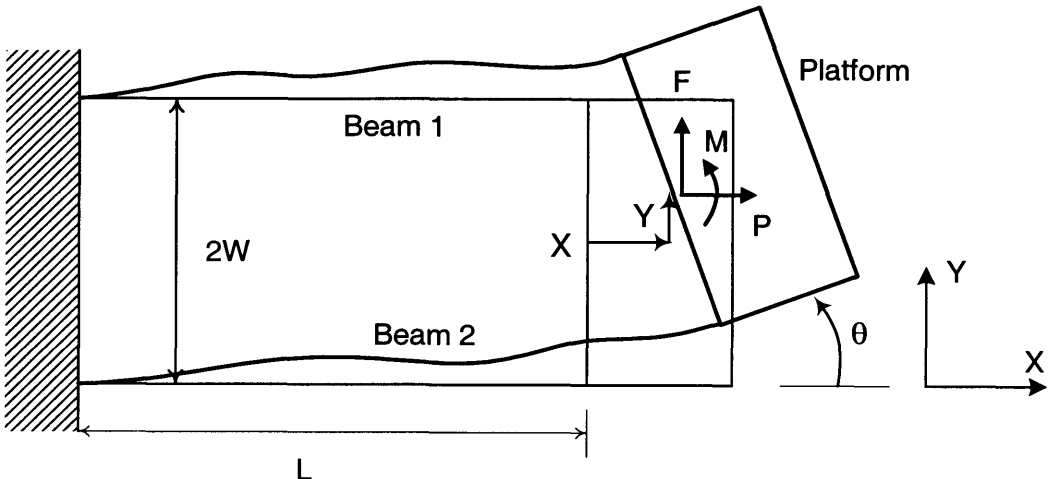


Fig. 4.1 Parallelogram Flexure

We start this discussion with some new engineering approximations. The platform connecting the two beams in a parallelogram flexure, illustrated in Fig. 4.1, is assumed to be rigid. The two beams are considered to be identical in the preliminary analysis, and therefore, loads and displacements can be normalized with respect to the properties of either beam.  $W$  is the distance between the two beams, and

following the notation convention of this thesis,  $w=W/L$ . From a linear analysis, we have an estimate for the platform rotation  $\theta$ . As opposed to a beam flexure, where tip rotation  $\theta$  and tip displacement  $y$  are of the same order for a given set of transverse loads, in the case of a parallelogram flexure the ratio between platform rotation  $\theta$  and displacement  $y$  is of the order of  $0.1(t/w)^2$ , which for typical dimensions is  $1e-4$ . For a maximum  $y$  displacements of  $0.1$ , the absolute value of  $\theta$  is seen to be of the order of  $1e-5$  radians. This observation allows us to drop out the higher order terms in  $\theta$  in many cases.

$x_1, y_1$  and  $\theta_1$  are the tip displacements of beam 1, and  $x_2, y_2$  and  $\theta_2$  are those of beam 2, all measured with respect to a coordinate frame attached to the undeformed configuration of the beams. Given the small  $\theta$  assumption, the conditions of geometric compatibility may be written as,

$$\begin{aligned}x_1 &= x - w\theta \\x_2 &= x + w\theta \\y_1 &= y_2 = y \\\theta_1 &= \theta_2 = \theta\end{aligned}\tag{4.1}$$

Furthermore, from results stated in Chapter 3,

$$\begin{aligned}x_1 &= x_l^e + x_l^k \\x_2 &= x_2^e + x_2^k \\\Rightarrow x &= \frac{(x_l^e + x_2^e)}{2} + \frac{(x_l^k + x_2^k)}{2} \triangleq x^e + x^k \quad \text{and} \quad w\theta = \frac{(x_l^e - x_2^e)}{2} + \frac{(x_l^k - x_2^k)}{2}\end{aligned}\tag{4.2}$$

For each beam, the force-displacement relations are given by,

Beam 1

$$\begin{aligned}\begin{bmatrix} f_1 \\ m_1 \end{bmatrix} &= \begin{bmatrix} a & c \\ c & b \end{bmatrix} \begin{bmatrix} y \\ \theta \end{bmatrix} + p_1 \begin{bmatrix} e & h \\ h & g \end{bmatrix} \begin{bmatrix} y \\ \theta \end{bmatrix} \\x_l^e &= \frac{1}{d} p_1 \\x_l^k &= [y \quad \theta] \begin{bmatrix} i & k \\ k & j \end{bmatrix} \begin{bmatrix} y \\ \theta \end{bmatrix} + p_1 [y \quad \theta] \begin{bmatrix} r & q \\ q & s \end{bmatrix} \begin{bmatrix} y \\ \theta \end{bmatrix}\end{aligned}\tag{4.3}$$

Beam 2

$$\begin{aligned}\begin{bmatrix} f_2 \\ m_2 \end{bmatrix} &= \begin{bmatrix} a & c \\ c & b \end{bmatrix} \begin{bmatrix} y \\ \theta \end{bmatrix} + p_2 \begin{bmatrix} e & h \\ h & g \end{bmatrix} \begin{bmatrix} y \\ \theta \end{bmatrix} \\x_2^e &= \frac{1}{d} p_2 \\x_2^k &= [y \quad \theta] \begin{bmatrix} i & k \\ k & j \end{bmatrix} \begin{bmatrix} y \\ \theta \end{bmatrix} + p_2 [y \quad \theta] \begin{bmatrix} r & q \\ q & s \end{bmatrix} \begin{bmatrix} y \\ \theta \end{bmatrix}\end{aligned}\tag{4.4}$$

Force equilibrium conditions may be derived from the Free Body Diagrams in Fig 4.2. Although it was stated earlier that force equilibrium needs to be applied in the deformed configuration to capture non-linear effects, due to the small  $\theta$  estimate made earlier in this section, its contribution in the equilibrium conditions is negligible.

$$\begin{aligned}
 p_1 + p_2 &= p \\
 f_1 + f_2 &= f \\
 m_1 + m_2 + (p_2 - p_1)w &= m \\
 \Rightarrow (p_2 - p_1) &= \frac{m - (m_1 + m_2)}{w}
 \end{aligned} \tag{4.5}$$

This, in turn, results in the following conclusions,

$$\begin{aligned}
 f &= f_1 + f_2 = (2a + pe)y + (2c + ph)\theta \\
 m_1 + m_2 &= (2c + ph)y + (2b + pg)\theta
 \end{aligned} \tag{4.6}$$

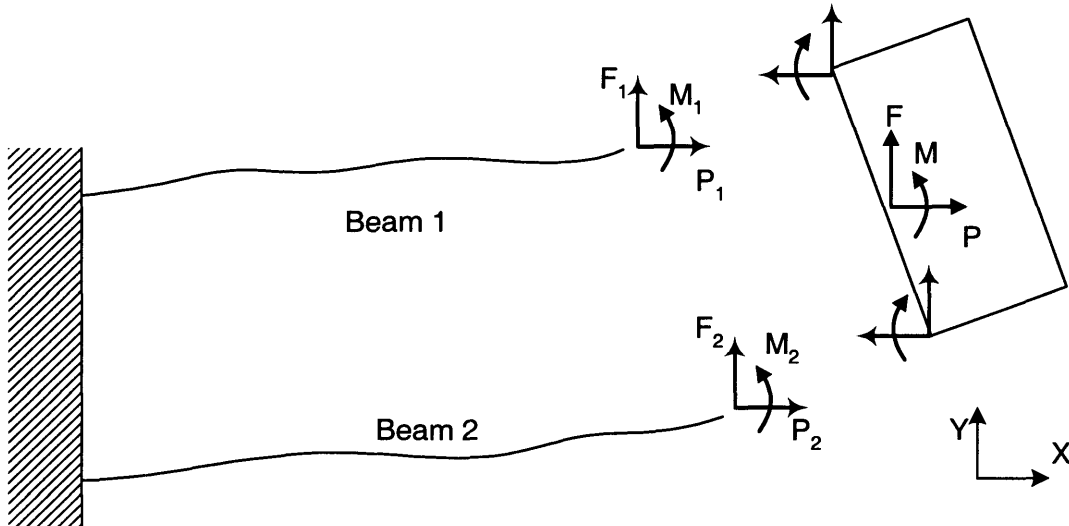


Fig. 4.2 FBD of the parallelogram flexure platform

Unlike in the linear analysis, it is important to recognize that neither  $f_1$  equals  $f_2$ , and nor  $m_1$  equals  $m_2$ , despite the fact that the tip displacement for the two beams are forced to be the same. This is due to the fact that the axial forces  $p_1$  and  $p_2$  are not the same, and therefore cause an unequal transverse stiffness change in the two beams. Using equations (4.1) - (4.6), one can now solve the force-displacement relationships of the parallelogram flexure.

$$\begin{aligned}
w\theta &= \frac{(p_2 - p_1)}{2d} + \frac{(p_2 - p_1)}{2} [y \quad \theta] \begin{bmatrix} r & q \\ q & s \end{bmatrix} \begin{bmatrix} y \\ \theta \end{bmatrix} \\
\Rightarrow 2w^2\theta &= \left\{ \frac{1}{d} + [y \quad \theta] \begin{bmatrix} r & q \\ q & s \end{bmatrix} \begin{bmatrix} y \\ \theta \end{bmatrix} \right\} \{m - (2c + ph)y + (2b + pg)\theta\} \\
x^e &= \frac{1}{2d}(p_1 + p_2) = \frac{p}{2d} \\
x^k &= [y \quad \theta] \begin{bmatrix} i & k \\ k & j \end{bmatrix} \begin{bmatrix} y \\ \theta \end{bmatrix} + \frac{p}{2} [y \quad \theta] \begin{bmatrix} r & q \\ q & s \end{bmatrix} \begin{bmatrix} y \\ \theta \end{bmatrix} \\
y &= \frac{f - (2c + ph)\theta}{(2a + pe)}
\end{aligned} \tag{4.7}$$

The expression for  $\theta$  in (4.7) provides some insight on the factors that contribute to it. The first term represents the consequence of elastic contraction and stretching of the top and bottom beams, respectively. The second term, which is rarely accounted for in the literature, is the consequence of the elastokinematic effect explained in Chapter 3. Since the axial loads on the two beams are different, apart from resulting in different elastic deflections of the two beams, this also causes slightly different beam shapes and hence different elastokinematic deflections. Because of its linear dependence on the axial load and quadratic dependence on the transverse displacement, the elastokinematic effect contributes a non-linear component to the platform rotation. For a typical maximum transverse displacement,  $y \sim 0.1$ , it can be shown that the coefficients of the linear effect and the non-linear effect,  $1/d$  and  $ry^2$  respectively, are of the same order. The purely kinematic part of the axial deflection of the beams is independent of the axial force, and depends only on the tip displacements. Since tip displacements are same for both the beams, the purely kinematic component does not contribute to  $\theta$ . But, as expected, it does contribute to the X direction displacement,  $x$ , of the stage. As expected, the  $x$  displacement has a purely elastic component and a kinematic component, which in turn has a purely kinematic and an elastokinematic part.

Substituting the last equation of (4.7) in the second last equation, one obtains a third order equation in  $\theta$ . Owing to the small  $\theta$  estimate, this equation may be easily solved for  $\theta$  by dropping all the higher order terms.

$$\theta = \frac{\begin{bmatrix} 1 & ep & e^2 p^2 & e^3 p^3 \end{bmatrix} \begin{bmatrix} -\frac{8ca^2}{d} & \frac{8a^3}{d} & -2cr & 2ar \\ -\frac{8ca}{d} - \frac{4ha^2}{ed} & \frac{12a^2}{d} & -\frac{hr}{e} & r \\ -\frac{2c}{d} - \frac{4ha}{ed} & \frac{6a}{d} & 0 & 0 \\ -\frac{4h}{ed} & \frac{l}{d} & 0 & 0 \end{bmatrix} \begin{bmatrix} f \\ m \\ f^3 \\ f^2 m \end{bmatrix}}{2w^2 \begin{bmatrix} 1 & ep & e^2 p^2 & e^3 p^3 \end{bmatrix} \begin{bmatrix} 8a^3 \\ 12a^2 \\ 6a \\ 1 \end{bmatrix}} \quad (4.8)$$

Restating the above,

$$\theta = [1 \ ep \ e^2 p^2 \ e^3 p^3] \begin{bmatrix} -\frac{8ca^2}{d} \\ -\frac{8ca}{d} - \frac{4ha^2}{ed} \\ -\frac{2c}{d} - \frac{4ha}{ed} \\ -\frac{4h}{ed} \end{bmatrix} \frac{f}{2dw^2(2a+ep)^3} + \frac{m}{2dw^2} + [1 \ ep] \begin{bmatrix} -2c \\ -\frac{h}{e} \end{bmatrix} \frac{rf^3}{2w^2(2a+ep)^3} + [1 \ ep] \begin{bmatrix} -2a \\ -l \end{bmatrix} \frac{rf^2m}{2w^2(2a+ep)^3} \quad (4.9)$$

This result confirms the order of magnitude estimates for  $\theta$  that were made earlier. The non-linear dependence on the transverse forces  $f$ , arising from the elastokinematic effect is evident. Furthermore, the consequence of the axial force  $p$  is also quantified. We can next make some further simplifications to the previously stated results,

$$y = \frac{f - (2c + ph)\theta}{(2a + pe)} \approx \frac{f}{(2a + pe)} \quad (4.10)$$

$$x \approx \frac{p}{2d} + y^2 i + \frac{p}{2} y^2 r \quad (4.11)$$

In the expression for  $y$ , the  $\theta$  dependence has been dropped since it is three to four orders smaller than  $y$ . Nevertheless, it should be recognized that since  $\theta$  is dependent on  $f$ , Maxwell's Reciprocity requires  $y$  to be dependent on  $m$ . It is just that the dependence of  $y$  on  $m$  is much weaker than that on  $f$ . The dependence on  $m$  does become important when the only end load applied is a moment.

Returning to the  $\theta$  expression (4.9), the relative significance of the linear and non-linear terms is governed by the numbers  $1/d$  and  $r$ .  $1/d$  is a measure of the elastic axial compliance of a beam, and is proportional to  $t^2$ , as given by expression (3.12), whereas  $r$  is a measure of the elastokinematic compliance, and is fixed for a given shape. Therefore, in order to manipulate the relative magnitudes of the linear and non-linear terms in  $\theta$ , one can either change the blade thickness or modify the blade shape.

For typical dimensions of  $t=1/60$  and  $w=1/3$ , and with no axial or moment loads, the difference between the  $\theta$  predictions of the linear and non-linear analyses is highlighted in Fig 4.3. Results from a Finite Elements Analysis are also plotted for comparison. The range for the transverse force  $f$  is chosen to be 5 since it corresponds to a  $y$  of approximately 0.2. The plot indicates that the non-linear effects are clearly important within our range of interest.

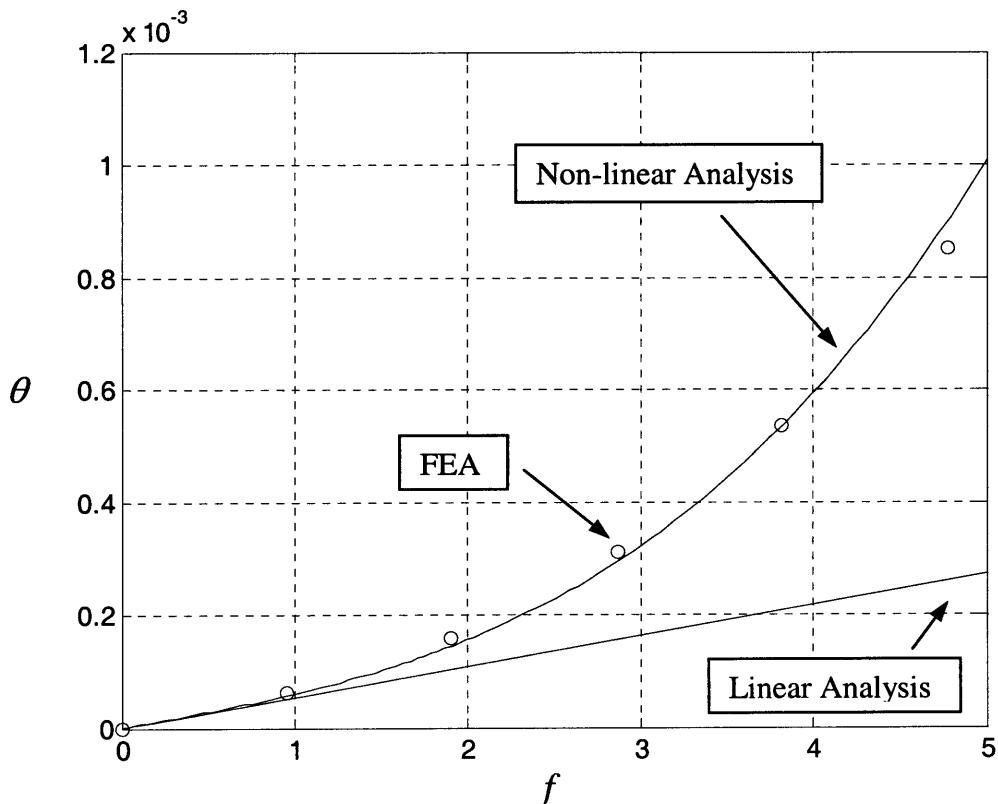


Fig. 4.3 Predictions of parallelogram platform rotation based on linear and non-linear analyses

The  $\theta$  dependence on the transverse force  $f$  changes with the application of an axial force, and this change is illustrated in Fig. 4.4

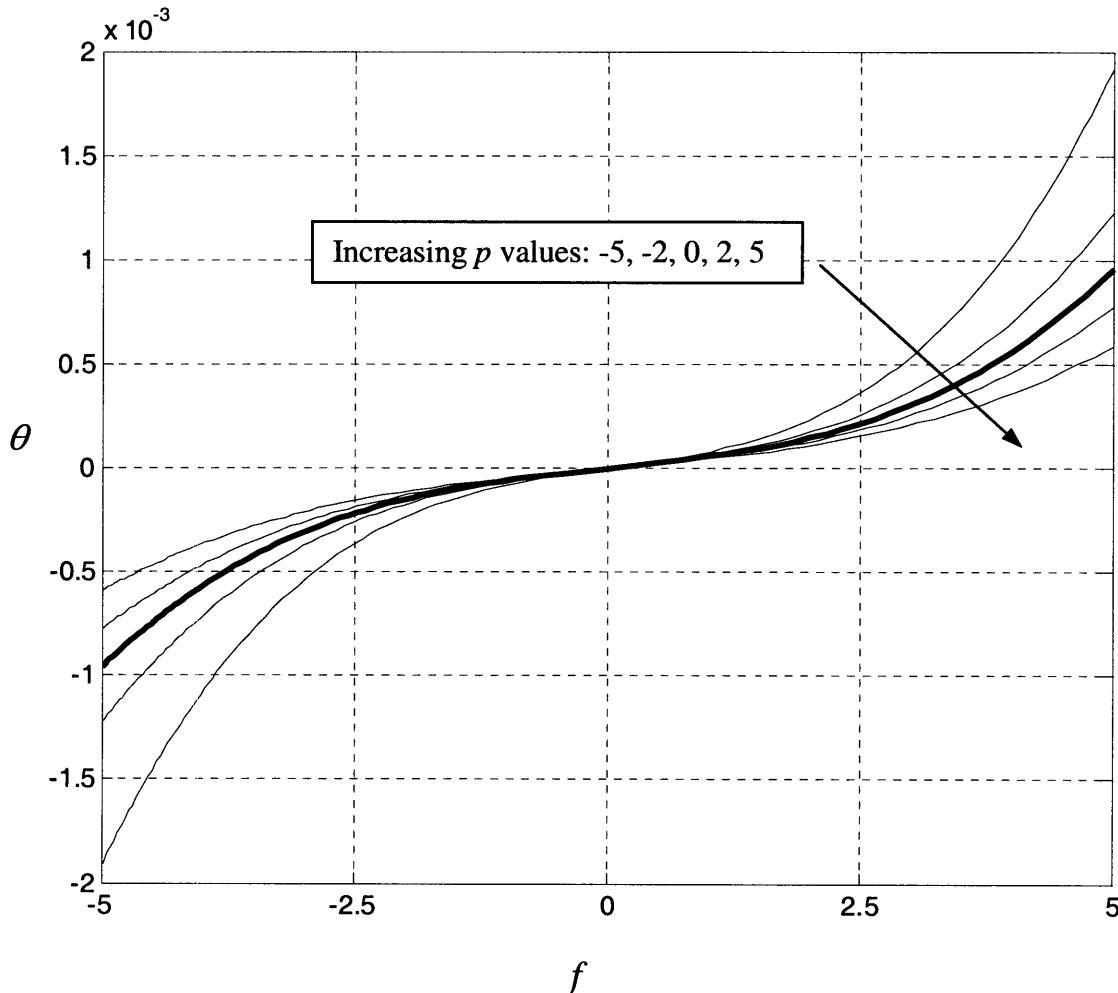


Fig. 4.4 Dependence of  $f$ - $\theta$  relationship on the axial load  $p$

The linear stiffness in the  $\theta$ - $f$  relationship increases almost linearly with  $p$ , whereas the non-linear stiffness increases at a much higher rate. Thus, as  $p$  increases, the non-linear contribution in  $\theta$  becomes smaller, which is evident in Fig 4.4.

A question of common interest is the center of stiffness of the parallelogram mechanism. In other words, where on the platform should one apply a transverse load to achieve zero platform rotation. Fig. 4.5 presents the ratio of  $m$  and  $f$  that is necessary to maintain zero platform rotation versus the applied axial load. This directly provides us the location of the center of stiffness. For zero axial loads, the answer is obvious either by employing symmetry arguments similar to Fig. 1, or by performing a quick linear analysis. In fact, it may be noticed that an  $m/f$  ratio of -0.5 both the linear as well as non-linear

components in the theta expression vanish. Thus the non-linearity in transverse force doesn't affect the center of stiffness, but the non-linearities associated with the axial load certainly do. The above analysis also allows one to state the sensitivity of this location in parametric terms.

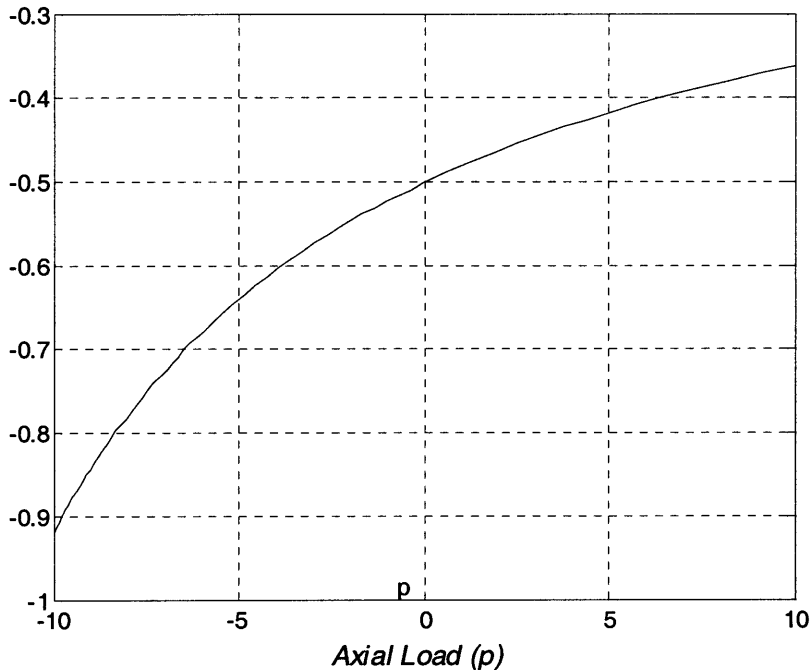


Fig. 4.5 m/f ratio required to maintain zero platform rotation

Expression (4.10) describes the transverse force displacement behavior of the parallelogram flexure. As expected, the transverse stiffness has a linear dependence on the axial load, and goes to zero for  $p=-20$ , which corresponds to the condition for buckling.

The axial force displacement characteristics are given by expression (4.11), which quantifies the dependence of axial compliance on transverse displacements and forces.

$$\frac{\partial x}{\partial p} = \frac{1}{2d} + \frac{1}{2} y^2 r = \frac{1}{2d} + \frac{1}{2} \frac{rf^2}{(2a + pe)^2}$$

Axial stiffness drops quadratically with  $y$  and is plotted in Fig. 4.6. The rate of this drop depends on the coefficient  $r$  which is 1/700 for a simple beam. If a transverse force instead of a transverse displacement is specified, then the axial stiffness also becomes dependent on the axial force itself. Stiffness is higher for higher axial forces.

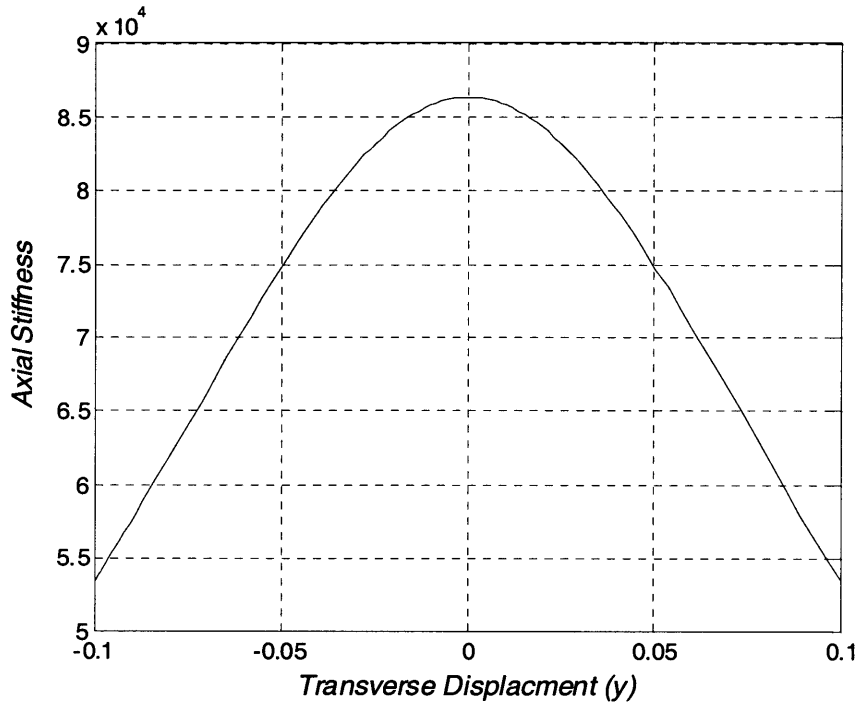


Fig. 4.6 Variation of axial stiffness with transverse displacement  $y$

For the specific case considered here,  $t=1/60$ , the axial stiffness reduces by about 40% for a transverse displacement of 0.1. This characteristic of the parallelogram flexure is important in evaluating some of the key performance measures of mechanisms that use it as a building block.

Note that a parallelogram flexure is constructed by imposing a geometric constraint on two beams, which is that their end slopes should stay the same. This is possible without overconstraint because the rotations of the two beams are DOF and therefore the internal forces generated to imposed these geometric conditions are not large enough to affect the stiffness along the transverse displacement. Also by doing so, we have made the mechanism very stiff in torsion, thus making it a DOC, because any rotation is resisted by the DOC of the individual beams. This is very desirable because the Y displacement now depends primarily on an applied Y force.

Based on the above results, a sensitivity analysis for a parallelogram flexure may be performed to determine the effects of differences between the two beams. There may be differences in material, shape, thickness, length or separation. For the sake of illustration, we shall consider two specific cases here.

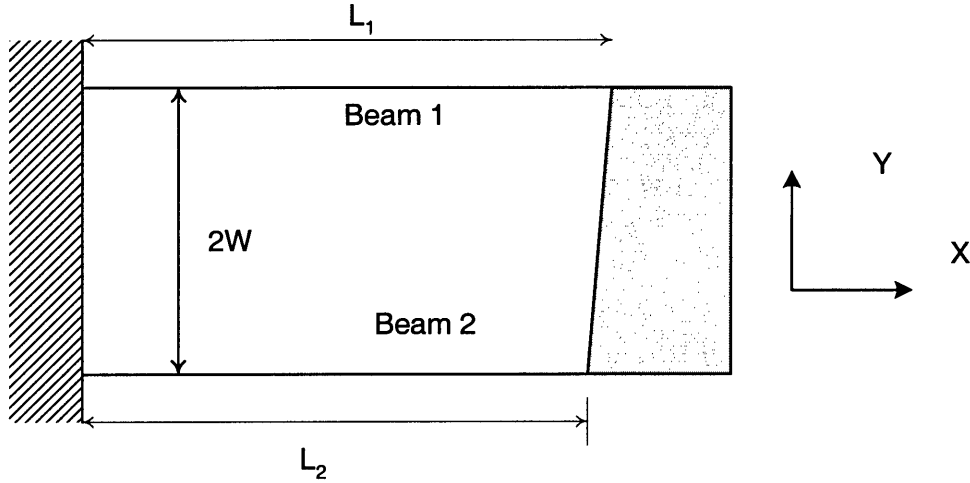


Fig. 4.7 Different beam lengths

In Fig. 4.7, a parallelogram flexure with unequal length beams is considered.  $L_1$  is treated as the characteristic length in the system. Error metric  $\Delta$  is defined to be  $(1-L_2/L_1)$ . In that case, the relationships for Beam 1 remain the same as earlier

$$\begin{bmatrix} f_1 \\ m_1 \end{bmatrix} = \begin{bmatrix} a & c \\ c & b \end{bmatrix} \begin{bmatrix} y \\ \theta \end{bmatrix} + p_1 \begin{bmatrix} e & h \\ h & g \end{bmatrix} \begin{bmatrix} y \\ \theta \end{bmatrix}$$

$$x_1^e = \frac{1}{d} p_1 \quad (4.12)$$

$$x_1^k = [y \ \theta] \begin{bmatrix} i & k \\ k & j \end{bmatrix} \begin{bmatrix} y \\ \theta \end{bmatrix} + p_1 [y \ \theta] \begin{bmatrix} r & q \\ q & s \end{bmatrix} \begin{bmatrix} y \\ \theta \end{bmatrix}$$

whereas those for Beam 2 change, as follows, for small  $\Delta$

$$\begin{bmatrix} f_2 \\ m_2 \end{bmatrix} = \begin{bmatrix} (1+3\Delta)a & (1+2\Delta)c \\ (1+2\Delta)c & (1+\Delta)b \end{bmatrix} \begin{bmatrix} y \\ \theta \end{bmatrix} + p_2 \begin{bmatrix} (1+\Delta)e & h \\ h & (1-\Delta)g \end{bmatrix} \begin{bmatrix} y \\ \theta \end{bmatrix}$$

$$x_2^e = \frac{(1-\Delta)}{d} p_2 \quad (4.13)$$

$$x_2^k = [y \ \theta] \begin{bmatrix} (1+\Delta)i & k \\ k & (1-\Delta)j \end{bmatrix} \begin{bmatrix} y \\ \theta \end{bmatrix} + p_2 [y \ \theta] \begin{bmatrix} (1-\Delta)r & (1-2\Delta)q \\ (1-2\Delta)q & (1-3\Delta)s \end{bmatrix} \begin{bmatrix} y \\ \theta \end{bmatrix}$$

Conditions of force equilibrium (4.5) and geometric compatibility (4.1)-(4.2) remain same as earlier. These equations may all be solved, for the specific case of  $m=p=0$ , to obtain the following results

$$\theta = \frac{x_2 - x_1}{2w} = -\frac{(c + \Delta)(2 - \Delta)}{2w^2} \left( \frac{y}{d} + ry^3 \right) + \frac{\Delta iy^2}{2w} \quad (4.14)$$

Obviously, setting  $\Delta=\theta$ , reduces this to the platform rotation for the ideal case. It may be seen that apart from contributing linear and quadratic variation terms to the ideal platform rotation, the variation  $\Delta$  also results in an additional linear variation term. This term, listed last in the above expression, is due to the purely kinematic effect in beams which had cancelled out earlier due to the identical geometric properties of the two beams. Another possible deviation from the ideal geometry of a parallelogram flexure, is shown in Fig. 4.8. Using the analytical tools developed here, it can be shown that the effect of this geometric variation produces a  $\theta$  error that has a dominant term proportional to both  $\Delta$  and  $y$ . For displacements of the order of 0.1 this is worse than the previous case where the dominant error term has a quadratic dependence on  $y$ . These quantitative results agree with the empirical observations made in the classic paper by R.V. Jones [1].

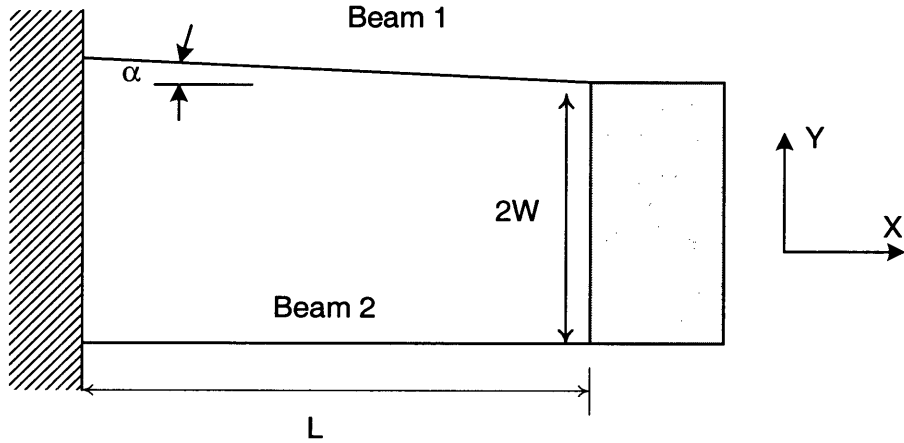


*Fig. 4.8 Different platform lengths*

It was shown in Chapter 3 that the analytical framework presented here can easily handle any variations in the constituent beam shape. Therefore, results analogous to the ones above may easily be obtained for parallelogram flexures that are made from the double notch beam.

## 4.2 Double Parallelogram Flexure

The results of the previous section are easily extended to a double parallelogram flexure, illustrated in Fig 4.9. The two rigid moving platforms are referred to as the primary and secondary platforms. Loads  $f$ ,  $m$  and  $p$  are applied at the primary platform. The two parallelograms are treated as identical, except for the beam spacing,  $w_1$  and  $w_2$ . Assumptions similar to the ones stated in the previous section hold here as well.

$x_1$ ,  $y_1$  and  $\theta_1$  are the absolute displacement coordinates of the secondary stage, and  $x_2$ ,  $y_2$  and  $\theta_2$  are those of the primary stage, along the directions indicated in Fig. 4.9. Force displacement results obtained in the previous section are applied to the constituent parallelograms in the present case. Force equilibrium conditions are obtained by drawing FBDs for each of the platforms. There are no additional conditions of geometric compatibility. With this, one can show that

$$\begin{aligned} y_1 &= \frac{f}{2a - ep} \quad \text{and} \quad y - y_1 = \frac{f}{2a + ep} \\ \Rightarrow y &= \frac{4af}{(2a)^2 - (ep)^2} \end{aligned} \tag{4.15}$$

The above are approximate expressions and do not include the dependence of  $y$  on  $m$ , which is required by reciprocity. But since the contribution of  $m$  is three to four orders of magnitude smaller than the contribution of  $f$  in the range of interest, this assumption is justified.

The above expression also reveals that, unlike the parallelogram flexure, the stiffness in the direction of transverse displacement  $y$ , always decreases quadratically with an axial load, positive or negative. This is reasonable because irrespective of the direction of the axial load, one of the parallelograms is always in tension while the other in compression, resulting in a quadratic dependence. A comparison of the transverse stiffness values for a parallelogram and double parallelogram flexure is shown in Fig. 4.10. There are two advantages to this: one, that the nominal stiffness along the DOF direction is reduced in half, and two, that because of the quadratic dependence, the variation of the stiffness with axial force in the range of interest is significantly reduced.

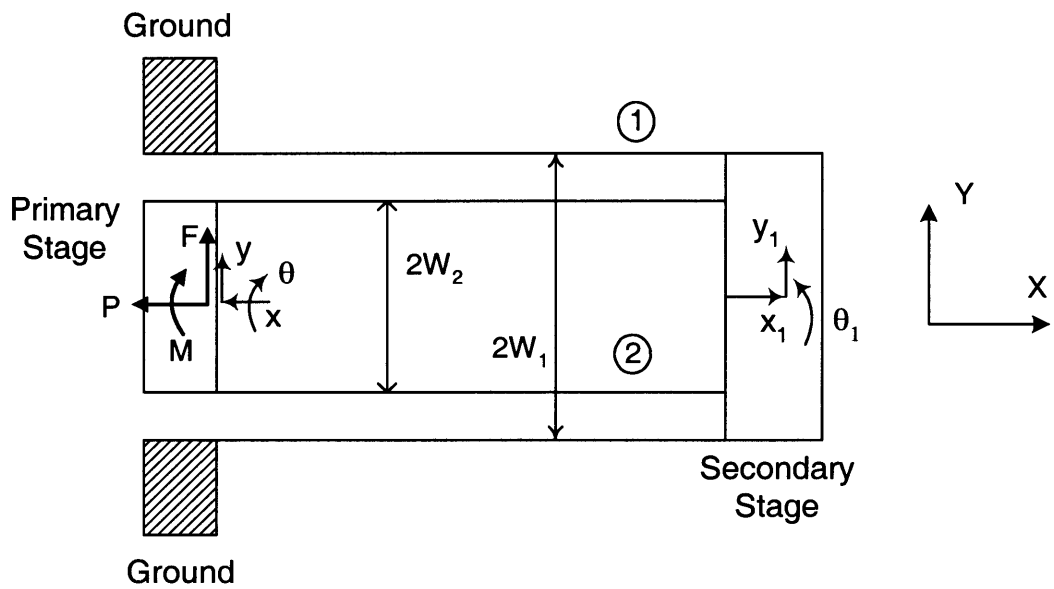


*Fig. 4.9 Double parallelogram flexure*

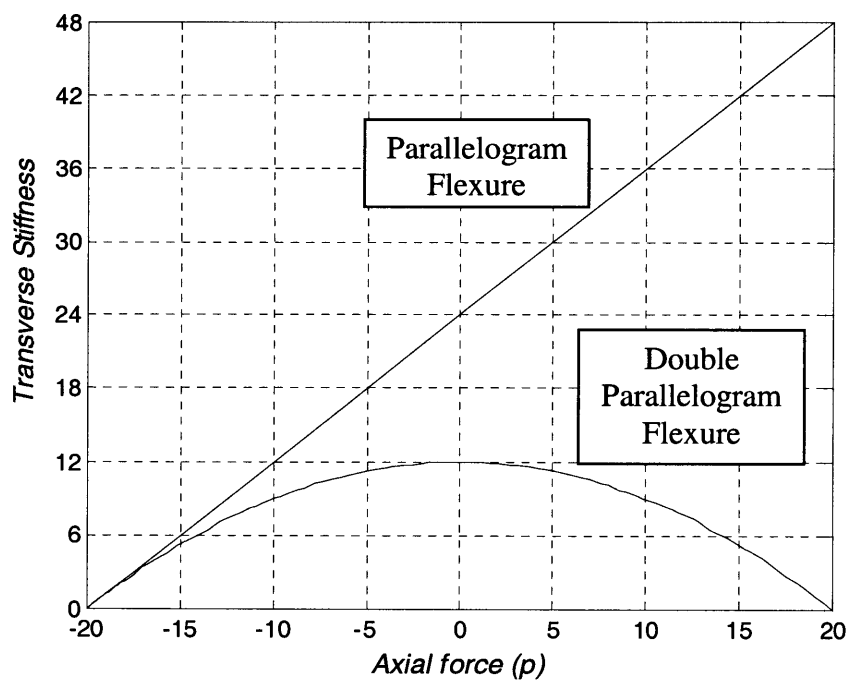


*Fig. 4.10 Comparison of transverse stiffness of parallelogram and double parallelogram flexures*

The primary platform rotation  $\theta$  can be derived to be,

$$\theta = [fn_1(p) \quad fn_2(p) \quad fn_3(p) \quad fn_4(p)] \begin{bmatrix} f \\ m \\ f^3 \\ mf^2 \end{bmatrix} \quad (4.16)$$

where,

$$fn_1(p) = \frac{\begin{bmatrix} 1 & p & p^2 \end{bmatrix} \begin{bmatrix} 4a^2w_2^2 + 4ac(w_2^2 - w_1^2) \\ -2ah(w_2^2 + w_1^2) + 2ce(w_2^2 + w_1^2) - 2aw_2^2 \\ he(w_1^2 - w_2^2) + w_2^2e(1-e) \end{bmatrix}}{dw_1^2w_2^2((2a)^2 - (ep)^2)}$$

$$fn_2(p) = \frac{(w_2^2 + w_1^2)}{2dw_1^2w_2^2}$$

$$fn_3(p) = \frac{r \begin{bmatrix} 1 & p & p^2 & p^3 & p^4 \end{bmatrix} \begin{bmatrix} 16a^4w_2^2 + 16a^3c(w_2^2 - w_1^2) \\ -8a^3h(w_2^2 + w_1^2) + 24a^2ce(w_2^2 + w_1^2) - 8a^3w_2^2(1-2e) \\ 12ace^2(w_2^2 - w_1^2) + 12a^2he(w_1^2 - w_2^2) - 4a^2w_2^2e \\ -6ahe^2(w_2^2 + w_1^2) + 2ce^3(w_2^2 + w_1^2) + 2aw_2^2e^2(1-2e) \\ he^3(w_1^2 - w_2^2) + w_2^2e^3(1-e) \end{bmatrix}}{2w_1^2w_2^2((2a)^2 - (ep)^2)^3}$$

$$fn_4(p) = \frac{r \begin{bmatrix} 1 & p & p^2 \end{bmatrix} \begin{bmatrix} 4a^2(w_2^2 + w_1^2) \\ 4ae(w_2^2 - w_1^2) \\ e^2(w_2^2 + w_1^2) \end{bmatrix}}{2w_1^2w_2^2((2a)^2 - (ep)^2)^2}$$

This expression is similar in structure to the  $\theta$  expression (4.8) for the parallelogram flexure, but the non-linear dependence on the axial load  $p$  is far more complex in this case. In general the angular stiffness of the parallelogram and double parallelogram flexure are of the same order.

In the absence of a moment load, the dependence of the  $f - \theta$  relationship for a double parallelogram flexure on axial load is shown in Fig. 4.11 . It is seen that the stiffness in general, and the non-linear contribution in particular reduces with a axial forces, and vice versa. This mathematical result may not be intuitively obvious, but can be rationalized by careful physical arguments.

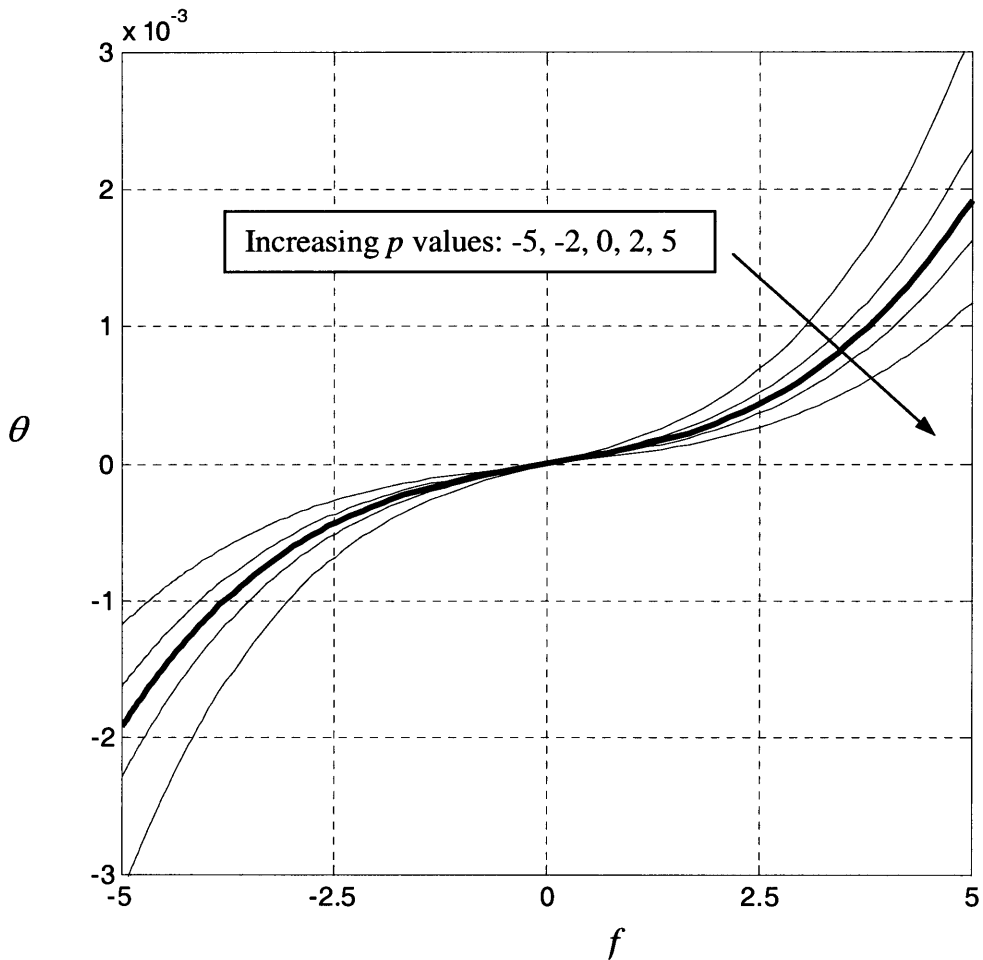


Fig. 4.11 Dependence of  $f - \theta$  relationship on the axial load  $p$

The center of stiffness for this mechanism may be obtained from Fig. 4.12. Once again, for zero axial force the  $m/f$  ratio required to keep  $\theta$  zero is  $-1/2$ , but this changes with the application of axial force  $p$ . In fact, it is easily seen from expression (4.16) that for no axial loads,  $\theta$  vanishes when

$$m = -\frac{w_2^2(a+c) - w_1^2c}{(w_2^2 + w_1^2)a} f$$

For an ideal double parallelogram flexure the above reduces to  $m = -f/2$

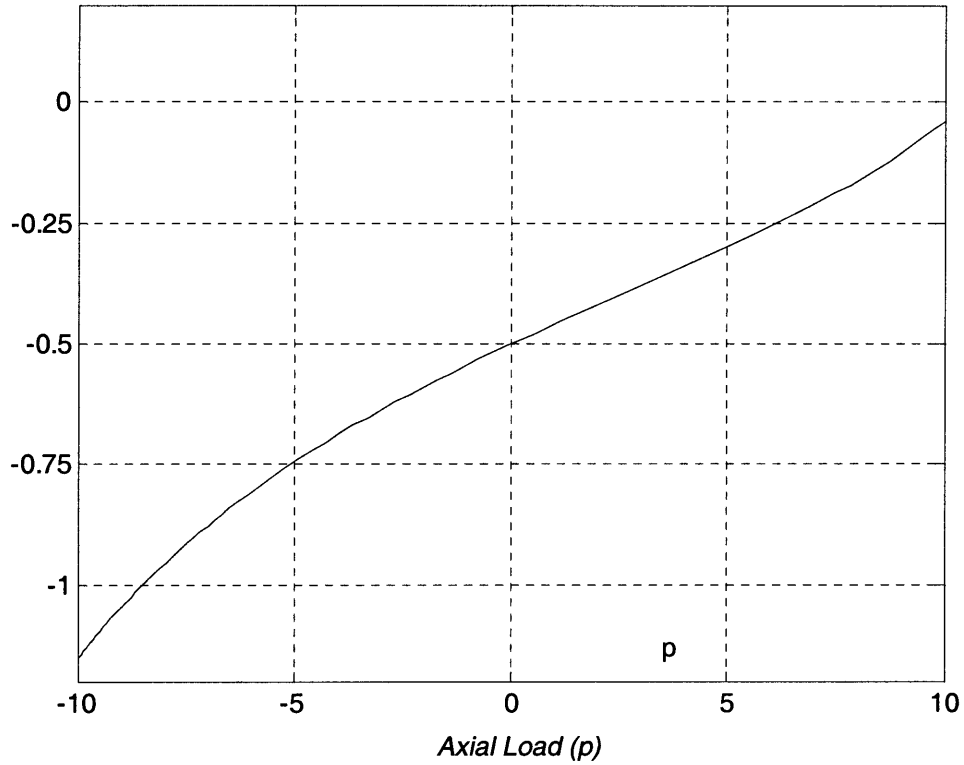


Fig. 4.12 m/f ratio required for zero platform rotation

We next shift our attention to the axial force-displacement results,

$$\begin{aligned}
 x_l &= -\frac{p}{2d} + y_l^2 (i - pr) & x + x_l &= \frac{p}{2d} + (y - y_l)^2 (i + pr) \\
 x &= \frac{p}{d} + (y - y_l)^2 (i + pr) - y_l^2 (i - pr) \\
 &= \frac{p}{d} + pf^2 \frac{2r[(2a)^2 + (ep)^2] - 8aei}{((2a)^2 - (ep)^2)^2} \\
 &= \frac{p}{d} + py^2 \frac{2r[(2a)^2 + (ep)^2] - 8aei}{(4a)^2}
 \end{aligned} \tag{4.17}$$

For typical values of  $p$ , the axial compliance may be approximated as,

$$\frac{\partial x}{\partial p} \approx \frac{1}{d} + \frac{y^2}{2} \left( r - \frac{ei}{a} \right)$$

The non-dimensional axial displacement expression has a purely elastic term, as well as an elastokinematic term, but no purely kinematic term. The purely kinematic term gets absorbed by the secondary platform due to the symmetry of the two parallelograms. The purely elastic term is as expected, but the elastokinematic term is somewhat unexpected at first sight. Note that now there are two factors contributing to the elastokinematic term,  $r$  and  $ei/a$ , the latter being 42 times larger than the former. Since this latter term dictates the axial compliance, we attempt to physically understand its existence.

If one imposes a displacement  $y$  on the double parallelogram, then as long there is no axial load, the transverse stiffness of the two parallelograms are equal, and  $y$  gets equally distributed between the two. Referring to Fig. 4.9, as one applies a tensile axial load, the transverse stiffness of parallelogram 1 decreases and that of parallelogram 2 increases by the same amount, which results in a redistribution of  $y$ . The increase in the transverse displacement of parallelogram 1, because of its reduced stiffness, is the same as the decrease in transverse displacement of parallelogram 2. Now since the axial kinematic terms have a quadratic dependence on the transverse displacements, the axial displacement of parallelogram 1 exceeds that of parallelogram 2. It is this difference that results in the unexpectedly large elastokinematic component in the axial displacement and compliance. This effect becomes more severe the axial load increases. Note that if the axial load is compressive in nature, the scenario remains the same, except that the two parallelograms switch their roles.

This is a subtle but very important observation. As has been mentioned on several earlier occasions, the axial stiffness of a flexure unit determines its utility in parallel kinematic mechanisms. In this case we see that by using the principles of reversal and symmetry, although one has succeeded in eliminating the purely kinematic  $x$  displacement of the double parallelogram, but the purely kinematic displacements of the constituent parallelograms conspire to result in a new elastokinematic term for the double parallelogram.

For a value of  $d=86400$ , the axial stiffness of a double parallelogram flexure is plotted against its transverse displacement  $y$ , in Fig. 4.13. As can be seen above, the axial stiffness drops to less than 15% of its nominal value for a transverse displacement of 0.05. Comparing this with the simple parallelogram, where although the drop in axial stiffness was also quadratic with  $y$ , the drop rate was dependent only on the  $r$  term, and therefore much smaller.

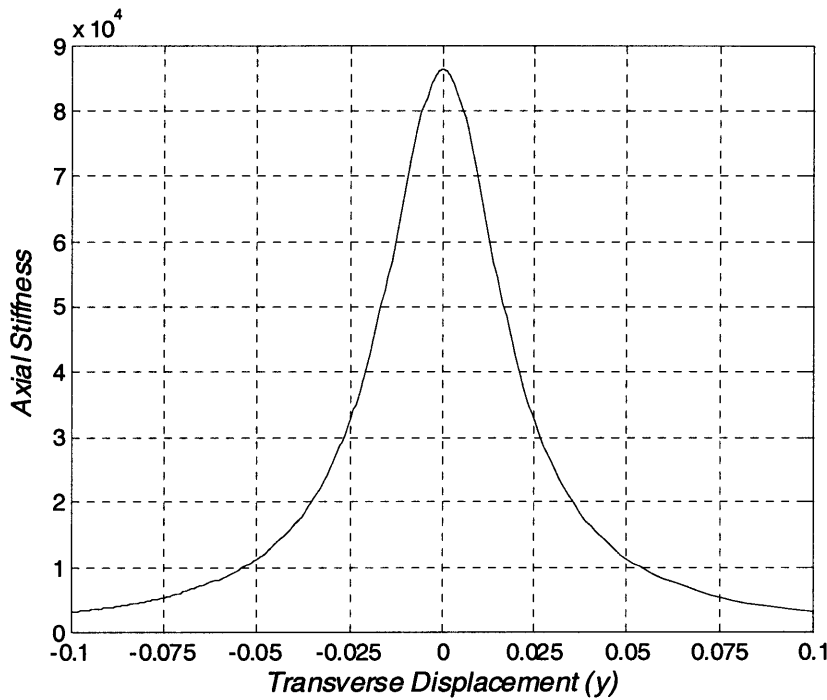


Fig. 4.13 Dependence of axial stiffness on the transverse displacement

It should be obvious from the above discussion that the reason for the dramatic fall in stiffness is due to the fact that the secondary platform, which has a DOF, is free to move transversely when an axial load is applied on the primary platform. In addition to loss in axial stiffness, this also introduces an unusual cross coupling between the two stages, which is benign in the static case, but may have interesting consequences in terms of the flexure unit's dynamics. Clearly, if one can impose a displacement on the secondary motion itself, these problems are resolved. In fact, this is exactly what has been empirically suggested in the past literature [1] while recommending the use of a double parallelogram flexure. The above analysis provides a thorough qualitative and quantitative explanation of the phenomena. When a lever arm is used to impose exactly half the motion of the primary stage on the secondary stage, the  $ei/a$  term vanishes from the compliance expression.

This example once again highlights the conflict between DOF and DOC. To improve the accuracy of DOC, one may use symmetry to eliminate parasitic errors, but as a consequence the quality of DOC suffers significantly.

Based on the analysis and simplifications presented in this chapter, several other interesting cases of parallelogram and double parallelogram flexures [83-85] may be considered and quantitative results may be obtained without resorting to either FEA or tedious conventional analysis.

# **Chapter 5. Static Non-Linear Analysis of Parallel Kinematic XY Flexure Mechanisms**

In this chapter we present the static non-linear analysis for some of the XY flexure mechanism designs that were proposed in Chapter 2. Based on the derivations and approximations presented in Chapters 3 and 4, the analysis here is carried out with the objective of evaluating the attributes and resulting performance measures of these XY flexure mechanism designs. The attributes that are of concern were explained in Chapter 2, and are repeated here briefly.

- 1) Specific range of motion: One of the fundamental limitations of flexure mechanisms in general is their small range of motion, whereas improved specific range is desirable in many applications.
- 2) Parasitic yaw error of the motion stage: For the sake of large range of motion, and to minimize the number of actuated axes, it is desirable to passively achieve small yaw of the motion stage.
- 3) Cross-axis coupling: A force or displacement input along one axis should result in minimal displacement of the motion stage along the other axis, so as to reduce the dependence on end-point feedback and calibration.
- 4) Actuator Isolation: The point of force application on the mechanism should not be affected by forces and displacements in other directions, so as to reduce the dependence on a decoupler, which limits the range of motion and the axial stiffness between the stage and the actuator.
- 5) In-line Axial Stiffness: Change in the axial stiffness of constituent flexure units that lie between the actuator and the motion stage, as a consequence of displacements and applied forces, is important in terms of lost motion and dynamic performance.
- 6) Manufacturing and assembly sensitivity: Robustness to manufacturing and assembly tolerance is desirable to keep fabrication costs low.
- 7) Thermal sensitivity: Low sensitivity to thermal disturbances allows the design to be functional in standard lab environment, and also reduces the dependence on end-point feedback.
- 8) Parasitic error motions in the out-of-plane directions: Since the out of plane directions are all DOFs, and not actively controlled, it is desirable to minimize the static and dynamic parasitic error motions associated with these directions.

Of the above list, we shall obtain analytical results for the first five attributes, and for specific cases of manufacturing and assembly tolerances. The remaining points are discussed qualitatively. While damping is important in achieving good static as well as dynamic performance, the flexure mechanism itself has

little damping of its own. Therefore, it is not included in the above list of structural design requirements, and is treated as an add-on. In this entire discussion we refer to the gross X and Y motions as the primary motions, and the stiffness associated with these motions is called the primary stiffness. The rigid stages are also referred to as nodes.

## 5.1 Preliminary Discussion

As we consider several XY flexure mechanism designs in the following sections, it shall become obvious that no one design is the best. Since there exist several trade-offs between the attributes and performance desirables listed above, each design is good in certain attributes and not as good in others. Therefore, the designer who employs these XY mechanisms has to make a decision based on the requirements the application at hand.

Furthermore, some more engineering approximations are made before carrying out this analysis.

- 1) Stiffness of the constituent flexure unit frames is assumed to be large enough to treat them as perfectly rigid bodies. For this to be true, it is important to make the bending stiffness of the frame at least one to two orders larger than the axial stiffness of the blades. If this is not done carefully, which is a common design lapse, the distortion of the frames also contributes to yaw motions in the mechanism, which are otherwise only dependent on the axial compliance of the blades. For example, in the case of a parallelogram flexure, if  $t_f$  is the thickness of the frame,  $t_b$  is thickness of the blade, and  $w$  is the width between the blades, then a general rule to follow is  $t_f^3 \gg t_b w^2$ . If space constraints do not allow this, then the compliance of the frame should also be taken into account in the analysis.
- 2) The above concern arises due to the fact that the rotation of stages in parallelogram or double parallelogram flexure units resulting from the axial compliance of the blades is very small, of the order of  $(t/w)^2$  as indicated in expressions (4.8) and (4.16). For typical values, this can be as small as  $1e-4$ . Therefore, linear approximations for the *sine* and *cosine* of these small angles can justifiably be used in equations of geometric compatibility. In some cases, the contribution of these terms may even be ignored. For example, in several conditions of geometric compatibility that we shall encounter later in this chapter, the terms  $\theta w$  and  $\delta_x$  occur in the same expression. For typical dimensions, it can be evaluated that the latter is about two orders of magnitude greater than the former, which therefore may be neglected.
- 3) Force equilibrium, as usual, will be applied in the deformed configuration of the mechanism, but the influence of the stage rotations will be neglected for the same reasons as cited above. The orientation

of internal forces does not need to be accounted for in the force equilibrium equations, which brings about a great degree of simplification in the calculations.

Apart from these general approximations that hold for all the cases discussed in this chapter, specific assumptions are also made at several stages in the analysis. All of these involve the dropping out of terms that make insignificant contributions to the performance parameters of interest; these terms are easily identified in the non-dimensional analysis. We expect the results of this analysis to be approximately within 5-7% of the actual behavior of the mechanisms, but at the same time we also expect that all the prominent physical phenomena are captured by this analysis.

At this point, it is also relevant to talk about the concept of Center of Stiffness. Center of stiffness is generally assumed to be the point where the application of an actuation force doesn't produce a rotation of the motion stage of interest, in a machine or mechanism. Since a flexure mechanism is comprised of several rigid nodes interconnected by compliant units, there isn't really one center of stiffness. The center of stiffness in this case is entirely dependent on the choice of the node where actuation forces are applied, and the node at which the rotation is of interest. So, for example, for the case of a generic XY flexure mechanism of Chapter 2, several possibilities exist.

What is the point of X force application on Intermediate Stage 1 and point of Y force application on Intermediate Stage 2, so as to produce zero rotation of the motion Stage? But instead, one can ask several alternate questions – Where should an X and Y force be applied on the motion stage itself to produce zero rotation of the motion stage? Or, Where should an X force on Intermediate Stage 1 and a Y force on Intermediate Stage 2 be applied to make the rotation of Intermediate Stage 1 vanish? The answer in each of these cases will be different. Therefore, it is important that one is clear about the exact objective while seeking the Center of Stiffness of a mechanism because, in general, there will be many.

For all these mechanisms an initial linear analysis is performed to determine a base value for some of the properties and attributes. Since, the linear analysis does not incorporate the fact that the values of stiffness change with loads and displacements, several cross-coupling effects are not captured in this formulation. For example, for all the mechanisms considered here, it predicts zero cross-axis coupling errors, and that the motion stage yaw may be completely eliminated over the entire range of motion of the mechanism. While reasonable estimates may be obtained for the primary stiffness, some of the conclusions pertaining to cross-axis coupling and motion stage yaw are clearly incorrect. We know that as deformations increase, the displacements and forces shall start affecting the properties of the constituent building blocks which will introduce non-linearities that in turn will result in coupling effects. A far more accurate analysis is provided by the non-linear formulation that is covered in this chapter.

Also, we can determine the Degrees of Freedom of the various mechanisms considered in the following sections. For XY Mechanism Designs 3 and 5, Gruebler criterion predicts a DOF of 1, and for Designs 4 and 6, the predicted DOF is -1. All these predictions are incorrect because the symmetric geometry in each of these cases results in redundant Degrees of Constraint which make the actual DOF of the mechanisms higher than predicted. Instead one may consider the alternative approach proposed in Section 3.4. The preliminary linear analysis is helpful here because it provides a basic estimate of the compliances involved in the system. Based on the DOF definition provided in Section 3.4, it can be shown that all the mechanisms considered in this chapter have 2 DOF.

A key objective in this analysis is to determine ways to passively minimize any possible motion stage yaw. Without actually conducting the entire non-linear analysis and simply based on an understanding of error motions gained in Section 3.5, we know that the rotation of the motion stage and the two intermediate stages are all elastic or elastokinematic in nature, and are parasitic errors. Because of this fact, these parasitic errors may be eliminated by the application of additional moments. Furthermore, as explained earlier, even though the moment stiffness is high, the errors themselves are low; hence moments required to suppress these yaw motions are not high enough to significantly affect the primary motions of the mechanism.

Moments that are geometrically dependent on the actuator forces may be added by judiciously locating the X and Y actuators. But with this strategy, the moment will not controlled actively, and hence we have to rely entirely on the mechanism geometry to achieve minimum stage yaw for a static force location. An active yaw control can be achieved by introducing a second independent actuator to either Intermediate Stage 1 or 2. While this requires added complexity and very careful control of the two actuators that act on the same stage, it can eliminate the motion stage yaw over the entire range of motion. Any lack of coordination between the two actuators that act on the same stage, can lead to extremely high internal force since stage rotations are DOCs. If second forces are added to both the intermediate stages, then the rotation of two of the three motion stages can be controlled independently. So we see that two actuators control the DOF, and the remaining to control the DOC. This is possible because the desired primary motions and the parasitic yaw motions are elastic in nature.

The fact that the linear analysis indicates a perfect decoupling between the two axes indicates that cross-axes coupling, if any, will be either purely kinematic and/or elastokinematic, but not purely elastic.

## 5.2 XY Flexure Mechanism Design 3

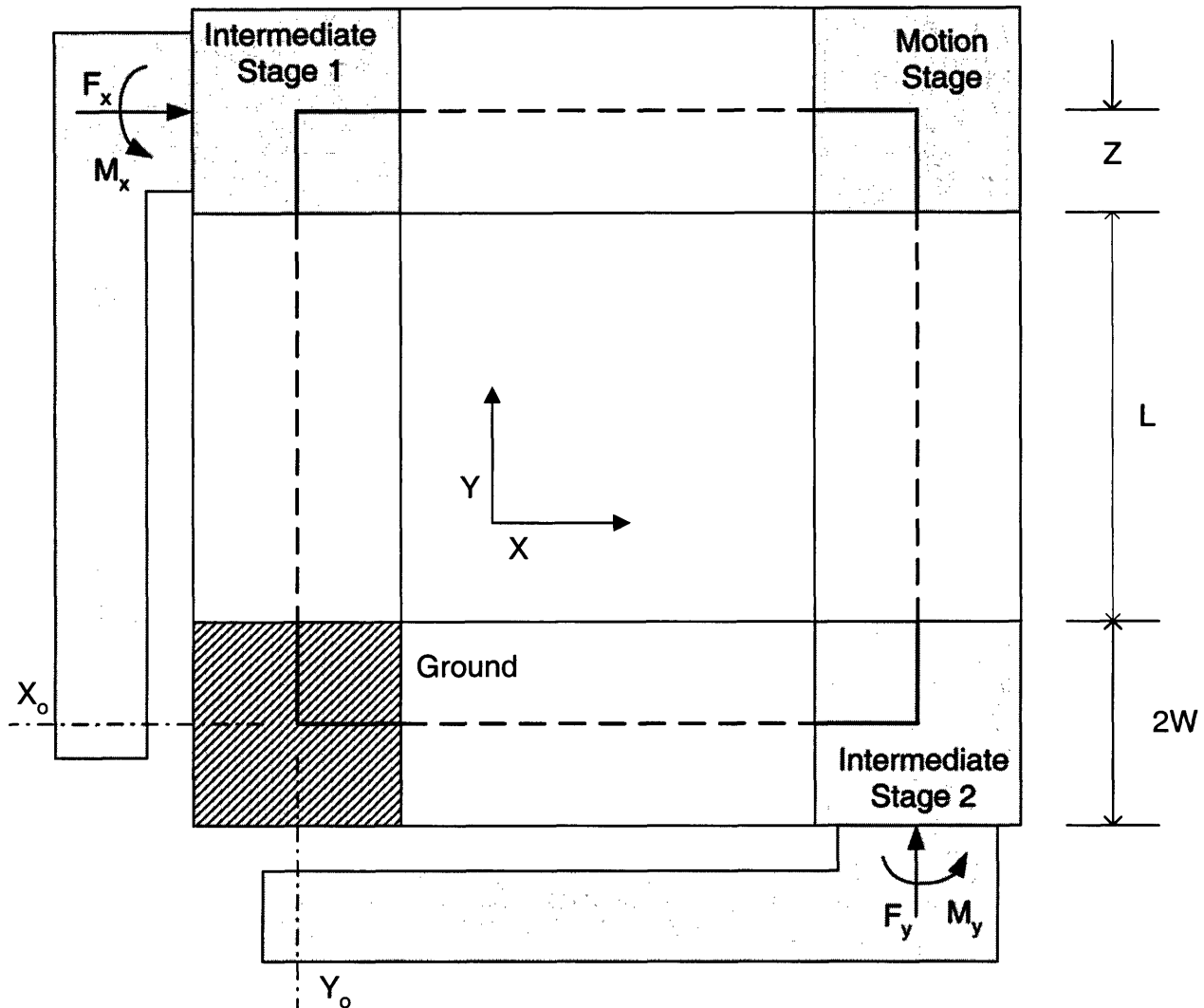


Fig. 5.1 XY Flexure Mechanism 3

Fig. 5.1 illustrates the XY Flexure Mechanism Design of Fig. 2.9, with rigid nodes and compliant units identified as solid lines and dotted lines, respectively. Also shown are extension arms of the intermediate Stages 1 and 2 where the X and Y actuation forces are to be applied. The extension arms allow the application of an additional moment that is geometrically dependent on the force, by moving the location of the force. This gives us some control over the rotation of the three moving stages. Fig. 5.2 shows the mechanism in a deformed configuration, along with the displacements of the nodes. Conditions of geometric compatibility are implicit in this figure.

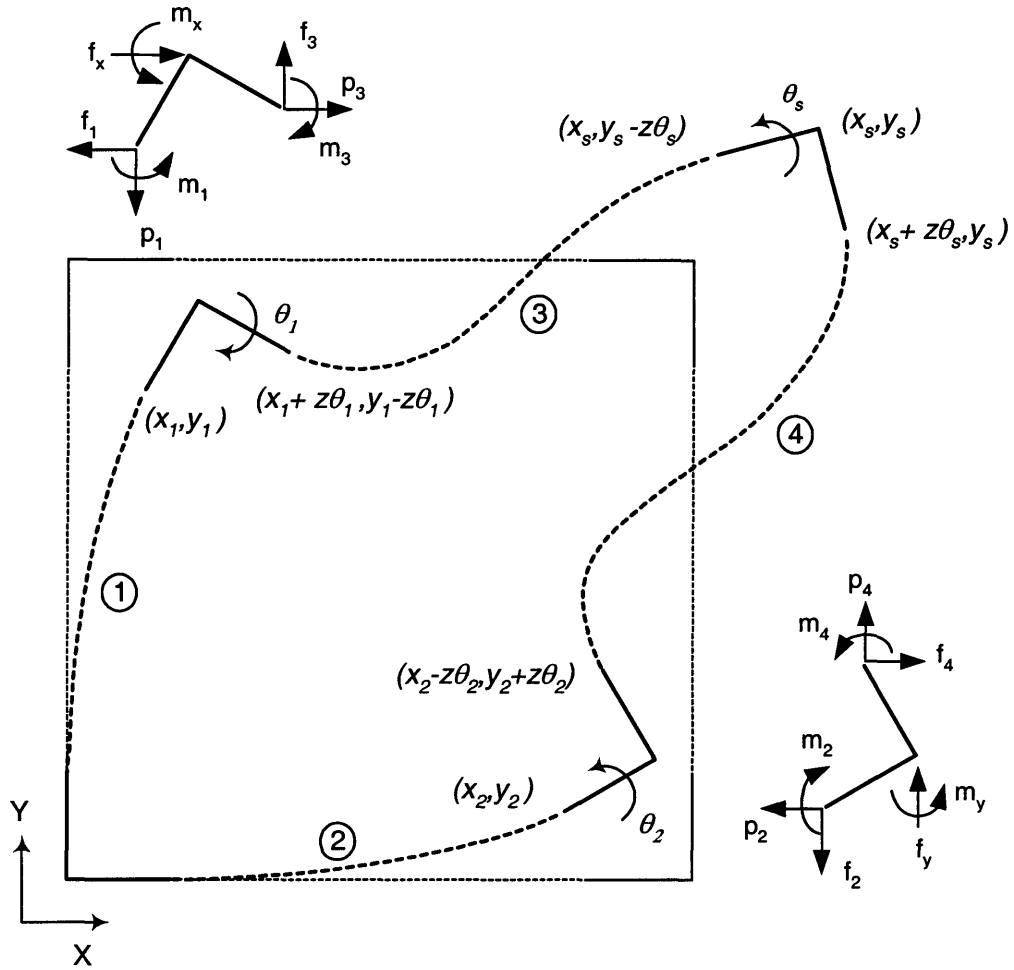


Fig 5.2 The XY mechanism in a deformed configuration and FBDs of intermediate stages

The non-dimensionalized coefficients that characterize the constituent parallelogram flexures, and other specific geometric dimensions in the above mechanism normalized with respect to the beam length ( $L = 60 \text{ mm}$ ) are listed below.

$a$	12	$e$	1.2	$i$	-0.6	$r$	1/700
$c$	-6	$h$	-0.1	$z$	1/6	$d$	43200
$t$	1/60	$w$	19/120				

Force displacement conditions for the  $\lambda^{\text{th}}$  parallelogram building block may be written as

$$\theta_\lambda = \frac{(4a^2 + 4p_\lambda ea + p_\lambda^2 e^2 + f_\lambda^2 dr)(2m_\lambda a - 2f_\lambda c + p_\lambda(m_\lambda e - f_\lambda h))}{2w^2 d(2a + ep_\lambda)^3}$$

$$y_\lambda = \frac{f_\lambda}{(2a + pe)}$$

$$x_\lambda = \frac{p_\lambda}{2d} + [y_\lambda \quad \theta_\lambda] \begin{bmatrix} i & k \\ k & j \end{bmatrix} \begin{bmatrix} y_\lambda \\ \theta_\lambda \end{bmatrix} + p_\lambda [y_\lambda \quad \theta_\lambda] \begin{bmatrix} r & q \\ q & s \end{bmatrix} \begin{bmatrix} y_\lambda \\ \theta_\lambda \end{bmatrix}$$

where,

$\lambda$	$\theta_\lambda$	$y_\lambda$	$x_\lambda$
1	$\theta_1$	$y_1$	$x_1$
2	$\theta_2$	$x_2$	$y_2$
3	$-\theta_1 - \theta_s$	$y_s - y_1 - z\theta_s + z\theta_1$	$x_s - x_1 + z\theta_1$
4	$-\theta_2 + \theta_s$	$x_s - x_2 + z\theta_s + z\theta_2$	$y_s - y_2 - z\theta_2$

Force equilibrium expressions can be obtained from the free body diagrams of the intermediate stages shown in Fig. 5.2. By solving the constitutive relations, force equilibrium and the geometric compatibility equations simultaneously, one may obtain the displacements in the system as functions of other displacements and applied forces. This involves a significant amount of algebraic manipulation, and also assumptions which are justified on the basis of the relative magnitudes of the non-dimensionalized coefficients, forces, and displacements. The following displacement results are obtained from this calculation,

$$\begin{aligned} x_s &= \frac{f_x}{4a} + iy_2^2 - i^2 y_2 x_1^2 \approx \frac{f_x}{4a} - i \left( \frac{f_y}{4a} \right)^2 \\ y_s &= \frac{f_y}{4a} + ix_1^2 - i^2 x_1 y_2^2 \approx \frac{f_y}{4a} + i \left( \frac{f_x}{4a} \right)^2 \end{aligned} \quad (5.1)$$

$$\begin{aligned} x_1 &= \frac{f_x}{4a} - i^2 y_2 x_1^2 \approx \frac{f_x}{4a} \\ y_1 &= ix_1^2 = i \left( \frac{f_x}{4a} \right)^2 \end{aligned} \quad (5.2)$$

$$\begin{aligned} y_2 &= \frac{f_y}{4a} - i^2 x_1 y_2^2 \approx \frac{f_y}{4a} \\ x_2 &= iy_2^2 = i \left( \frac{f_y}{4a} \right)^2 \end{aligned} \quad (5.3)$$

Based on these results several observations may be made.

1. The force required to achieve a desired motion of 0.1 is approximately 5. These numbers are kept in mind while making simplifying approximations. Also, all subsequent plots are generated for the force range of -5 to 5.
2. Expressions (5.1) show that the primary compliance in Y direction is not affected by the actuation force in the X direction, and vice versa. The reason for this is that the two parallelograms, indexed 2 and 3 in Fig. 5.2, that generate the Y displacement experience internal axial forces in response to an X actuation force. These internal axial forces are equal in magnitude but opposite in sign, which implies that the increase in transverse stiffness of one parallelogram is very closely matched by the reduction in transverse stiffness of the other parallelogram, thus keeping the overall stiffness in Y direction largely unchanged.
3. Cross-axis coupling terms are very noticeable in this design, and are purely kinematic in nature. The dominant cross-axis error term along any given direction is a quadratic function of the primary displacement along the other direction. It may be noticed that there is also a higher order cross-axis coupling terms in expressions (5.1), that has a coefficient of  $i^2$ . Quite interestingly, this term represents a secondary error motion resulting from the primary error motion. For example, a primary X displacement causes a primary cross-axis error of the motion stage in the Y direction. This small motion in Y direction causes a yet smaller secondary cross-axis error motion in the X direction.
4. The contribution of the elastic and elastokinematic terms in the difference between  $x_I$  and  $x_s$ , or  $y_I$  and  $y_s$ , is two orders of magnitude smaller than the purely kinematic effects, and therefore these terms have been neglected in the above expressions. Yet, for the sake of estimating the dynamic performance, it is important to assess the change in stiffness or compliance between the point of force application and the motion stage. This inline compliance can be shown to be

$$\frac{\partial(x_I - x_s)}{\partial f_x} = \frac{1}{4d} + \frac{ry_2^2}{4}$$

For the particular geometry considered here,  $d = 43200$  and  $r = 1/700$ , which results in an approximately 60% increase in compliance and 40% reduction in stiffness over the range of motion of  $y_2 = 0.1$ .

5. Because of the geometry of the configuration and the properties of the constituent parallelograms, although the motion stage itself has significant cross-axis motion, the displacement of intermediate stage 1 in response to the Y actuation force is a second order term in  $i^2$ , which as earlier, is a kinematic error associated with another kinematic error. Despite this effect being small, complete actuator isolation is not achieved. It can be seen that intermediate stage 1 has a small Y motion given

by expression (5.2), and intermediate stage 2 has a small X motion given by expression (5.3). Hence a decoupler will be necessary between the actuators and the intermediate stages to absorb this off-axis motion.

Although the applied moments play an insignificant role in the determination of displacements, they are key to determining the rotation of the three stages. The analysis for internal moments and stage rotations is carried out assuming independent moment and forces, but we know that it is ultimately desirable to use only forces for actuation. As has been discussed in Section 5.1, only geometrically dependent moments may be applied by locating the forces appropriately.

The objective is to determine the center of stiffness of the mechanism and then apply the actuation forces through it, so that these forces and the resulting moments minimize the motion stage rotation. But the center of stiffness for a mechanism depends on where the loads are applied and where the rotation is measured. In our case, the loads are applied at intermediate stages 1 and 2 only, and the rotation of the motion stage is of primary interest.

The general expressions for the rotations,  $\theta_1$ ,  $\theta_2$  and  $\theta_s$  are too complex to be presented here, and instead the dependence of stage rotations on applied forces is explained graphically. The rotations, in general, are functions of the four applied loads

$$\theta_1 = fn_1(f_x, m_x, f_y, m_y)$$

$$\theta_2 = fn_2(f_x, m_x, f_y, m_y)$$

$$\theta_s = fn_s(f_x, m_x, f_y, m_y)$$

As a first step, we solve the equation  $fn_3(f_x, m_x, f_y = 0, m_y = 0) = 0$  for  $m_x$ . The resulting expression tells us what the moment  $m_x$  has to be for a given X force  $f_x$ , so that the motion stage rotation  $\theta_s$  is zero. For the particular case considered here,

$$m_x = 0.001000000000 f_x (0.3275589344 \cdot 10^{36} - 0.1596685376 \cdot 10^{30} f_x^6 + 0.2518311500 \cdot 10^{20} f_x^{12} + 0.3071844239 \cdot 10^{32} f_x^4 + 0.1748026727 \cdot 10^{17} f_x^{14} + 0.7673506731 \cdot 10^{34} f_x^2 + 0.2355608959 \cdot 10^{27} f_x^8 - 0.1489545925 \cdot 10^{24} f_x^{10} + 0.1367968387 \cdot 10^{10} f_x^{18} - 0.9426214162 \cdot 10^{13} f_x^{16}) / (0.2456692007 \cdot 10^{33} - 0.4984045074 \cdot 10^{14} f_x^{14} + 0.8949378025 \cdot 10^{31} f_x^2 - 0.2738538858 \cdot 10^{27} f_x^6 + 0.4687565947 \cdot 10^{24} f_x^8 + 0.5255526947 \cdot 10^{29} f_x^4 + 0.5252998603 \cdot 10^{10} f_x^{16} + 0.1960817653 \cdot 10^{18} f_x^{12} - 0.4078741223 \cdot 10^{21} f_x^{10})$$

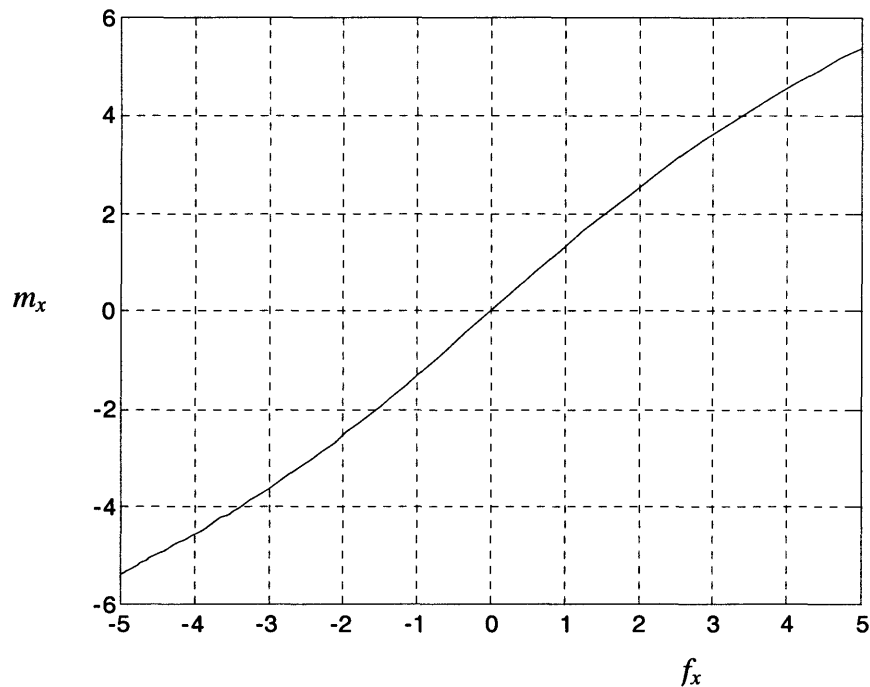


Fig.5.3  $m_x$  required to maintain  $\theta_s=0$ , when  $f_y=m_y=0$

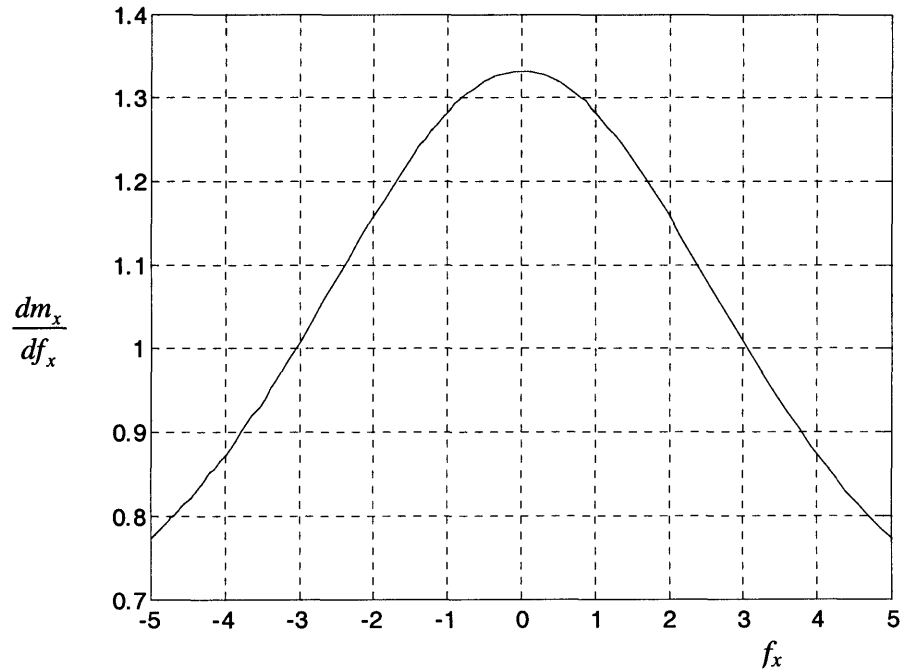


Fig.5.4 Variation of center of stiffness for X Actuation

This expression is plotted in Fig. 5.3, and indicates a close to, but not perfect, linear behavior. To check for linearity, we also plot the slope of this function in Fig. 5.4. For a perfectly linear behavior, the slope would have been constant, and based on this, one could pick up the center of stiffness. However, that is not the case, and Fig. 5.4 indicates that there is no single point where the force  $f_x$  can be applied, over the entire range of  $f_x$ , without resulting in a motion stage rotation. For small values of  $f_x$ , the two plots indicate that the X force should be applied at a distance of  $l+z$  ( $=1.333$ ) from its current location. This location corresponds to the axis  $X_o$  in Fig 5.1. As the magnitude of applied force increases, the center of stiffness shifts by the amount predicted by Fig. 5.4.

Identical results are obtained when we repeat the same process with the equation  $\theta_s = f n_s(f_y, m_y, f_x = 0, m_x = 0) = 0$  to determine center of stiffness with respect to the Y actuation force. This is expected because of symmetry about the geometric diagonal axis. In this case, it can be determined that the Y force should be applied along the  $Y_o$  axis to minimize the stage yaw for small values of  $f_y$ .

Clearly, actuation forces applied along the axes  $X_o$  and  $Y_o$ , will not produce a zero motion stage yaw as the forces increase, but given the fact that we cannot adjust the moments on the intermediate stages independently, these are our best choices.

The next obvious step to investigate is the effect of X forces on Y relationships and vice versa. We therefore apply varying amounts of Y force along the  $Y_o$  axis, and plot the resulting center of stiffness location for the X force in Fig. 5.5. Note that this plot provides normalized distance from the current force location as shown in Fig. 5.1. Clearly, the presence of the Y force significantly affects the center of stiffness with respect to X force, which is an indication of the amount of coupling present between the two axes.

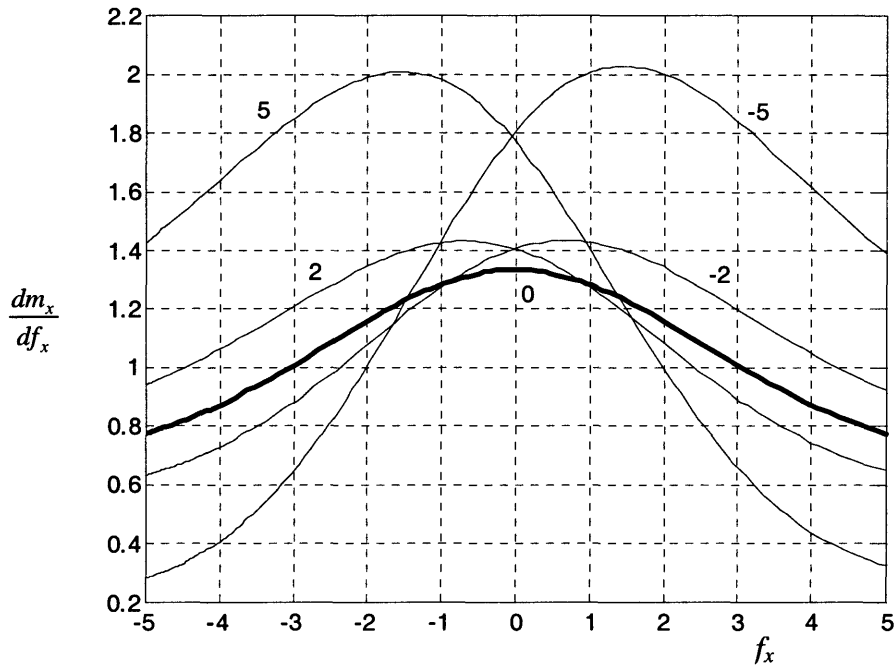


Fig.5.5 Center of stiffness for X actuation, for different values of  $f_y$

We next consider the actual motion stage rotation  $\theta_s$ , for forces applied along axes  $X_o$  and  $Y_o$ . For the particular case being considered here, the following expression provides the dependence of  $\theta_s$  on  $f_x$ , when  $f_y=0$ .

$$\begin{aligned} \theta_s = & 0.4690087793 \cdot 10^{-33} (-0.1367968387 \cdot 10^{83} f_x^{19} + 0.2362592387 \cdot 10^{94} f_x^{13} \\ & + 0.1643021230 \cdot 10^{87} f_x^{17} - 0.8393420159 \cdot 10^{90} f_x^{15} + 0.3894478970 \cdot 10^{100} f_x^9 \\ & - 0.3948775706 \cdot 10^{97} f_x^{11} - 0.2054699768 \cdot 10^{103} f_x^7 + 0.3935525023 \cdot 10^{105} f_x^5 \\ & + 0.4258997299 \cdot 10^{107} f_x^3 - 0.1 \cdot 10^{100} f_x) / (-0.3795365942 \cdot 10^{62} f_x^{12} + 0.3673200210 \cdot 10^{72} f_x^6 \\ & + 0.4991374238 \cdot 10^{79} + 0.1501485868 \cdot 10^{66} f_x^{10} - 0.3149856223 \cdot 10^{69} f_x^8 \\ & + 0.4813110873 \cdot 10^{77} f_x^2 + 0.3984496720 \cdot 10^{58} f_x^{14} - 0.2214365245 \cdot 10^{75} f_x^4) \end{aligned}$$

Based on the maximum value of  $f_x$  that we are interested in, the above expression may be further simplified by dropping out the terms that have a negligible contribution. This expression, and analogous expressions for values of  $f_y = -5, -2, 2, 5$ , are plotted in Fig. 5.6. Once again this plot shows a strong coupling between the axes as far as rotations are concerned. The maximum motion stage rotation or yaw, in this case is seen to be 600 µradians or 2 arc minutes.

When we repeat this exercise for the Y actuation force instead of X actuation force, we obtain identical results, except for reversed signs of  $\theta_s$ . This is expected because of geometric symmetry in the design validates our analysis. Next, we present a series of 3D plot of the motion stage rotation  $\theta_s$  versus  $f_x$  and  $f_y$ , in Fig. 5.7a. through c. These provides a much better understanding of the nature of motion stage yaw and its dependence on the actuation forces.

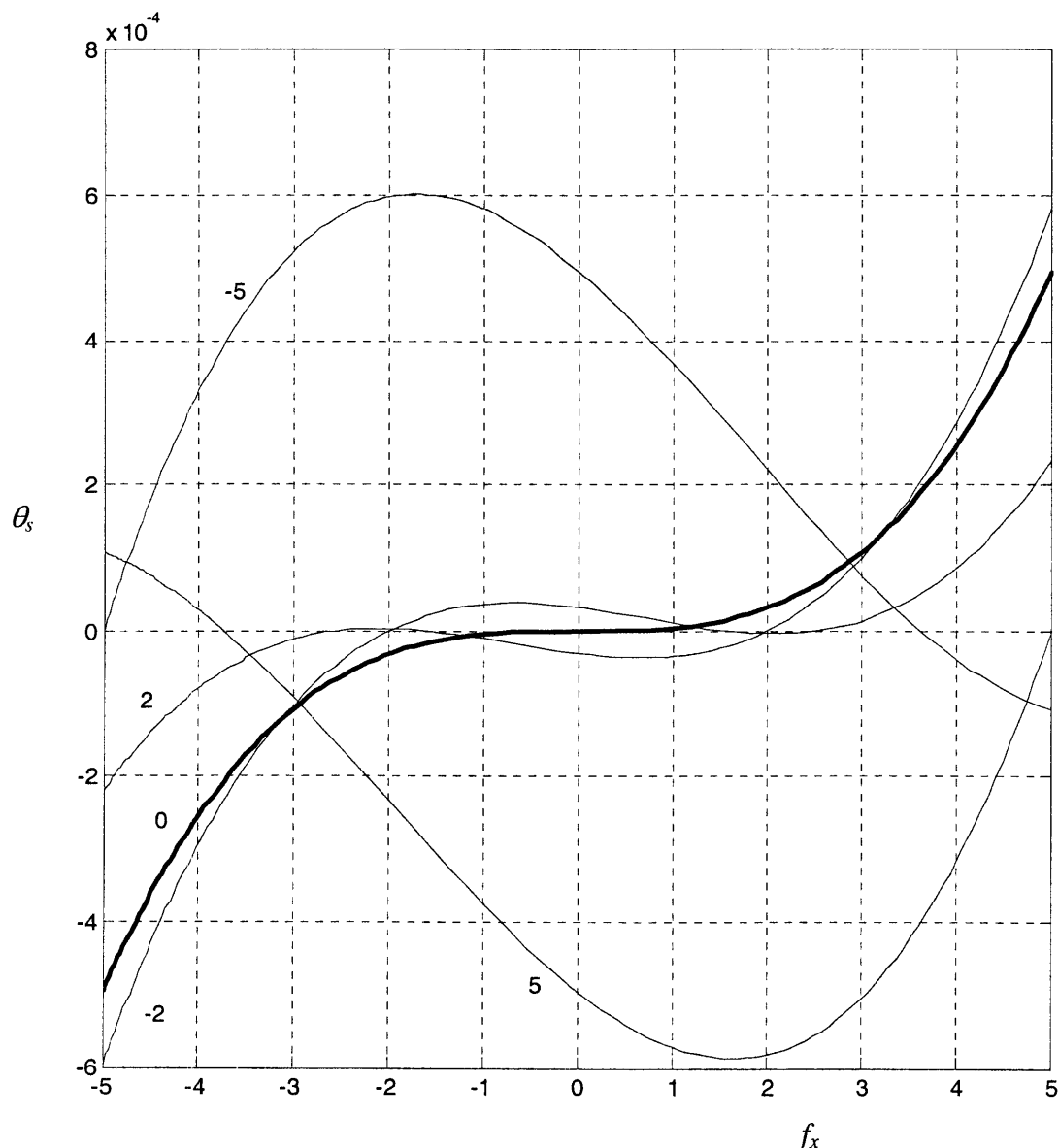


*Fig. 5.6 Motion stage rotation vs. X force, for different values of Y force*

*Fig. 5.7a. Motion Stage Yaw vs. X force and Y force*

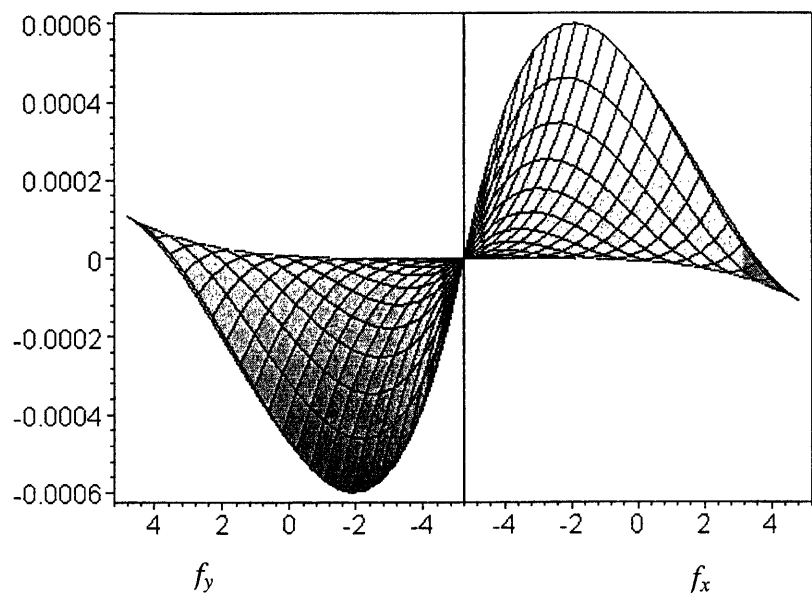


*Fig. 5.7b. Motion Stage Yaw vs. X force and Y force*

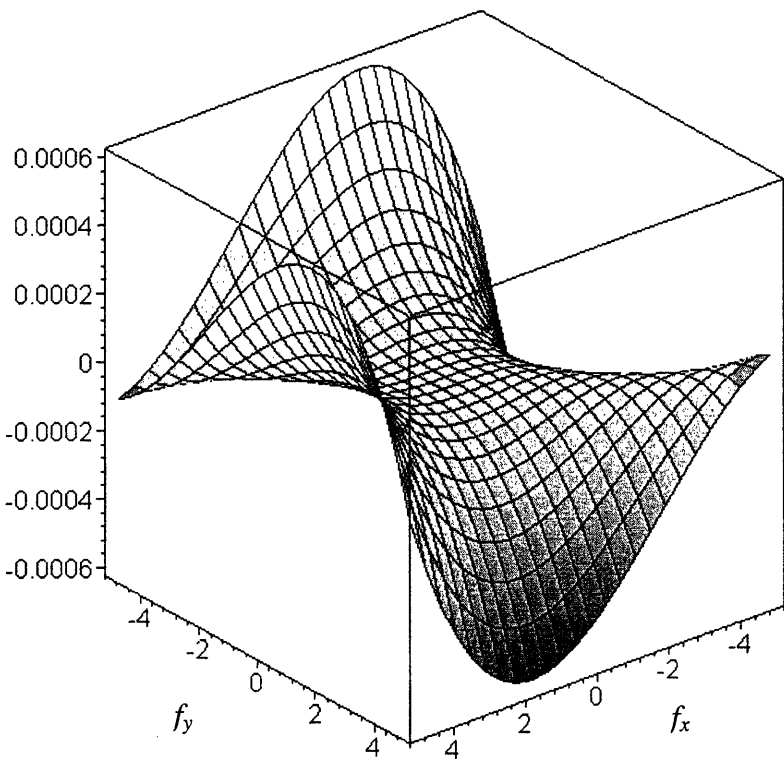
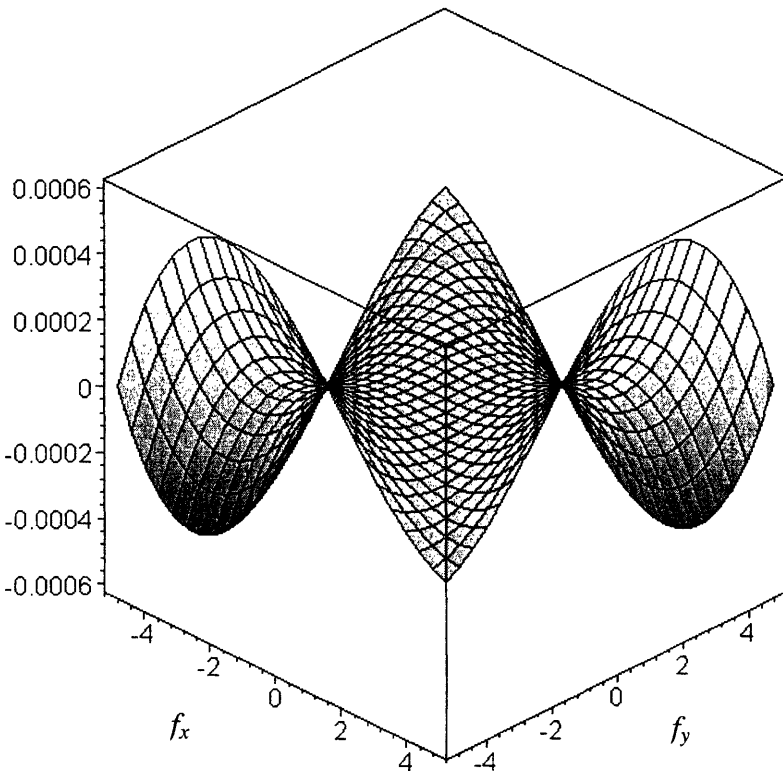


*Fig. 5.7c. Motion Stage Yaw vs. X force and Y force*



There are several observations to be made here. For this particular XY Flexure mechanism, there is a fairly small range of forces, and therefore displacements, over which the motion stage rotation  $\theta_s$  stays small, as is apparent from small flat region in the center of Fig. 5.7b. As forces are increased,  $\theta_s$  grows non-linearly to values as high as 600  $\mu$ radians. In fact, if the maximum allowable  $\theta_s$  is 5  $\mu$ radians, or 1 arc second, then the useful range of motion of this mechanism is limited to force values of 1 and displacements of 0.02.

Also, the mechanism is geometrically symmetric about its diagonal axis, and this fact may be used in predicting the nature of  $\theta_s$  for special loading situations, without resorting to any analysis. The symmetry about the geometric diagonal axis is maintained if the X and Y forces are equal in magnitude and sign. In this situation, if the mechanism is flipped by 180 degrees about its diagonal axis, nothing should change. This necessitates that the motion stage rotation for this particular loading case be zero. This is exactly what we notice in Fig. 5.7a, where  $\theta_s$  can be seen to be zero, or very close to zero, along the positive diagonal axis in the  $f_x - f_y$  plane.

Extending these arguments of symmetry, if we next consider a loading situation where  $f_x=a$  and  $f_y=b$ , then the resulting  $\theta_s$  will be negative of the  $\theta_c$  when  $f_x=b$  and  $f_y=a$ . This should produce a negative symmetry in the  $\theta_s$  contour about the  $+45^\circ$  line in the  $f_x - f_y$  plane, and this indeed is corroborated by Figures 5.7a and b. Similarly, one can argue without any analysis that there should be a positive symmetry in  $\theta_s$  about the  $-45^\circ$  line in the  $f_x - f_y$  plane, and this exactly as our analysis predicts in plot 5.7c. These validations provide some amount of confidence in the analysis presented here. Also, the above discussions reveal the nature of mapping between the symmetry in the performance space of  $\theta_s$  versus  $f_x$  and  $f_y$ , and symmetry in the geometric space, which is quite interesting.

Neither the location of the center of stiffness nor the range of forces over which it is effective is intuitively obvious, and therefore the above analysis is quite helpful to the designer. A linear analysis, which does not include the non-linear effects modeled in Chapters 3 and 4, also predicts the location of the center of stiffness. But this linear analysis predicts zero motion stage yaw if forces are applied along the  $X_o$  and  $Y_o$  axes, and sheds no light on the deviation from this ideal behavior.

Based on the above analysis, we can also determine other centers of stiffness for the mechanism. For example, the location of X force which results in minimum rotation of stage 1 is given by  $1/2+z$ , which corresponds to the mid-span of parallelogram 1.

The next step in our analysis is to obtain an estimate of the sensitivity to the exact location of the actuation forces. Such variations may occur in the real world, due to assembly and manufacturing tolerances. For this purpose, we choose the point from Fig. 5.7, that has the maximum error rotation. This point happens to be,  $f_x = -1.75$  and  $f_y = -5$ , and the resulting stage yaw is about  $0.0006$ . For this situation, we look at the effect of varying the X actuation force by  $+/-.3\text{mm}$  about the  $X_o$  axis, and plot the results in Fig. 5.8. For variation of  $+/-.1\text{mm}$  in force location, the motion stage yaw changes by about  $3.5\%$ . For standard manufacturing and assembly processes, tolerance are at  $10-20$  times better than this. Thus, the design is fairly insensitive to such variations.

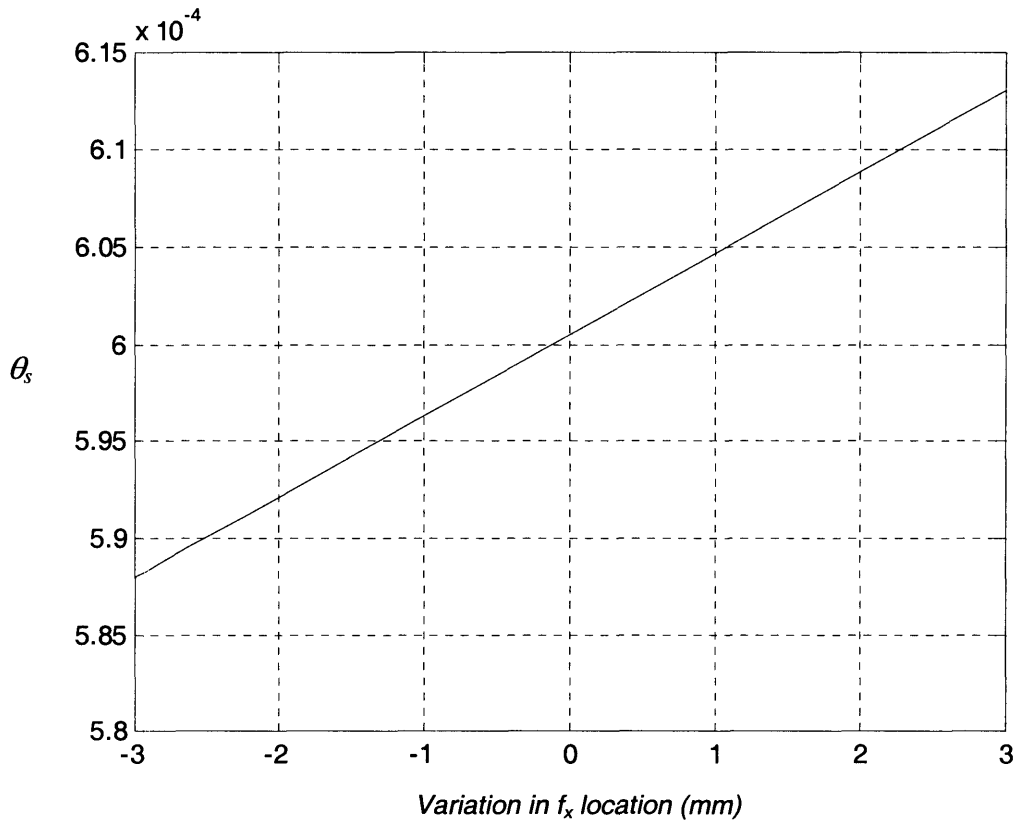


Fig. 5.8 Sensitivity of  $\theta_s$  to X force location

Finally, as far as thermal sensitivity is concerned, this design is not thermocentric, and will be affected by thermal variations. Also, the out of plane stiffness is relatively low. In fact, a thorough dynamics analysis is required to determine the modes shapes of the structure, and determine how that affects the positioning performance.

### 5.3 XY Flexure Mechanism Design 4

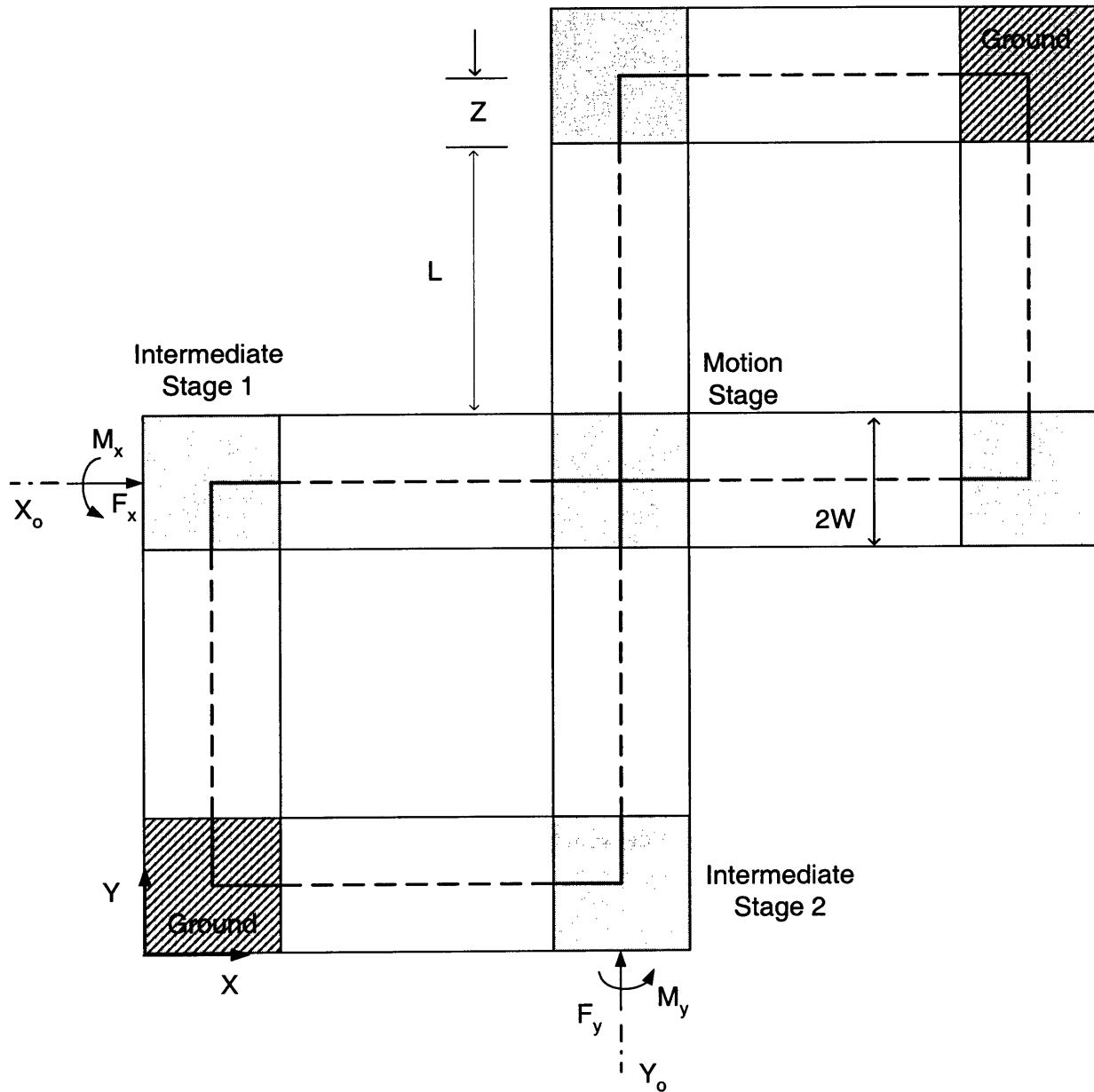


Fig 5.9 XY Flexure Mechanism 4

Fig. 5.9 shows the XY Mechanism Design 4 from Chapter 2, and indicates the rigid nodes and compliant units by means of solid and dashed lines, respectively. Fig. 5.10 shows the mechanism in a deformed configuration, along with the relative displacement of nodes. This design is simply a mirrored version of the previous design, and therefore dimensions remain the same as earlier. Force displacement

relationships for the constituent parallelogram flexure units, and geometric constraint conditions are also the same.

$$\theta_\lambda = \frac{(4a^2 + 4p_\lambda ea + p_\lambda^2 e^2 + f_\lambda^2 dr)(2m_\lambda a - 2f_\lambda c + p_\lambda(m_\lambda e - f_\lambda h))}{2w^2 d(2a + ep_\lambda)^3} \quad (5.4)$$

$$y_\lambda = \frac{f_\lambda}{(2a + pe)}$$

$$x_\lambda = \frac{p_\lambda}{2d} + [y_\lambda \quad \theta_\lambda] \begin{bmatrix} i & k \\ k & j \end{bmatrix} \begin{bmatrix} y_\lambda \\ \theta_\lambda \end{bmatrix} + p_\lambda [y_\lambda \quad \theta_\lambda] \begin{bmatrix} r & q \\ q & s \end{bmatrix} \begin{bmatrix} y_\lambda \\ \theta_\lambda \end{bmatrix}$$

where,

$\lambda$	$\theta_\lambda$	$y_\lambda$	$x_\lambda$
1	$\theta_1$	$x_1$	$y_1$
2	$\theta_2$	$y_2$	$y_2$
3	$-\theta_1 - \theta_s$	$y_s - y_1$	$x_s - x_1$
4	$-\theta_2 + \theta_s$	$x_s - x_2$	$y_s - y_2$
5	$-\theta_7 - \theta_s$	$x_7 + x_s$	$y_7 - y_s$
6	$-\theta_8 + \theta_s$	$y_8 + y_s$	$x_8 - x_s$
7	$\theta_7$	$y_7$	$x_7$
8	$\theta_8$	$x_8$	$y_8$

The Free Body Diagrams of the nodes corresponding to the four intermediate stages are shown in Fig. 5.10 and provide the force equilibrium relationships for the mechanism.

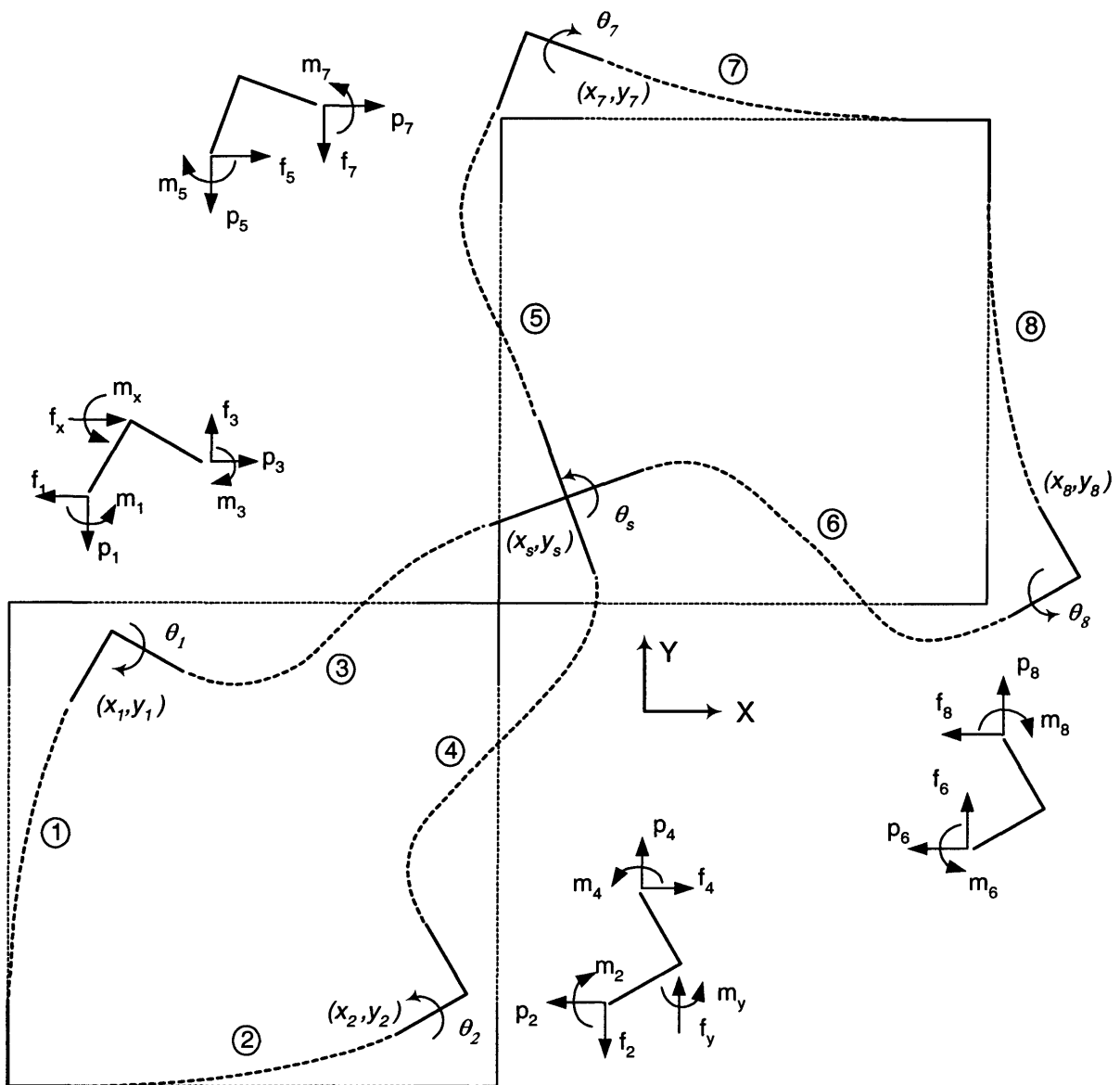


Fig. 5.10 Deformed configuration of XY Mechanism 4

The constitutive relationships, geometric compatibility and force equilibrium, are all solved simultaneously. As earlier, these calculations get very complex, and terms are dropped at each stage if they are too small to make a contribution. The displacements thus obtained are

$$x_s = \frac{f_x}{8a - ef_y} - \frac{y_2^2 f_x r}{4} \quad y_s = \frac{f_y}{8a - ef_x} - \frac{x_1^2 f_y r}{4} \quad (5.5)$$

$$x_1 = x_s - y_2^2 i + \frac{3}{4} f_x y_2^2 r = \frac{f_x}{8a - ef_y} - y_2^2 i + \frac{1}{2} f_x y_2^2 r \quad y_1 = x_1^2 (i + \frac{1}{4} f_y r) \quad (5.6)$$

$$x_8 = x_s + y_2^2 i - \frac{1}{4} f_x y_2^2 r = \frac{f_x}{8a - ef_y} + y_2^2 i - \frac{1}{2} f_x y_2^2 r \quad y_8 = x_1^2 (i - \frac{1}{4} f_y r) \quad (5.6)$$

$$y_2 = y_s - x_1^2 i + \frac{3}{4} f_y x_1^2 r = \frac{f_y}{8a - ef_x} - x_1^2 i + \frac{1}{2} f_y x_1^2 r \quad x_2 = y_2^2 (i + \frac{1}{4} f_x r) \quad (5.7)$$

$$y_7 = y_s - x_1^2 i - \frac{1}{4} f_y x_1^2 r = \frac{f_y}{8a - ef_x} - x_1^2 i - \frac{1}{2} f_y x_1^2 r \quad x_7 = y_7^2 (i - \frac{1}{4} f_x r) \quad (5.7)$$

The following observations are made based on these results.

1. This design is twice as stiff with respect to the as compared to the previous one, which is an obvious consequence of the fact that there are twice as many parallelogram units in this case. The maximum force needed to produce a desire motion of 0.1 is also twice as large, approximately 10. Furthermore, this design also takes up four times as much space as the previous design because of its geometry.
2. From (5.5), we note that the primary stiffness in X direction does change with a force in Y direction. This is because of the fact that the force in Y direction produces internal axial forces in the parallelograms that generate the X motion, indexed as 1, 4, 5 and 8 in Fig. 5.10. The axial force in each of these units is approximately  $+f_y/4$ ,  $-3f_y/4$ ,  $-f_y/4$  and  $-f_y/4$ , respectively. Because of these unequal amounts of axial forces, the change in the transverse stiffness of the above four units is different, and the overall affect does not cancel out. The same argument holds true for the Y direction primary stiffness as well. The change in primary stiffness in a given direction is approximately  $\pm 12\%$ , over the entire range of force in the other direction. It may be recalled that in the case of XY Mechanism 3, the primary stiffness remained largely unchanged with applied loads.
3. As was predicted in Chapter 2 by intuitive reasoning, the cross axis coupling indeed has been reduced by about two orders of magnitude. In the previous case, the cross axis coupling was dominated by a purely kinematic error term, whereas in the coupling here is a dominated by elastic and elastokinematic term. For the given range of motion and forces, the elastokinematic term is about 40 times smaller than the purely kinematic term.
4. While we have seen the cross-axis coupling has been reduced in the mechanism, actuator isolation suffers in this design. The kinematic component of the axial motion between intermediate stage 1 and motion stage, shows up at stage 1 while the motion stage is spared due to symmetry. In the absence of an X force, intermediate stages 1 and 8 have X displacements of the order of  $i y_2^2$ . Thus the trade-off between cross-axis coupling and actuator isolation is apparent in the XY Mechanism Designs 3 and 4. Apart from experiencing an X displacement in response to a Y force, the point of X force application

on intermediate stage 1 also experiences a Y displacement in response to an X force, as shown by the  $y_1$  expression in (5.6) .

5. The stiffness between the point of actuation and motion stage along X drops quadratically with primary motion in the Y direction, and vice versa. The inline compliance in this case is given by

$$\frac{\partial(x_l - x_s)}{\partial f_x} = \frac{3}{8} \left( \frac{1}{d} + r y_2^2 \right)$$

Once again, this predicts a 60% increase in compliance and about 40% reduction in stiffness for a maximum primary Y displacement of 0.1.

6. Thermal sensitivity is not analytically determined, but based on the symmetry of this design, one can say that the motion stage will be relatively less sensitive to thermal disturbances. Any changes in beam length should be accommodated by the intermediate stages without significantly perturbing the motion stage. Furthermore, out of plane stiffness is better than in the previous case because of the added connections to ground.

Next we proceed to solve for the internal moments and the resulting stage rotations. There are 8 unknown moments, one associated with each parallelogram unit, and only 5 moment balance equilibrium conditions, corresponding to the 5 rigid nodes or stages. On the other hand while there are only 5 unknown angles, there are 8 constitutive relations between moments and angles as given by (5.4). Thus, with the given number of equations all the moments and rotations can be solved for. The calculations and resulting expressions for moments and angles are quite complicated despite dropping insignificant terms based on the non-dimensional analysis. As earlier, these results are therefore presented graphically.

Motion stage rotation  $\theta_s$ , can be obtained in terms of the four applied loads

$$\theta_s = fn_s(f_x, m_x, f_y, m_y)$$

Once again the our objective is to minimize the rotation of the motion stage by suitably locating the actuation forces, without having to apply independent moments. We start with solving the equation  $fn_3(f_x, m_x, f_y = 0, m_y = 0) = 0$  for  $m_x$ , to determine the ratio between  $m_x$  and  $f_x$  needed to keep  $\theta_s$  zero. If this ratio is constant, then the center of stiffness is fixed with respect to the X actuation force. To determine whether this is the case, we plot the above function for  $m_x$  and its slope, vs.  $f_x$  in Fig. 5.11. Interestingly, we find out that the moment required to keep the motion stage rotation zero for values of  $f_x$  ranging from -5 to 5, is extremely small, in fact smaller than the accuracy of our analysis. Based on this, we conclude that the current position of the X force, along the  $X_o$  axis, is the most suitable actuation point. Furthermore, the slope also stays extremely small, which reasserts that this center of stiffness location is effective for large actuation forces as well.

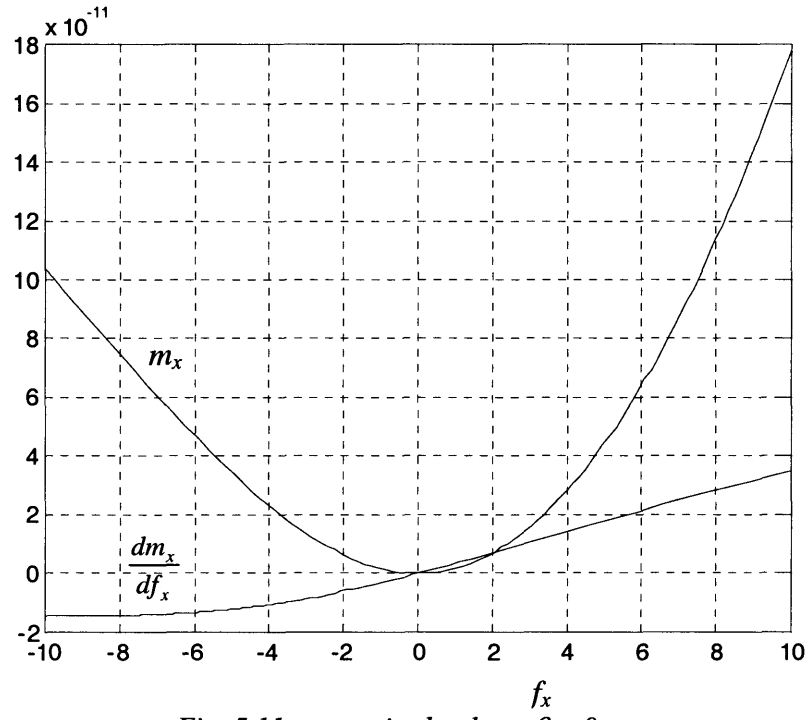
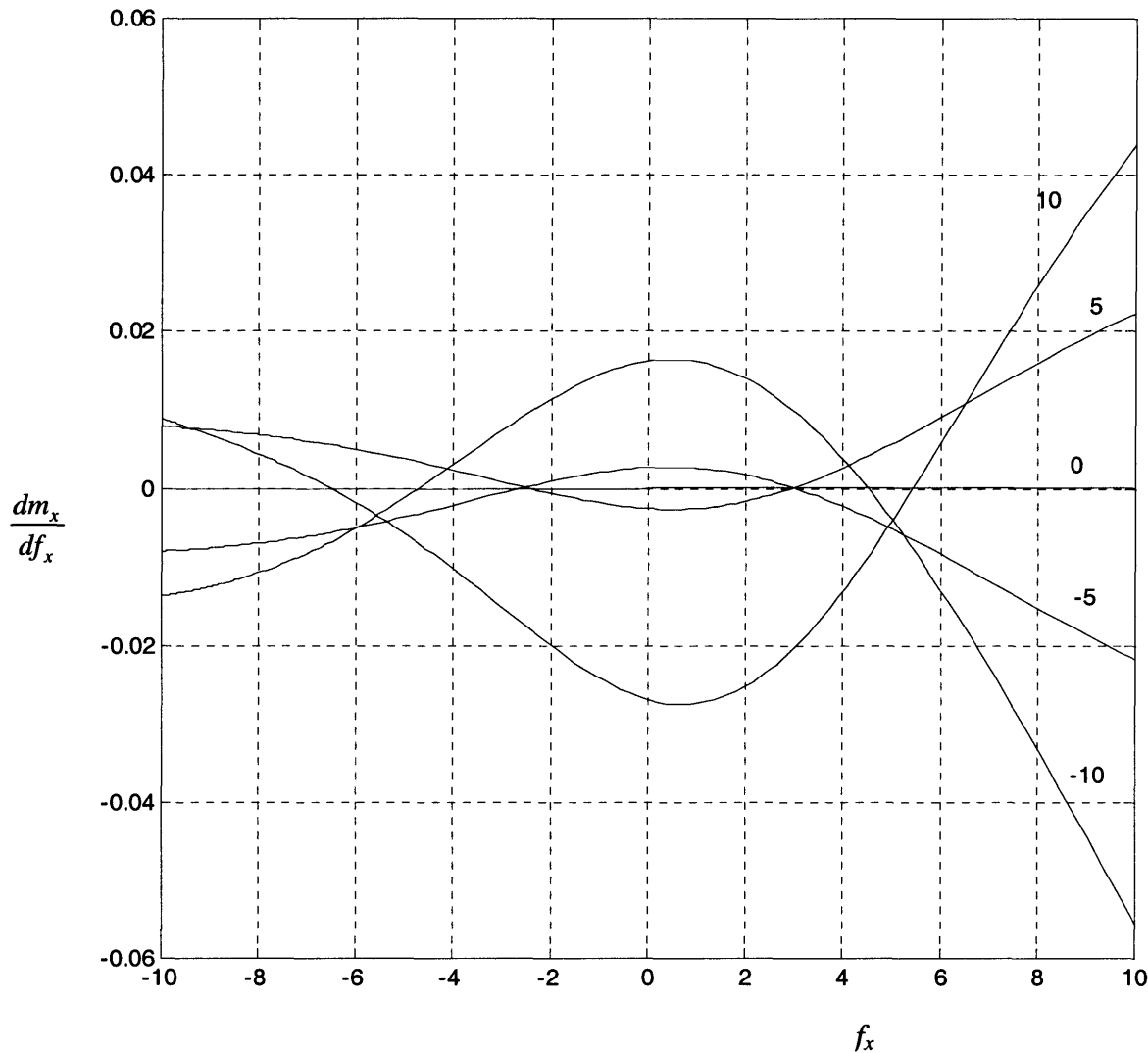


Fig. 5.11  $m_x$  required to keep  $\theta_s = 0$

Since this design is symmetric about its geometric diagonal axis, running between the two ground support points, identical results are expected and obtained for Y force as well. It is therefore concluded that the original location of the Y force along the  $Y_o$  axis is the best location for minimizing motion stage yaw.

The obvious next check to consider how this above conclusions for X actuation change when a Y force is applied along  $Y_o$ . The equation  $fn_3(f_x, m_x, f_y, m_y=0) = 0$  is solved for  $m_x$  again but for different values of  $f_y$  this time.  $dm_x/df_x$  which provides the center of stiffness location, is plotted in Fig. 5.12 for all these cases. These plots indicate that the presence of the Y force changes the center of stiffness with respect to X actuation. In fact, a maximum variation of  $dm_x/df_x$  by 0.04 corresponds to a shift in the center of stiffness by 2.4 mm for a 60mm long parallelogram. Once again, the strong coupling between the two axes is very obvious as far as stage rotations are concerned.



*Fig. 5.12 Center of Stiffness for X actuation for different levels of  $f_y$*

Results for Y actuation are identical to above, and are therefore not presented here. Despite the fact that the center of stiffness for each actuation axis shifts with a force along the other axis, the current choice of actuation points is the best option available. Therefore, we next proceed to predict the actual motion stage rotation, as  $f_x$  and  $f_y$  are varied over their entire range of interest. Fig. 5.13 presents variation of  $\theta_s$  with  $f_x$  for different values of  $f_y$ .

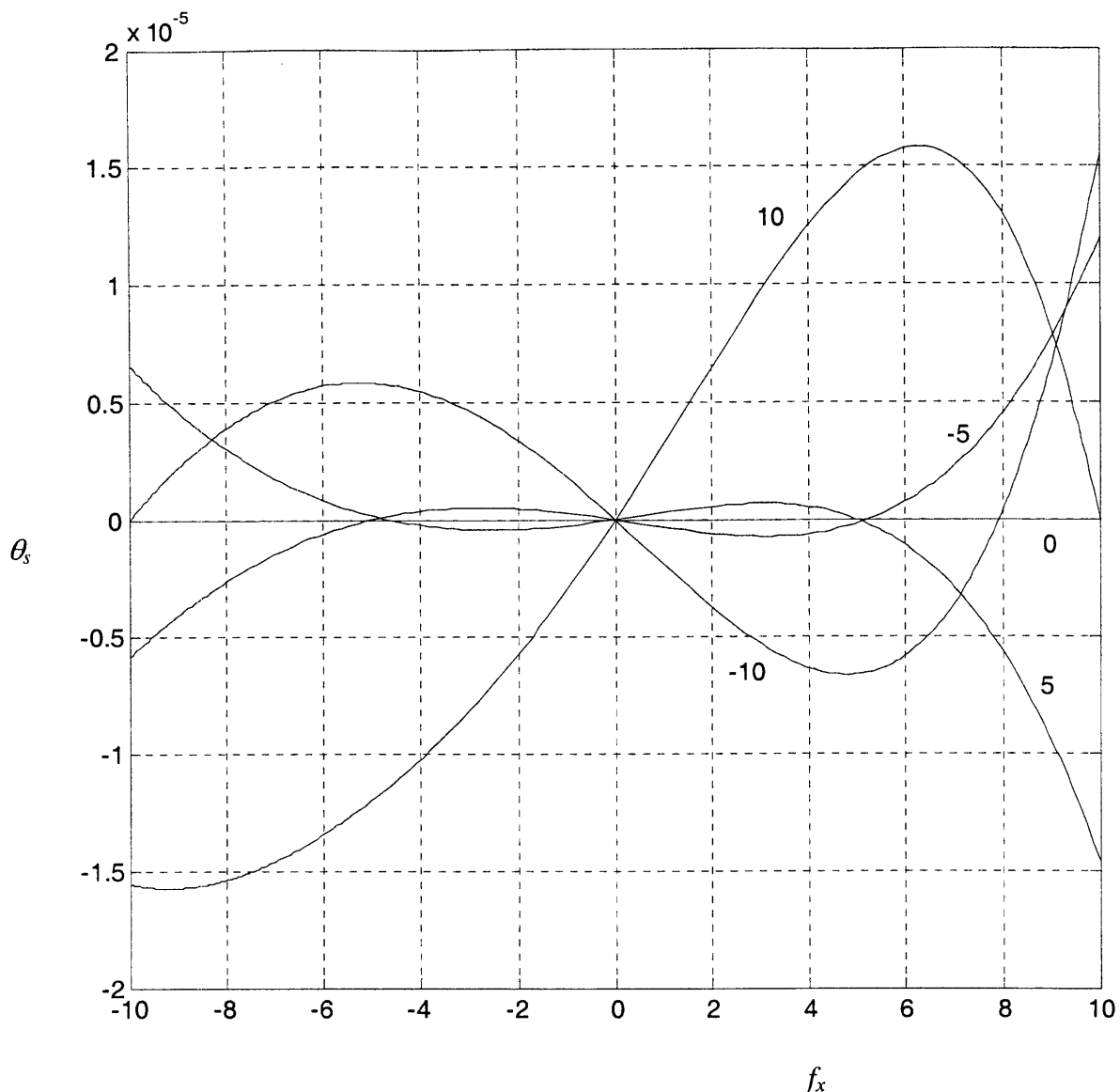
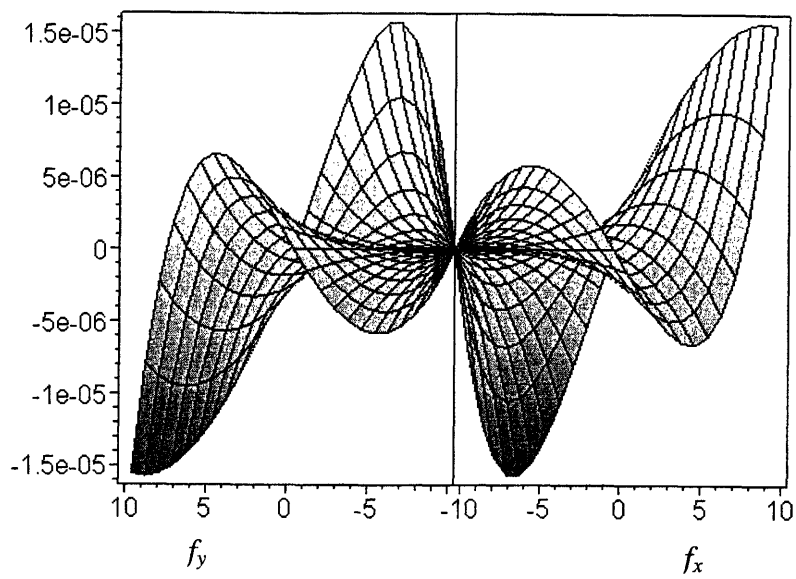


*Fig. 5.12 Motion stage rotation versus  $f_x$ , for different values of  $f_y$*

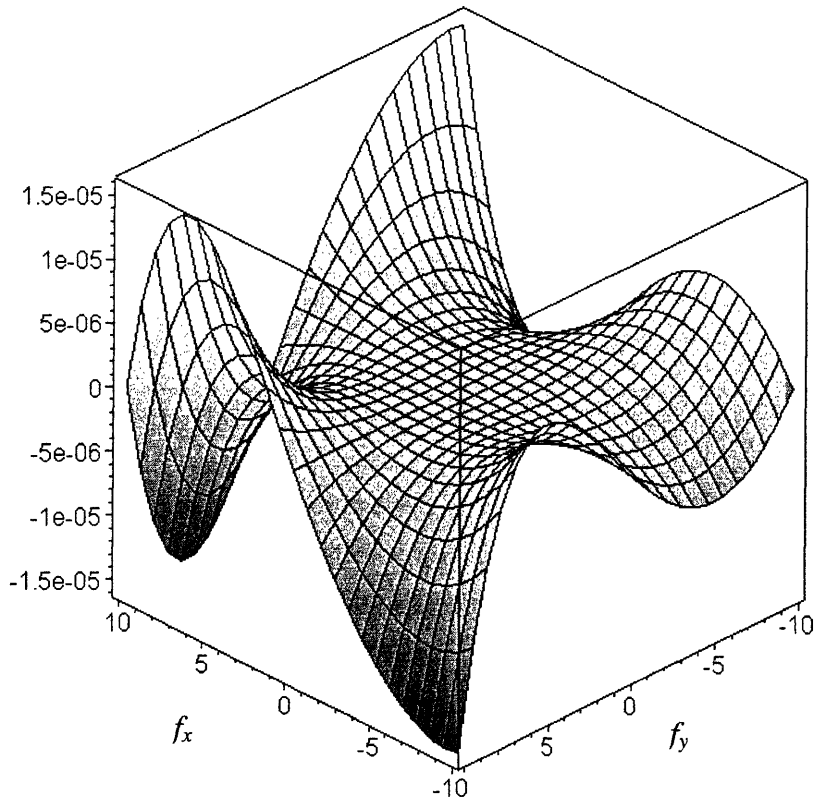
Once again the effect of the coupling between the axes is very evident here. While the stage rotation stays essentially zero for the entire range of  $f_x$  when there is no Y force, the rotations increase rapidly with increasing magnitudes of  $f_y$ . It is also worthwhile to note the highly non-linear dependence of the plots on  $f_y$ . This is not unexpected, since geometric symmetry does not require a positive force and negative force of the same magnitude to produce the same magnitude of rotation.

Fig. 5.14 presents a series of 3D contours that illustrate the variation of  $\theta_s$  with both  $f_x$  and  $f_y$  over the entire range of applied forces. This also corresponds to a primary motion range of  $-0.1$  to  $0.1$ .

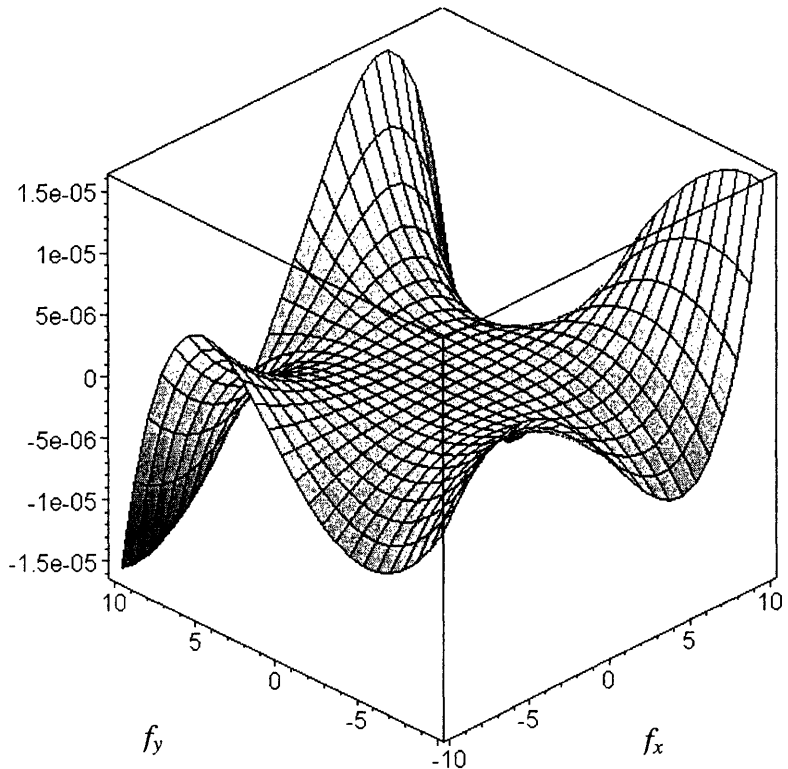
*Fig. 5.13a. Motion Stage Yaw vs. X force and Y force*



*Fig. 5.13b. Motion Stage Yaw vs. X force and Y force*



*Fig. 5.13c. Motion Stage Yaw vs. X force and Y force*



The contours of Fig. 5.13 show that the motions stage yaw in this case has reduced dramatically as compared to the previous design, over the specified range of motion. The maximum rotation here is approximately  $15 \mu\text{radians}$ , about 40 times less than earlier. Also it is visually evident from Fig. 5.13 b and c, that there is a relatively larger flat region in the middle of the contour. In fact, stage rotations of less than  $5 \mu\text{radians}$ , or 1 arc second are achievable within a motion range of  $\pm 0.08$ , or a force range of  $\pm 8$ . This, in fact, quantitatively confirms the conjecture made in Chapter 2, that symmetry in design and the additional rotational constraints should improve the motion stage yaw.

To further validate this analysis, we consider some special loading cases where the results are known from symmetry arguments, and compares these with the predictions of Fig. 5.13. Because of the geometric symmetry of the mechanism about its diagonal axis, for loads such that  $f_x = f_y$ , the motion stage yaw should be zero. This is exactly what is seen in Fig. 5.13 a. Furthermore, the two loading conditions,  $f_x=a$   $f_y=b$ , and  $f_x=b$   $f_y=a$ , should produce equal and opposite rotations of the motion stage. This agrees with the negative symmetry in the  $\theta_s$  contour about the  $+45^\circ$  line in the  $f_x - f_y$  plane, seen in Fig. 5.13.

Another important attribute to note is that the motion stage yaw due to any actuation load by itself is approximately zero, as opposed to the previous where the  $\theta_s$  and force relation was strongly non-linear

even in the absence of the second load. Thus, symmetry in the design results in better linearity and decoupling.

The next important performance metric to investigate is the sensitivity of motion stage to assembly errors and manufacturing tolerances. The most common form of assembly error is a lack of alignment between the actuator and the flexure axes, resulting in additional moments on the intermediate stage. To estimate the effect of such an alignment error we choose the worst loading situation in Fig. 5.13.  $f_x=10$  and  $f_y=-10$  correspond to the maximum  $\theta_s$  predicted within the range of motion. In this loading situation, the effect of a misalignment  $\varepsilon_x$  can be derived to be for this particular mechanism to be,

$$\theta_s = 0.000015558 + 0.00017\varepsilon_x$$

This expression is plotted in Fig. 5.14. It may be seen that a misalignment of 0.01, which corresponds to 600 microns in this case, results in a change of stage rotation by about 10%. With standard manufacturing and assembly techniques it is common to obtain tolerances within 100 microns.

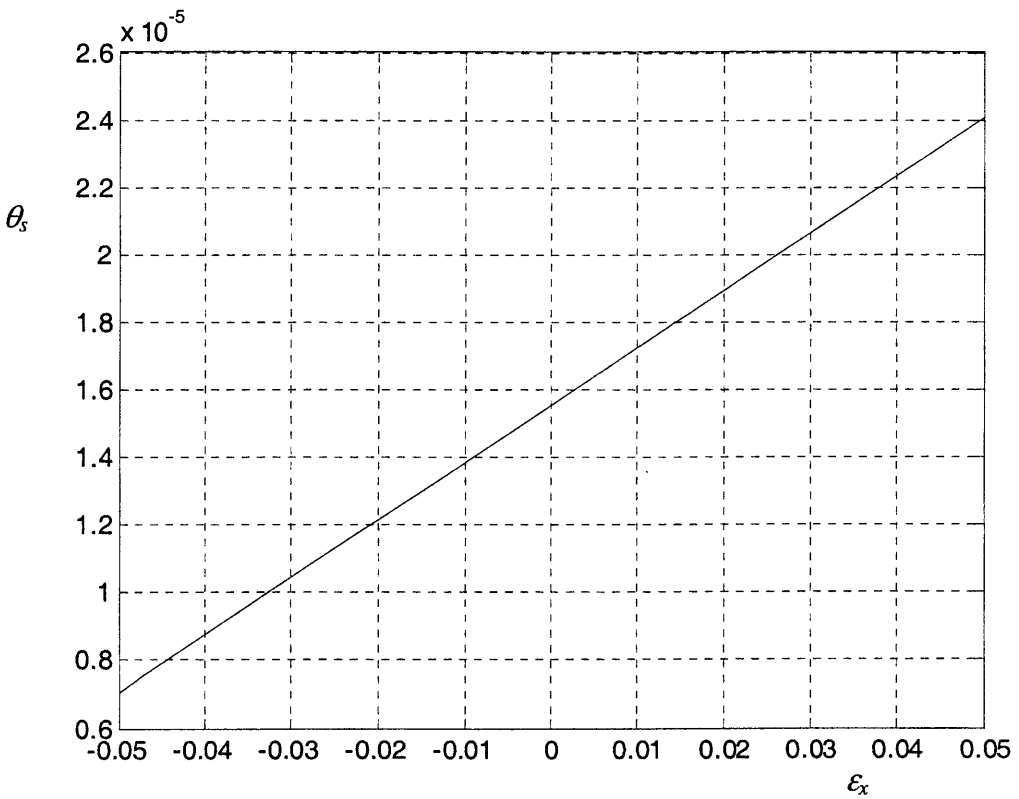


Fig. 5.14 Motion stage yaw vs. X actuator misalignment

We are also interested in determining the rotation of the intermediate stages 1 and 2 where the actuation forces are applied. The transverse rotation of these stages, which has already been derived earlier, and their yaw rotation dictates the choice of the decoupler design. One can do an identical analysis as above,

to predict the rotation of Stage 1. It can be shown that the center of stiffness with respect to stage 1 and X actuation force, lies a distance 0.1333 from the  $X_o$  axis. But the X actuation force location is governed by the requirement of motion stage rotation and therefore cannot be shifted. Thus, we have no other choice but to determine the Stage 1 rotation in response to an X force applied along  $X_o$ , and use this estimate in the decoupler design.

Fig. 5.15 presents the Stage 1 rotation  $\theta_1$  plotted over the entire range of X and Y forces. The maximum rotation is approximately 1 milliradian, or 3.5 arc minutes. Results for  $\theta_2$  are identical because of symmetry.

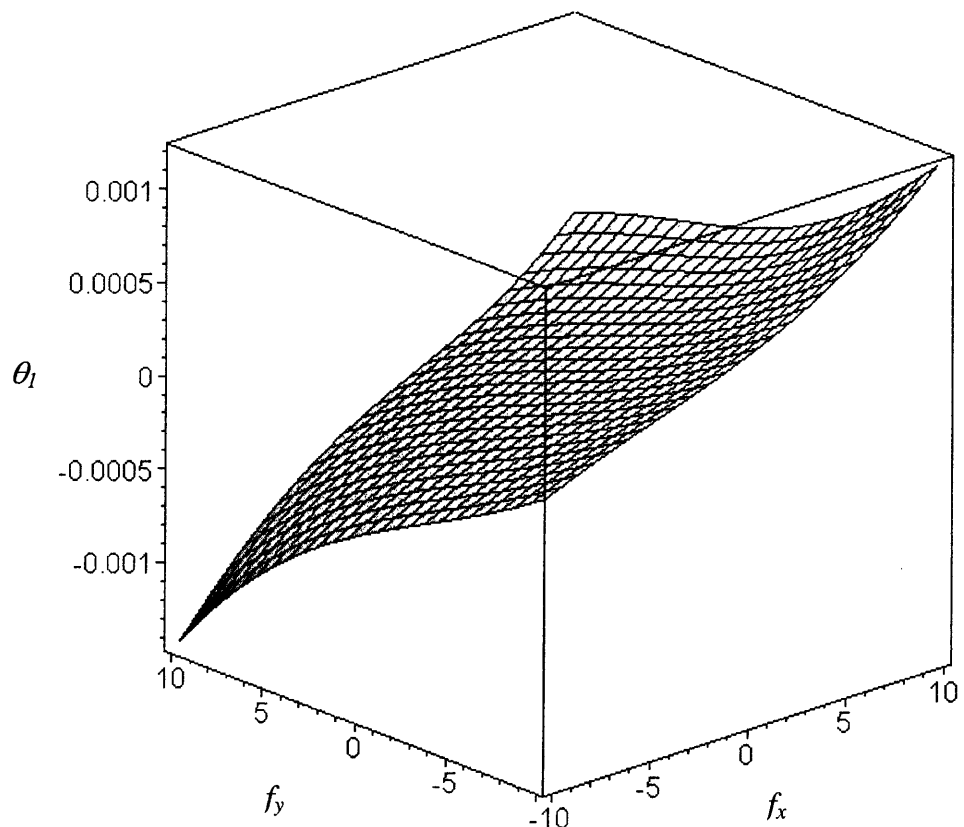


Fig 5.15 Stage 1 rotation versus  $f_x$  and  $f_y$

## 5.4 XY Flexure Mechanism Design 5

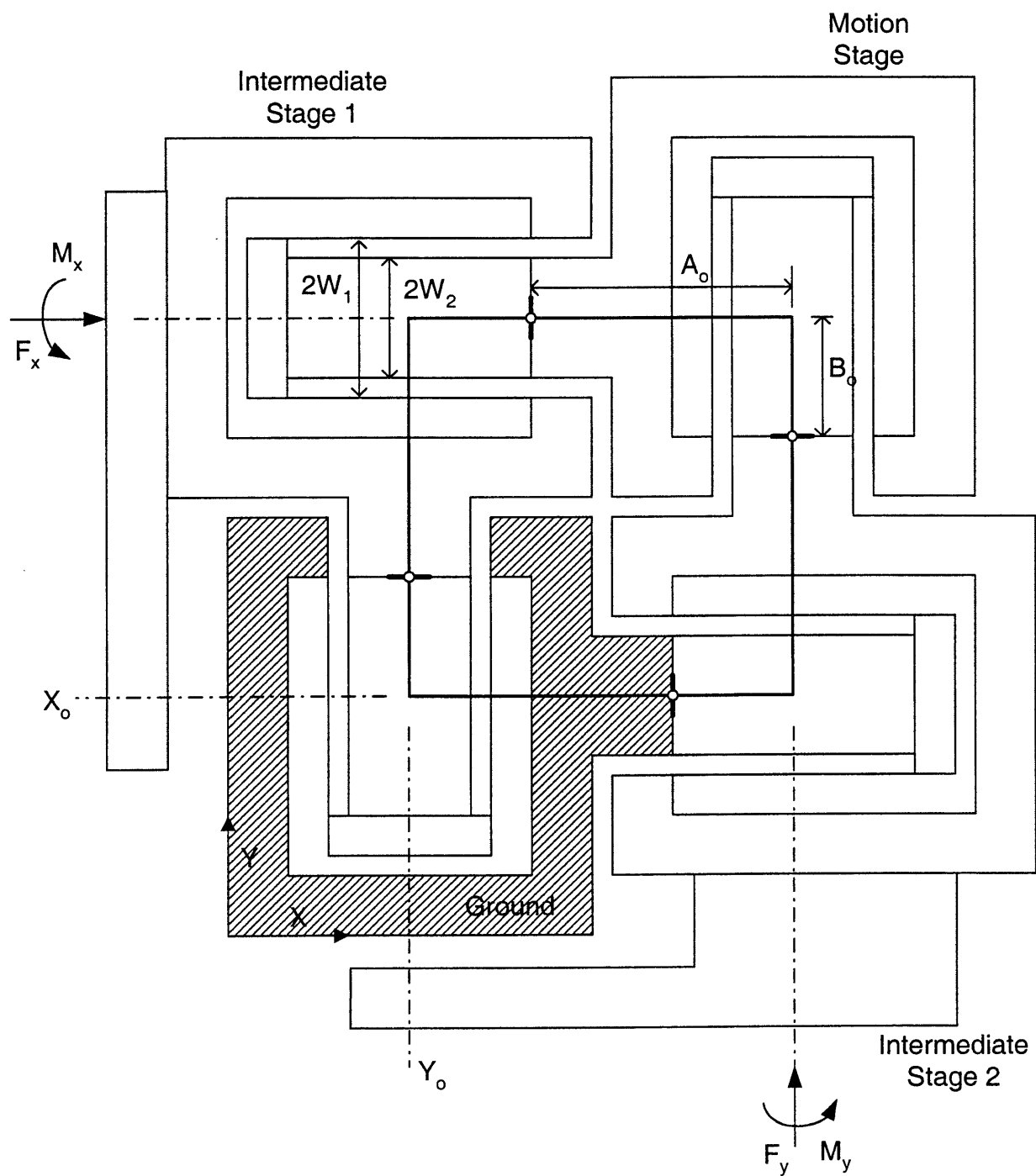


Fig. 5.16 XY Mechanism Design 5

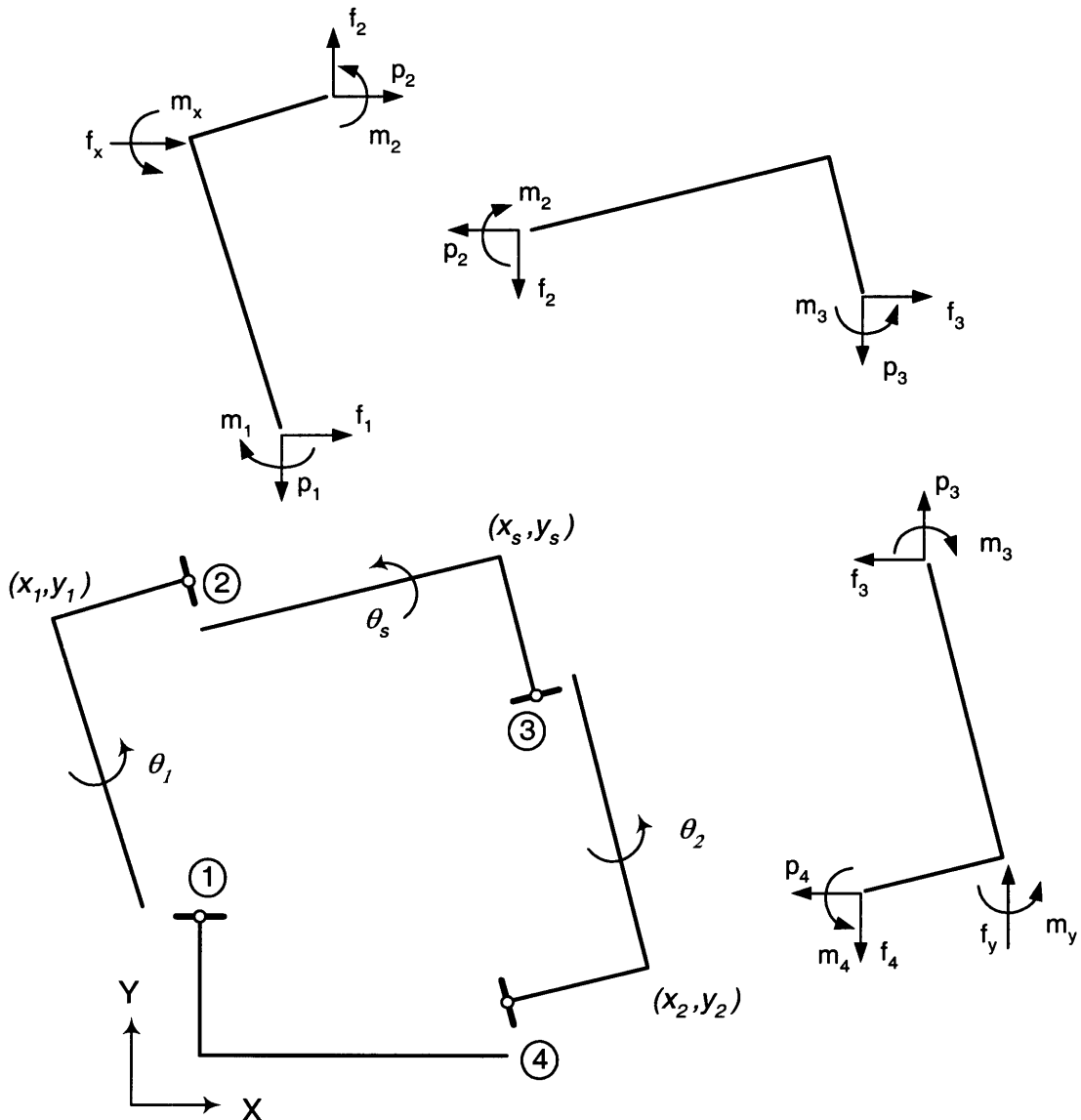


Fig. 5.17. Mechanism 5 in a deformed configuration and FBD of the stages

Fig. 5.16 presents yet another XY flexure mechanism design that was proposed earlier in Chapter 2. The rigid nodes including ground, motion stage and the two intermediate stages are represented by solid lines, while the compliance of the double parallelogram is represented by the small circles. Fig. 5.17 shows this mechanism in a deformed configuration, and the double parallelograms are indexes from 1 to 4. Free body diagrams of the three moving stages are also included on the sides. There are no explicit geometry constraints conditions here. The list of all relevant non-dimensional coefficients and normalized dimensions specific to this geometry is given below.

$a$	12	$e$	1.2	$i$	-0.6	$r$	1/700
$c$	-6	$h$	-0.1	$t$	1/60	$L$	60mm
$w_1$	0.25	$w_2$	0.20	$a_o$	1.3833	$b_o$	0.5

The optimal choice of  $a_o$  and  $b_o$ , which are the key geometric parameters of this design can be obtained by means of a linear analysis. These values minimize the rotation of the intermediate stages. But as mentioned earlier, the linear analysis does predict neither the parasitic and cross-axis error terms, nor the stiffness variation, all of which require the non-linear analysis that follows.

The general set of approximations set forth in Section 5.1 are applicable. Following the same sequence of steps as in the previous two cases, one can solve the constitutive relations for the constituent parallelogram flexure (4.15) – (4.17) and force equilibrium conditions simultaneously to obtain displacements summarized below.

$$x_s = \frac{8af_x}{(4a)^2 - (ef_y)^2} \quad y_s = \frac{8af_y}{(4a)^2 - (ef_x)^2} \quad (5.8)$$

$$x_l = \frac{8af_x}{(4a)^2 - (ef_y)^2} + \frac{y_2^2(ra - ei)f_x}{4a} \quad y_l = \frac{x_l^2(ra - ei)f_y}{4a} \quad (5.9)$$

$$y_2 = \frac{8af_y}{(4a)^2 - (ef_x)^2} + \frac{x_l^2(ra - ei)f_y}{4a} \quad x_2 = \frac{y_2^2(ra - ei)f_x}{4a} \quad (5.10)$$

Based on these results we can determine some of the attributes and performance measures of the XY mechanism under consideration.

1. The range of motion is better in this case because of the double parallelogram flexure constituent units. Alternatively, same range of motion can be achieved for half the stress levels and half the actuation forces. To achieve maximum motion of 0.1, the actuation force needed is 2.5, half of what was required in Design 3.
2. Primary motion stiffness in one direction drops as a weak quadratic function of the actuation force in the other direction. Over the maximum force of 2.5, or displacement of 0.1, the primary stiffness variation is less than 0.3 percent.
3. Cross-axes coupling in this case is minimal, and the elastokinematic errors arising between the double parallelogram units are taken up by the intermediate stages.
4. By achieving low cross-axes coupling, actuator isolation is compromised in this case. For example, intermediate stage 1 experiences both an X displacement as well as a Y displacement in response to the Y actuation force. The former is a consequence of the elastokinematic effects in double

parallelogram 2, while the latter results due to the elastokinematic effect in double parallelogram 1. Both these displacements are quantified in expression (5.9). The magnitude of Y displacement at the intermediate stage 1 is one of the contributing factors in the decoupler design. Over the range of displacements and forces in the mechanism, the maximum transverse motion seen by both the intermediate stages is approximately 0.0004. For a beam length of 60 mm, this corresponds to 24 microns. This is a fairly small number and is of the order of machining and assembly tolerances.

5. The inline stiffness between the X force and the motion stage is given by the axial stiffness double parallelogram 2.

$$\frac{\partial(x_l - x_s)}{\partial f_x} = \frac{1}{2d} + \frac{y_2^2(ra - ei)}{4a}$$

For the given mechanism geometry, this shows that the compliance increases by approximately 13 times, and the stiffness drops to less than 7 percent of the nominal value for a Y displacement of 0.1. This certainly is a drastic variation in the inline stiffness which is of concern as far as the system dynamics is concerned. It can be seen that if one uses the double parallelogram of Fig. 4.7 as the building block, then the only variable in the above expression is  $d$ , which depends on the blade thickness.  $r$ ,  $a$ ,  $e$  and  $i$  are all characteristic of the uniform beam constituting the double parallelogram, and change only when the beam shape changes.

6. No quantitative results are obtained for thermal sensitivity, but in general since the flexure units comprising the overall mechanism are insensitive to thermal disturbances, the mechanism itself is also expected to be good in terms rejecting these disturbances. The out of plane stiffness is low due to the relatively lower out of plane stiffness of the constituent flexure units, and due to the fact that the motion stage overhangs with support only from one side.

We next shift our attention to the internal moments and stage rotations. There are four unknown moments, one associated with each flexure unit interface, but only three moment balance equations from the FBDs of the three moving stages. But at the same time, there are three unknown rotations but four constitutive relationships, one associated with each flexure unit. One can therefore solve for all internal moment and stage rotations, by solving the seven equations simultaneously. The stage rotations thus obtained are very complicated expressions, as earlier, despite simplifications based on non-dimensional analysis.

The first objective is determine the center of stiffness with respect to the X and Y actuation. This step is similar to the previous two cases. The X moment required to keep the motion stage from rotating, given an X force, when there is no Y actuation is plotted in Fig. 5.18. The variation in the ratio between  $m_x$  and  $f_x$  is plotted in the  $dm_x/df_x$  plot in Fig. 5.19.

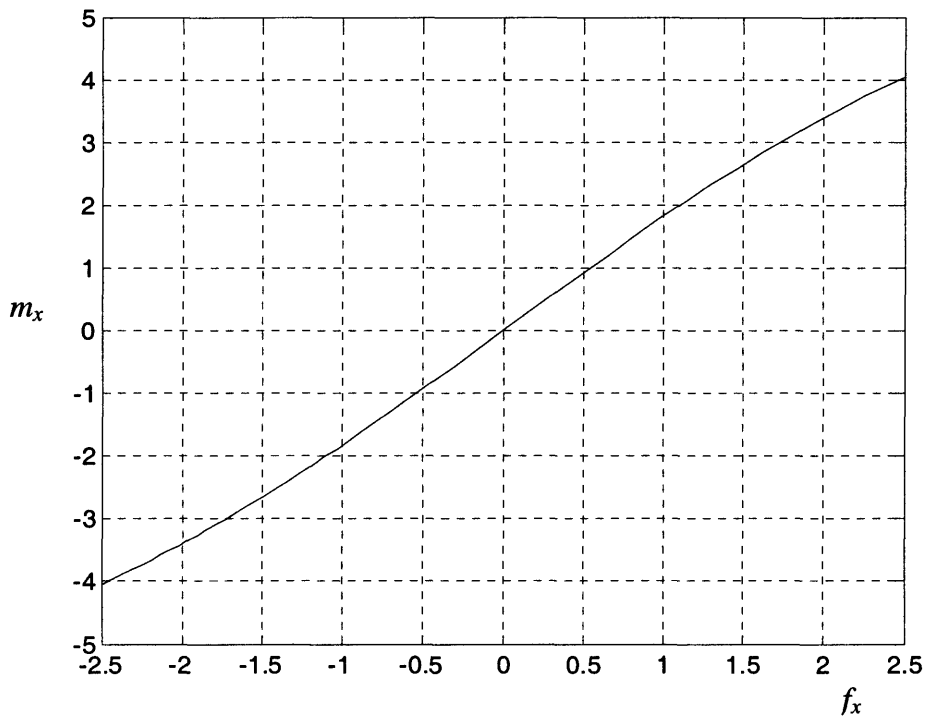


Fig. 5.17  $m_x$  required to maintain  $\theta_s=0$ , when  $f_y=m_y=0$

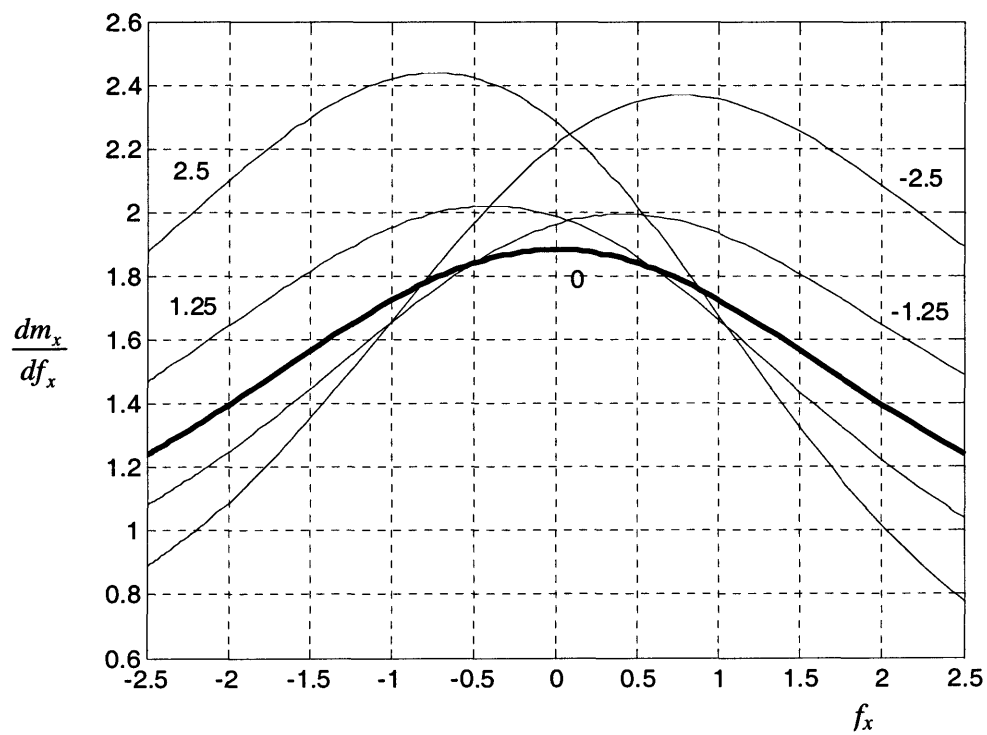


Fig. 5.18 Center of Stiffness for X actuation for different levels of  $f_y$

It can be shown that for no Y actuation, and small X forces, the center of stiffness is at a distance of  $a_o+b_o$  ( $=1.8833$ ) from the current force location. This corresponds to the  $X_o$  axis on Fig. 5.16. As the magnitude of the X force increases, the center of stiffness moves closer to the current location.

A similar analysis is carried out for the Y actuation as well. Note that in this case there is no symmetry about any diagonal axis, and therefore the results obtained with respect to Y actuation need not be identical to the above results. Nevertheless the center of stiffness for Y force, is determined to be  $a_o+b_o$  distance away from the current location. This corresponds to the  $Y_o$  axis on Fig. 5.16. Although the  $X_o$  and  $Y_o$  locations for force application do not eliminate the motion stage rotation, but given the constraints of the problem these are the best possible choices that are available. With this information, we return to Fig. 5.18 which also presents the variation in the center of stiffness with respect to X force, for different values of  $f_y$  applied along  $Y_o$ .

Given that forces are applied along the axes  $X_o$  and  $Y_o$ , we next determine the resulting motion stage rotation over the entire range of applied forces and resulting displacements. Fig. 5.19 plots the dependence of  $\theta_s$  on  $f_x$ , for different values of  $f_y$ . The coupling between the two axes in terms of rotations is quite evident here. Fig. 5.20 presents a series of 3D contours that illustrate the variation of  $\theta_s$  with both  $f_x$  and  $f_y$  over the entire range of applied forces. This also corresponds to a primary motion range of  $-0.1$  to  $0.1$ .

The maximum parasitic yaw error of the motion stage is about  $60 \mu\text{radians}$  or about  $12$  arc seconds. This is an order of magnitude less than the yaw errors of XY Mechanism Design 3. It is also worthwhile to note that while the displacement behavior of this design is significantly different from of Design 3, the stage rotation behavior is very similar for the two cases. This is due to the fact that while transverse and axial properties of a parallelogram and double parallelogram markedly differ, their rotational properties are very similar.

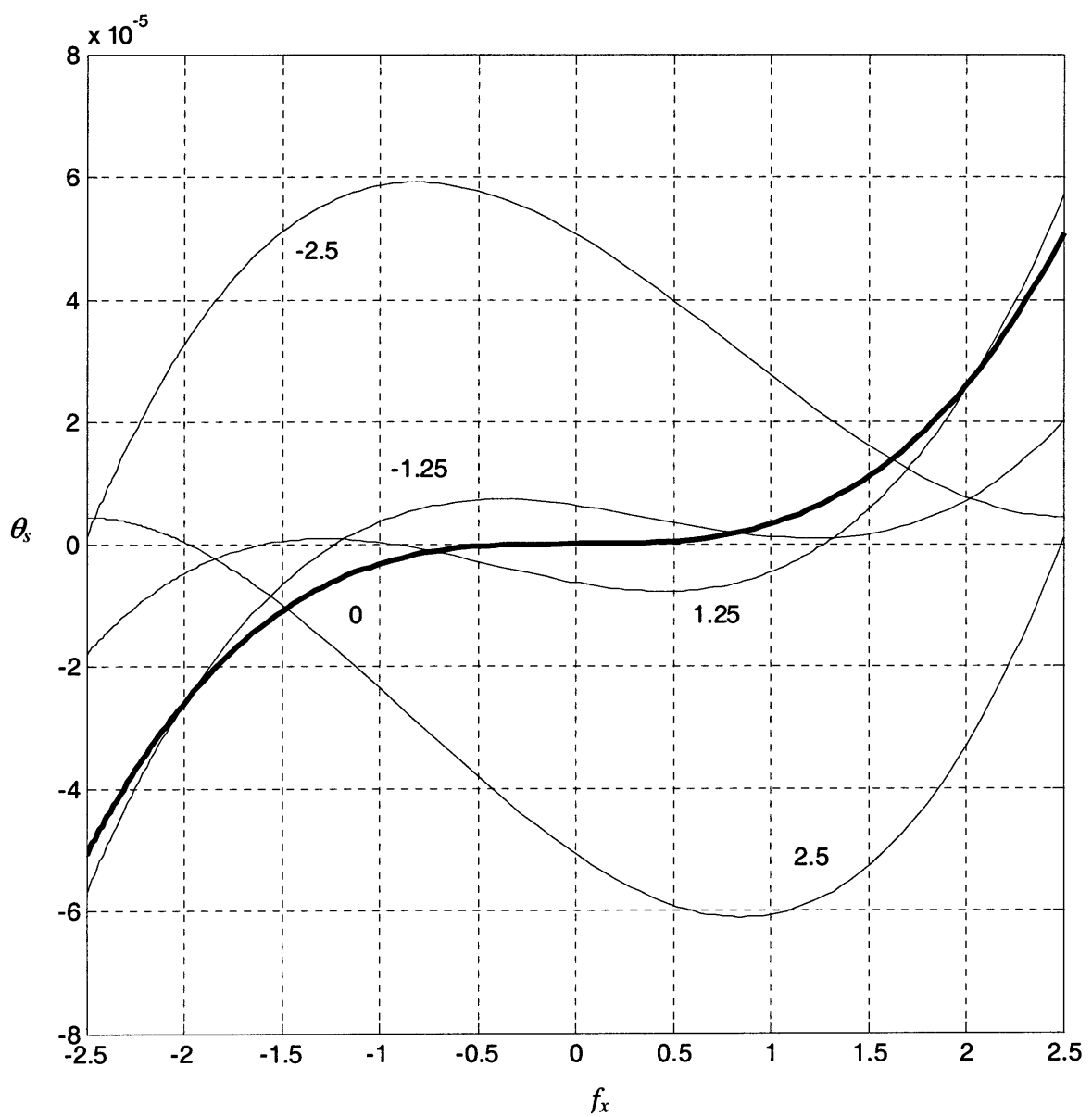
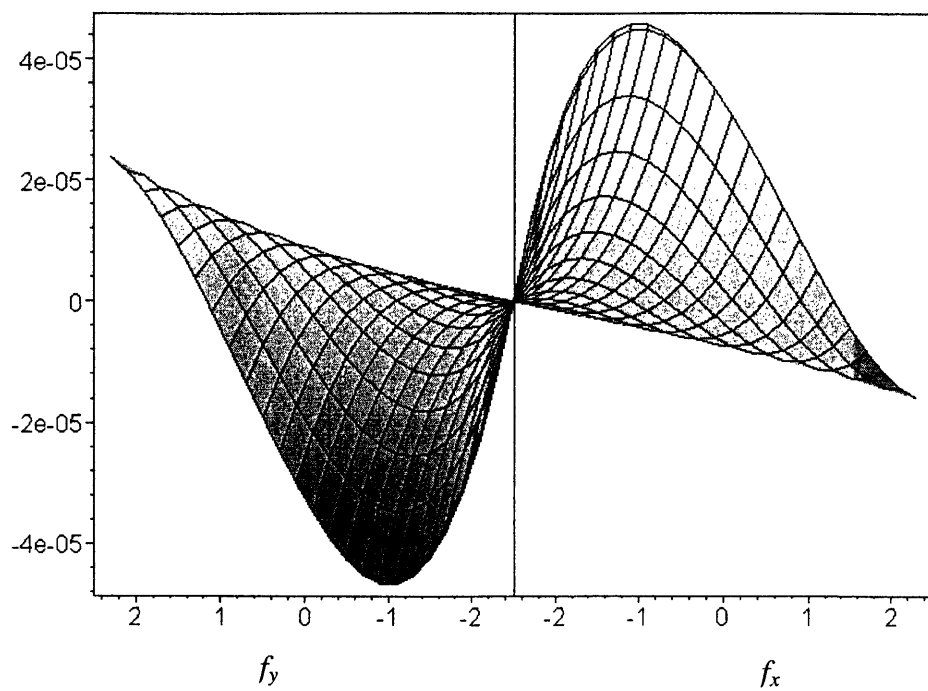
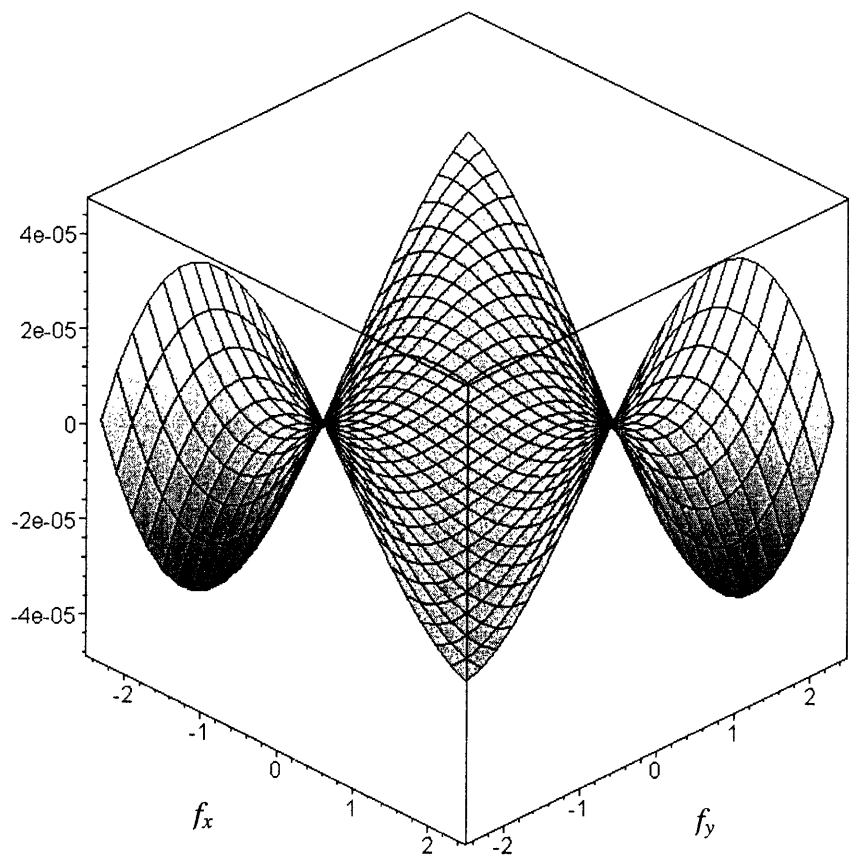


Fig. 5.19 Motion stage rotation versus  $f_x$  for different values of  $f_y$

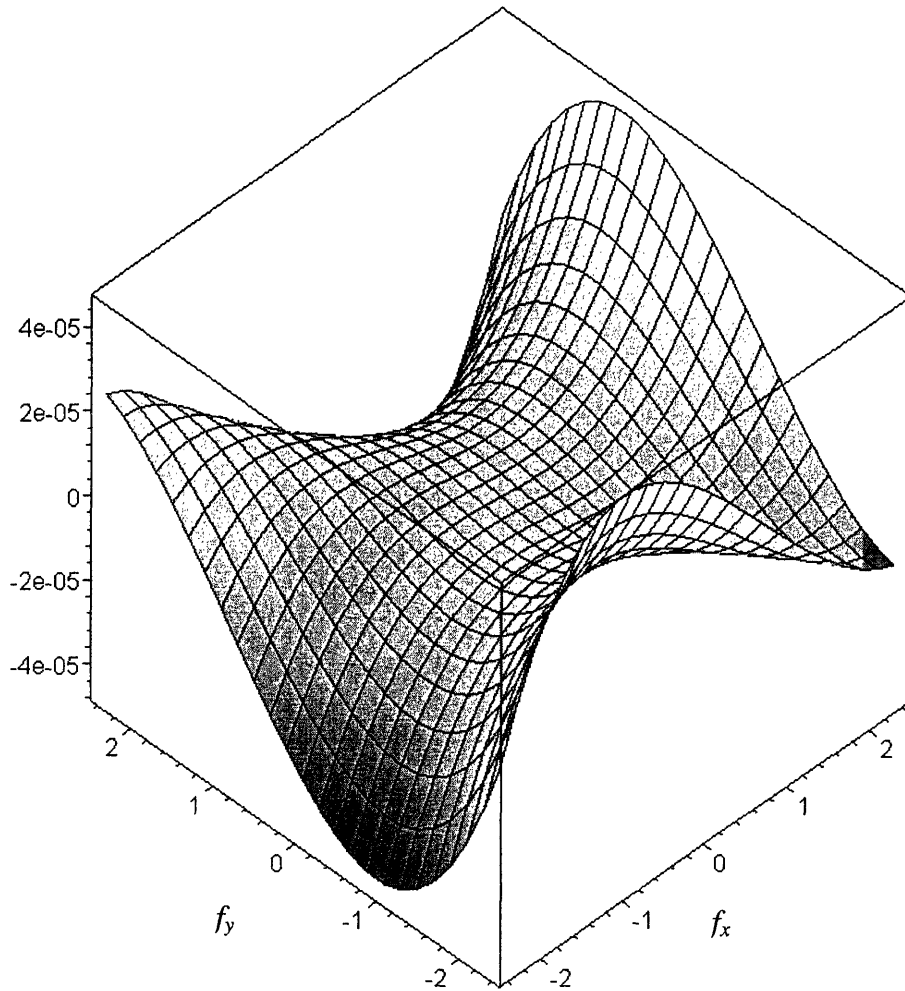
*Fig. 5.20a.*  
*Motion Stage*  
*Yaw vs. X*  
*force and Y*  
*force*



*Fig. 5.20b.*  
*Motion Stage*  
*Yaw vs. X*  
*force and Y*  
*force*



*Fig. 5.20c.*  
*Motion Stage*  
*Yaw vs. X*  
*force and Y*  
*force*



Sensitivity of the motion stage yaw to the location of center of stiffness may be determined as in the previous cases. This simulates assembly and manufacturing tolerances that cause a misalignment between the flexure axis and the actuator axis.

The maximum rotation of  $6e-5$  occurs for the loading situation  $f_x=0.8$  and  $f_y=2.5$ . The change in this rotation, corresponding to a misalignment  $\varepsilon_x$  between the X force and  $X_o$  axis, is given by

$$\theta_s = 0.000057627 \varepsilon_x - 0.0000611$$

This relationship is plotted in Fig. 5.21, and indicates a less than 1% change in the yaw motion due to a misalignment of 0.01.

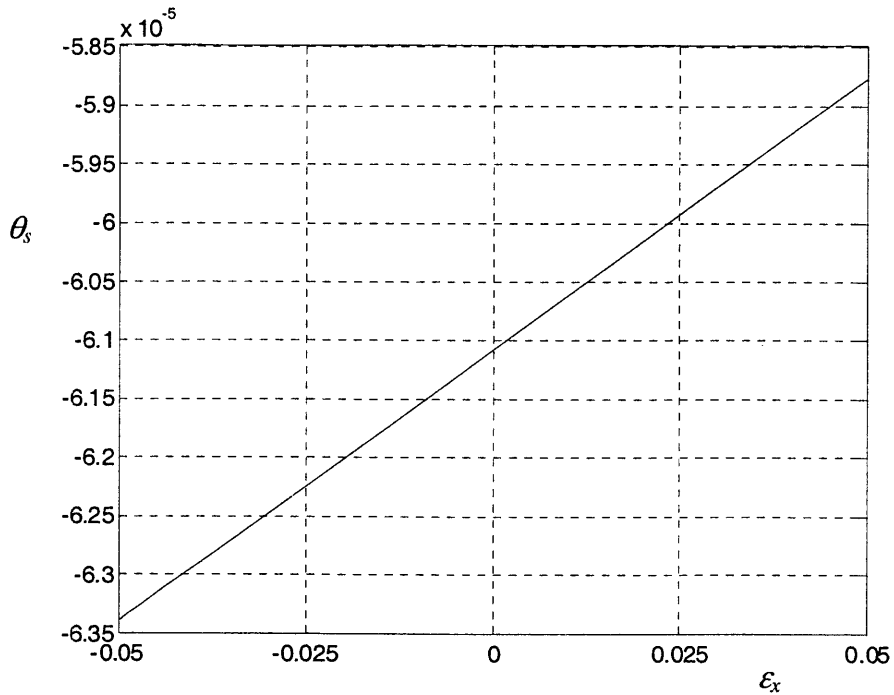
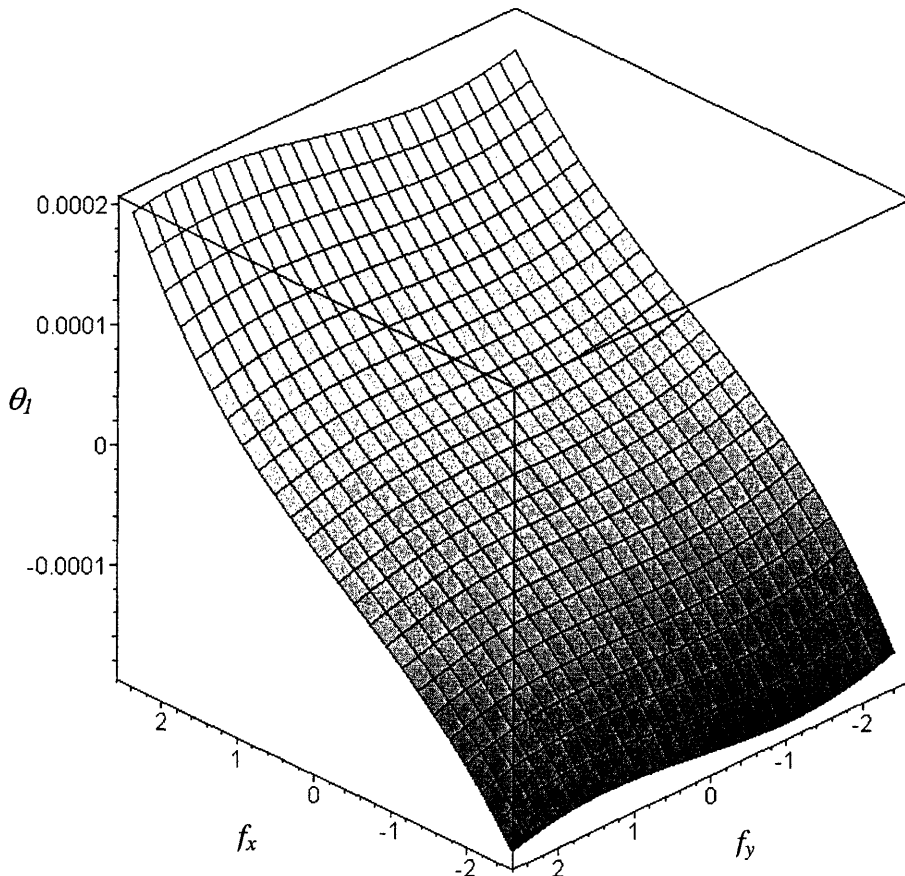


Fig. 5.21 Motion stage yaw vs. X actuator misalignment

The final result that we seek is the rotation of the intermediate stages. This is done in a fashion similar to the determination of the motion stage. It is found that the center of stiffness for X force with respect to rotation of Intermediate stage 1 is located at a distance  $1.2555$  from the original location, and center of stiffness of Y force with respect to Stage 1 rotation is located at  $-1.8833$ , which actually corresponds to the  $Y_o$  axis. With respect to stage 2, the center of stiffness for X force is located at distance  $3.76$  and for Y force is located at distance  $-0.6278$ , measured from the original location. A force location that results in positive moment, following the convention of Fig. 5.16 is deemed positive, and vice versa.

The rotation of Stage 1 is plotted over the entire range of X and Y forces in Fig. 5.22. Since the forces are applied at the center of stiffness with respect to Motion Stage and not Stage 1, the rotation of Stage 1 is as large as 200 microradians. In particular, it is interesting to note that the variation with  $f_y$  is far smaller than that with  $f_x$ . This is due to the fact that the center of stiffness for Y actuation forces is the same with respect to Motion Stage as well as Stage 1.



*Fig 5.22 Stage 1 rotation versus  $f_x$  and  $f_y$*

Similarly, the rotation of Stage 2 is plotted in Fig. 5.23, over the entire range of forces that correspond to a maximum displacement of 0.1. The maximum rotation observed here is higher as compared to Stage 1, which is due to the fact that both the actuation forces contribute to the Stage 2 rotation. Since there isn't a perfect symmetry between the two intermediate stages, the center of stiffness of both are entirely different, and therefore the rotations of the two stages are also different. This is unlike XY Mechanism Designs 3 and 4, where intermediate Stages 1 and 2 enjoyed perfect symmetry, and therefore exhibited identical behavior.

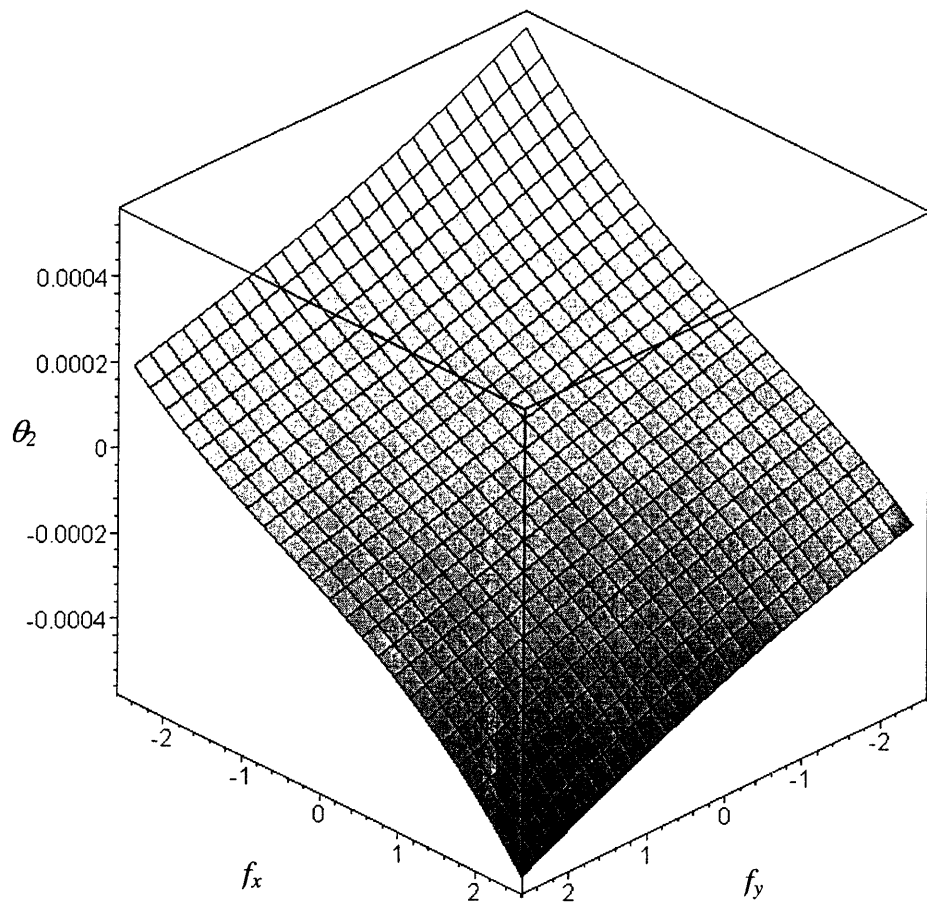


Fig5.23 Stage2 rotation versus  $f_x$  and  $f_y$

## 5.5 XY Flexure Mechanism Design 6

Finally, we arrive at a balanced version of the XY Flexure Mechanism design based on double parallelogram flexure units, as illustrated in Fig.5.23, and earlier in Fig. 2.15. Because of its symmetry we do expect this design to perform better than the previous one, at least in some aspects if not all.

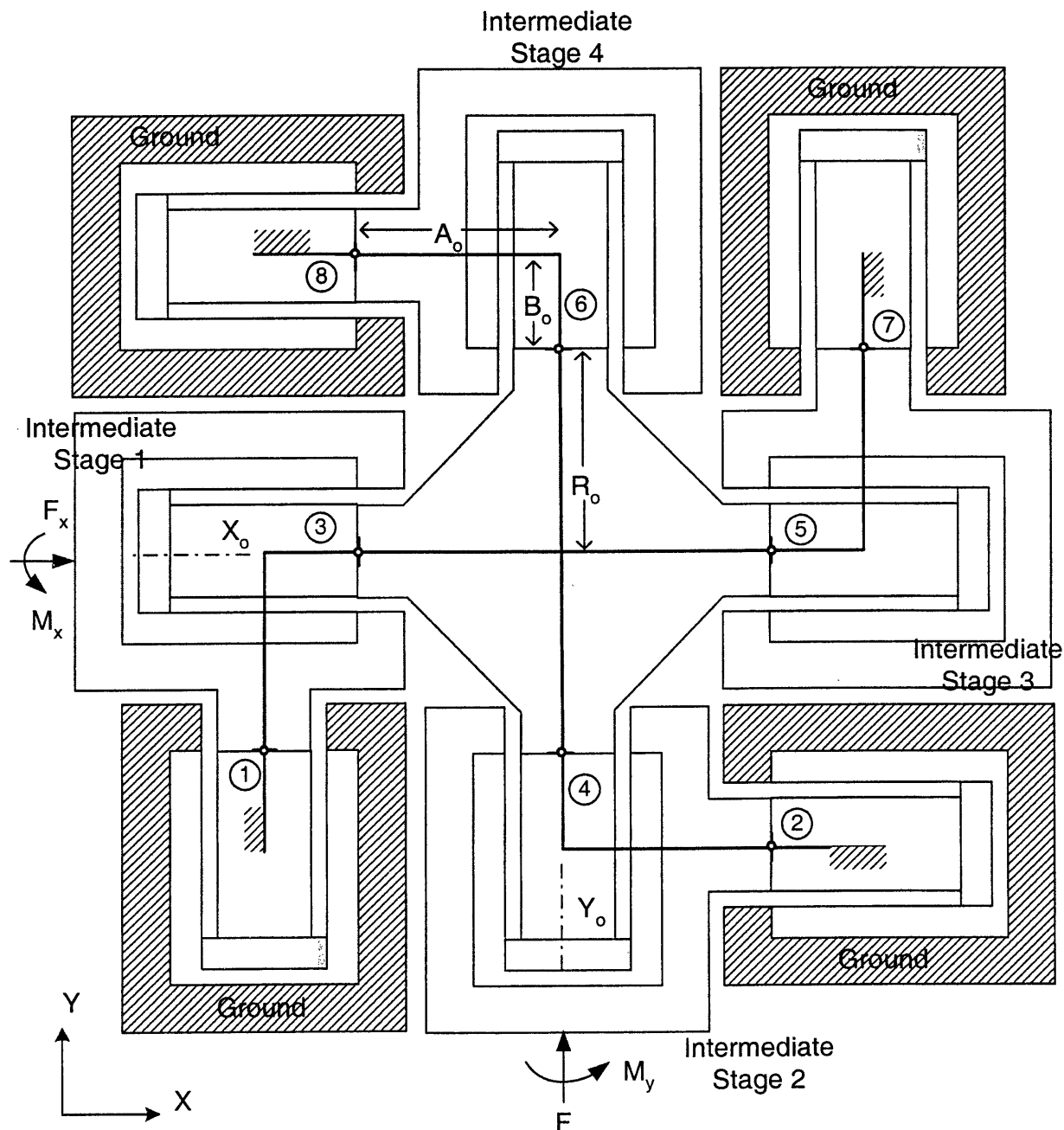


Fig. 5.23 XY Flexure Mechanism 5

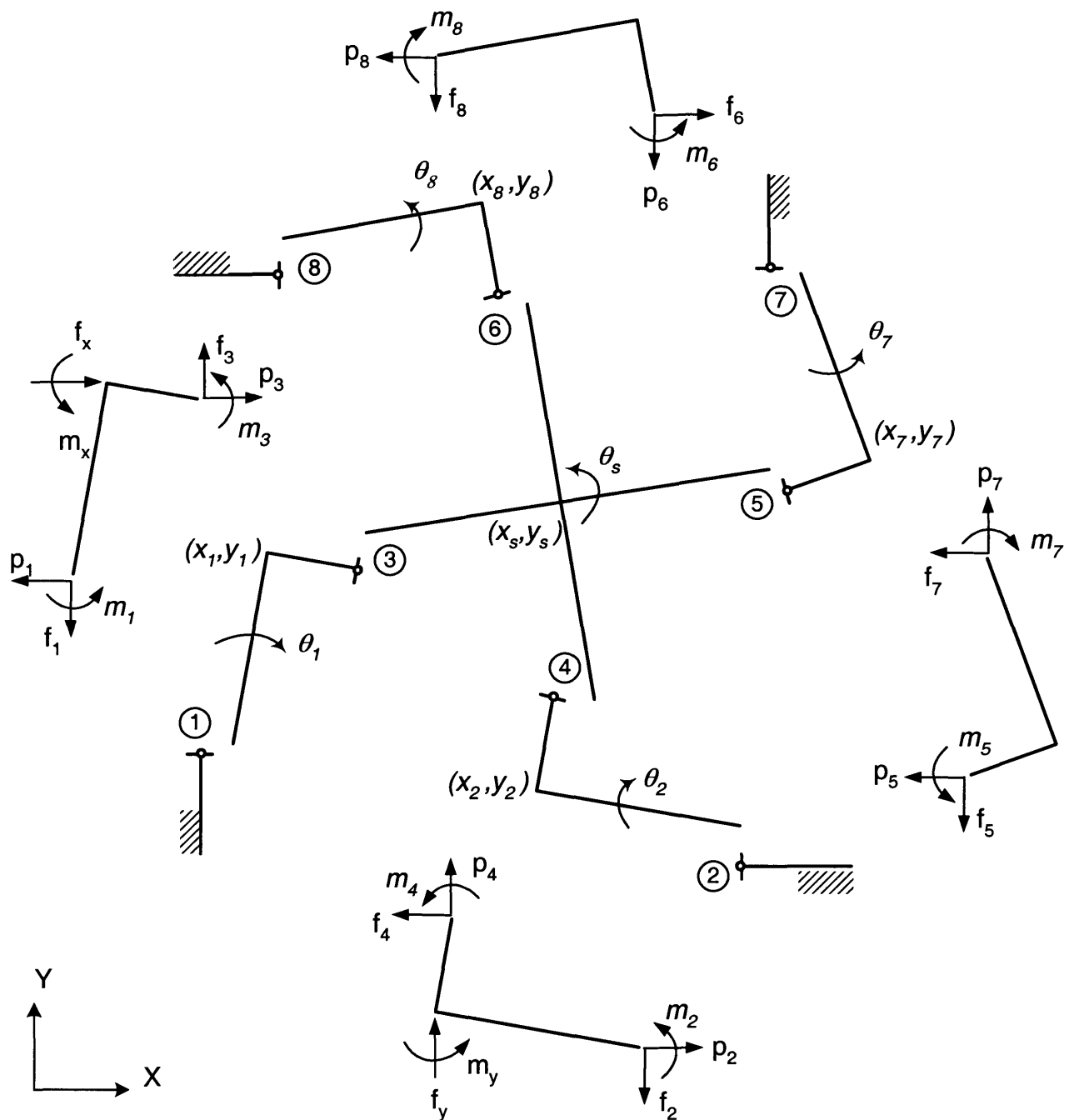


Fig. 5.24 XY Mechanism 5 in a deformed configuration, and FBDs of intermediate stages

Fig. 5.23 shows the overall mechanism along with a stick-figure representation of the constituent double parallelogram units. The rigid motion stage and intermediate stages are represented by solid lines, whereas all the compliance of the flexure units is represented by the small circles at the interface of the rigid nodes. Visually, it is obvious that space utilization in this design is best so far, and therefore it should be able to provide good specific range. Fig.5.24 shows the same mechanism in its deformed configuration, and the relative displacements of each rigid node along the XY axes. Conditions of geometric compatibility are implicit and force equilibrium conditions for the five rigid stages maybe obtained from the Free Body Diagrams of each, also shown in the same figure. The constitutive relationships for each double parallelogram unit is given by [ref] in Chapter 4. General approximations set forth in Section 5.1 also apply here. The non-dimensional coefficients are same as earlier, and the specific dimensions used in this design, and normalized with respect to a beam length of  $L=47.5mm$ , are listed below.

$a$	12	$e$	1.2	$i$	-0.6	$r$	1/700
$c$	-6	$h$	-0.1	$t$	1/76	$r_o$	0.9737
$w_1$	0.3816	$w_2$	0.2632	$a_o$	0.9737	$b_o$	0.5

Solving the constitutive relations, and the geometric and force equilibrium conditions simultaneously and simplifying the analysis based on the engineering approximations, the following displacement results are obtained.

$$x_s = \frac{f_x}{4a} \frac{64a^2}{(64a^2 - 3e^2 f_y^2)} + \frac{f_x}{4a} \frac{y_2^2 e^3 i f_y^2}{(64a^2 - 3e^2 f_y^2)} \approx \frac{f_x}{4a} \frac{1}{1 - \frac{3e^2 f_y^2}{64a^2}} \quad (5.11)$$

$$y_s = \frac{f_y}{4a} \frac{64a^2}{(64a^2 - 3e^2 f_x^2)} + \frac{f_y}{4a} \frac{x_1^2 e^3 i}{(64a^2 - 3e^2 f_x^2)} \approx \frac{f_y}{4a} \frac{1}{1 - \frac{3e^2 f_x^2}{64a^2}}$$

$$x_1 = \frac{f_x}{4a} \frac{64a^2}{(64a^2 - 3e^2 f_y^2)} - \frac{f_x}{8a} \frac{y_2^2 e i (192a^2 - 11e f_y^2)}{(64a^2 - 3e^2 f_y^2)} \approx \frac{f_x}{4a} \frac{64a^2}{(64a^2 - 3e^2 f_y^2)} - \frac{3f_x y_2^2 e i}{8a} \quad (5.12)$$

$$x_7 = \frac{f_x}{4a} \frac{64a^2}{(64a^2 - 3e^2 f_y^2)} + \frac{f_x}{8a} \frac{y_2^2 e i (64a^2 - e f_y^2)}{(64a^2 - 3e^2 f_y^2)} \approx \frac{f_x}{4a} \frac{64a^2}{(64a^2 - 3e^2 f_y^2)} + \frac{f_x y_2^2 e i}{8a}$$

$$y_1 = \frac{f_y x_1^2 e i}{8a} \quad y_7 = -\frac{f_y x_1^2 e i}{8a} \quad (5.13)$$

$$y_2 = \frac{f_y}{4a} \frac{64a^2}{(64a^2 - 3e^2 f_x^2)} - \frac{f_y}{8a} \frac{x_l^2 ei (192a^2 - 11ef_x^2)}{(64a^2 - 3e^2 f_x^2)} \approx \frac{f_y}{4a} \frac{64a^2}{(64a^2 - 3e^2 f_x^2)} - \frac{3f_y x_l^2 ei}{8a} \quad (5.14)$$

$$y_8 = \frac{f_y}{4a} \frac{64a^2}{(64a^2 - 3e^2 f_x^2)} + \frac{f_y}{8a} \frac{x_l^2 ei (64a^2 - ef_x^2)}{(64a^2 - 3e^2 f_x^2)} \approx \frac{f_y}{4a} \frac{64a^2}{(64a^2 - 3e^2 f_x^2)} + \frac{f_y x_l^2 ei}{8a}$$

$$x_2 = -\frac{f_x y_2^2 ei}{8a} \quad x_8 = \frac{f_x y_2^2 ei}{8a} \quad (5.15)$$

The following observations may be made based on these results.

1. Assuming a primary motion of 0.1, we see that the maximum stresses generated in the beams in this case are half as compared to XY Design 4. The force required to generate this motion is approximately 5, which is also half of that required in Design 4, and twice that in Design 5, for obvious reasons. It may be noticed in (5.11) that the stiffness in a primary direction, say X, changes with the application of a Y force. This is expected because as one applies the Y force, flexure units 4, 6 and 7 experience a compressive axial force, while unit 1 sees a tensile axial force. Irrespective of whether the axial force is tensile or compressive, the transverse stiffness of all these units drop resulting in an overall all change in the primary motion stiffness. But over the full range of force and displacements, the drop in primary stiffness is as small as 1.2%.
2. The cross-axes coupling is reduced because of symmetry. While there are no purely elastic or purely kinematic terms, there do exist elastokinematic error terms associated the double parallelogram. These error terms do not show up at the motion stage, and instead are absorbed by the intermediate stages. In expression (5.11), the higher order elastokinematic term represents the error associated the change in primary motion due to reduced primary stiffness, and is approximately 6400 times smaller than the primary term.
3. Actuator isolation is not perfect and is comparable to the previous design. Intermediate stage 1 experiences an additional X displacement arising from the elastokinematic effect of flexure unit 3, in the presence of an X actuation force and Y primary motion. It also has a Y displacement resulting from the elastokinematic effect of flexure unit 1, in the presence of a Y actuation force and X primary motion. The latter is given by expression (5.13), and is approximately 4e-4, which corresponds to 20 microns for the given dimensions. In expressions (5.12) and (5.14), the higher order elastokinematic terms may be dropped because they are about two orders smaller than the next larger terms.

4. As in the previous case, since the constituent flexures in this design are double parallelogram flexures, the inline stiffness between the actuator and motion suffers significantly. The compliance of the flexure unit 3, which connects the intermediate stage 1 and the motion stage.

$$\frac{\partial(x_l - x_s)}{\partial f_x} = \frac{3}{8} \left( \frac{1}{d} + \frac{y_2^2(r_a - e_i)}{2a} \right) \quad (5.16)$$

For the given dimensions, this corresponds to an increase in compliance by approximately 20 times, and a stiffness drop of 95% from for a primary Y displacement of 0.1. This variation in stiffness plays an important role in dynamic characteristics of this mechanism. Furthermore, with the given double parallelogram geometry the only variable is the beam thickness, which determines  $d$ . All other parameters are the geometric properties of the double parallelogram flexure of Fig. 4.7.

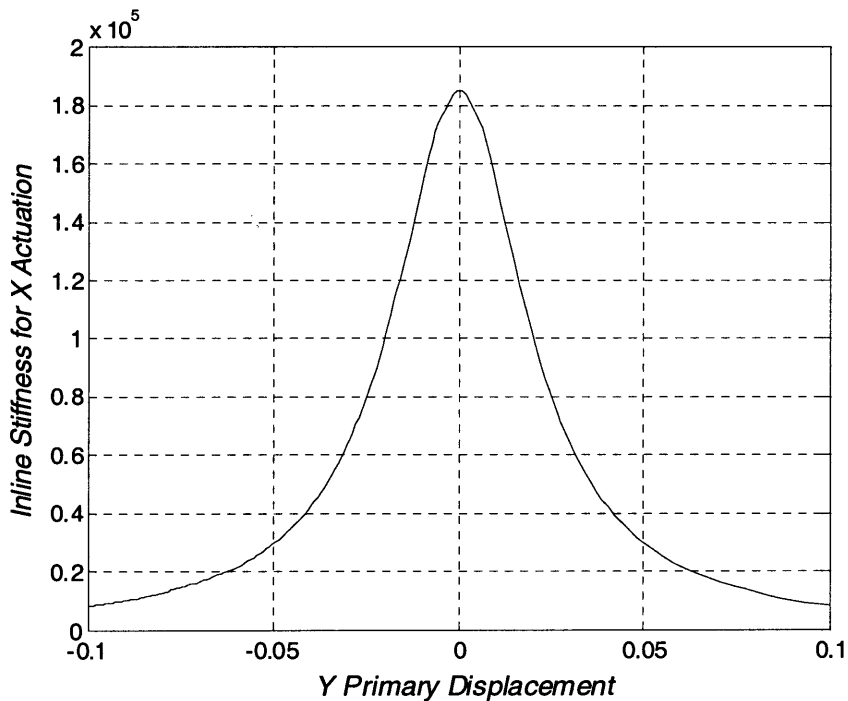


Fig. 5.25 Variation of X Actuation inline stiffness with primary displacement Y

Next, we consider the rotations of the motion stage and intermediate stages. As earlier, the primary objective is to determine the locations of X and Y actuation forces to minimize the motion stage parasitic yaw. The procedure followed here is identical to the previous three cases. The motion stage rotation can be obtained in terms of the four loads as  $\theta_3 = fn_3(f_x, m_x, f_y = 0, m_y = 0)$ .

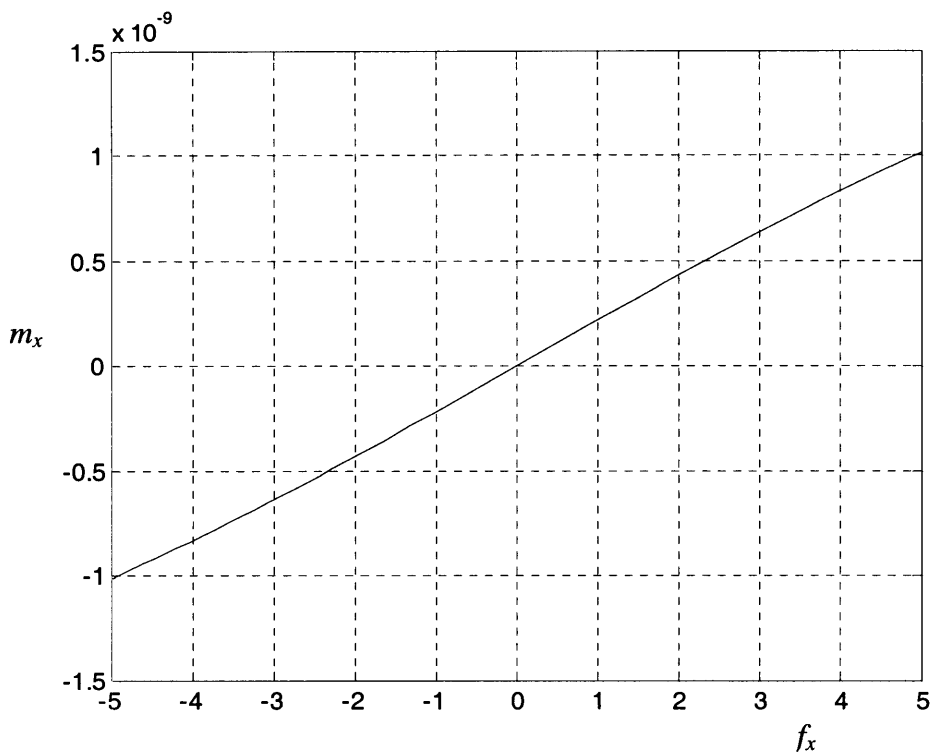


Fig. 5.26  $m_x$  required to maintain  $\theta_s=0$ , when  $f_y=m_y=0$

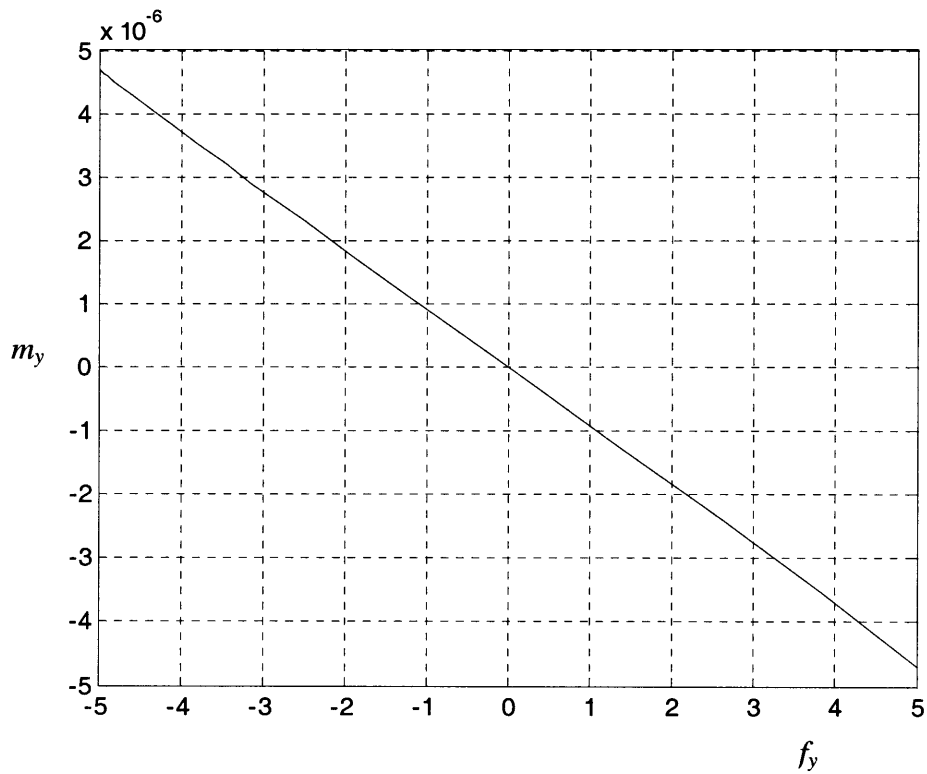


Fig. 5.27  $m_y$  required to maintain  $\theta_s=0$ , when  $f_x=m_x=0$

The equation  $fn_3(f_x, m_x, f_y = 0, m_y = 0) = 0$  is then solved for  $m_x$ , to determine the  $m_x$  needed to keep  $\theta_s$  zero for a given  $f_x$ , when there are no Y loads. This function is plotted in Fig. 5.26, and is seen to be very small over the entire range of X force. Thus, the ratio between  $m_x$  and  $f_x$  necessary to eliminate  $\theta_s$  is close to zero in the absence of Y loads. This leads to the conclusion that the current location of the X force, acting along axis  $X_o$  is the best choice. An identical analysis is done to determine that the current location of Y force along the  $Y_o$  axis also coincides with the center of stiffness for Y actuation with respect to the motion stage, in the absence of X loading. Fig. 5.27 presents the Y moment  $m_y$  that is necessary to keep the motion stage rotation zero for a given Y force  $f_y$ .

The above conclusions change when loading is applied along the other axis. For example the variation in the center of stiffness for X actuation for different levels of  $f_y$  is provided by the  $dm_x/df_x$  plot in Fig. 5.28.

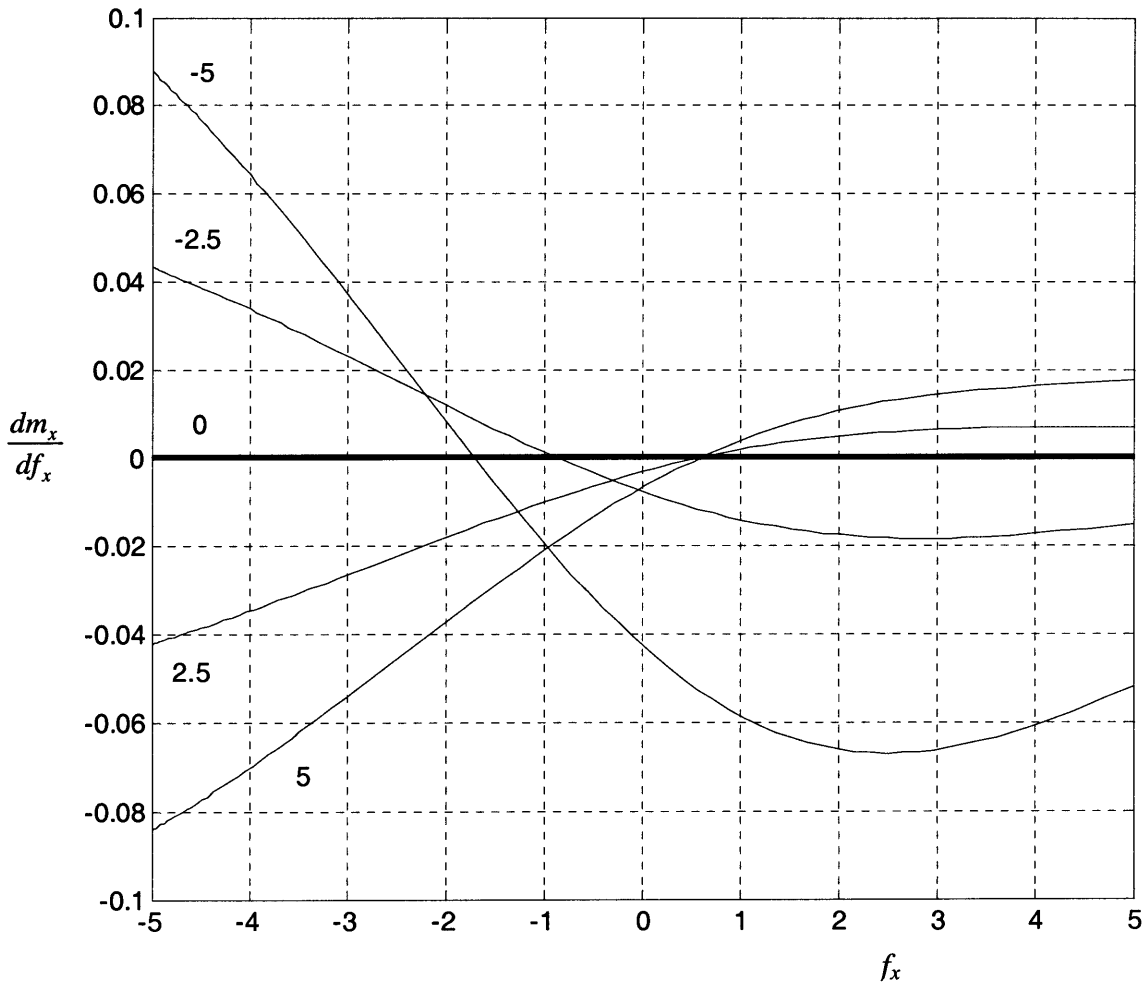


Fig. 5.28 Center of Stiffness for X actuation for different levels of  $f_y$

Fig. 5.28 tells us that in the presence of the maximum Y force,  $f_y = 5$ , the ideal location for X actuation shifts by 0.08, which for the given dimensions corresponds to approximately 4 mm. Similar results are obtained for the Y actuation in Fig. 5.29.

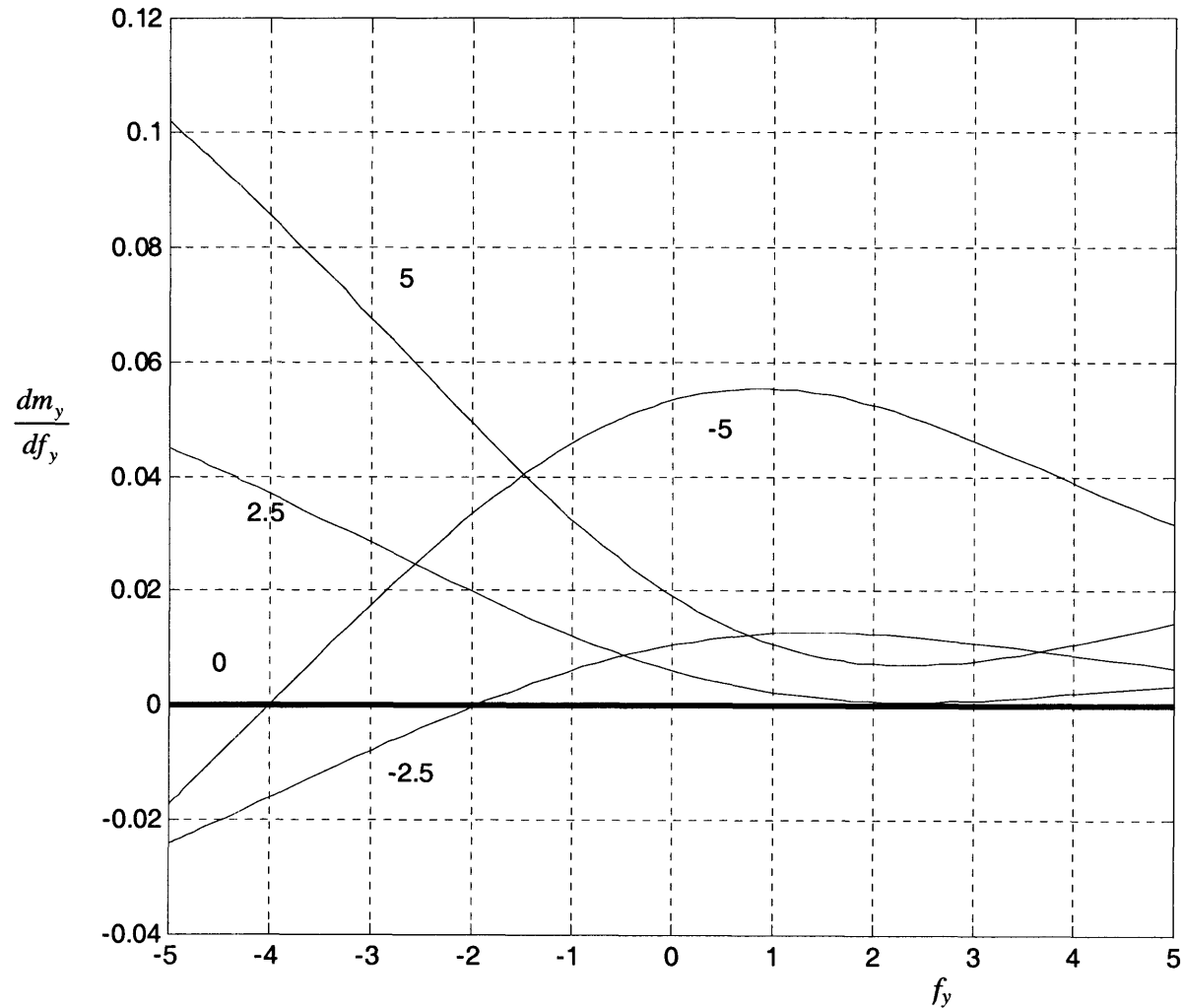


Fig. 5.29 Center of Stiffness for Y actuation for different levels of  $f_x$

Figures 5.28 and 5.29 reflect the extent of coupling between the two axes as far as stage rotations are concerned.

We next proceed to determine the actual motion stage rotation over the entire range of applied forces  $f_x$  and  $f_y$ , applied along the axes  $X_o$  and  $Y_o$ , respectively. Fig. 5.30 shows the dependence of  $\theta_s$  on  $f_x$  for different values of  $f_y$ , and Fig. 5.31 shows the dependence of  $\theta_s$  on  $f_y$  for different values of  $f_x$ . The coupling between the two axes in terms of rotations is once again quite evident here. Fig. 5.32 presents a series of 3D contours that illustrate the variation of  $\theta_s$  with both over the entire range of applied forces, and provides a better understanding of the motion stage rotation. Results are plotted for force range of +/- 5, which corresponds to a motion range of +/- 0.1.

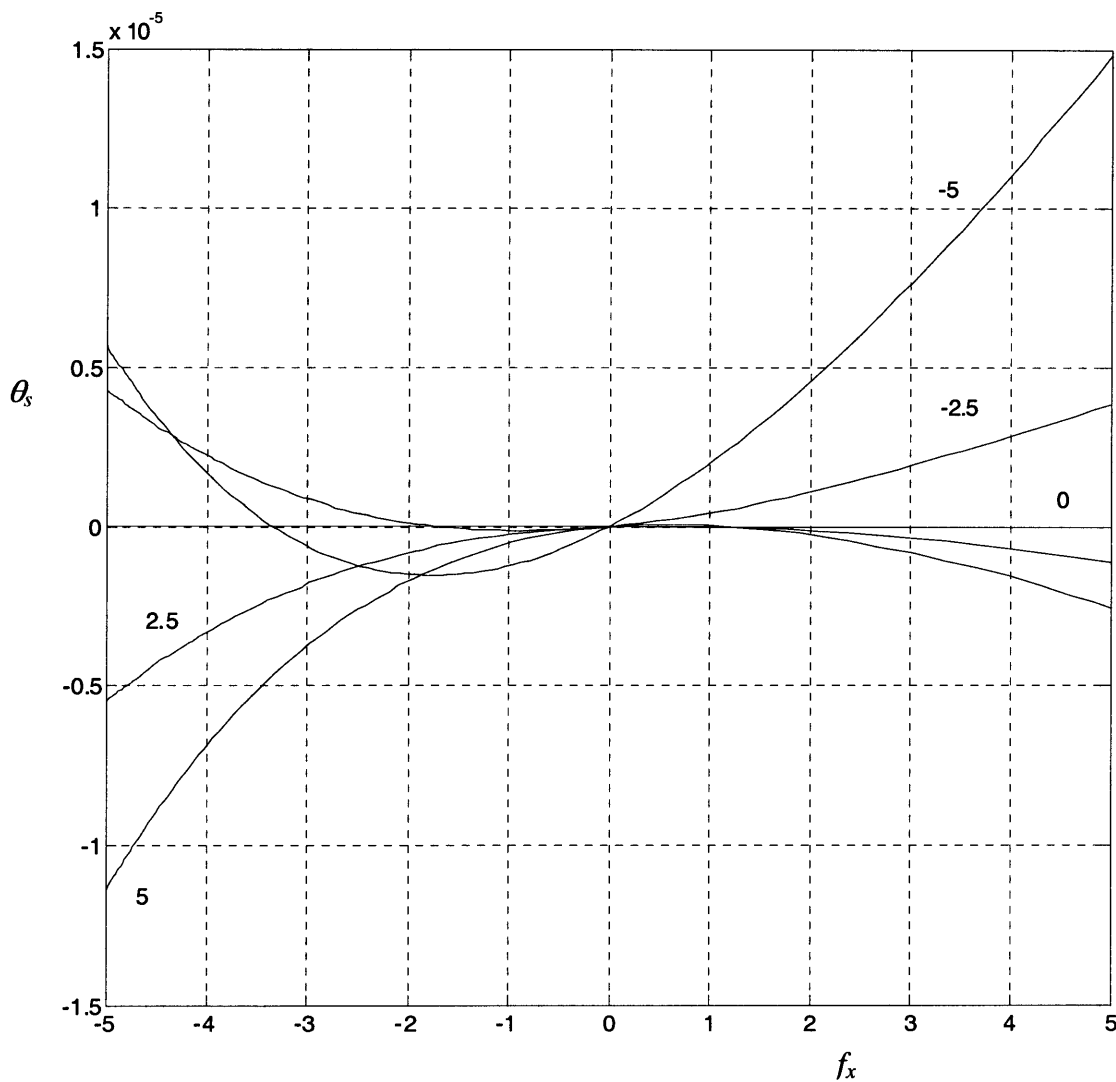


Fig. 5.30 Motion stage rotation versus  $f_x$  for different values of  $f_y$

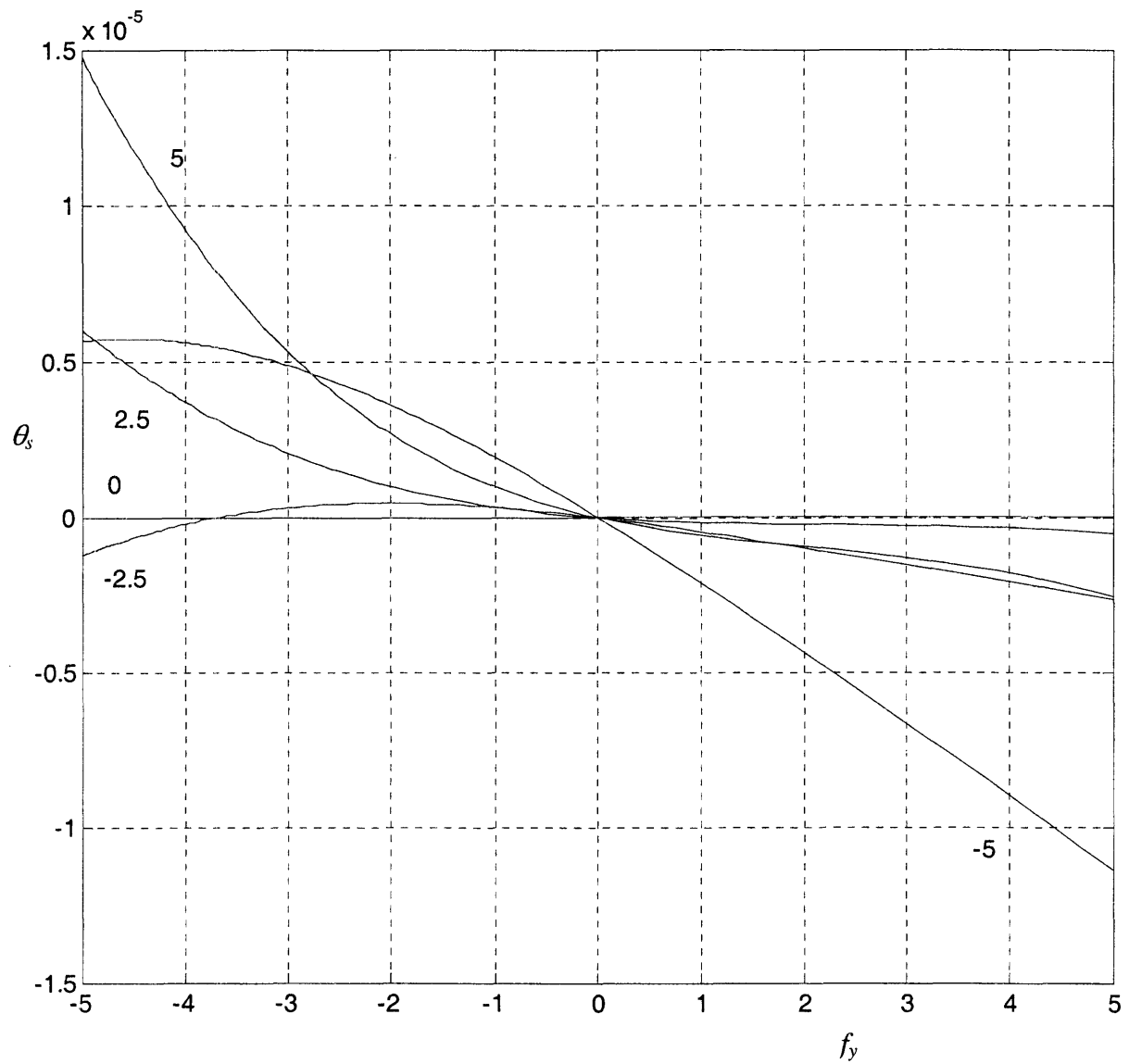
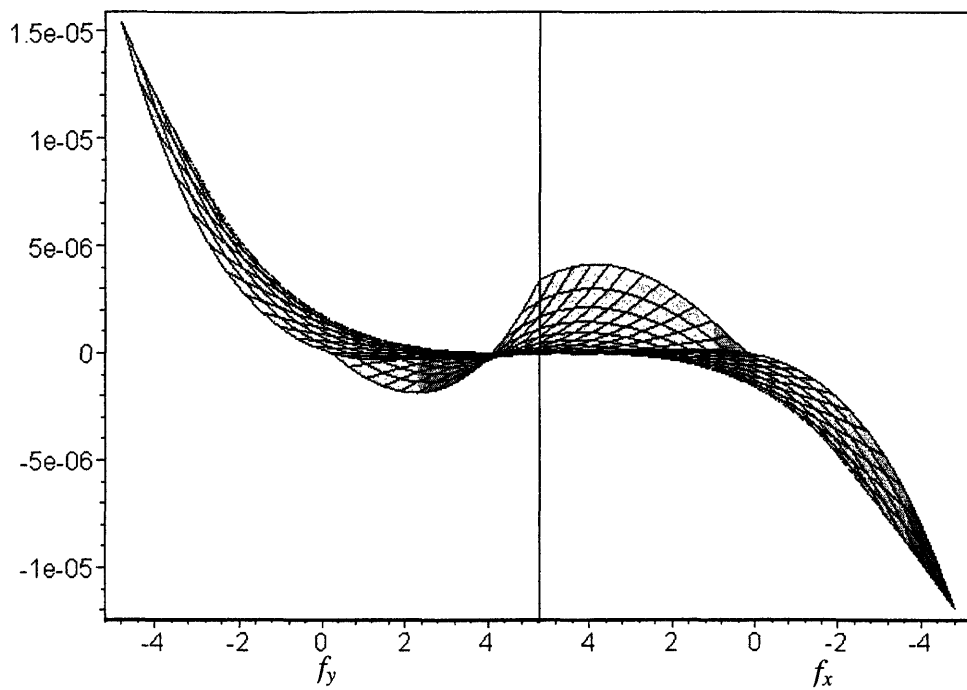
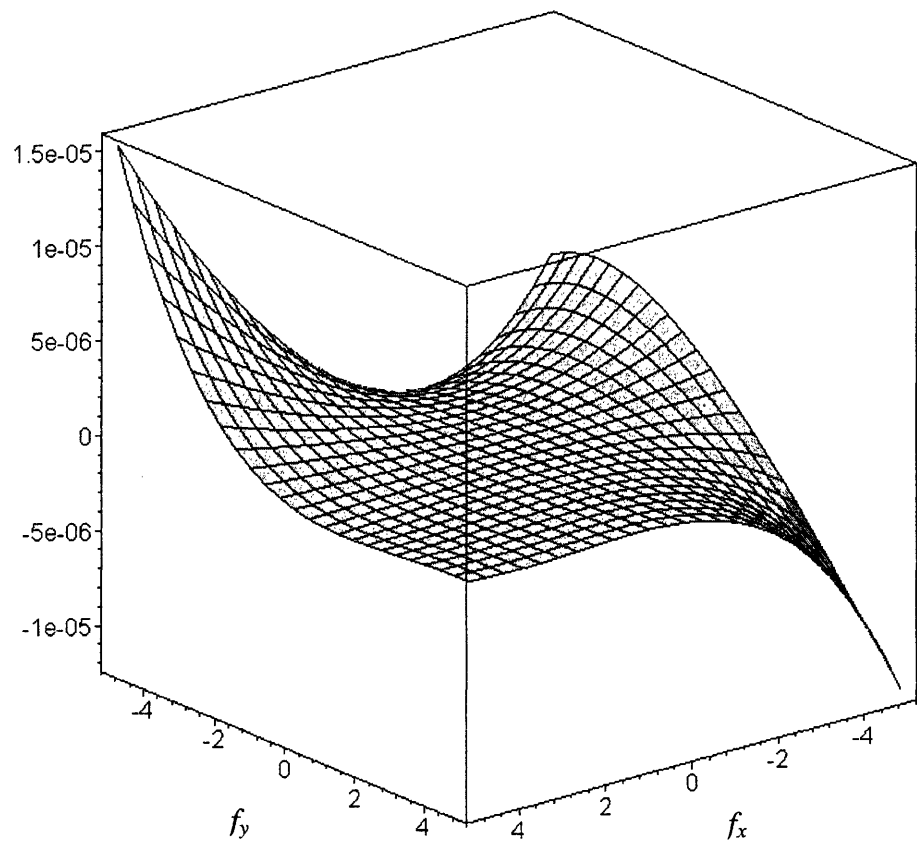


Fig. 5.31 Motion stage rotation versus  $f_y$  for different values of  $f_x$

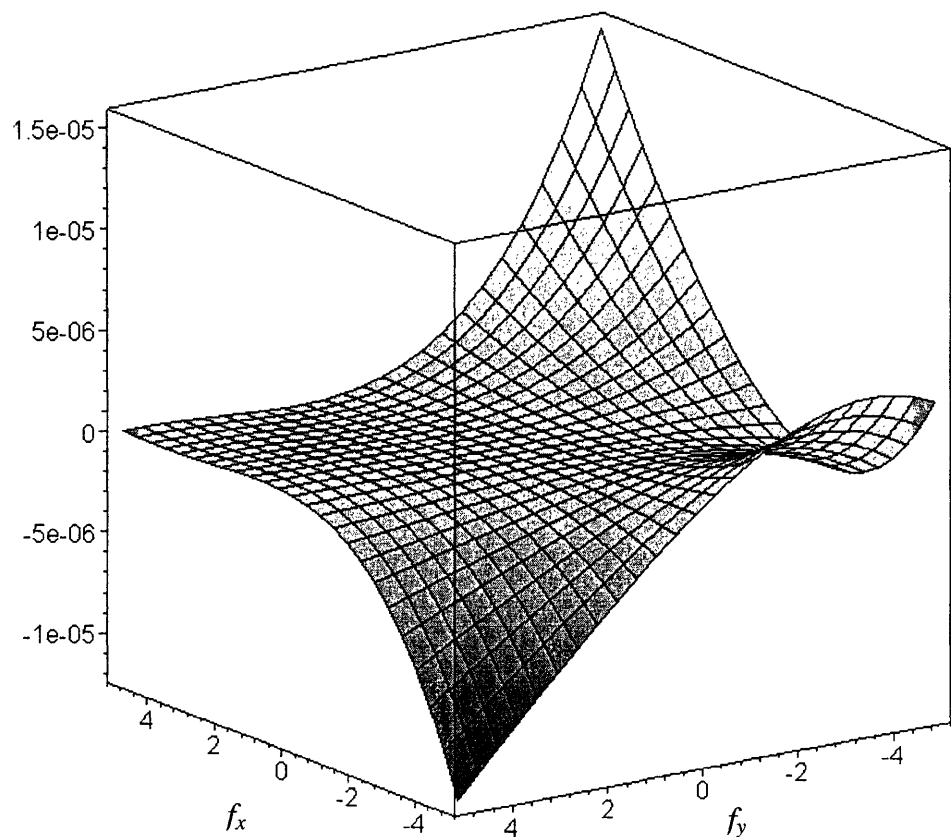
*Fig. 5.32a.*  
*Motion Stage*  
*Yaw vs. X*  
*force and Y*  
*force*



*Fig. 5.32b.*  
*Motion Stage*  
*Yaw vs. X*  
*force and Y*  
*force*



*Fig. 5.32c.*  
*Motion Stage*  
*Yaw vs. X*  
*force and Y*  
*force*



It is apparent from the contours in Fig. 5.32 that there is a very large flat region in the middle. This implies the stage rotation remains very small for a large range of actuation forces, and primary displacements. The extent of decoupling between the two axes in terms of  $\theta_s$  is unnoticeable within this range. The maximum  $\theta_s$  attained in the specified range is about 15  $\mu$ radians or 3 arc seconds. These motion stage rotation results are quite impressive, and in this regard, the current mechanism proves to be the best among the embodiments considered so far. Stage rotation increases non-linearly along the  $-45^\circ$  line in the  $f_x - f_y$  plane, for reasons that are not intuitively obvious.

It is important to check the sensitivity of the motion stage yaw with respect to the exact locations of the actuation forces. To do this check we pick up the worst loading condition for  $\theta_s$  which corresponds to  $f_x = 5$  and  $f_y = -5$ , and  $\theta_s = 1.5e-5$ . At this location we simulate the possibility of an actuator misalignment by introducing a shift of  $\varepsilon_x$  and  $\varepsilon_y$  in the X and Y forces, with respect to  $X_o$  and  $Y_o$  axes, respectively. This results in the following expression.

$$\theta_s = 0.000014793 + 0.0000499 \varepsilon_x + 0.0000499 \varepsilon_y \quad (5.17)$$

The dependence  $\theta_s$  on  $\varepsilon_x$  and  $\varepsilon_y$  is identical, and is plotted over a range of  $+/-0.05$  in Fig. 5.33. This indicates a variation of about 3% for a misalignment of 0.01, or 470 microns for the given dimensions. Typically, manufacturing and assembly tolerances can easily produce a ten times better alignment than this. Thus, we see that the sensitivity of the motion stage yaw is low with respect to actuator misalignment errors.

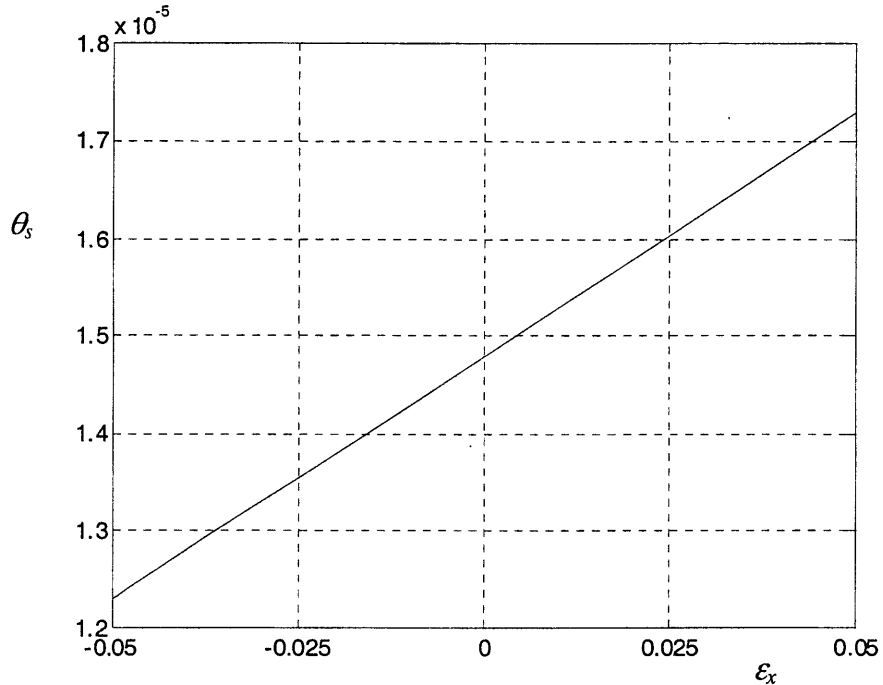
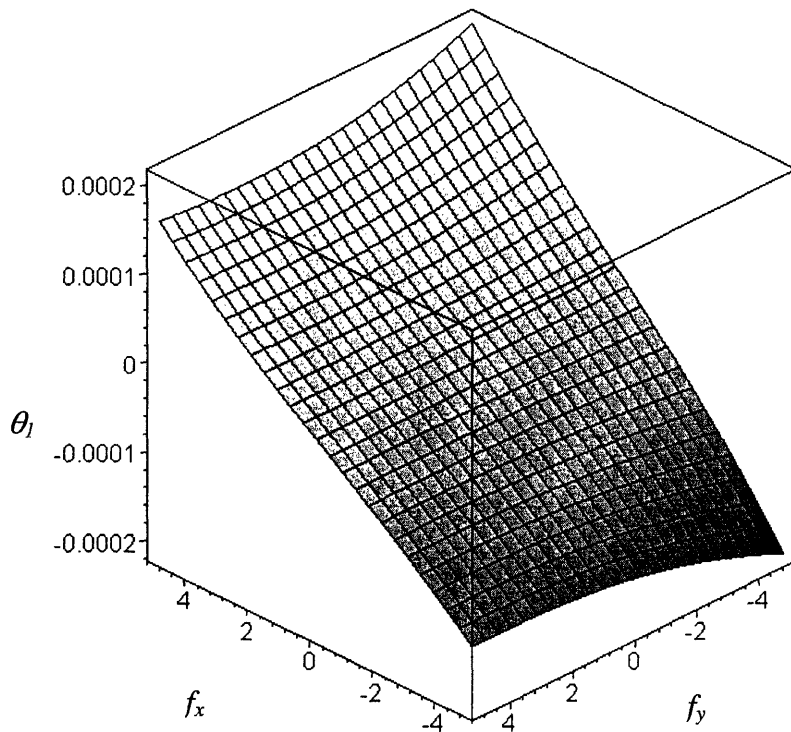


Fig. 5.33 Motion stage yaw vs. X actuator misalignment

As a last step in this exercise, we seek to determine the rotation of the intermediate stages. A combination of several factors including actuator misalignment, and the transverse motion as well as rotation of the intermediate stage dictate the decoupler design.

Center of Stiffness for X actuation with respect to Intermediate Stage 1 can be derived to be located at distance 0.2947 from the  $X_o$  axis, whereas the center of stiffness for the Y actuation with respect to Intermediate Stage 1 coincides with the  $Y_o$  axis. For actuation forces acting along  $X_o$  and  $Y_o$  axes, the intermediate stage 1 rotation  $\theta_i$  is plotted in Fig. 5.34, over the entire range of  $f_x$  and  $f_y$ . It may be noticed that variations with the Y force are much less as compared to those with the X force, and the maximum intermediate stage rotation is approximately 200 microradians, or 40 arc seconds.



*Fig 5.34 Stage 1 rotation versus  $f_x$  and  $f_y$*

Similarly, rotation of intermediate stage 2 may be obtained, and is plotted in Fig. 5.35. The maximum value recorded in this case over the entire actuation force range is, once again, approximately 200  $\mu$ radians.

It should be noted that apart from the performance measures determined here, out of plane and yaw stiffness are also important parameters since they affect the mechanism's dynamic behavior.

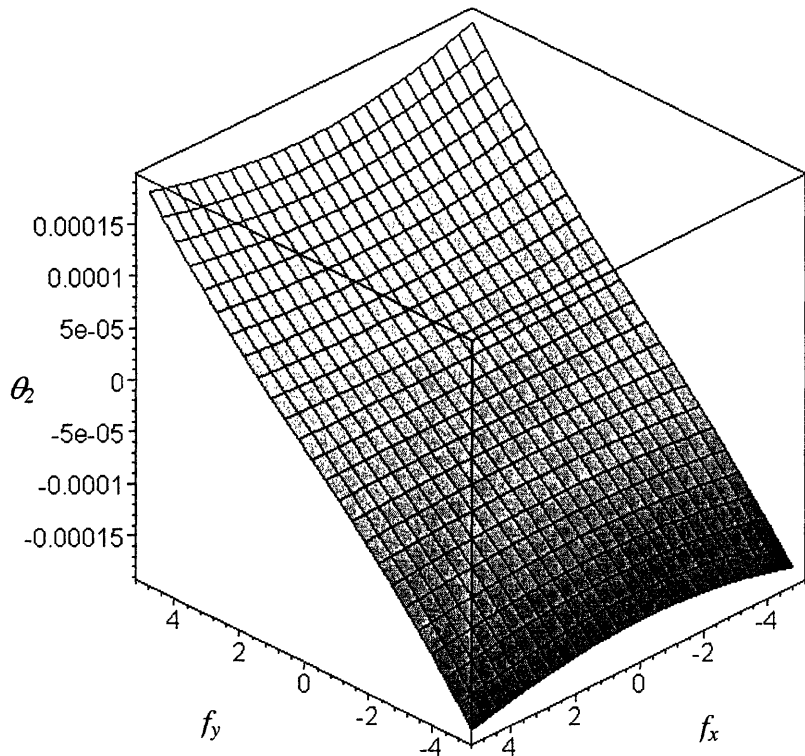


*Fig 5.35 Stage 2 rotation versus  $f_x$  and  $f_y$*

## 5.6 Concluding Remarks

Most of the results presented in the previous four sections have been verified using Finite Element Analysis. Analytically predicted results match with FEA results to within 5-10 %, which is as expected. More importantly though, the non-linear behavior resulting from the above modeling is in perfect match with FE results as far as the trends are concerned, which indicates that the model captures all the important physical effects in the system. The FEA application used in these studies is ProMechanica<sup>1</sup>, which offers a large deformation analysis that is based on a non-linear formulation.

There may be some performance aspects that were intuitively reasoned in Chapter 2 and the results of that reasoning was validated by the above analysis. But at the same time there are several other attributes, such as the location of center of stiffness, and the range over which this center of stiffness is effective, that are not intuitively obvious at all. This mathematical analysis presented here proves to be a powerful tool in determining these aspects without resorting to FEA.

---

<sup>1</sup> Trademark of Parametric Technologies Corporation

# Chapter 6. Fabrication, Assembly and Experimental Test Set-up

In the preceding chapters we have proposed several XY flexure mechanism designs, and also a performance analysis for each. Of all the designs considered, Design 6 is chosen for fabrication and testing because of its large range of motion, low cross-axes coupling errors, small parasitic yaw rotation of the motion stage, good actuator isolation and thermal insensitivity. The only drawback in this design is the variation in its inline axial stiffness over the range of motion, which is important while designing the motion system for a high bandwidth.

The objective of this experimental test set-up is to validate the analytical predication of the previous chapters. For the particular design being considered, we would like to measure the static, dynamic and thermal performance. Range of motion, primary stiffness, cross-axes coupling, actuator isolation, parasitic yaw error, change in inline stiffness are some of the static parameters of interest. Analysis and testing to determine the dynamic behavior and thermal response are part of the future work planned. Although the hardware and testing system has been designed to be able to allow all these tests, at present only static performance tests have been performed.

## 6.1 Metrology Objectives

It is desirable to measure the following aspects of the XY flexure stage and compare it with the analytically predicted behavior

- Range of motion and primary stiffness in the X and Y directions
- Variation of primary stiffness in X direction with Y loads, and vice versa
- Y displacement of the motion stage in response to an X actuation force, and vice versa
- Y displacement of Intermediate Stage 1, and X displacement of Intermediate Stage 2 in response to X and Y forces
- Rotation of the motion stage in response to X and Y forces
- Rotation of intermediate stages in response to X and Y forces
- Variation of inline axial stiffness between stage 1 and motion stage in response to a primary Y displacement, and vice versa

## 6.2 Choice of Material

To minimize assembly and manufacturing errors, a monolithic design was an obvious decision. The choice of material and raw stock is a key step in the hardware design. It is desired to start with a plate that a) has very low internal stresses because once the flexures are cut on the plate, the internal stresses relieve by distorting the thin flexure structures, and b) is very flat so as to make sure that the subsequent machining processes and the metrology alignment have a good reference plane. A plate coming from the supplier will typically not have the desired level of flatness, and any machining done to achieve flatness will add internal stresses to the plate. Although annealing the plate eliminates the internal stresses, it significantly reduces the yield strength of the material resulting in extremely poor range of motion. Furthermore, any annealing after a machining step, so as to reduce the machining stresses, results in a loss of dimensional tolerances obtained by the machining. Thus, it is very difficult to balance the requirements of high strength, good dimensional accuracy and low internal stresses. Based on the application one has to live with some compromises.

For the purpose of our experiments, we have chosen AL6061-T651. Invar and super invar were other choices that were considered because of their low coefficient of thermal expansion (CTE). But the design is thermocentric and therefore CTE was not a critical factor. Furthermore, these two materials have poor Yield Strength to Young's Modulus ratios as compared to Aluminum. Beryllium Copper was another choice because of its excellent  $S_y/E$  ratio, but was rejected due to fabricability reasons.

Several Aluminum alloys are available that provide low internal stresses, good strength and phase stability. Among the AL alloys, 2000, 6000 and 7000 are the only heat treatable series, where strength improvement can be achieved by precipitation hardening without any cold working, which adds significant amounts of internal stresses. AL 2024 and AL7075 are aircraft alloys that offer very high strengths, whereas AL 6061 is common for regular use and has a moderate strength. AL 2024 T851, is strong and stable but has some amount of cold work done on it. AL 6061 T651 has intermediate strength, stable and very low internal stresses. Temper T6 corresponds to the highest strength level achieved only by precipitation hardening. The suffix -51 implies that plate stress are relieved by stretching the plate after it has gone through the rolling mill. Temper T6 is not recommended for AL 7075 because it is prone to fatigue corrosion. Instead tempers T7351 and T7651 are recommended. The literature recommends AL 6061 and AL 7075 for precision instruments due to their phase stability of long periods of time [87]. Ultimately, AL6061-T651 was selected because of its ease of availability, and good overall properties.

For our application we choose Kaiser plates, which are usually considered to have better dimensional tolerances. Flatness is quoted for 0.001inch per 1 inch, which is usually interpreted as follows – if an N inch long plate is placed on a flat table, then a shim of thickness 0.001N can be slid between the plate and

the table. The flatness of a 18 inch x 18 inch plate was actually measured on the Coordinate Measuring Machine (CMM), and was found to be flat within approximately 0.005 inch. Blanchard grinding or high speed machining may improve the surface flatness without introducing significant stresses. Also, the amount of machining required to make the above measured plate flat within 0.001 inch, which is desirable for the purpose of obtaining good reference surfaces, is not very significant.

### **6.3 Choice of manufacturing process**

Two methods of cutting the flexure features on the above selected AL plate were considered and implemented: water-jet cutting (WJC) and wire electric discharge machining (EDM). Both these processes add minimal machining stresses to the part.

Wire EDM has traditionally been the machining method of choice for fabricating precision flexure mechanisms. Dimensional tolerances better than 0.0005 inch or 12 microns are easily achievable, and parallelism and perpendicularity of the machined feature can be tightly controlled. Also, with wire EDM the thickness of the plate being machined is not a concern, and uniform thickness flexure blades may be produced. But the process requires a fairly significant amount of set-up and is generally expensive.

The other machining option that has not been used much in the past is water-jet cutting. Several test cuts were made on an OMAX<sup>1</sup> water-jet cutting machine, to assess its machining capabilities because no such studies are available in the literature. The machine uses a mini-jet nozzle with an orifice size of .010 inch and operates at a pressure of 40,000 psi. The conclusions derived from these tests are presented here.

1. The true positioning accuracy of the machine axes is of the order of 0.001- 0.002 inch. Accuracy of the resulting part and features also depends critically on how well the plate is fixtured to the machine-bed. Part shift is a common source of dimensional variations. Straightness of cut has been measured to be within 0.001 inch over 15 inches. Cuts are flared close to the ends because the nozzle has to slow down as it approaches ends and corners. Therefore longer cuts are straighter. Parallelism of 0.001 inch over 15 inches, and perpendicularity of 0.004 inch over 15 inches was measured.
2. One of the biggest drawbacks of waterjet cutting is that it does not produce straight walls. The walls are not only tapered, but the taper varies with the location of the cut. During long straight cuts, kerf width is larger on the top as compared to the bottom, because the abrasive loses momentum as it reaches the bottom. On the other hand, when the nozzle is cutting close to a corner, a different phenomenon dominates the quality of cut. Since there is a lag between the top and bottom in the

---

<sup>1</sup> Trademark of OMAX Corporation

cutting frontier, corners tend to get rounded at the bottom. Obviously, this lag, illustrated in Fig 6.1a, increases as the nozzle speed increases. To minimize this, the machine slows down so that this lag is reduced to some extent. Nevertheless, corner radii are larger at bottom as compared to the top. Also, the slowing down of the nozzle increases the material wear and therefore the kerf width at the bottom. Thus, if a blade is cut on the waterjet machine, its resulting geometry is as illustrated in Fig. 6.1b.

The wall taper depends on many factors including the nozzle wear, abrasive grit size, the material being cut, water-pressure speed of the nozzle, and is hard to predict in a deterministic fashion. The most critical of these factors is the quality of the nozzle which includes a jewel, to create the water jet, and a mixing tube, to mix the abrasive and high pressure water. If the two have worn down, the jet is flared and the above effects become very prominent. With a brand new nozzle, and with a fine grit abrasive, tapers of less than 0.001inch over 1 inch were measured. For worn down nozzles, this number was as large as 0.008inch over 1 inch.

The XY flexure mechanism was eventually fabricated using both methods, to allow for a comparison between the two manufacturing options. All alignment features that shall be used in metrology should be machined in the same set-up as the rest of the flexure blades. This is important to ensure that the metrology axes are aligned well with the flexure axis. This significance of this alignment is described in Section 6.7.

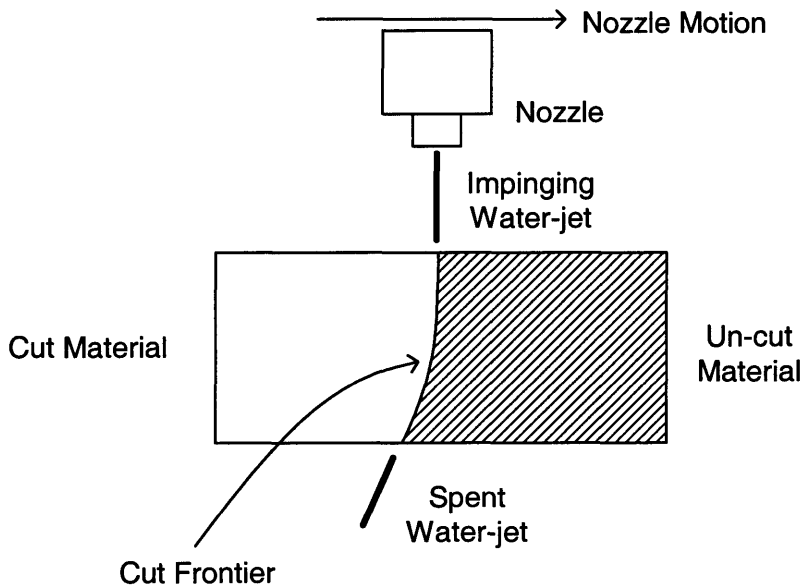


*Fig. 6.1a Cut frontier shape and lag between top and bottom in water-jet cutting*

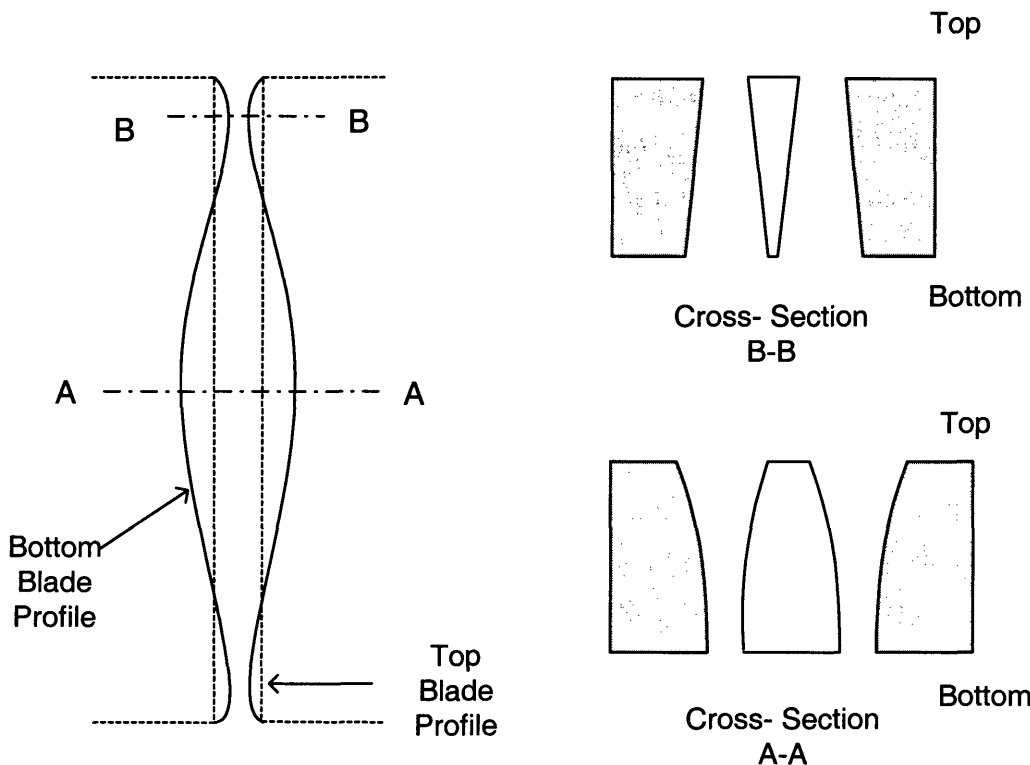


*Fig. 6.1b Exaggerated geometry of a blade cut by a waterjet machining*

The design of the experimental set-up includes the choice of sensors and actuators and their integration with the flexure mechanism. The experimental set-up used in this case has been designed such that it may be tested using multiple sensors and actuators. Also, the assembly is modular so that various different flexure mechanism designs can be tested using the same set-up. Particular care has been placed in ‘designing in’ alignment features for the actuator and sensors. Also, it has been ensured that the assembly has no interfaces that may introduce friction or backlash. All connections are designed to be friction based and the use of set-screws has been eliminated.

#### 6.4 Actuation Methods

Selection of actuators that provide the desired range of motion and that too accurately is a tough challenge. Most voice coil or similar electromagnetic actuators that provide a direct force source become bulkier with the increased force requirements associated with large ranges of motion. Electromagnetic actuators, for example DC or stepper motors, with a gear-head and/or micrometer do not have the resolution necessary for nano-positioning. These actuators allow for a large range of motion and are

generally suitable for micro-positioning. Piezoelectric actuators are excellent in terms of quality of motion and the force generated, but provide very small ranges of motion. It is common to use these in conjunction with motion amplifiers [35-36] to achieve larger ranges of motion. Issues associated with amplifiers, such as reduction in effective actuator stiffness and lost motion, are discussed in much detail in the literature [6]. Piezo based inch-worm actuators are another choice for large range motions but have limited resolution.

To achieve both large range and high resolution, we decide to use a coarse-fine actuation scheme. The coarse actuator selected for this application is a PhysikInstrumente (M-227.25) DC mike actuator. This actuator is powered by a 2Watt Faulhaber DC motor with a gearhead and an integrated optical encoder. The output of the gearhead is connected to a precision PI micrometer with a non-rotating tip feature. The sensor resolution is 3.5 nanometers, and a backlash of about 2 microns. By means of feedback control, unidirectional repeatability of about 0.25 microns has been achieved. This motion accuracy and repeatability is limited by the significant amount of friction present in the gearhead and micrometer. Furthermore, because of the micrometer drive, the actuator is isolated from the system that it actuates. The only affect of the system is in the form of a variation in the friction depending upon the axial force. Several advanced techniques of motion control design in the presence of friction [89] were investigated to achieve better positioning capabilities, but were not successful. All these strategies are based on a somewhat deterministic model of friction that is expected to be repeatable. The friction present in this actuator was measured to be non-deterministic and non-repeatable. It was therefore decided to attain higher resolution by means of a piezo actuator attached to the tip of the coarse actuator.

The X and Y actuators are mounted in-plane on the flexure plate using a very simple yet effective clamping mechanism shown in Fig. 6.2. This mechanism ensures a well-distributed holding pressure over a length of the micrometer without damaging the lead-screw, and also a very well aligned axis of actuation. Further details on the clamping mechanism are presented in Section 6.6.

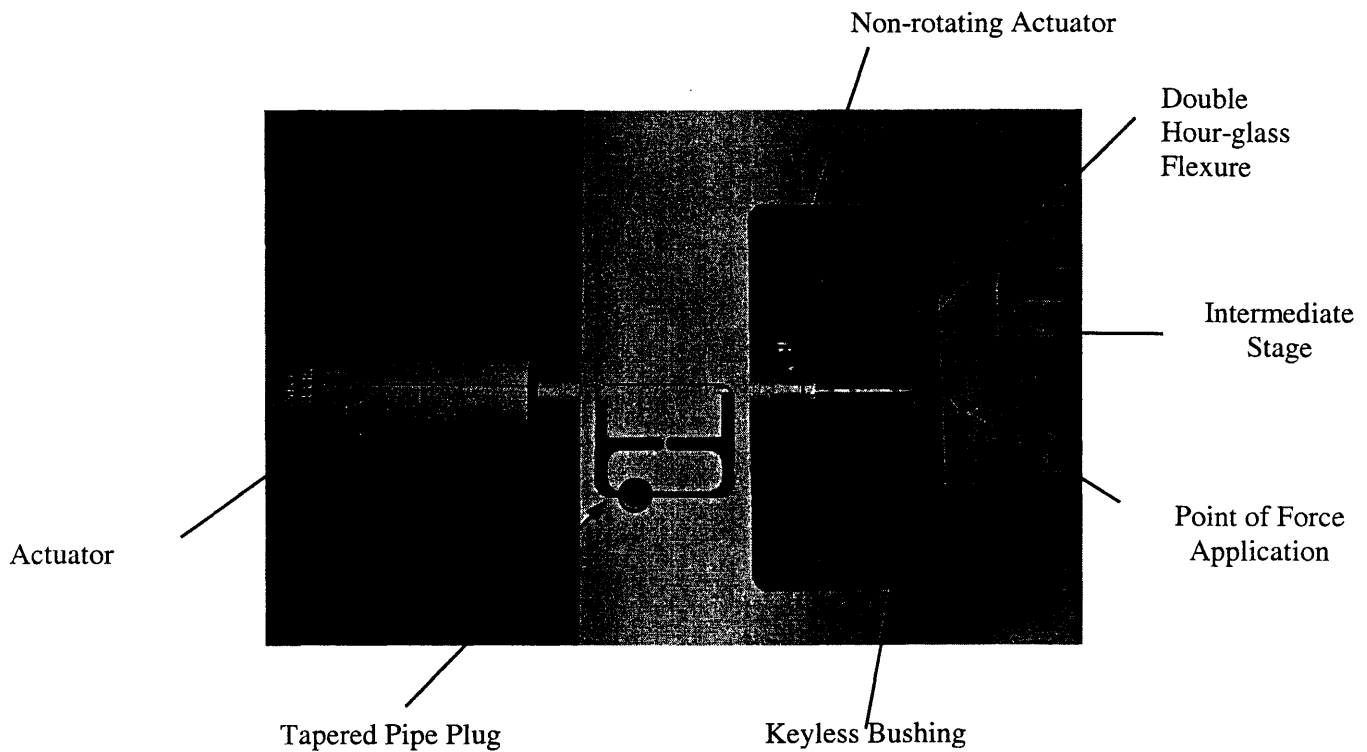


*Fig.6.2 Actuator Clamping Assembly*

Based on estimates of the transverse displacement and rotation of the intermediate stage a decoupler is needed between the actuator tip and the point of force application. This ensures that only an axial force is transmitted to the intermediate stage and any other loads arising due to misalignments are absorbed by the flexible coupling. A double hour-glass flexure, shown in Fig. 6.3a serves the purpose of this flexible coupling. One end of the double hourglass flexure is attached to the non-rotating cylindrical actuator tip by means of a friction clamp, while the other end is attached to the point of force application on the intermediate stage by means of a keyless bushing. Thus, throughout the actuation assembly all connections are based on friction clamping, and therefore free of backlash.

Furthermore, an piezoelectric stack that provides fine motion can be incorporated within the decoupler design, as shown in Fig. 6.3 b. The piezoelectric actuator used is from Queensgate Instruments and provides a 15 micron range of motion, and nanometric resolution.

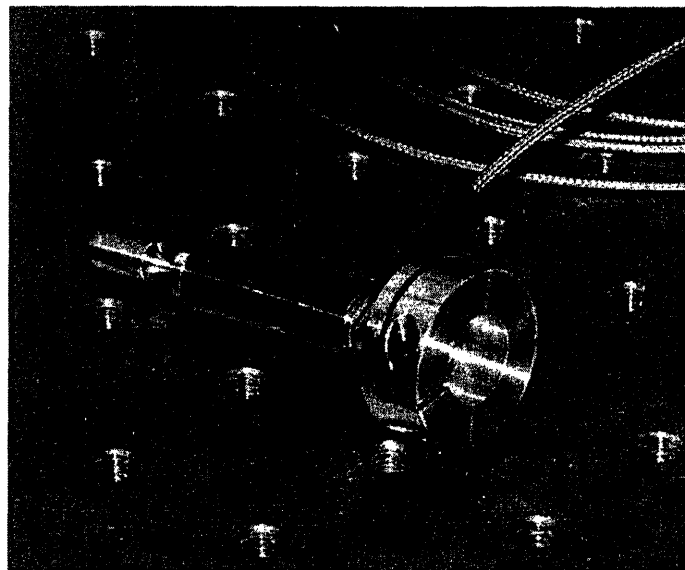
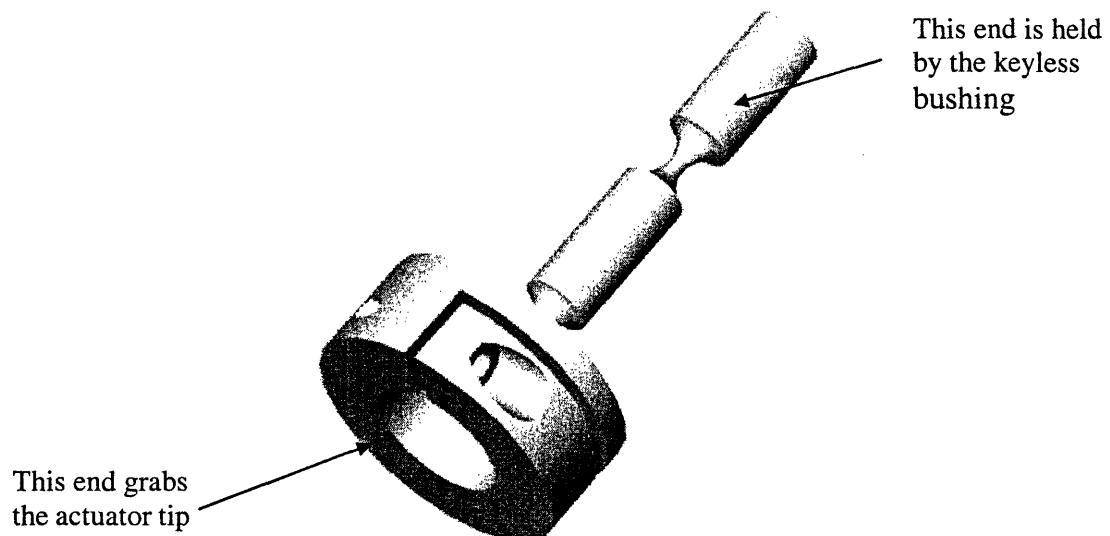


*Fig. 6.3 a) Passive decoupler design. B) Decoupler with an integrated fine actuator*

For the purpose of testing we also decided to use calibrated weights. This is a simple and inexpensive way of applying forces, as opposed to the previous actuators that are displacement sources. The same keyless bushing as earlier connects a support wheel to the intermediate stage. A fishing line can be threaded through one of several fine holes in the support wheel and is supported on a pulley on the other end. This allows us to apply additional moments to the intermediate stage, and test the mechanism for sensitivity against alignment errors arising from machining or assembly tolerances. The support wheel can be rotated 90° to test the out of plane parasitic motion behavior of the mechanism. These ideas are illustrated in Figures 6.4a and b.

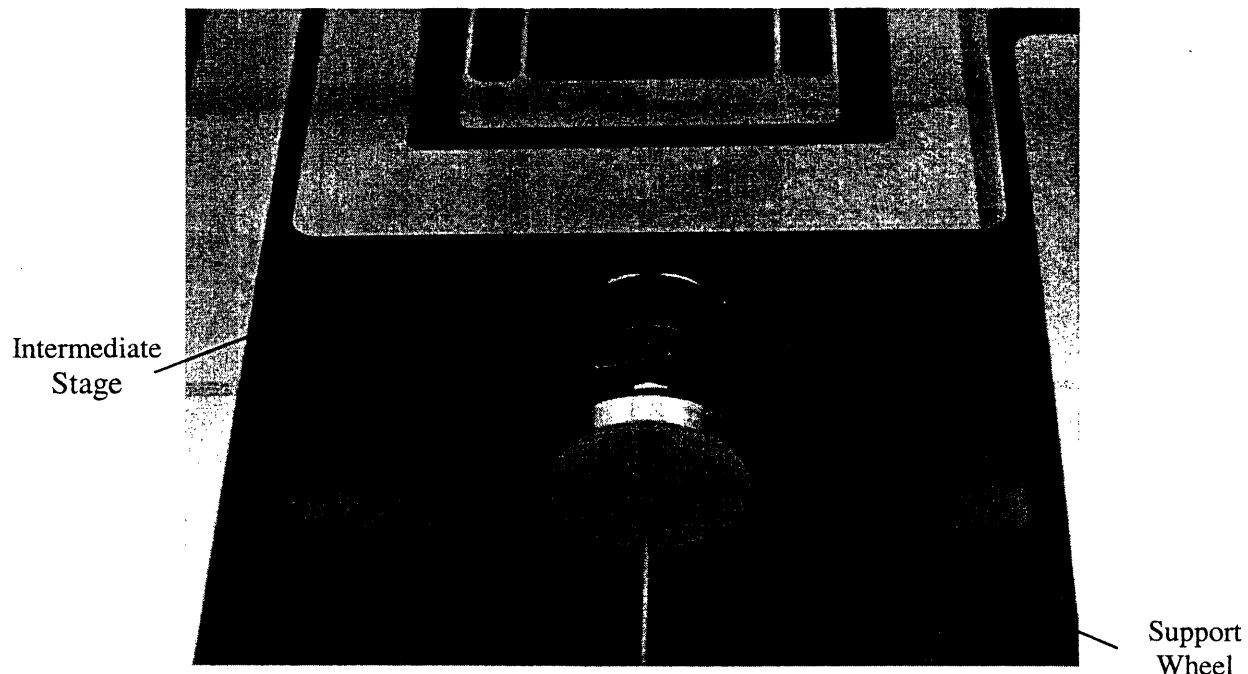


*Fig. 6.4a. Support wheel to transmit forces using a fishing line*

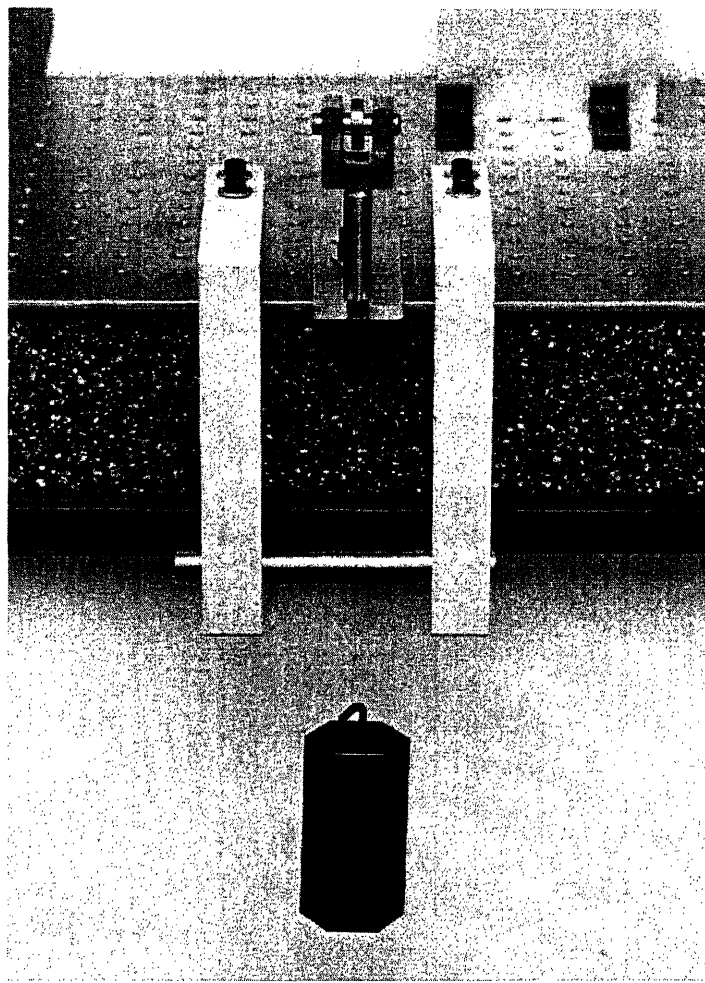


*Fig. 6.4b. Ball bearing based pulley to support the actuation weights*

The entire arrangement is very simple to assemble and disassemble, and the two actuation schemes based on force source and displacement source can be switched with relative ease. In the latter case, we notice that introduction of a ball bearing as the pulley, which becomes the source of non-deterministic effects that are observed in the measurements. A much better strategy to implement the above idea is by means of a virtual pulley as shown in Fig. 6.5, which eliminates the problems of friction, creep and hysteresis.

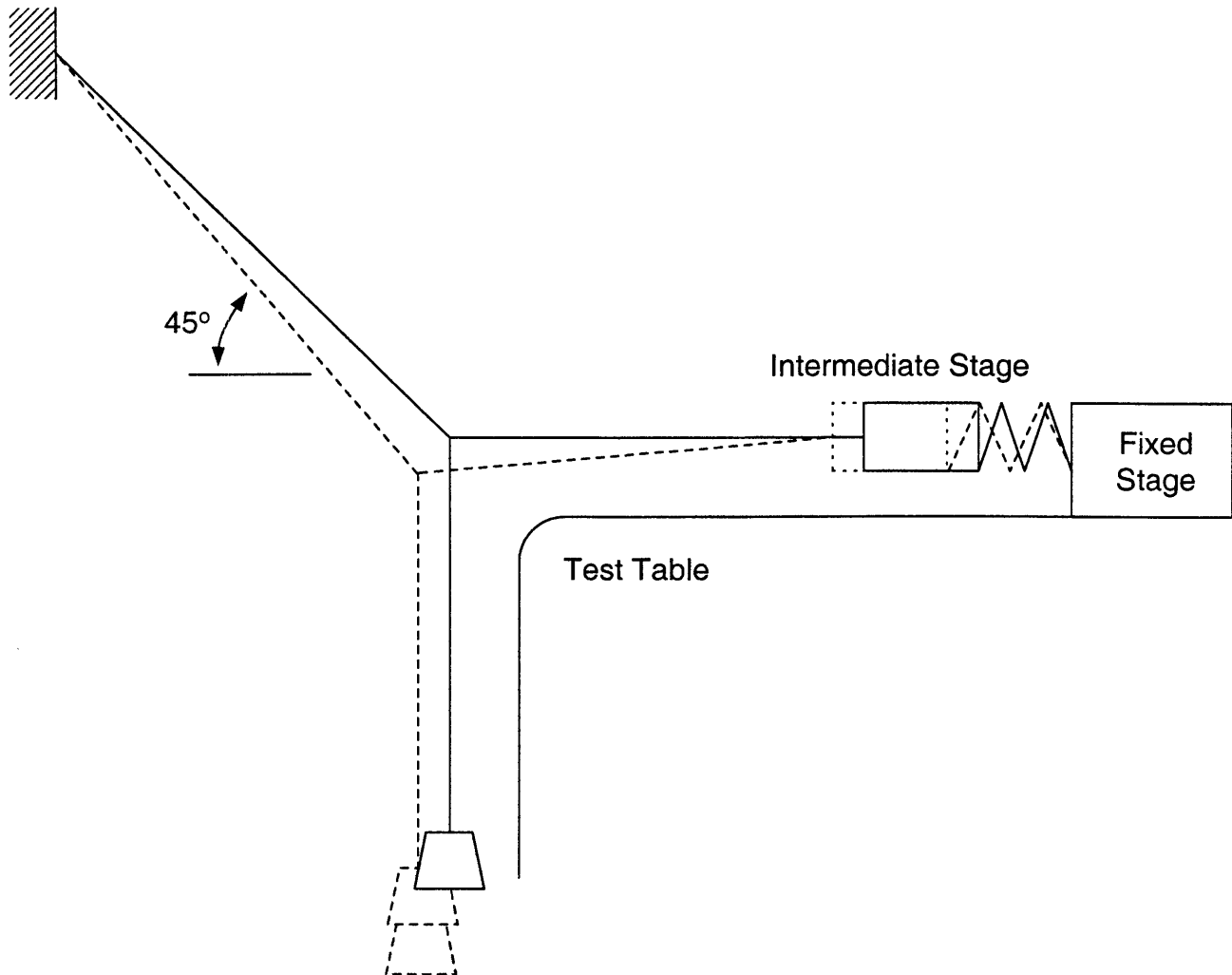


*Fig. 6.5 Concept of virtual Pulley*

## 6.5 Sensor Schemes

Multiple sensor schemes are incorporated in the experimental test design to maintain redundancy in measurement. This provides a check on the quality of data being measured.

As was discussed in Section 2.1, it is very difficult to obtain a sensor that has a high dynamic range, i.e., large range and small resolution. In fact both the sensor schemes that were used for testing, optical interferometry and capacitance sensing, are used only for the purpose of characterization, and cannot be used if the flexure mechanism were to be used for a motion control stage. Laser interferometry based

equipment is too bulky to be practical for regular use, and capacitance probes have a small dynamic range. High resolution two axis optical scales have become available only recently, and will be used in future measurements and motion stage design based on this flexure mechanism.

In both the sensing schemes, we mount a target block at the center of the motion stage, and it is the motion of this target block that is sensed by the transducers. The importance of the alignment between the flexure axes and the target block may be evident and is discussed in much detail in Section 6.6. One of the steps taken to ensure good alignment is that the holes for the three pins that position the target block with respect to the motion stage are machined during the same step as that for the flexure blades. Fig. 6.6 provides a close-up of the target block aligned and attached to the motion stage. The target block is a True Square from Starret, that is provides highly flat and orthogonal surfaces that are polished to mirror finish.

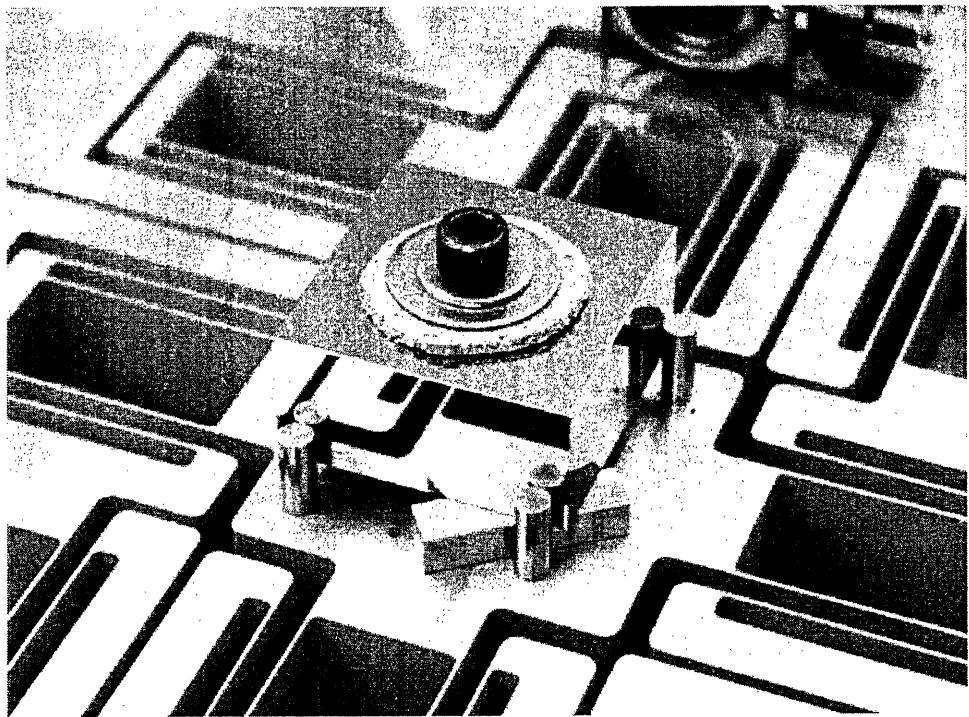


*Fig. 6.6 Metrology Target Block*

Fig. 6.7 presents a schematic of the optical metrology that is used to measure the displacements of the motion stage. A standard plane mirror interferometry arrangement is employed to measure the X and Y displacements of the motion stage. The interferometry equipment used is from HP/Agilent and provides a resolution of 5nm.

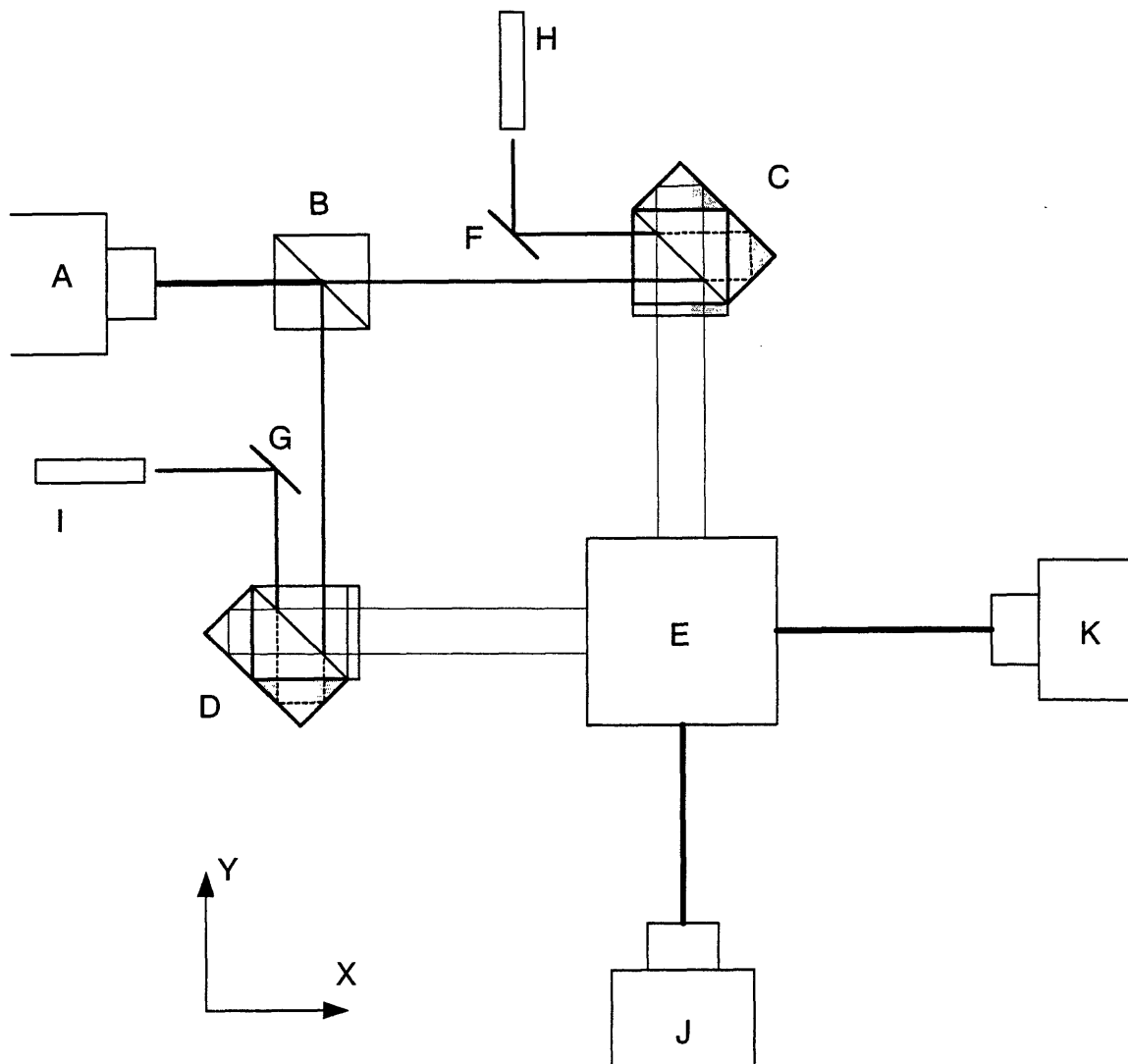


*Fig.6.7 Schematic of Optical metrology set-up*

In the above figure, A is the laser head, B is 50-50 beam splitter, C and D are plane mirror interferometers, E is the target block that moves with the motion stage, F and G are plane mirrors, and H and I are receivers that gather the two returning laser beams. Fig. 6.8 provides a picture of the above schematic during a measurement.

Apart from the plane mirror interferometry, two autocollimators are also used to simultaneously measure the motions stage rotations. J and K are dual axis autocollimators that measure  $\theta_z$  and  $\theta_x$ , and  $\theta_z$  and  $\theta_y$  respectively. The angular resolution that can be obtained with these is 0.01 arc seconds.

Ideally it is desirable to take measurement from all these transducers during one single set-up, but that may not always be possible due to practical reasons.

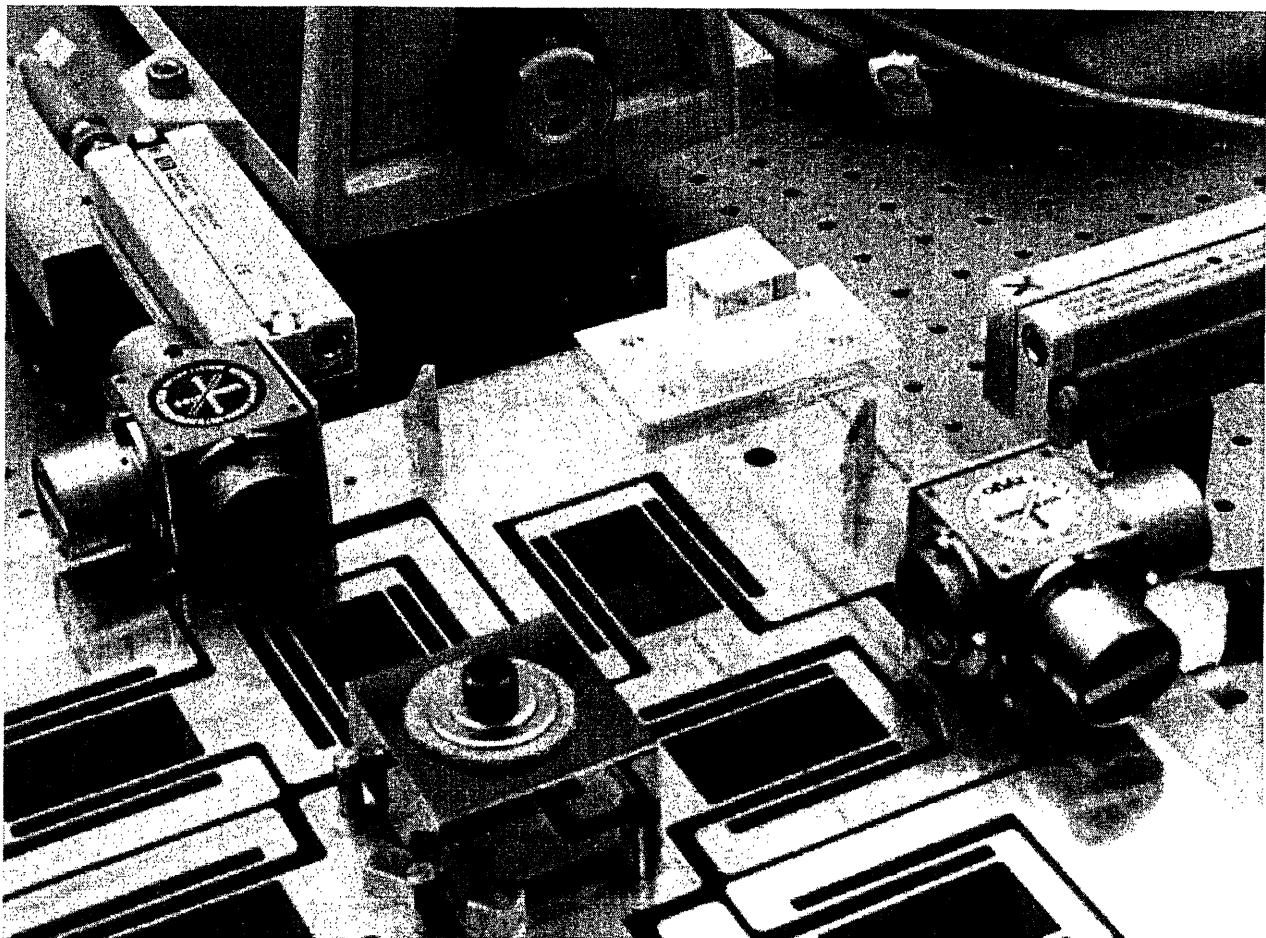


*Fig. 6.8 Plane mirror interferometry for X and Y displacement measurement*

The other set of sensors used are capacitance probes, which allow measurements over a 50 micron range and provide a resolution of 5nm. Cylindrical capacitance probes by Lion Precision Inc. have been used for this purpose. The capacitance probes are mounted on a metrology plate that surrounds the target block. The metrology plate is attached to the static periphery of the flexure mechanism and kinematically aligned with respect to the flexure axes by means by three pins. Spring are used to preload the three arms of the metrology plate against the pins. This may be evident in Fig 6.8, which shows an assembly which is set-up for capacitance probe based measurements.

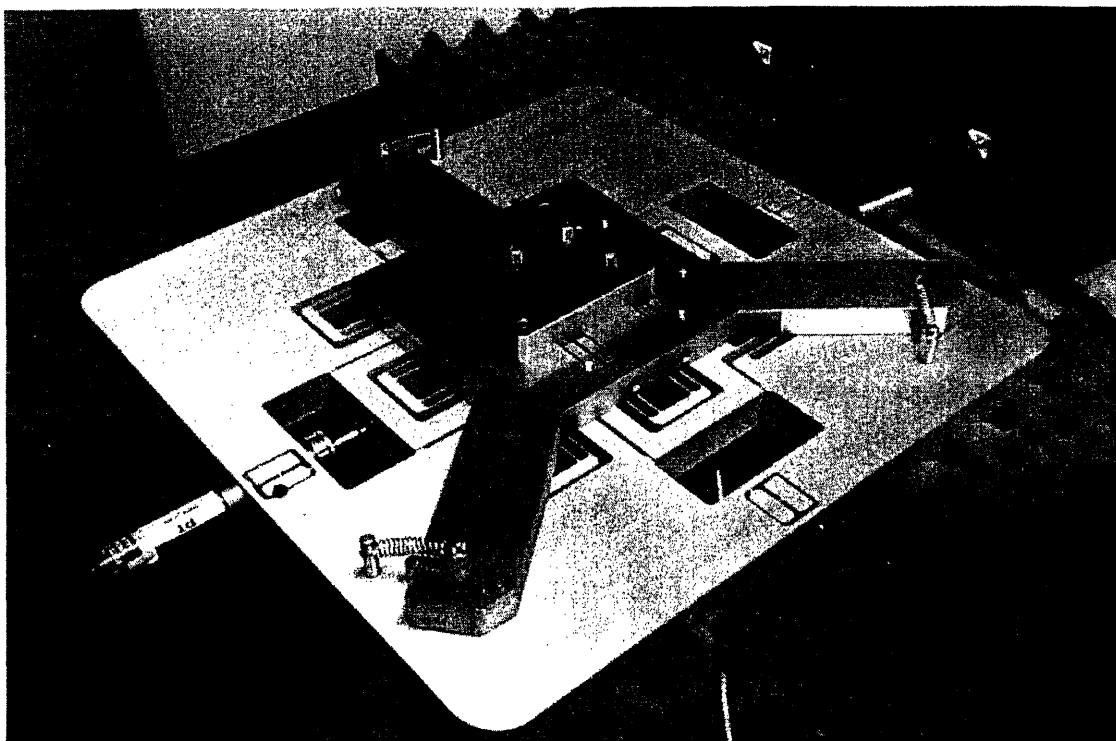


*Fig. 6.9 Capacitance probe based meteorology set-up*

The holes for the cap probes are drilled with reference to these machined surfaces that rest against the pins. Clamping mechanisms similar to that in Fig. 6.2 are used to hold the in-plane cap probes effectively in place. Another plate which holds three cap probes normal to the target block goes on top of the metrology plate. Thus, all six motions of the target block may be measured with the same sensor arrangement. This arrangement of cap probes, also referred to as the sensor nest, is shown in Fig. 6.10.

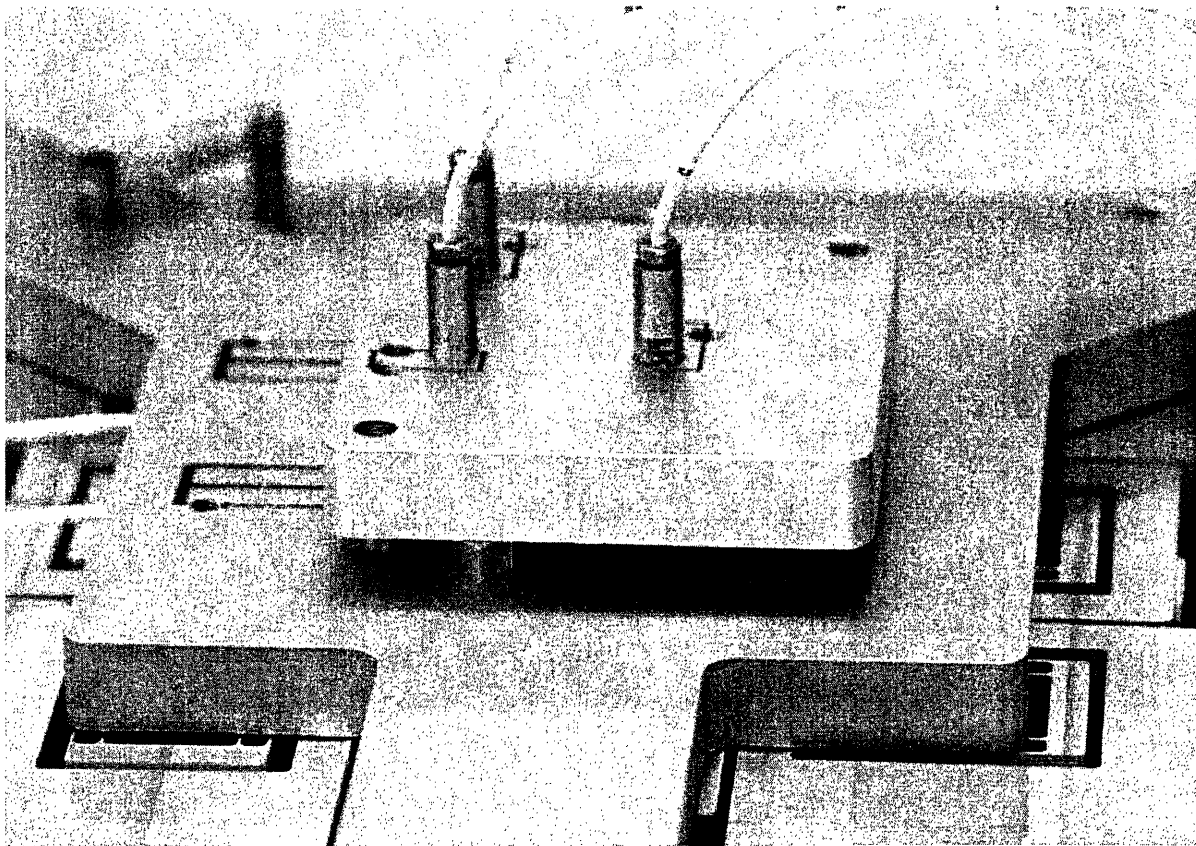


*Fig. 6.10 Capacitance sensor nest*

## 6.6 In-plane Capacitance Probe/Actuator Clamping Mechanism

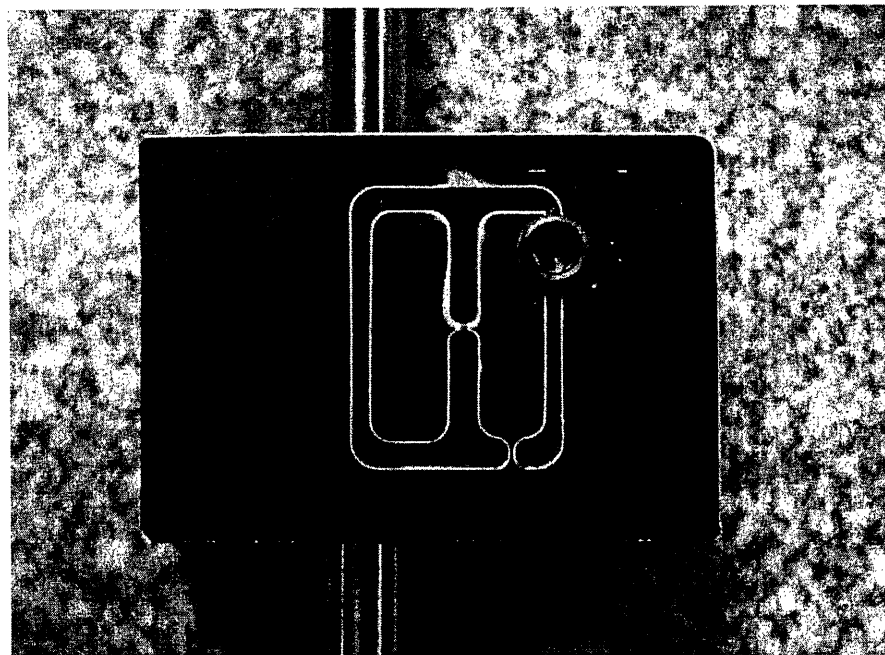


*Fig. 6.11 Clamping mechanism*

In our application, and in precision metrology in general, it is frequently required to hold capacitance probes such that they are properly aligned and held well. Alignment, i.e., parallelism between the sensor surface and the target surface, is important for measurement accuracy. Deviation from parallelism introduces cosine errors in the measurements. The sensor also needs to be held snugly in place by means of a well distributed nestling force. A loosely held cap probe is prone to mechanical as well as electrical noise. On the other hand, applying a large localized force, for example by means of a direct-contact set screw, can damage the cap probe and permanently alter its calibration. Furthermore, before the sensor is held in place, it must be free to move along the sensing axis to allow an adjustment of the initial gap between the sensor and the target. Thus, an ideal probe holding mechanism should enable the following:

1. Proper alignment
2. Nestling force distributed over a length of approximately two to three times the diameter of the probe
3. Easy movement of the probe along the sense axis before it is clamped

Similar concerns exist in actuator mounting as well.

While it is quite easy to hold a cylinder normal to plane, the same cannot be said about holding it in-plane for the simple reason that normal to plane cuts are far more feasible and inexpensive to make as compared to in-plane cuts, which may even be impossible as illustrated in Fig. 6.12.

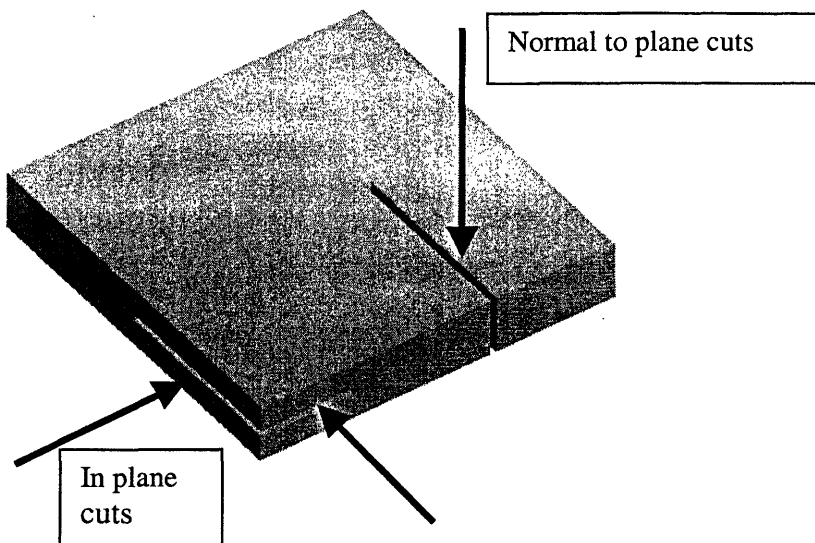


*Fig 6.12 In-pane and normal to plane cuts*

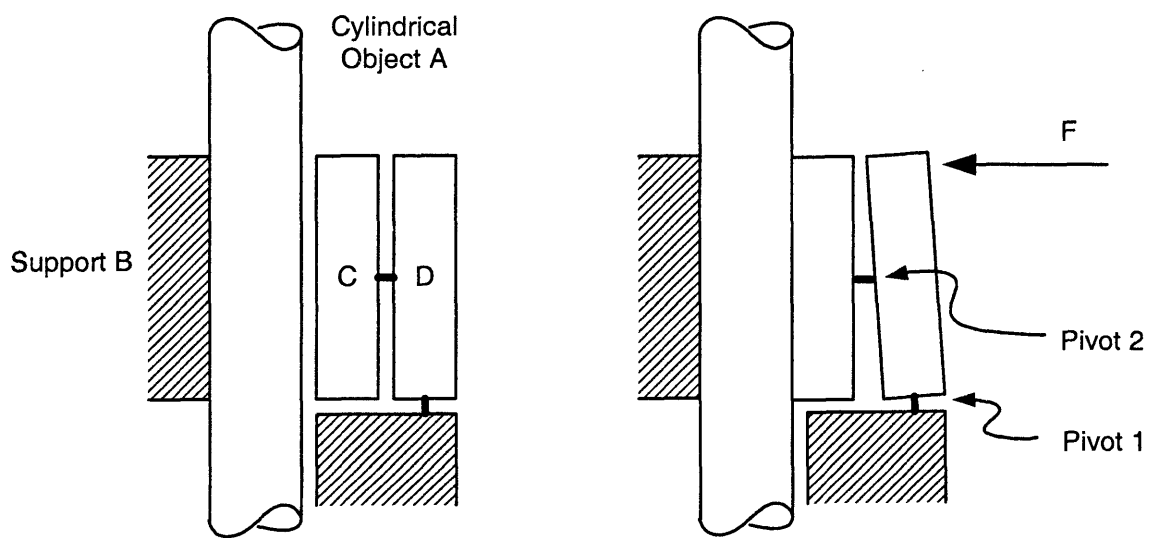


*Fig. 6.13 Proposed clamping mechanism*

In Fig. 6.13, we describe a very simple yet effective mechanism that we have employed to hold cap-probes and micrometers without damaging them. The arrangement consists of a cylindrical object A that is to be held firmly with respect to fixed support B. Furthermore, there are two blocks C and D connected by means of flexural pivot 2. Block D is connected to ground via the flexural pivot 1. Pivots 1 and 2 are designed such that they have a very high axial stiffness but low moment stiffness. Thus, flexural pivot 1 ensures that the force F that is applied on block D is not countered by any significant moment at Pivot 1 and is instead transmitted on to block C. Meanwhile, pivot 2 transmits this force to block C which nestles the object A against support B, without transmitting large moments. Pivot 2 allows a small relative rotation between blocks C and D without producing any significant enough moment on block C, since its moment stiffness is very small.

Thus ultimately, only a normal force acting at the middle gets transmitted to block C. This force distributes itself over the entire length of block C which secures part A against the fixed support B. The resulting pressure distribution at the interface of part A and block C is somewhat like a bell-curve, as is shown in a subsequent FEA study. Barring space constraints, it is very easy to increase the width of block C, which will result in a yet more uniform distribution of the applied force. This is guaranteed by St. Venant's Principle. The use of a single lever, i.e., block C without block D, supported by Pivot 1 would cause a stress concentration at the tip of the lever where it touches the cap probe, and potentially damage it. On the other hand, Pivot 2 in the proposed mechanism transmits only a normal force, and allows block C to align with Object A without producing any significant moment loads on Object A.

The in-plane nestling force can be applied very easily by means of an NPT tapered pipe plug, which is simply a set screw with tapered threads. While fabrication might seem to be a concern in this case, in reality it is quite straightforward as long as a particular order is followed. First the entire 2-D pattern can be cut using a waterjet machine or a wire EDM. This results in a part with blocks C and D supported merely by thin flexures. To drill the hole that will hold the object A, blocks C and D have to be temporarily held strongly in place. This is accomplished by gripping the part between two sheets of emery paper in a regular vice. As the vice jaws are tightened, the grit particles of the emery paper dig into the part including blocks C and D, and hold them firmly in place. Now the part can be drilled and reamed as though it were rigid. A spiral flute reamer is recommended since the cut is discontinuous. Once the part is drilled and reamed, either the object A or an artifact of the same diameter should be slid into the hole. With this in place, the hole for the tapered pipe plug can be tapped easily. Alternatively, one can leave supporting tabs while cutting the part initially on the waterjet / wire EDM. These supporting tabs keep the part stiff during subsequently machining. Once all the machining is done, these supporting tabs may be removed by using a very fine end mill cutter, or a fine saw blade, or even by a waterjet. Another way

would be to drill and ream the hole first, then align the part on a waterjet machine or wire EDM, and finally cut the 2-D pattern. Depending on the machine used this alignment may or may not be a straightforward step.

## 6.7 Metrology Alignments

In the error mapping of an XY stage, the primary objectives are to measure the cross-axis and yaw motion errors of the stage. There are several deviations from ideal behavior that can occur in this measurement. Some of these are attributed to the stage itself and other are attributed to the metrology set-up. We proceed to define various kinds of errors that are traditionally associated with serial stage design and metrology. In Fig. 6.14, X and Y represent the ideal system axes along which all components of the system would be aligned if the manufacturing and assembly were flawless.

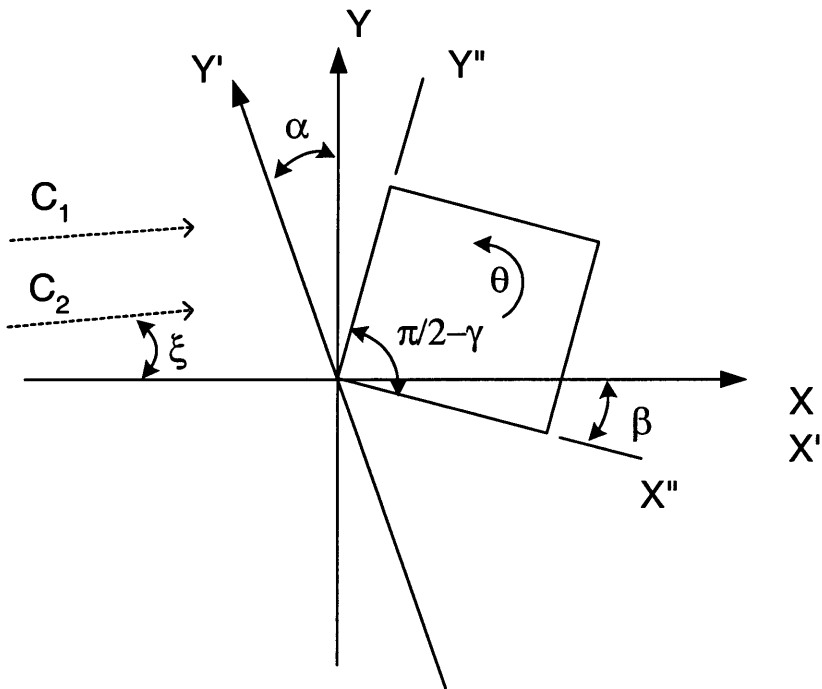


Fig. 6.14

Errors resulting from imperfect behavior of the stage are -

- 1) Orthogonality error: The actual axes of the stage,  $X'$  and  $Y'$ , may not be perfectly orthogonal. For serial stages, this is typically due to an improper mounting and assembly of the bearing-ways. A motion along the  $Y'$  results in a cosine error along the  $Y$  axis measurement and a sine error along the

X axis measurement. The deviation from orthogonality is quantified as the angle  $\alpha$  in the above figure.

- 2) Straightness error: Straightness error shows up during a motion along  $Y'$  as a non-linear variation in the X axis measurement, and results due to a non-ideal Y axis bearing-way. Since this error is not linear, it cannot be expressed in terms of an angle, and is therefore not shown in the above figure.
- 3) Yaw error: Yaw error is the actual yaw,  $\theta$ , of the motion stage as it moves within its range of motion

The above definitions are based on a serial arrangement of the X and Y bearing ways. For parallel stages, the idea remains similar, but the interpretations are slightly different. In this case, the orthogonality error and the straightness error are not two independent entities because they arise from the same kinematics or mechanics. The two together form the cross-axis error, which will have a linear component (corresponding to the orthogonality error), and a non-linear component (corresponding to the straightness error).

The metrology set-up invariably involves a set of sensors that are fixed to the ground and aligned with the ideal stage axes, an artefact attached to the motion stage that acts as the target for the sensors and is aligned with the stage axes. Irrespective of whether the stage is serial or parallel, the errors associated with metrology remain the same. These are,

- 1) Artefact geometry error: The artefact is usually such that it provides two very straight edges that are close to perpendicular.<sup>2</sup> The lack of orthogonality between the artefact axes  $X''$  and  $Y''$  is captured by the angle  $\gamma$  in Fig. 6.14.
- 2) Artefact alignment error: This represents the misalignment between the artefact axes and the stage axes, for example the angle  $\beta$  shown between  $X'$  and  $X''$  in the above figure. One usually employs precision ground pins pressed into precision drilled holes to achieve the best possible alignment. Nevertheless this misalignment remains, and results in a sine error in the X axis measurement when the stage moves along the  $Y'$  axis.
- 3) Artefact straightness error: This relates to the lack of straightness of the artefact faces, and is not shown in the above figure. Typically artefact straightness is several orders of magnitude better than the stage straightness error itself and is therefore not an important contributor.
- 4) Sensor alignment error: This is the angle that the sensor line of measurement makes with the ideal system axes. This is the typical cosine error, represented by  $\xi$ , which can be minimized by careful alignment of the sensor axes.

---

<sup>2</sup> Manufacturing a straight-edge is much easier than producing two perfectly orthogonal edges.

While the importance of careful metrology set-up is unquestionable, it is an objective of the metrologist to design the experiment to be insensitive to the metrology set-up errors, and be the most responsive to the stage errors. By making multiple in-plane measurements and employing principles of reversal, one can cleverly discard some of the metrology related errors. Some examples are presented here. From Fig. 6.14, one can easily determine that,

$$C_1 \cos \xi_1 = x_1 = y' \sin \alpha - y' \sin(\beta + \gamma) + R_1 \sin \theta \quad (6.1)$$

where  $x_1$  is displacement along the X axis at location  $C_1$ ,  $y'$  is the displacement along the  $Y'$  axis, and so on. The misalignment angles in expression (6.1) are typically of the order of 1ppm. One can justifiably use the small angle approximation, without incurring errors of more than 1ppb. Thus,

$$\begin{aligned} C_1 \cos \xi_1 &= x_1 = y' \alpha - y' (\beta + \gamma) + R_1 \theta \\ &= y' (\alpha - \beta) - y' \gamma + R_1 \theta \end{aligned} \quad (6.2)$$

$$\text{Similarly, } C_2 \cos \xi_2 = x_2 = y' (\alpha - \beta) - y' \gamma + R_2 \theta \quad (6.3)$$

If  $\xi_1$  and  $\xi_2$  are small, one can easily obtain the stage yaw error  $\theta$  using two measurements  $C_1$  and  $C_2$ , irrespective of what the other stage errors and metrology errors are. Furthermore,  $\gamma$  can be eliminated by performing a standard reversal trick. Referring to Fig. 6.15, the artefact is reversed and a third sensor is introduced. This allows for the following additional measurement,

$$C_3 \cos \xi_3 = x_3 = -y' (\alpha - \beta) - y' \gamma - R_3 \theta \quad (6.4)$$

Comparing expressions (6.3) and (6.4), it can be noticed that the sign of the  $\gamma$  term has been reversed with respect to the other terms, due to the physical reversal of the artefact. Subtracting the two expression eliminates the  $\gamma$  term.

As shown in Fig. 6.15, while some of the metrology set-up errors can be eliminated simply by the use of reversal and symmetry, others may pose a more difficult problem. One may notice, for example, that in all of the measurements (6.2) - (6.4), the parameters  $\alpha$  and  $\beta$  always occur in a particular combination,  $(\alpha - \beta)$ . Some amount of careful thought reveals that no matter what configuration of sensors is used,  $\alpha$  and  $\beta$  will always occur in the same combination. Hence, it become not just difficult but impossible to distinguish between the two errors.

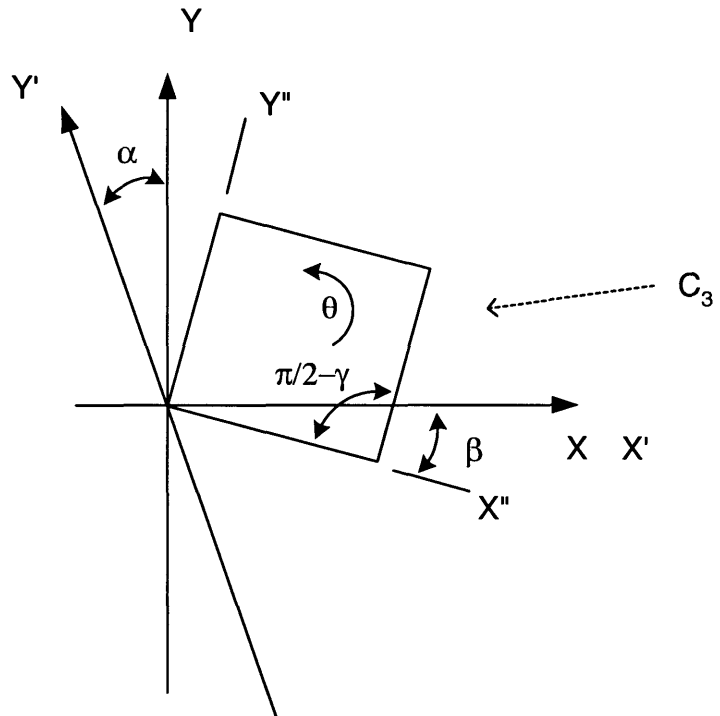


Fig 6.15

This brings us to one of the classic problems in metrology – in the error measurement of an XY stage, how does one differentiate between two errors: orthogonality error of the stage and alignment error of the sensor target artefact, without resorting to an explicit measurement of either one. Based on literature searches [88] and discussions with several metrology experts, we have arrived at the conclusion that the two errors remain indistinguishable irrespective of the number and arrangement of sensors used.

The straightness error of the stage and the artefact share the same fate. But in this case, the latter is several orders of magnitude lower than the former, and hence is not as bothersome. On the other hand, a relatively large artefact misalignment error may masquerade as an orthogonality error, thus giving an incorrect assessment of the cross-axis error characteristics of an XY stage. The only suggested remedy to resolve this situation is to explicitly measure the misalignment between the stage and the artefact, which we refer to as target block in the previous discussion. All subsequent measurement should be corrected based on this initial measurement. Another fact that becomes obvious based on this discussion is that good sensor alignment is critical in avoiding cosine errors, and there does not exist an obvious way to cancel these out.

**This page is intentionally left blank**

## Chapter 7. Experimental Measurements

This chapter attempts a comparison between the analytical predictions of the performance of XY Flexure Mechanism Design 6 made in Chapter 5, and the experimental measurements obtained from the test set-up described in Chapter 6. This section presents the experimental measurements based on the prototype fabricated by wire EDM.

In all the laser interferometry based experiments, the uncertainty in measurement is due to cosine errors resulting from laser optics misalignment, and change in ambient temperature, pressure and humidity. To minimize these error sources, the optics were very carefully aligned, the dead paths were kept small, and a compensation for the wavelength of light based on temperature, pressure and humidity measurements, was included. The overall uncertainty in measurement as a consequence of all these effects is of the order of 25nm. Other important sources of errors arise from actual physical effects such as thermal expansion and misalignment of the target block. The former was taken care of by conducting the experiments in a temperature controlled environment, whereas the latter was resolved by measuring the target block misalignment explicitly on a CMM. The single most detrimental effect on the measurements arose from the ball bearing used in the pulley for suspending free weights. Hysteresis and creep at the interface of the fishing line and the pulley, and the balls and the race, resulted in large unexplained variations in the measurements of the order of 200nm. As pointed out earlier, this problem may be resolved by implementing a virtual pulley instead of a real pulley.

When weights are used for actuation, there is an uncertainty in the actual value of the weight, which is of the order of 0.5%. The PI motors that were used for actuation provide displacements with an uncertainty of 1-2 microns, resulting from friction and backlash in the system. Referring to Fig. 5.23, the actual dimensions of flexure mechanism that has been tested are as follows,

$L$	47.5mm	$U$	25mm	$T$	0.625mm	$R$	46.25mm
$A_o$	46.25mm	$B_o$	23.75mm	$W_1$	18.44mm	$W_2$	12.81mm

### 7.1 Primary Motion and Stiffness

The first step is to measure displacement and stiffness in X direction for different values of Y loads, and vice versa. The analysis predicts these to be

$$x_s = \frac{f_x}{4a} \frac{1}{\left(1 - \frac{3e^2 f_y^2}{64a^2}\right)}$$

$$y_s \approx \frac{f_y}{4a} \frac{1}{\left(1 - \frac{3e^2 f_x^2}{64a^2}\right)}$$

Fig. 7.1 presents a plot of primary X displacement versus weights  $W_x$  applied to the X axis for different values of Y force. This experiment is conducted using calibrated weights. A 5 kg weight (or 49N force) produces a primary displacement of approximately 2.5mm. The corresponding primary stiffness is in agreement with the above prediction. The analytical result predicts less than 2% change in the primary stiffness, which is corroborated by the apparently overlapping lines in Fig.7.1. These different lines correspond to the X force – X displacement measurement, in the presence of Y forces ranging from 0 to 30N. Linearity over the entire range of travel indicates the lack of any over-constraining phenomena in the system. A range of motion of 2.5 mm, or approximately 0.05 non-dimensional units, is chosen keeping in mind the predicted loss in axial stiffness (5.16).

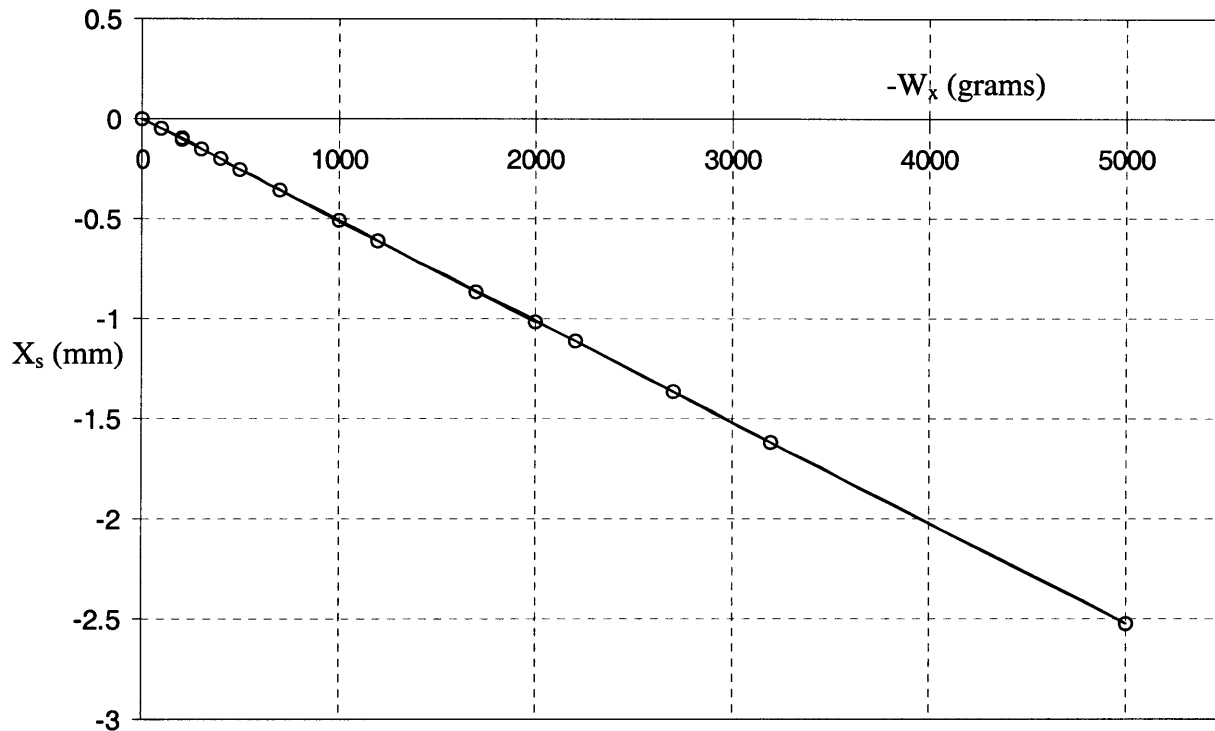


Fig. 7.1

The applied weights correspond to a negative force in our notation of Fig. 5.24, and hence the negative values of primary displacement. Similar plots are obtained for the primary Y displacement and stiffness as well. The measured stiffness in the X and Y directions differ by less than 0.1%, which is actually within the error of the measurement.

## 7.2 Cross-axes Coupling Error

From expression (5.11), we can determine that the contribution of an X direction force to Y displacement of the motion stage, in the presence of a Y force.

$$y_s^* = y_s - y_s \Big|_{f_x=0} = \frac{f_y}{4a} \left( \frac{e^2 f_x^2 (3 + x_l^2 ei)}{64a^2 - 3e^2 f_x^2} \right) \approx \frac{3e^2}{256a^3} f_x^2 f_y$$

An analogous expression can be derived for the other direction as well. This relationship indicates that the cross-axis coupling has a weak quadratic dependence on the transverse load.

This is verified by an experiment where the Y force was kept constant, and Y displacement was measured for varying X forces. The experiment was repeated for different values of Y forces. Both X and Y forces were applied by means of free weights. Fig. 7.2 presents the results for the case when the Y force was zero.

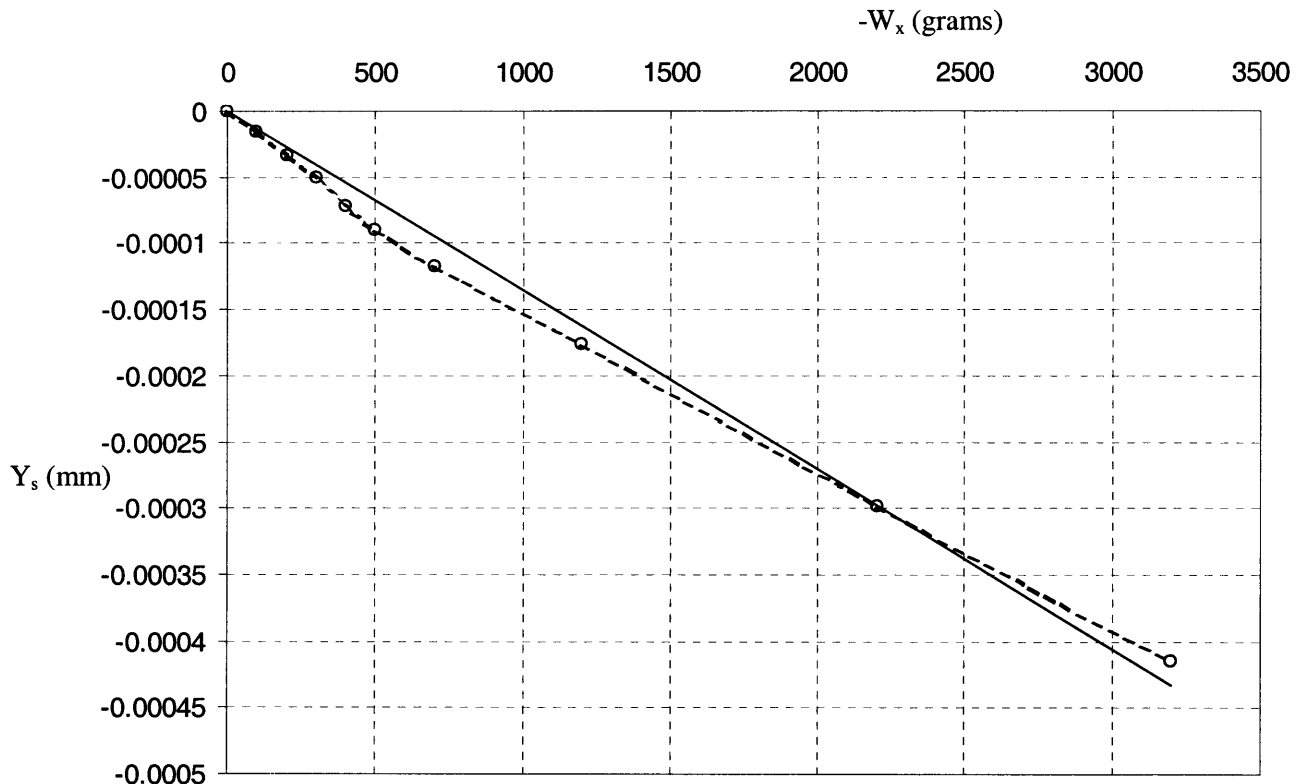


Fig. 7.2

The above plot indicates an approximately linear variation of the Y displacement with X force which does not agree with the analytical predictions. 135 microns of Y displacement is measured per 1000 gram of X force, or 0.5 mm of X displacement. This measurement can be a consequence of one or more of the following effects

- 1) True cross-axis error in the mechanism, if the manufacturing was perfect: Based on the analysis this is not expected.
- 2) Orthogonality error in the mechanism due to manufacturing: This is a possibility and therefore the orthogonality of the blades axes needs to be measured.
- 3) Misalignment between stage axes and artefact axes: Based on the discussion of Section 6.6, this is the most likely source of error, and therefore needs to be measured explicitly.

The last two possibilities were checked using a Coordinate Measuring Machine. Fig. 7.3 indicates the Y measurements made along four blades that are aligned with the mechanism's X axis. This measurement is made with reference to the target block axes. Similar measurements of the X coordinates were also made along multiple Y blades.

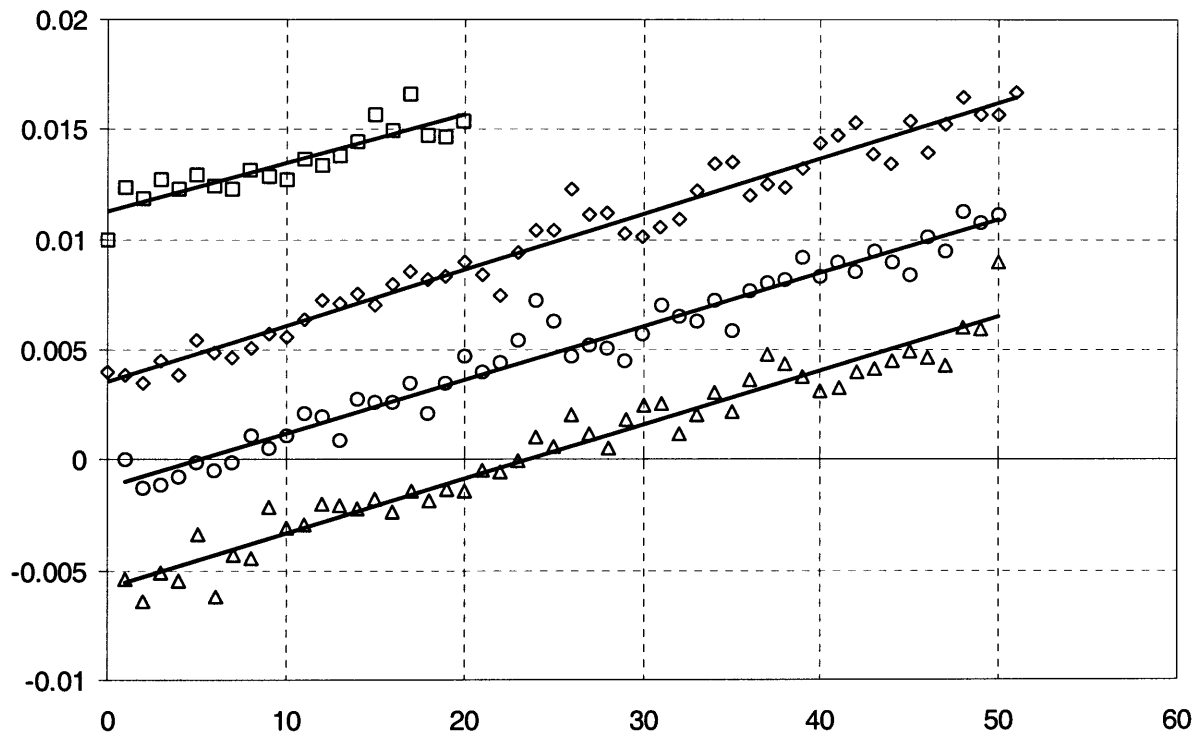


Fig 7.3

These results indicate that the blades along one mechanism axis maintain excellent parallelism among themselves and excellent orthogonality with the blades in the other flexure axis. This is expected, given the capabilities of wire EDM machining, and rules out the second possibility above. The results also clearly indicate an angular misalignment between the blades and the flexure axes, which is seen to be approximately 12.5 micron / 50mm, or 250  $\mu$ radians. Given the tolerances of the pins that locate the target block, this is a reasonable number.

This almost perfectly explains the cross-axes error measurement of 270nm/mm made earlier. Similar measurements were made with the roles of the two axes switched, and once again we measured a cross-axis error of approximately 255nm/mm. This further confirms the target block misalignment conjecture. If the cross-axis measurements are corrected for this misalignment, the range of Y motion vs. X forces, for zero Y force is smaller than what can be reliably measured in this experiment. This agrees well with the analytical predication above. Next we measure the Y displacement with X force, in the presence of finite Y forces, and the results are presented in Fig. 7.4. In reporting all these measurements, we take into account the target block misalignment.

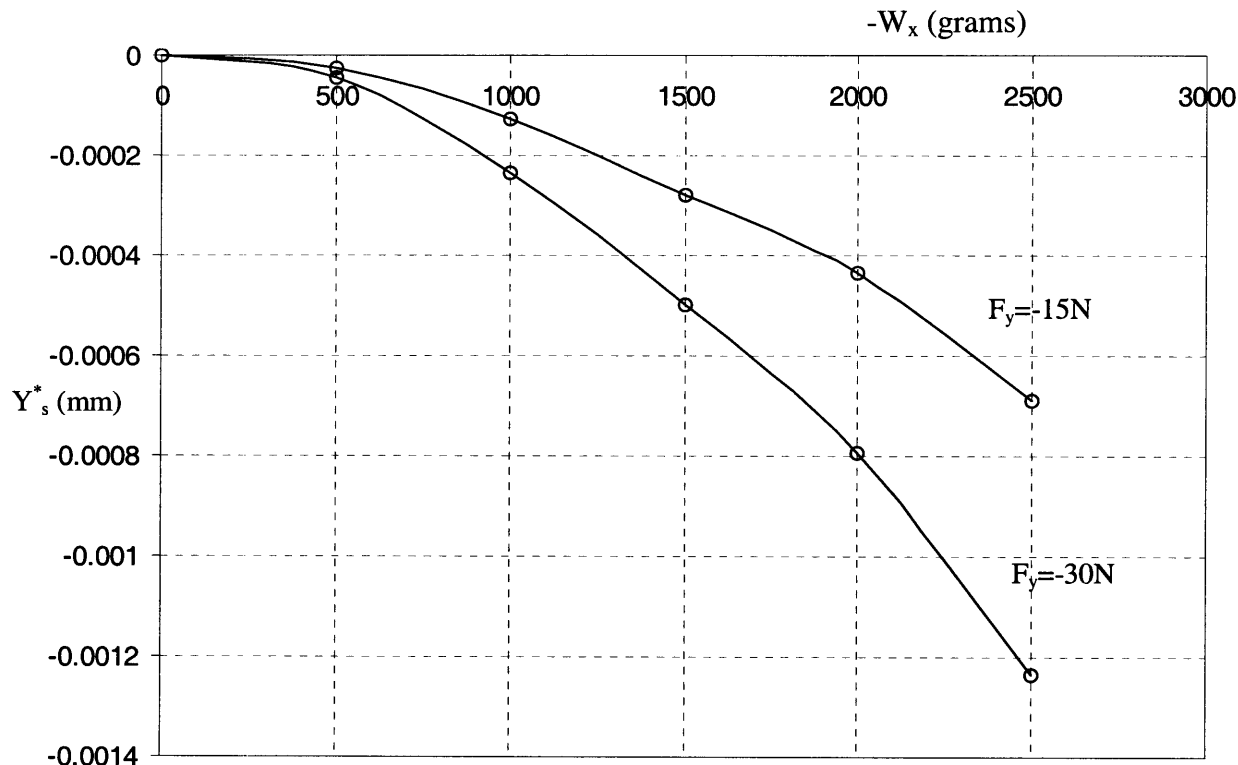


Fig. 7.4

As predicted by the analysis, this indicates that the cross-axes errors in Y increase quadratically with forces in X direction. For a primary motion of 1mm, this error can be as large as 1 micron.

Similar tests were repeated with other loading configurations, for example, the primary motion in X direction was produced with the DC motor instead of the free weights, while weights were used for loading the Y axis. Measurements that match Fig. 7.4 were obtained.

A yet another method of checking the cross-axis errors, and the axial component of actuator isolation is by holding the Intermediate Stage 2 at specified positions using the Y motor, and loading the X direction by means of weights. This will provide us with several pieces of information including: the difference between the Intermediate Stage 2 displacement and motion stage displacement, variation in the axial stiffness between intermediate stage 2 and motion stage, and actuator isolation.

Based on the results of Chapter 5, it may be shown that the deviation of motion stage Y displacement, from its nominal displacement, in response to X force, is given by the following expression. Nominal is defined by the condition when X force is zero.

$$\begin{aligned}
 y_s^* &= y_s - y_s \Big|_{f_x=0} \\
 &= y_s - y_1 \approx \frac{3}{8} \frac{f_y x_l^2 e i}{a} \\
 &\approx \frac{3 e i}{8 a} 4 a y_2 \left( 1 - \frac{3 e^2 f_x^2}{64 a^2} \right) \frac{f_x^2}{16 a^2} \left( 1 - \frac{3}{2} e^2 y_2^2 \right) \\
 &= \frac{3 e i}{32 a^2} y_2 \left( 1 - \frac{3}{2} e^2 y_2^2 \right) f_x^2 \left( 1 - \frac{3 e^2 f_x^2}{64 a^2} \right) \approx \frac{3 e i}{32 a^2} y_2 f_x^2
 \end{aligned}$$

Fig. 7.5 presents the results of a corresponding measurement. This time, Y displacement of Intermediate Stage 2 is set at several locations between  $-1.25$  and  $+1.25$  mm. At each of these locations X load is varied by applying free weights, and Y displacement of motion stage is measured.

Once again, in this case the effect of target block misalignment is apparent when we consider the case of  $Y=0$ . This case appears to be an approximate straight line, whereas the analysis predicts zero variation here. On measurement using a CMM, it found that indeed this corresponds to the target block misalignment, which in this case is approximately, 480nm/mm, or 480  $\mu$ radians. If one eliminates the linear part from the measurements of Fig. 7.5, they match with the analysis.

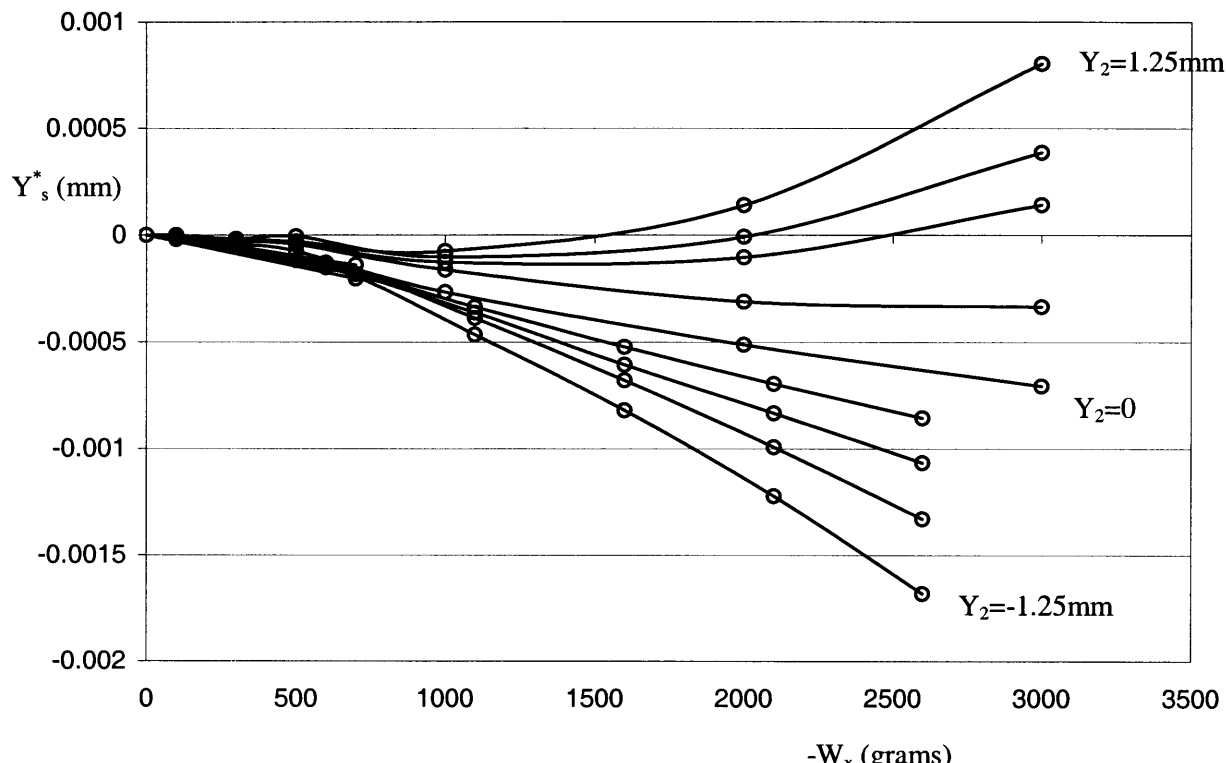


Fig. 7.5

From the above measurements, the quadratic dependence of the inline stiffness between  $Y_s$  and  $F_y$ , on force  $F_x$  is also verified.

Variation in these displacement results under the application of off-centered loads is unnoticeable. The analysis also shows that the moments on the system and displacements are fairly decoupled.

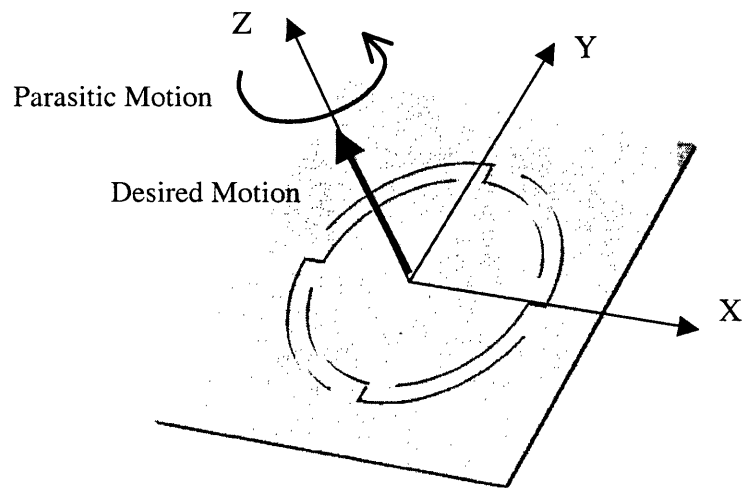
### 7.3 Parasitic Yaw Error

Parasitic yaw is measured by moving the motion stage over its entire range of motion, which is  $\pm 2.5\text{mm}$  in both directions. The measured values of stage rotation stayed within 0.5 arc seconds and did not show any noticeable trend. This observation agrees with Fig. 5.32, which predicts extremely small rotation angles over the tested range of the mechanism.

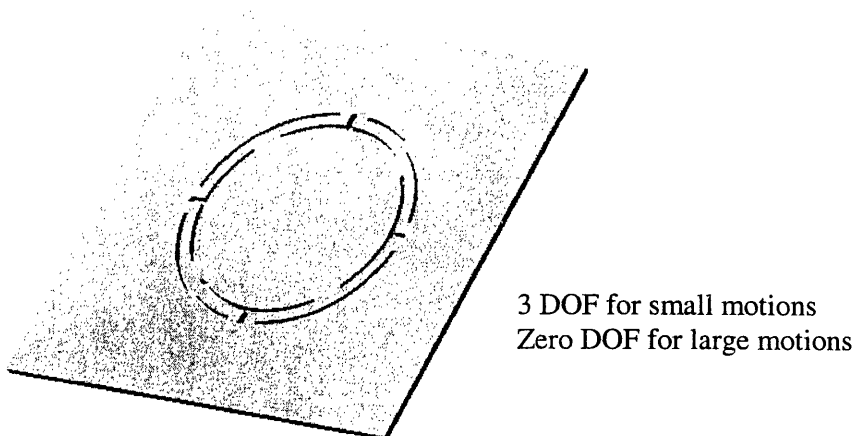
**This page is intentionally left blank**

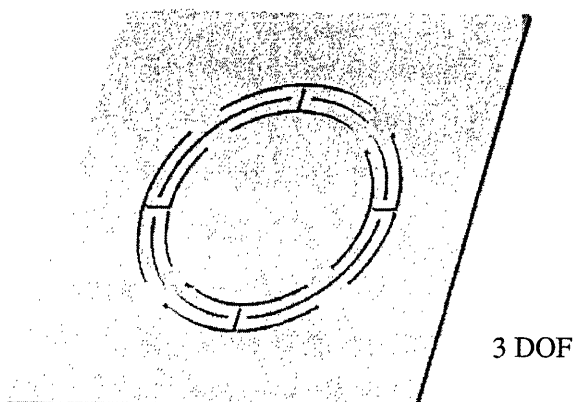
## Appendix A. Multiple DOF Flexure Mechanism Designs

### 1. Conventional Diaphragm Flexure: 3 DOF

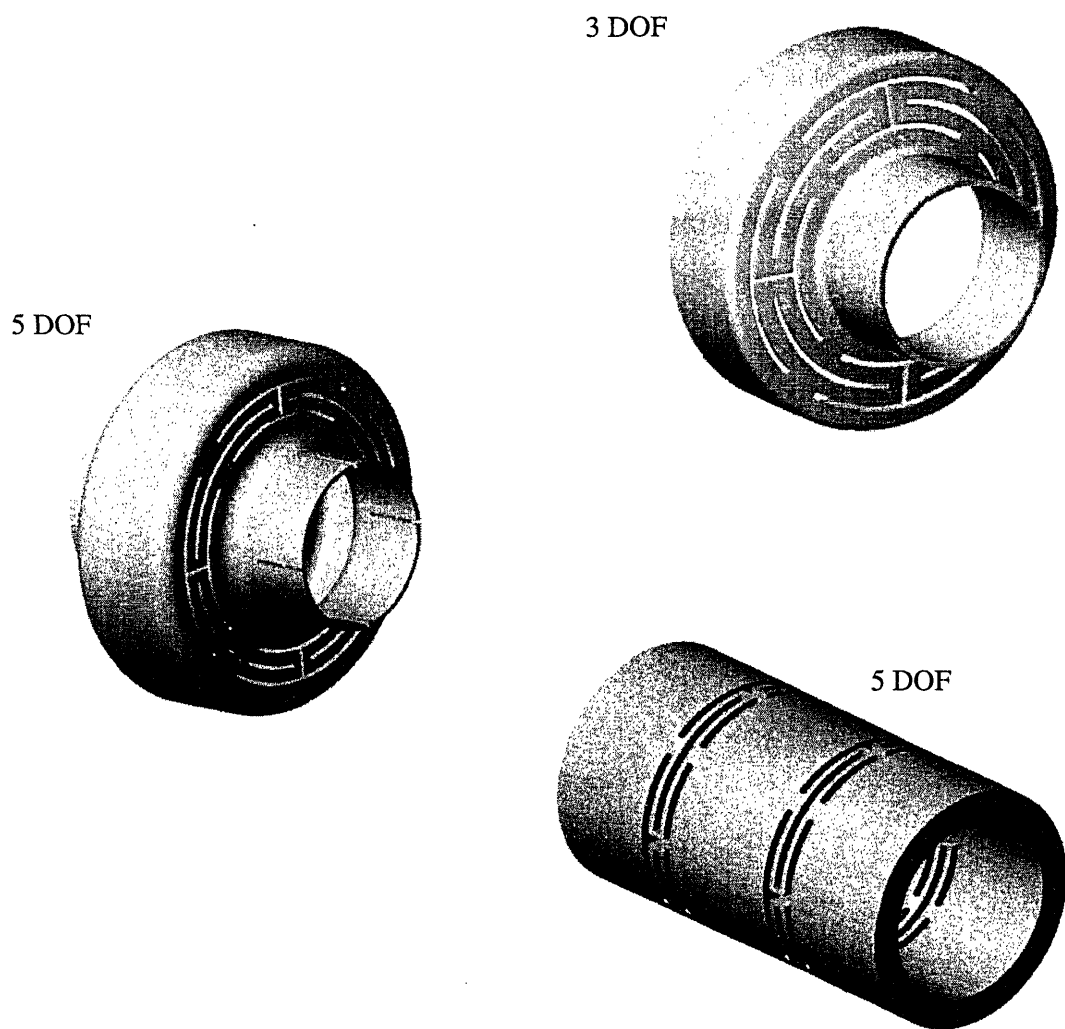


### 2. Symmetric Diaphragm Flexures free of parasitic error

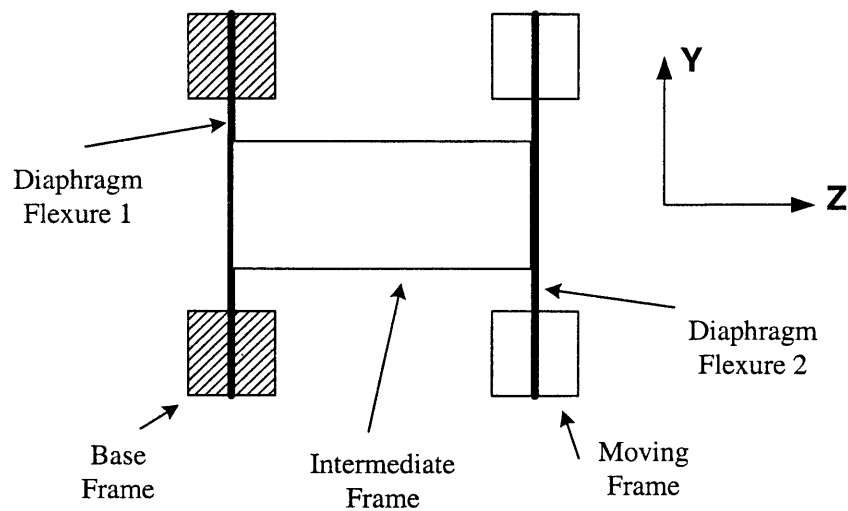




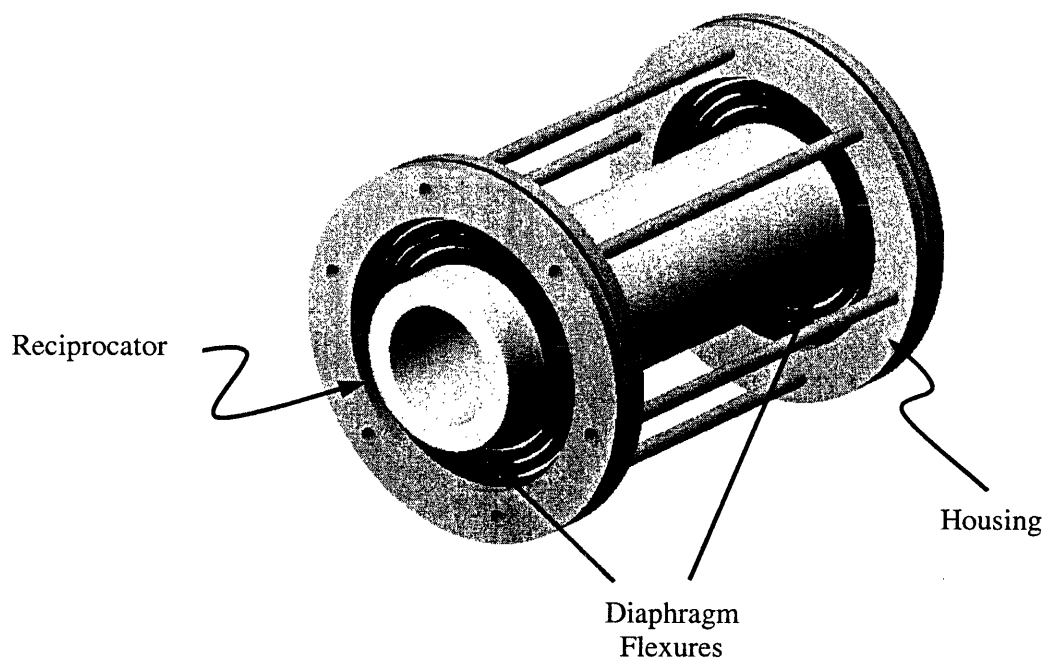
3. Flexible Couplings based on the symmetric diaphragm flexure



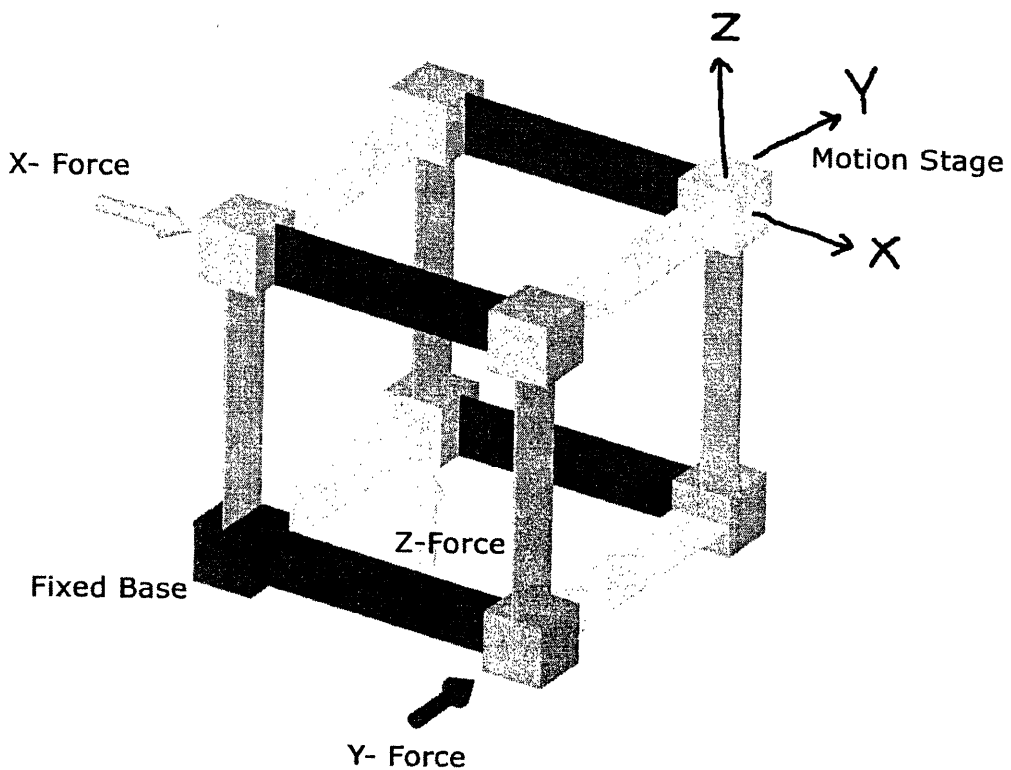
4. Five DOF flexure stage based on the diaphragm flexure



5. Single DOF linear bearing based on the symmetric diaphragm flexure



6. Three DOF decoupled XYZ mechanism



## References

1. Jones R.V., 1988, *Instruments and Experiences: Papers on Measurement and Instrument Design*, John Wiley & Sons
2. Slocum A.H., 1992, *Precision Machine Design*, Society of Manufacturing Engineers, Dearborn, MI
3. Blanding, D.K., 1999, *Exact Constraint: Machine Design Using Kinematic Principles*, ASME Press, New York
4. Hale L.C., 1999, *Principles and Techniques for Designing Precision Machines*, Ph.D. Thesis, Massachusetts Institute of Technology, Cambridge MA
5. Motsinger R.N., 1964, “Flexural Devices in Measurement Systems”, Chapter 11 in *Measurement Engineering* by P.K. Stein, Stein Engineering Services
6. Midha A., 1993, “Elastic Mechanisms”, Chapter 9 in *Modern Kinematics – The developments in the Last Forty Years*, John Wiley & Sons
7. Smith S.T., and Chetwynd D.G., 1992, *Ultra-Precision Mechanism Design*, Gordon and Breach Science Publishers
8. Smith S.T., 2000, *Flexures: Elements of Elastic Mechanisms*, Gordon and Breach Science Publishers
9. Howell L.L, 2001, *Compliant Mechanisms*, John Wiley & Sons
10. Lobontiu N., 2003, *Compliant Mechanisms: Design of Flexure Hinges*, CRC Press
11. Paros J. M., and Weisbord L., 1965, “How to Design Flexure Hinges”, *Machine Design*
12. Eastman F.S., 1937, “The Design of Flexural Pivots”, *Journal of Aerospace Science*, Vol. 5, Nov.
13. Ejik J.V., “On the Design of Plate Spring Mechanism”, Ph.D. thesis, Delft University of Technology, Delft, The Netherlands, 1985
14. Burns R.H., and Crossley F.R.E., 1968, “Kinetostatic synthesis of flexible link mechanisms”, ASME Paper No. 68-MECH-36
15. Her I., 1986, “ Methodology for Compliant Mechanisms Design,” Ph.D. Thesis, Purdue University, West Lafayette
16. Jensen B.D. et al, 1997, “The design and analysis of Compliant MEMS Using the Pseudo-rigid-body Model”, *Microelectromechanical Systems*, at the ASME International Mechanical Engineering Congress and Exposition, Vol. 62, pp 119-126
17. Ananthasuresh G. K., 1994, “A new design paradigm in microelectromechanical systems and investigations on compliant mechanisms”, Ph.D. Thesis, University of Michigan, Ann Arbor, MI
18. Ananthasuresh G.K., Kota S., and Gianchandani Y., “ A Methodical Approach to design of compliant Micromechanisms”, *Solid State Sensor and Actuator Workshop*, Hilton Head Island, SC, pp 189-192

19. Petri, P.A., 2002, *A Continuum Mechanic Design Aid for Non-planer Compliant Mechanisms*, M.S. Thesis, Massachusetts Institute of Technology, Cambridge MA
20. Her I. and Midha A., 1987, "A Compliance Number Concept for Compliant Mechanisms, and Type Synthesis", *ASME Journal of Mechanisms, Transmission, and Automation in Design*, Vol. 109, No.3, pp 348-355
21. Ananthasuresh G.K., and Howell L.L., 1996, "Case Studies and a Note on the Degree-of- Freedom in Compliant Mechanism", *Proceedings of the 1996 ASME Design Engineering Technical Conferences*, 96-DETC/MECH-1217
22. Murphy M. D., Midha A., and Howell L. L., 1994, "On the Mobility of Compliant Mechanism", *Proceedings of the 1994 ASME Mechanisms Conference*, DE-Vol.71, pp. 475-479
23. Den Hartog J.P., 1952, *Advanced Strength of Materials*, McGraw Hill
24. Erdman A., and Sandor G., 1984, *Mechanism Design: Analysis and Synthesis*, Prentice-Hall, New Jersey
25. Haftka R.T., and Gurdal Z., 1990, *Elements of Structural Optimization*, Kluwer Academic, Dordrecht, The Netherlands
26. Saggere L., and Kota S., 2001, "Synthesis of Planer Compliant Four-Bar Mechanisms for Compliant Segment Motion Generation", *ASME Journal of Mechanical Design*, Vol. 123, pp 535-541
27. Hetrick J., and Kota S., 1999, "An energy formulation for parametric Size and Shape Optimization of Compliant Mechanism" *ASME Journal of Mechanical Design*, Vol. 21, No. 2 , pp 229-234
28. Sigmund O., 1997, "On the design of Complaint Mechanisms Using Topology Optimization," *Mechanics of Structures and Machines*, Vol. 25, No. 4, pp 495-526
29. Frecker M.I., Ananthasuresh G.K., Nishiwaki S., Kickuchi N., and Kota S., 1997, "Topological Synthesis of Compliant Mechanisms Using Multi-criteria optimization," *Journal of Mechanical Design*, Vol. 119, pp 238-245
30. Nishiwaki S., Frecker M.I., Min S.J., Kickuchi N., 1998, "Topology optimization of Compliant Mechanisms Using the Homogenization Method," *International Journal for Numerical Methods in Engineering*, Vol. 42, No. 3, pp. 535-559.
31. Awtar S., and Slocum A.H., 2004, "Apparatus Having motion with Pre-determined degree of Freedom", US Patent 6,688,183 B2
32. Products P-721, P-750 and P-780, Physik Instrumente Product Catalog, 2001, MicroPositioning, NanoPositioning, NanoAutomation: Solutions for Cutting-Edge Technologies
33. US Patent 5808435, "Micropositioning Device for Disk Head Testing System", KMY Instruments, 1998

34. US Patent 6282066, "MicroActuator Suspension with Multiple Narrow Beams", Seagate Technologies LLC, 2001
35. Chang S.H., and Du, B.C., 2002, "A precision piezodriven micropositioners mechanism with large travel range", *Review of Scientific Instruments*, Vol 69, No. 4, pp 1785-1791
36. Chen, J-L, Chang, H-Y, and Wu, C-S, 2003, "A Study on a Long Range Nano-Precision Positioning system", *Proceedings of ASME-IMECE 2003*, Washington DC, Nov 15-21
37. Products P-280 and P-762, Physik Instrumente Product Catalog, 2001, MicroPositioning, NanoPositioning, NanoAutomation: Solutions for Cutting-Edge Technologies
38. Fischer F.L., 1981, "Symmetrical 3 DOF Compliance Structure", US Patent 4447048
39. Smith A.R., Gwo S., and Shih C.K. 1994, "A new high resolution two-dimensional micropositioning device for scanning probe microscopy", *Review of Scientific Instruments*, Vol. 64, No. 10, pp 3216-3219
40. N.G. Dagalakis, J.A. Kramer, E. Amatucci, R.Bunch, "Kinematic Modelling and Analysis of Planer Micro-positioner", *Proceedings of ASPE 2001 Annual Meeting*, pp 135-138
41. "Agilent Technologies NanoStepper", MIT Technology Review, June 2003, pp. 14. Details also available at [www.labs.agilent.com](http://www.labs.agilent.com) and J7220 Data Sheet
42. Bednorz J.G., et al, 1985, Piezoelectric XY Positioner, US Patent 4520570
43. M-850, F-206 HEXAPOD, Physik Instrumente Product Catalog, 2001, MicroPositioning, NanoPositioning, NanoAutomation: Solutions for Cutting-Edge Technologies
44. Culpepper M.L., 2003, "Multiple Degree of Freedom Complaint Mechanism," US Patent Application 20030086751
45. Dagalakis N.G., and Amatucci E.G., 2002, "Six Degree of freedom Micropositioner", US Patent 6484602
46. Davies P.A., 2001, "Positioning Mechanism", US Patent 6,193,226
47. Jokiel B., Benavides G.L., Bieg L.F., Allen J.A., 2001, "Planer and Spatial Three Degree of Freedom Micro Stages in Silicon MEMS", *Proceedings of ASPE 2001 Annual Meeting*, pp 32-35
48. T.B. Eom and J.Y. Kim, "Long Range Stage for the Metrological Atomic Force Microscope", *Proceedings of ASPE 2001 Annual Meeting*, Pg. 156-159
49. Kanai et al, 1983, "An Elastic Fine Positioning Mechanism Applied to Contactless X-Y Table", *Bulletin of JSPE*, Vol 17, No. 4, pp 265-266
50. Agilent Technologies Inc., 2002, "Precision Positioner for Optical Elements", US Patent 6414785
51. Hitachi Ltd., 1986, "Ultra-Precision Two-Dimensional Moving Apparatus", US Patent 4575942
52. IBM Corp., 1991, "Two-Dimensional Positioning Apparatus", US Patent 5059090

53. Chen K.S., Trumper D.L., and Smith S.T., 2002, "Design and Control for an electromagnetically driven X-Y-q Stage", *Journal of Precision Engineering and Nanotechnology*, Vol 26, pp 355-369
54. Products P-733 and 750 P-770, Physik Instrumente Product Catalog, 2001, MicroPositioning, NanoPositioning, NanoAutomation: Solutions for Cutting-Edge Technologies
55. Ryu J.W., Gweon D.-G., and Moon K.S., 1997, "Optimal Design of a Flexure hinge based X-Y-θ wafer stage", *Journal of Precision Engineering*, Vol.21 No.1, pp 18-28
56. Correspondence with Layton H.C.
57. Chang S.H., Tseng C.K., and Chien H.C., 1999, "An ultra-Precision XYθ<sub>Z</sub> Piezo-Micropositioner Part I: Design and Analysis", *IEEE Transactions on Ultrasonics, Ferroelectrics, and Frequency Control*, Vol 46, No. 4, pp 897-905
58. Chang S.H., Tseng C.K., and Chien H.C., 1999, "An ultra-Precision XYθ<sub>Z</sub> Piezo-Micropositioner Part I: Experiment and Performance", *IEEE Transactions on Ultrasonics, Ferroelectrics, and Frequency Control*, Vol 46, No. 4, pp 906-912
59. Teague E.C., et al, 2001, "Molecular Machine Design and Performance", *ASPE Conference*, 2001
60. Gorman, J. J. & Dagalakis, N. G., "Force control of linear motor stages for microassembly", *ASME International Mechanical Engineering Conference and Exposition*, Washington, DC, 2003, IMECE2003 – 42079
61. "Overview of the High Precision Microscope Project", University of Illinois Laboratory for Fluorescence Dynamics, UIUC, 2000
62. Vettiger, P., et al, 2000, "The Millipede – More than one thousand tips for future AFM data storage", *IBM Journal of Research and Development*, Vol 44, No. 3, pp 323-340
63. iMEMS Accelerometers (ADXL Series) and Gyroscopes (ADXRS Series), Analog Devices, [www.analog.com](http://www.analog.com)
64. Xu. Y., Atherton, P.D., Hicks, T.R., McConnell, M. and Rhead, P. , "Design and Characterization of an Ultra-Precision X-Y Stage", Queenstage Instrument Limited
65. Culpepper, M.L., Anderson G., "Design of a Low-Cost Nano-manipulator which utilizes a monolithic spatial compliant mechanism", submitted to *Journal of Precision Engineering*
66. Piezoelectrics Tutorial, Physik Instrumente Product Catalog, 2001, MicroPositioning, NanoPositioning, NanoAutomation: Solutions for Cutting-Edge Technologies
67. Heidenhain Exposed Two-coordinate Encoders, [www.heidenhain.com](http://www.heidenhain.com)
68. Slocum A.H., MIT Design and Manufacturing I (2.007) Lecture Notes
69. Den Hartog, 1952, J.P., *Advanced Strength of Materials*, McGraw Hill 1952
70. Archer, R.R., et al, 1972, *An Introduction to the Mechanics of Solids*, McGraw Hill , New York
71. Timoshenko S.P., Goodier, J.N., 1970, *Theory of Elasticity*, McGraw Hill, New York

72. Timoshenko, S.P., 1953, *History of Strength of Materials, with a brief account of the Theory of Elasticity and the Theory of Structures*, McGraw Hill, New York
73. Bisschopp, K.E., and Drucker, D.C., 1945, "Large Deflection of Cantilever Beams", *Quarterly of Applied Mathematics*, Vol. 3, No. 3, pp.272-275
74. Frisch-Fay, R., 1963, *Flexible Bars*, Butterworth, Washington DC
75. Mattiasson, K., 1981, "Numerical Results from Large Deflection Beam and Frame Problems Analyzed by Means of Elliptic Integrals", *International Journal for Numerical Methods in Engineering*, Vol 17, pp 145-153
76. Plaineaux J.E., 1956, "Etude des deformations d'une lame de suspension elastique", *Nuovo Cimento*, Vol. 4, pp 922-928
77. Mallik A.K., Ghosh A., and Dittrich G., 1994, *Kinematic Analysis and Synthesis of Mechanisms*, CRC Press
78. Tauchert T.R., 1974, *Energy Principles in Structural Mechanics*, McGraw Hill
79. Dym C.L., and Shames I.H., 1996, *Energy and Finite Element Methods in Structural Mechanics*, Hemisphere Publishing Corporation
80. Tabarrok B., 1984, "Complementary Variational Principles in ElastoDynamics", *Computers and Structures*, Vol. 19, No. 1-2, pp 239-246
81. Westergaard H.M., 1942, "On the method of Complementary Energy", *Transactions of the American Society of Civil Engineers*, Vol. 112, pp 765-803
82. Mikkola M.J., 1989, "Complementary Energy Theorem in Geometrically Non-linear Structural Problems", *International Journal of Non-Linear Mechanics*, Vol.24, No.6, pp 499-508
83. Zhou G. and Dowd P., 2003, "Tilted folded-beam suspension for extending the stage travel range of comb-drive actuators", *Journal of Micromechanics and Microengineering*, Vol. 13, pp 178-183
84. Legtenberg R., Groeneveld A.W. and Elwenspoek M., 1996, "Comb-drive actuators for large displacements", *Journal of Micromechanics and Microengineering*, Vol. 6, pp 320-329
85. Jaecklin V.P., Linder C., and de Rooij N.F., 1992, Novel Polysilicon Comb Actuators for XY stages, *Proceedings of IEEE MicroElectro Mechanical Systems' 92*, pp 147- 149
86. Zelenika S., and DeBona F., 2002, "Analytical and experimental Characterization of high precision flexural pivots subjected to lateral load", *Precision Engineering*, Vol. 26, 381-388
87. ASM Metals handbook
88. Bobroff, N., 1993, "Critical alignments in plane mirror interferometry", *Journal of Precision Engineering*, Vol 15, pp 33-38

89. Brian A. H., Dupont P., and Canudas de Wit C., 1994, ‘Friction in Servo machines: Analysis and control methods”, part of “Friction Induced Vibrations” edited by Ibrahim R.A. and Rivin E., Applied Mechanics Reviews, Vol 47, No 7, July